Repair of Aluminum Alloy Aerospace Components and Cold Gas Dynamic Spray Flow Distribution Study

by

Aleksandra Nastic

A thesis submitted to the Faculty of Graduate and Postdoctoral Studies
in partial fulfillment of the requirements for the degree of

MASTER OF APPLIED SCIENCE

in Mechanical Engineering

Ottawa-Carleton Institute for Mechanical and Aerospace Engineering
Faculty of Engineering
University of Ottawa

Ottawa, Canada 2015

Abstract

Aluminum alloys have been used for decades in aircrafts as they offer a wide range of properties explicitly developed to provide a set of characteristics adapted to structural and non-structural components. Properties such as high strength-to-weight ratio, good corrosion resistance and good fracture toughness can be achieved in aluminum alloys through the optimisation of their chemical composition and processing parameters. Despite their good mechanical properties, aircraft components inevitably undergo degradation and damage during service due to their extensive use and exposure to harsh environments, which ultimately affect their load carrying capacity and overall performance. The damaged component is most often replaced due to the lack of adequate repair technology, which is not considered as an economical long-term solution. Typical repair and restoration technologies consist of ion vapour deposition, laser beam cladding, welding and thermal spray processes. However, these methods are either inefficient for large scale repairs due to their low material growth rate, unsuitable for field repair or involve the use of high process temperatures. Use of excessive heat can alter the chemical composition and mechanical properties and induce oxidation of both the deposited metallic particles and the base material. As property alterations are not desired and represent a major throwback, the aerospace industry is continuously on the search of innovative repair technologies.

The present research aims at evaluating the cold gas dynamic spray (CGDS) process as a potential repair technology. The current research studies the repair of Al7075-T6 nose landing gear steering actuator 3.75-12UNJ-3A threads found on the Boeing 757 aircraft using pure aluminum powder. Moreover, it studies the deposition ability and process of Al2024 material on Al2024-T3 components. The influence of process parameters on the material deposition efficiency and resulting microstructural and mechanical repair properties has been evaluated. The substrate material surface profile (i.e. roughness represented by the arithmetic mean value “Ra”) effect on the coating adhesion/cohesion strength has been investigated.

The results from this study show that adequate repair of the nose landing gear system threads is achieved through the use of the CGDS process based on the preliminary set of requirements established by the Boeing Company. The component dimensional restoration was achieved by depositing material at the highest rate using a system process temperature and pressure of 500 °C and 3.45 MPa respectively. During the entire repair process, the Al7075-T6

substrate surface temperature was kept under 93 °C to avoid any changes to the base material heat treatment. Moreover, the CGDS threads were able to withstand a torque of 303 N·m. Further testing is required in order to fully evaluate and assess the CGDS threads performance under various types of loading at different stress magnitudes. Adhesion test results have demonstrated that the coating adhesion strength can be improved by increasing the substrate surface roughness and consequently the particle to substrate contact area.

Al2024 particles were successfully deposited on flat and circular Al2024-T351 substrates. The adhesion of thick Al2024 coatings on circular substrates has been found to be a major issue, as the coatings would slide along the substrate interface during testing without any additional grip. However, subsequent adhesion tests conducted on various substrate surface profiles, as per the ASTM C633 standard, have demonstrated that increasing the surface roughness (i.e. increasing the surface area) can drastically improve the coating bonding strength.

Finally, the polymer nozzle wear process during material deposition has shown to have a drastic impact on the particle distribution within the flow stream at the exit of the nozzle. Particle in–flight measurements and single line and spot coatings have demonstrated that the nozzle material removal process displaces the particles position inside the flow, which consequently produces an inhomogeneous deposition. To reduce the effect of nozzle wear on the coating deposition shape, a Mica ceramic nozzle has been machined and preliminary depositions have been generated for Al2024. Larger deposition efficiencies are achieved using the ceramic nozzle due to the heat exchange at the nozzle wall that causes increased particle softening. Moreover, smooth ceramic internal walls are required to reduce particle deposition inside the nozzle at high spraying temperatures. Further optimization of the spray parameters is needed to achieve high quality Al2024 coatings using the ceramic nozzle.

Acknowledgments/Preface

I am using this opportunity to thank my supervisor, Professor Bertrand Jodoin, for his comments and valuable engagement throughout my research work. I am more than grateful for his insightful directions, encouragement and continued support. I truly consider myself privileged to have had him as a mentor during my master's degree because not only has he increased my interest in research but also and most importantly he has helped me grow as a person.

I am more than thankful to have had the opportunity to work and collaborate with industrial partners during this project. Thank you to the Boeing Company, Centerline and Mitacs for making this experience fulfilling.

I would like to thank Dr. Mohammed Yandouzi for his involvement throughout my work and his more than valuable knowledge in material science and analysis.

I also wish to thank the technicians from the Department of Mechanical Engineering machine shop at the University of Ottawa. Thank you to Paul, Stan, Michael, Leo and John for their encouragement and contribution during this project.

Thanks to my fellow colleagues in the office for making this experience truly amazing: Deliange (Leon) Goudl, Ruben Fernandez, Daniel MacDonald, Tyler Samson, Samuel Leblanc Robert, Guillaume Archambault, Daniel Cormier, Patrick Trahan, Antoine Bacciochini, Yannick Cormier, Philippe Dupuis and Aslan Farjam. Thanks for all the talks we have had on different random subjects!

Last but not least, a huge and special thanks to my family for their precious support and encouragement during my studies. Thank you for everything.

Table of Contents

List of Tables

List of Figures

Legend/Nomenclature

Symbols

A	Area
ρ	Mass density at a point
C_p	Specific heat at constant pressure
C_v	Specific heat at constant volume
ν	Specif volume
γ	Ratio of specific heats, $\frac{C_p}{C_v}$
m	Mass
W	Molecular weight
P	Pressure
T	Absolute temperature
R	Gas constant
ℜ	Universal gas constant
V	Speed
h	Enthalpy per unit mas
u	Internal energy
M	Mach number
M^*	V/c^*
c	Velocity of sound
F	Force
C	Coefficient
d	Diagonal length
r	Radius
h	Length of repaired area
P_B	Back Pressure
τ	Shear stress

$( )_s$	constant entropy
$( )^*$	State at which M=1
$( )_{pr}$	Projected
$( )_p$	Particle
$( )_D$	Drag

Abbreviations

APS	Air plasma spray	IBAD	Ion beam-assisted deposition
ASTM	American society for testing and materials	ID	Internal diameter
BSE	Back-scatter electron	IVD	Ion vapour deposition
CGSD	Cold gas dynamic spray	LPCS	Low pressure cold spray
CP	Commercially pure	LPPS	Low pressure plasma spray
CS	Cold spray	MIL	Military
CSM	Cold spray meter	NCMH	Normal cubic meters per hour
CT	Computed tomography	PBI	Polybenzimidazole
CTE	Coefficient of thermal expansion	PZT	Lead zirconate titanate
DE	Deposition efficiency	PIV	Particle image velocimetry
EBSD	Electron back-scatter diffraction	SCFH	Standard cubic feet per hour
EDS	Energy-dispersive X-ray spectroscopy	SEM	Scanning electron microscope
EP	Extra pressure	SOD	Standoff distance
FCC	Face centered cubic	TIG	Tungsten inert gas
HAZ	Heat-affected zone	UN	Unified National
HB	Brinell hardness	UNC	Unified national coarse
HPCS	High pressure cold spray	UNF	Unified national fine
HV	Vickers hardness	VPS	Vacuum plasma spray
HVOF	High velocity oxygen fuel	YSZ	Yttira-stabilized zirconia

CHAPTER 1

Introduction

1.1 Background

The aerospace industry is known for being innovative, adaptive and strategic. Over the years, it has been engaged in the research of new technologies and repair procedures that ought to be used to restore corroded or damaged parts. Replacing damaged components that are complex is known to induce manufacturing and operational delays along with extra costs related to inventory, lead time, labor, assembly and testing. In the aerospace field, where the replacement of specific components can cost millions of dollars every year [1], restoration and repair are being preferred over replacement.

The predominant use of aluminum in the aircraft industry, as shown in Figure 1.1, is attributed to its attractive mechanical properties, proven performance, reliable inspection techniques and well established design and manufacturing processes. Moreover, the possible improvement and development of advanced aluminum alloy materials through the use of different methods such as rapidly solidified alloys, metal matrix composites and aluminum-lithium alloys [2], [3] promotes the use of aluminum in many different structures. The 2xxx and 7xxx aluminum alloy series are currently widely used in aircraft structures and components from fuselage skin to landing gear beams [4]. Through the application of various heat-treatment processes and the development of well-controlled chemical composition, they provide a high strength-to-weight ratio, good machinability, maintain a good stress corrosion cracking resistance, acceptable fracture toughness levels and good fatigue strength [3].

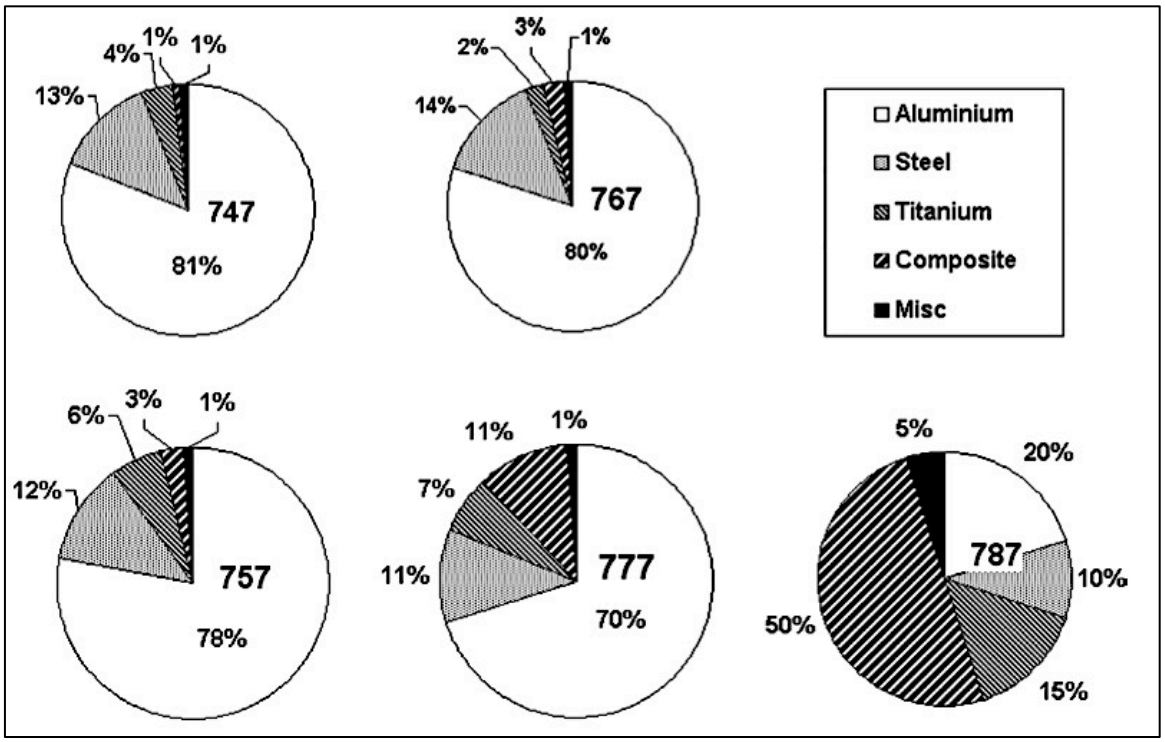

Figure 1.1: Different materials used in Boeing aircrafts [3].

However, the challenges remain in finding solutions to reduce the cost of aircraft related to its purchase and operation. It is well known that the lightweight property of the aluminum alloy plays a major role in the cost reduction through savings made on reduced fuel consumption. Nevertheless, the cost of maintenance, service and inspections of aircrafts are estimated to surpass the original purchase price by a factor of two, over the anticipated 30 year life of the airliner [3].

Aerospace parts, such as gas turbine blades, transmission and gearbox housing for rotorcraft, power equipment shafts and nose landing gear steering actuators amongst others are being prematurely removed due to corrosion, wear or cracking [1], [5]. Many processes have been developed and used to repair damaged components. Those manufacturing methods include laser beam build-up welding (laser cladding), tungsten inert gas (TIG) welding, plasma transferred arc (PTA) welding, gas flame spraying, electro spark alloying, aluminum shim bonding and ion-vapour deposition (IVD) to name a few [1], [5], [6]. However, some of these processes induce undesirable high thermal residual stresses, deposit-substrate dilution, component distortion, reduced mechanical properties and altered substrate microstructure and oxidation [7]. Other processes present particular technical issues related to the possible moisture penetration at the

bond line, the limited strength of the adhesive and possible corrosion of either the repair member or aluminum substrate [8]. As such, the current repair processes are inclined to cause premature and unexpected failure of the repaired components.

The exponential increase of the industrial demand for innovative alternative techniques for the manufacturing sector has encouraged the development of a non-melting deposition process known as Cold Gas Dynamic Spray (CGDS), or simply Cold Spray. CGDS is the latest of thermal spray processes. This new method has proven to produce high quality products while minimizing environmental impact as opposed to currently used repair techniques and consequently is considered to be a green repair process.

In the cold spray process, micron-size solid particles are accelerated to high velocities and are subjected to high-strain rates during impact with a substrate surface, to a degree dependant on the particle material properties. The jet dynamics, the sprayed material properties and the substrate gas flow interaction greatly influence the deposition process and affect the obtained coating mechanical properties. Up to now, investigations on the impact process and particle deformation has been made through experimental and numerical methods to characterize the deposition efficiency of a wide range of metallic and thermoplastic particles deposited on metal, polymer or composite substrates [6], [9]–[12], [12]–[22]. Although the cold spray technique has initially been reference to as a novel method that can be used in manufacturing as a freeform fabrication procedure, there is only few demonstrations of cold spray in the production of bulk parts [23]–[31].

1.2 Motivation and Research Objectives

The current research will evaluate the potential of the cold spray technology to be used to repair and restore the structural integrity of damaged aluminum alloy threads typically found on nose landing gear steering actuator components. Figure 1.2 shows the actual targeted part to be repaired and its location within the nose landing gear system of the Boeing 757 aircraft. Exposed to a harsh environment, the external threads of the component become damaged through wear and excess usage and, as a result, the load carrying capacity and the level of performance of the damaged threads are considerably reduced. The part is deteriorating too often to consider the current replacement method a valuable and economical long-term solution.

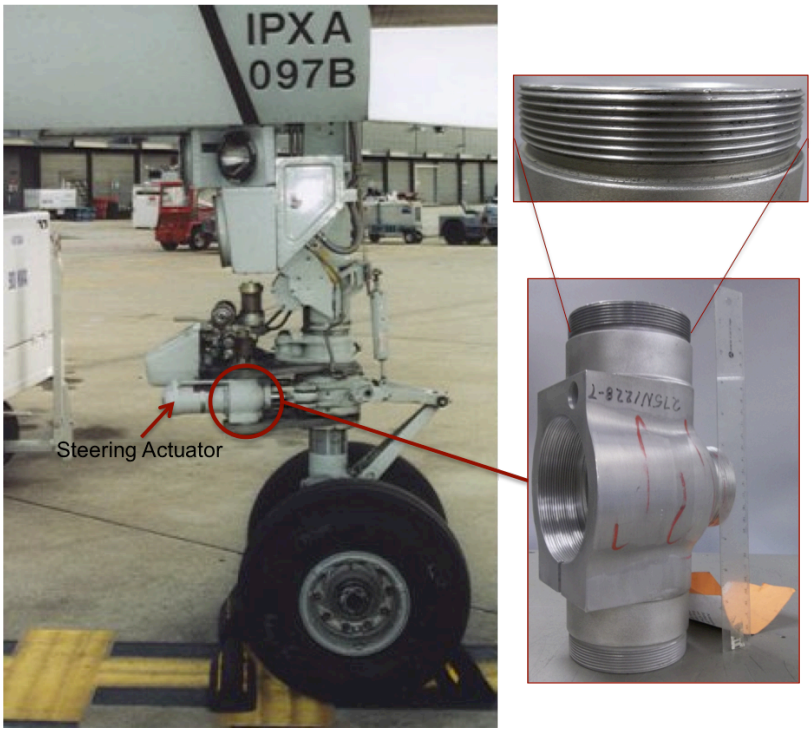

Figure 1.2: The steering actuator assembly in the Boeing 757 nose landing gear system [4]. The component and threads that need to be repaired are circled and shown separately.

There are currently no methods perceived as suitable for the restoration and repair of aluminum alloy threads as they generally all require high processing temperatures to generate proper material deposition. Elevated process temperatures induce strong substrate surface heating, which can deteriorate and change the properties of the base material. Moreover, the deposited particles can also undergo chemical transformations due to excessive heating, which will generate inconsistency and uncertainty in the repair performance. Other chemical interactions initiated at high temperatures, such as material oxidation, give rise to poor repair quality, as it introduces oxide inclusions at the grain or particle boundaries within the repair. The process temperature can significantly affect the residual stress state and its distribution across the repair thickness. For elevated material deposition temperatures, the solidification and cooling process of the molten material lead to internal tensile residual stress, commonly referred to as quenching stress. Those stresses arise as the deposited material adherence to the substrate surface restricts its contraction. During post-deposition cooling, the difference in thermal expansion between the repair and substrate material can induce thermal mismatch residual stresses. As a result, due to large heat inputs, tensile residual stresses may develop. Tensile residual stresses facilitate crack

initiation/propagation and delamination and reduce fatigue life. Finally, high process temperatures can induce large distortion in the repaired component.

In addition, for appropriate thread repair, proper microstructural qualities and mechanical properties must be achieved at the as-deposited state. Use of post-annealing treatments on repaired components is restricted due to the strict dimensional tolerances used in the aerospace field, which further limits the repair procedures.

To meet these challenges, the use of the CGDS technology as a repair method for the aluminum threads found on the nose landing gear steering actuators will be evaluated. The CGDS uses a high-pressure gas jet to accelerate small particles (1-50 μm) through a converging-diverging nozzle resulting in coating formation in the solid state. The jet of compressed gas can be heated to temperature below the melting point of the sprayed material. Therefore, the cold spray deposition process allows minimizing some drawbacks characteristic to the high temperature processes, such as, phase transformation, decomposition, sensitivity against oxidation, residual stress and alteration of the base material. In cold spray, impact velocity and critical velocity of the sprayed particles, which depend on powder properties and cold spray conditions, primarily affect the deposition process and the final coating properties. The interface bonding between the particles and the substrate material is associated with the shear instability, which is related to the high strain rate experienced by the particles during impact. The kinetic energy of the particles dispended during the impact ruptures the oxide layer around the powder and plastically deforms the particles to enhance their bonding to the substrate material.

Therefore, in this study, thick multi-pass (~6 mm) coatings will be sprayed to repair and restore the external initial dimensions of damaged aluminum alloy components. Following the metallic material deposition, threads will be re-machined into the sprayed coatings. In order to achieve these objectives, various studies will be performed:

(1) Explore the potential of the CGDS process to be applied as an additive manufacturing process by studying the deposition of thick aluminum coatings.
(2) Determine the spraying parameters best suited to repair large circular components.
(3) Study the long-term influence of the repair method on the nozzle used in the cold spray process.

(4) Investigate the dynamics of the powder flow distribution and deposition during repair.

(5) Examine various surface preparation procedures and determine their influence on the repair properties.

(6) Characterize the machinability of the repairs by analyzing the machined surface roughness and profile.

(7) Evaluate the adhesion strength of the repairs and measure their load carrying capacity through shear, torque and compressive tests.

1.3 Thesis Outline

The content in this thesis has been organized into nine chapters. Chapter 1 presents a general outline of the background information relevant to the current research. It offers a brief preview of the existing technologies and their specific drawbacks that motivate the proposed study. Moreover, it lists the general objectives that will be taken to accomplish the current work.

Chapter 2 provides a detailed review of the literature relevant to the following study. It covers, describes and compares the current additive manufacturing processes used to repair and restore the initial dimensions of aerospace components. The drawbacks, results and concerns in using these processes for repair purposes are also specified. Various thermal spray techniques are presented and the CGDS process is also described in full details. A summary of the current results found in the literature regarding the CS deposition, flow dynamics and stress analysis is also presented.

Chapter 3 is intended to describe and explain in full details the objectives of the current research. It presents the procedures and tasks that have been set in order to achieve the goals summarized in section 1.2. Thus, it will give the reader a sense of what will be accomplished in this research for the development of an adequate repair procedure using the CGDS process.

Chapter 4 presents the experimental approach and procedures taken to achieve the objectives. Described are the powder feedstock material, the geometry and material of the component to be repaired, the experimental equipment that includes the different investigated nozzles, the characterization equipment, the industrial and military standards followed and the various apparatus and tests used to determine the level of performance of the repairs.

Chapter 5 is dedicated to presenting in details the initial set of experimental tests that served to determine the feasibility of using the CGDS technology to produce thick repairs. This chapter provides the analysis and characterization of numerous coatings produced using different parameters and two distinct metallic powders. A mapping of the mechanical, microstructural and physical characteristic of the coatings is presented and explained.

Chapter 6 presents in details the produced repairs and the tests and procedure used to efficiently deposit and restore the initial dimensions of the different damaged parts. The mechanical properties of the repairs and their limitations in terms of performance are described. Results from torque and compression tests are also presented and analysed.

Chapter 7 presents the study conducted to determine the influence of the component surface profile and roughness on the adhesion of the coatings. The tests are performed using both tested powders and the results are analyzed, compared and explained through theorized statements.

Chapter 8 serves to present an interesting and limiting aspect of the CGDS equipment, encountered during the repair of large components. It was discovered that the polymer nozzle used to spray metallic powder wears in specific manners over time. This can eventually become an important issue for commercial and high production applications. Thus, the consequences of the polymer nozzle deterioration in terms of powder flow and material deposition distribution are analyzed. A possible solution to this concern is also presented.

Finally, chapter 9 provides key conclusions and principal findings reported in this thesis. In addition, comments, recommendations and suggestions for future work related to using the CGDS technology as a repair process will also be given.

CHAPTER 2

Literature Review

The following chapter presents an in depth review of the literature relevant to this research work. It describes the current industry practices for the repair of structural and non-structural components. The mechanical and microstructural properties of different aerospace materials and the applied heat treatments along with their respective benefits will be described. It will present the theory and previous studies of thermal spray processes and more precisely the CGDS technology and its use as an additive manufacturing process. Finally, the flow dynamics and recent developments of the CGDS process will be presented.

2.1 Aircraft Graded Aluminum Alloys

Various aluminum alloys are being used in the aerospace industry due to their high specific properties, fatigue performance, corrosion resistance and reduced weight. The predominant aircraft alloys are the 2XXX and 7XXX series used when high damage tolerance or strength is required [32], [33]. Both of these alloys are composed of different alloying elements, which play a critical role in the strengthening by precipitation process. This process involves a solution heat treatment of the material up to a temperature that puts the alloying element in solution. The material is then quenched after being held at the solution treating temperature for a certain period of time. At this stage, the alloying elements are trapped in solution. Finally, the material undergoes an aging process where the alloying elements precipitate to generate uniformly distributed fine particles within the material. The aging procedure is either done at room or intermediate temperatures. Therefore, the precipitation process of the aluminum alloy materials limits their maximum service temperature. Repeated exposure of the material to the aging or higher temperatures leads to a loss of strength due the growth and dissolution of the precipitates [34]. Appendix I offers a guideline on the maximum time and temperature exposure of specific aluminum alloys to avoid softening and variation of properties.

The original aluminum alloys that have been developed and used in the aerospace industries in the first commercial aircrafts correspond to Al2024 and Al7075 [35]. Many Boeing commercial aircrafts, to this day, use those aluminum alloys for various components in the nose landing gear steering actuator system[1]. As such, the following subsections will only concentrate on describing the properties and composition of those specific aluminum alloys. Moreover, only T351 and T6 heat treatments procedures for the Al2024 and Al7075 alloys respectively will be covered.

2.1.1. Aluminum 2024

Aluminum 2024 is primarily composed of copper (3.8-4.9 wt.%) and magnesium (1.2-1.8 wt.%) as alloying elements. Its alloying elements offer high strength, good resistance to fatigue, good fracture toughness and superior damage tolerance through the precipitation of Al_2Cu and Al_2CuMg phases [3]. However, these intermetallic phases significantly decrease the

[1] Information given by The Boeing Company

corrosion resistance of the alloy material. The Al2024 is primarily used in fuselage and lower wing skin applications [3]. A T3 heat treatment is usually applied to increase the fracture toughness and resistance to fatigue crack growth. Once heat treated, the material is cold worked and naturally aged at room temperature to a stable condition. Another applied heat treatment is designated by T351, which consist of stretching the material for stress relief purposes after the heat treatment [34].

2.1.2. Aluminum 7075

Aluminum 7075 is predominantly composed of zinc (5.1-6.1 wt.%), magnesium (2.1-2.9 wt.%) and copper (1.2-2 wt.%) as alloying elements. Although the alloy provides superior strength-to-weight ratio it is the least corrosion resistant [3]. It is used in aircraft structural parts and in other highly stressed applications. A T6 solution heat treatment is generally applied, where the material is heat treated and then over-aged above room temperature [34].

2.2 Current Repair and Restoration Methods

Many aircraft parts are currently being restored and repaired using different repair technologies. However, the restoration of some components requires that the procedure and process parameters be adequate in order to limit the influence on the component properties and its surroundings. For example, heat sensitive substrates cannot tolerate high process temperatures without undergoing microstructural changes and important mechanical properties variations. As an example, the Al2024 and Al7075 materials undergo artificial aging at 190 °C and 121 °C respectively [36], [37]. Moreover, for the repair of localized areas, special masking procedures can be necessary to avoid contamination of the non-damaged surfaces [25], which increases the total repair cost and time. Component distortion can also result from high residual stresses due to the use of high temperatures. The following subsections will present some of the current repair techniques employed for different aircraft components and discuss about their specific disadvantages.

2.2.1. Ion-Vapor Deposition

The ion-vapor-deposited (IVD) aluminum is a metal vaporization process used to deposit pure aluminum onto metallic and non-metallic parts. The substrate surface is bombarded by positively charged ions of an inert or reactive gas extracted from plasma or obtained through a separate ion gun when the process is conducted in a vacuum environment (often called ion beam-assisted deposition (IBAD)) [1], [38], [39]. This continuous ion surface attack cleans the substrate surface prior to the deposition. An aluminum wire is fed into the anode of the system and melted at the passage of high current. Once discharged, the material combines with the ionized elements and is accelerated and projected onto the cathode substrate surface to form a well-adhered and dense coating. However, for the repair of big components, complex equipment and a large vacuum chamber are required, which increases the cost of operation. For localized deposition, precise and time consuming masking procedures using masking tapes, rubber or metal masks are needed to restrict the region of deposition [40]. Adequate cleaning of damaged parts is difficult and field repair by IVD is impossible. Moreover, as a chemical treatment procedure is used during the cleaning process, pits can form at the substrate surface and act as fatigue crack initiators [41]. Lastly, the IVD process is usually used to deposit thin film such that the production of thick aluminum coatings would be time consuming.

2.2.2. Laser Beam Cladding

In laser beam cladding, a laser beam is directed onto the damaged surface part and a localized melt pool is generated. A continuously powder fed jet propels the cladding material onto the melted substrate surface to create a metallurgical bond between the repair and damaged part [5], [42]–[45]. To avoid oxidation, the cladding powder is accelerated using an inert carrier gas such as argon. Figure 2.1 shows the repair of an injection mold through the cladding process.

Figure 2.1: Laser beam cladding process used in industry [46]. The eroded part is machined down prior to the laser cladding process. The last step is the milling of the repair down to the original dimensions and tolerances.

The powder is generally heated to 55 °C and delivered into the carrier gas, which is heated to 180 °C [43]. The gas is used to direct the powder deposition jet and to prevent oxidation once the powder is deposited into the melt pool. Overlapping of the weld beads can form thick material deposition as shown in Figure 2.2 for the repair of high pressure turbine blade tip. This technologies is used for the repair and restoration of high-end parts such as turbine blade, internal combustion engine parts and numerous components in the military sector [45].

Figure 2.2: Turbine blade tip formed by laser cladding process [43].

Despite its extensive use as a repair process, laser cladding is often uneconomic due to the slow repair time and the enormous cost of the laser and control systems [42]. Poor

reproducibility caused by the high sensitivity of the process to small variations in the operating parameters such as the powder feed rate, beam velocity and laser power is another drawback of the laser cladding repair method. The repaired component surface also undergoes abrupt hardness variations near the dilution zone [43].

2.2.3. TIG Build-Up Welding

Tungsten inert gas (TIG) welding is an arc welding process that uses direct or alternating current to produce an electric arc between a non-consumable tungsten electrode and the component surface. The weld area is shielded against the atmospheric contamination through the use of an inert gas such as helium or argon. A filler material is fed as a wire into the welding current arc and is deposited as molten material onto the component surface. Figure 2.3 depicts the repair of a turbine blade using the laser cladding and welding methods. The laser cladding provides higher control on the deposition by generating thinner weld beads as compared to the TIG repair process. The TIG process generates larger weld layers, which can enable greater fill rates but reduce consistency and repair precision.

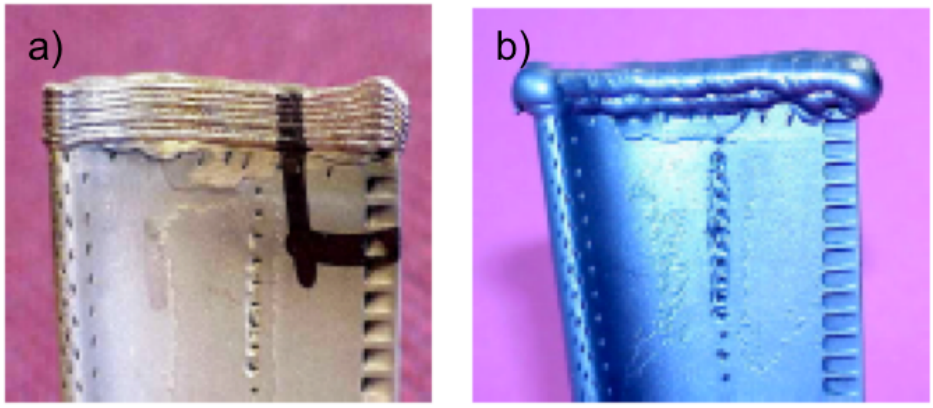

Figure 2.3: Comparison between a) the cladding and b) welding repair of the turbine blade tip [46].

However, the TIG process inputs a high amount of heat into the substrate surface, which creates a large heat-affected zone (HAZ). This zone is characterized by partial recrystallization and material properties weakening [47]. The thickness of the melted substrate material affected zone is generally irregular and unpredictable.

2.2.1. Thermal Spray Processes

Based on the energy source used to heat the feedstock material, thermal spray processes are divided into four major categories: combustion spray, electric arc spray, plasma spray and kinetic spray. These coating deposition processes are non-atomistic as they do not generate material through the successive deposition of single atoms, ions or molecules such as electrochemical plating or directed vapor deposition [48]. Instead, feedstock material in the form of powder, wires or rods is deposited onto a surface in the liquid, semi-liquid or solid state. During thermal spray processes, the coating material is heated up by the process gases, which are heated by means of electrical (plasma or arc) or chemical (combustion of fuels with oxygen or air) methods. However, in the kinetic spray process, the thermal energy is limited and the deposition process characteristics differ from the usual spray processes. Figure 2.4 is a representation of important thermal spray coating features.

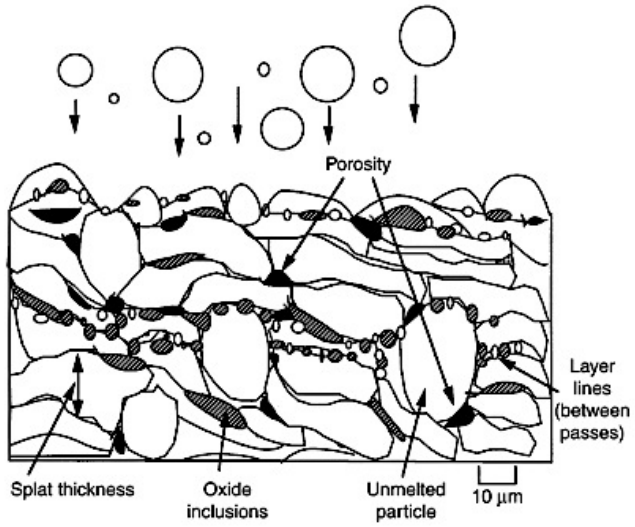

Figure 2.4: Typical thermal spray coating aspects [48].

Coating microstructures include pores, oxide inclusions, various material phases, cracks, unmelted particles and different splat structures. Figure 2.5 shows the various subsets of the different thermal spray processes.

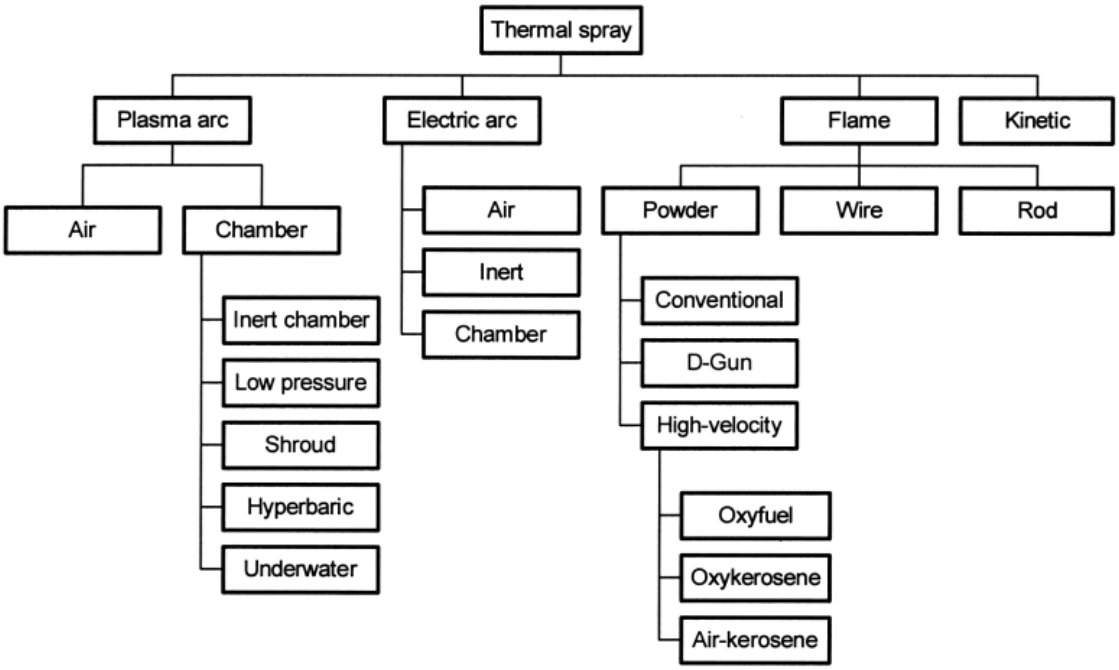

Figure 2.5: Thermal spray processes categories [48].

In the following subsections, the plasma arc spray, electric arc spray and the high-velocity oxy-fuel spray (HVOF) processes will be described.

2.2.1.1. Electric Arc Spray

In electric arc spray, consumable electrode wires are fed into a direct current arc formed between the oppositely charged wires, which directly melt the wires tip. The continuously formed melted material is sheared away by a high-velocity compressed air jet located behind the wires as depicted in Figure 2.6. This process breaks the material into fine particles and accelerates them toward the substrate surface. Since the material is already in a molten state when entrained in the jet, the only source of heat input to the substrate surface is through the individual particles contained in the stream. Therefore, due to its low temperature deposit characteristics, the arc spray provides many processing advantages for application where the substrate surface temperature is the limiting factor. Thus, deposition of material can be made on polymer, wood, fiberglass, metallic and glass substrates.

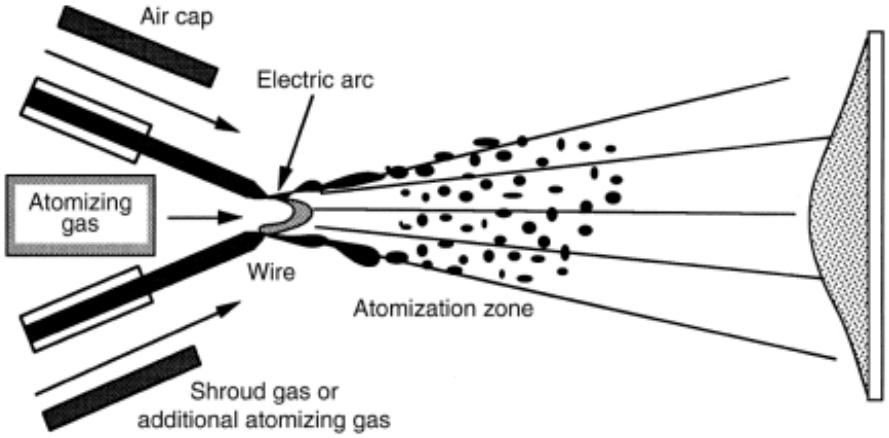

Figure 2.6: Twin-wire spray gun process [48].

The arc spray coating characteristics can be controlled and improved through the use of different wire diameters, use of an inert gas to accelerate the particles and minimize the oxidation, reduce the traveling distance of the particles and reduce voltage to control the melting features of the material. Particles of 33 μm to 53 μm in size can be produced and their velocity can range between 50 m/s and 190 m/s before impacting the substrate [49], [50].

This process is currently used in application requiring high rate deposition and formation of thick coatings such as municipal and civil constructions, bridge structure, water and storage tanks and steel tooling [48], [51]. It is also used as a protective coating for improved wear and corrosion resistance in marine applications. However, as the sprayed particles are brought to their molten state, the composition (phase transformation), properties and characteristics of the obtained coating cannot be controlled properly. Excessive heating of the feedstock material can result in the burning-off of specific alloying elements [40]. Moreover, the cooling process of the molten particles induces tensile residual stresses in the coating as the substrate surface constrains particle thermal contractions [51], [52].

2.2.1.2. Plasma Spray

The ionization process to generate a plasma state is made by injecting an inert gas, usually argon, argon-hydrogen mixture, helium, nitrogen or hydrogen, between two electrodes. A direct current electric arc is created between the cylindrical electrodes and ionizes the gas to form

an electrically conductive and high temperature plasma state (up to 20000 °C) [40] as shown in Figure 2.7. The powder injection location, upstream or downstream relative to the plasma jet, mainly affects the time exposure of the particles to the high temperature flow, which dictates the average particle form (liquid or liquid-solid) prior to the impact with the substrate.

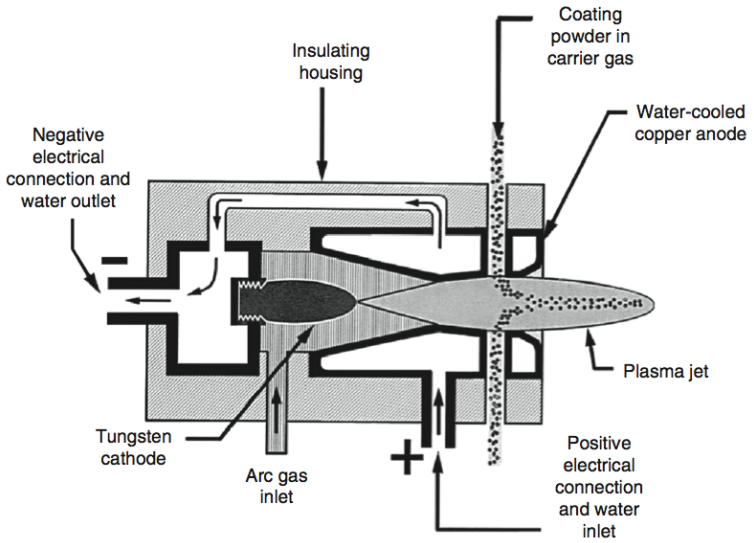

Figure 2.7: Diagram of the plasma spray gun [40].

The gas composition described by its ionization potential and thermal heat capacity plays a major role in the heating capability of the particles in the plasma spray process. Different gas and gas mixtures can generate different coating characteristics and qualities [48]. Due to the gases viscosity, the plasma can reach different velocities such as 1200 m/s, 800 m/s and 400 m/s for pure hydrogen, nitrogen and argon gases respectively [53]. The melted particles can reach velocities ranging between 80 m/s and 500 m/s once injected in the expanding plasma.

Coatings with porosity ranging between 1% and 40% can be obtained. The plasma gas jet reduces the oxide content in the coating but the plasma spray process is still influenced by the ambient air mixing effects. The plasma spray process can be used to deposit numerous type of material such as metals, ceramics, glasses and some polymers and therefore is described as a versatile process. It is mainly applied to provide high temperature resistance as in thermal barrier coating for gas turbines, erosion and abrasion resistance, corrosion protection, fretting wear as applied in seal ring grooves in gas turbines and in anti-galling applications [43], [47]. However,

the plasma jet temperature can reach up to 10000 °C downstream from the nozzle exit, which can significantly affect the substrate properties [40]. The high thermal profile of the process and exposition to the air environment induces the oxidation of in-flight metallic particles and significantly increases the oxide content in the coating. Another limitation of the high process temperature is the presence of phase composition shifting and crystal structure alteration in the feedstock material during its deposition. In addition, due to the cooling process from high temperature, the resulting residual stress profile in the plasma sprayed coatings is of tensile nature [40]. As a consequence, the coating thickness is often limited and cracking along with coating delamination can alter the coating quality, efficiency and performance.

Other variants of the air plasma spray (APS) process exist, which use an environmentally controlled spraying chamber. This process is known as low-pressure plasma spray (LPPS) or vacuum plasma spray (VPS). The processes are operated in a vacuum chamber. The gas inflow from the plasma process is continuously pumped out in order to keep a balanced operating internal pressure. The coatings obtained with the LPPS process are of very high quality due to the limited presence of oxides and inclusions and high density (up to 98 % of theoretical density) [54]. However, due to the expensive equipment and complex assembly, this process is only used for high-end application such as coatings for aerospace and biomedical components.

2.2.1.3. High-Velocity Oxyfuel (HVOF)

The HVOF process uses chemical reactions to generate the thermal energy necessary to melt different materials, such as ceramics, metals and polymers. A fuel gas or liquid fuel is mixed with oxygen and is burned in the combustion chamber, as shown in Figure 2.8. The HVOF spray process operates at high combustion chamber pressures and the heated gas exits through a converging/diverging nozzle, which produces a supersonic flow. The reaction produces pressures up to 0.91 MPa and temperatures up to 3087 °C, depending on the overall parameters. The high kinetic energy is generated through the conversion of the thermal energy as the jet expands in the diverging portion of the nozzle and cools down. Powder particles entrained in the gas jet are typically accelerated to velocities much larger than in other thermal spray process and are observed to range between 450 m/s and 1000 m/s. In the HVOF process, partially melted particles travelling at high velocities can produce a peening effect on the deposited coating, which helps reduce porosity and establishes a favourable compressive residual stress state.

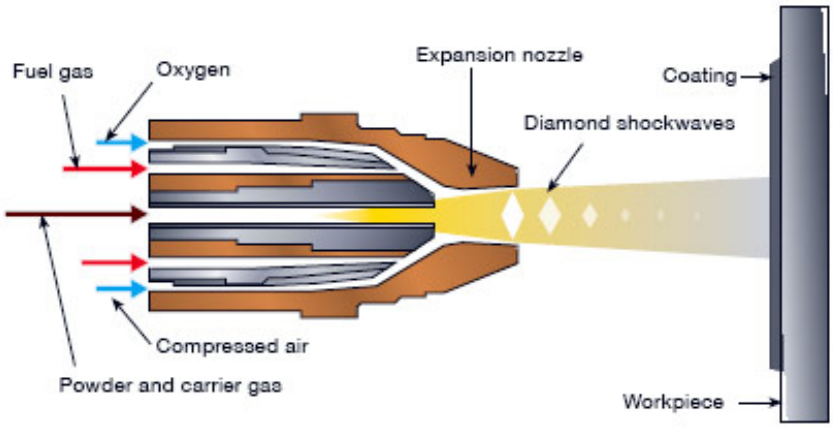

Figure 2.8: Schematic of the HVOF spray process [55].

Coatings with a level of porosity of less than 1% and bonding strength of 80 MPa can be produced [56]. The thermally induced microstructural changes are much lower than in the plasma spray process.

The HVOF spray process is used in numerous industries to improve performance, extend component life and reduce maintenance cost. As examples, it is currently used to deposit WC/Co based coatings for drilling tools to improve their wear resistance, YSZ-based thermal barrier coatings on turbine blades to improve high temperature resistance and nickel-based coatings on chemical reactors to improve corrosion resistance of the base material [52]. However, despite having the ability to deposit coatings with low porosity and an internal compressive residual stress state, the HVOF process still operates at gas temperatures reaching 3000 °C to 4500 °C. Therefore, uncontrolled particle oxidation, phase transformation and preferential vaporization are still major disadvantages of the process when it comes to spraying metallic particles such as aluminum alloys. In addition, heat sensitive substrates properties can be substantially altered due to the high thermal inputs.

2.3 Cold Gas Dynamic Spray Technology

As presented and described in the previous sections, the conventional repair techniques involve the use of high process temperatures, which significantly alter the substrate properties and the feedstock material composition. A low temperature and high velocity kinetic deposition

process known as cold spray can be used to avoid the undesirable effects of high thermal inputs. As this process is the focus of this study, it will be described in much more details than the previously presented repair techniques. The historical background, the gas dynamic principles, the concept of material deposition and deformation, the bonding mechanisms and the theory of critical velocity will be thoroughly described.

2.3.1. Historical Setting

The cold gas dynamic spray method has been discovered in the 1980's by a group of scientists from the Institute of Theoretical and Applied Mechanics of the Siberian Branch of the Russian Academy of Science in Novosibirsk, Russia. The group has stumbled upon what they have called the 'cold spray' phenomenon during an unrelated experimental and theoretical study of the interaction of a two-phase flow for immersed objects [58]. The tests were made in a supersonic wind tunnel and small tracer particles where placed in the flow. During the experiments, the scientists have observed that above a critical particle velocity, the particles in the flow would adhere and deposit onto the target surface instead of eroding it [59]. The flow stagnation temperature was approximately 280 K and the supersonic flow had aluminum particles traveling to velocities of 400-450 m/s

Following the discovery, the group was able to successfully deposit a large variety of pure metals, metal alloys, polymers and composites onto different substrate materials. Since then, numerous cold spray patents have been issued, which claim improvements on specific cold spray parts [58]. Over the years, extensive research and improvement on the technology has permitted the development of many commercial and in-house systems. Currently, the CGDS process is being considered in many fields as a repair and restoration method.

2.3.2. Cold Gas Dynamic Spraying Process Synopsis

Figure 2.9 is a schematic of a typical layout of a cold spray system. A highly pressurized gas, generally nitrogen, helium or air, is preheated below the particle material's melting point before being expanded through a converging-diverging De Laval nozzle. The use of air as the working gas decreases the operating costs however; an increase of oxides in the deposits is inevitable. Application of nitrogen as the main gas, which has a similar velocity of sound as air

(~334 m/s at T=273K), limits the oxidation to happen only after the nozzle exit at the free jet mixture with the atmosphere. Finally, the use of helium, characterized by a high velocity of sound (~965 m/s at T=273K), as the working gas is known to provide superior quality deposits but the operational cost limits its use to very few high-end coatings.

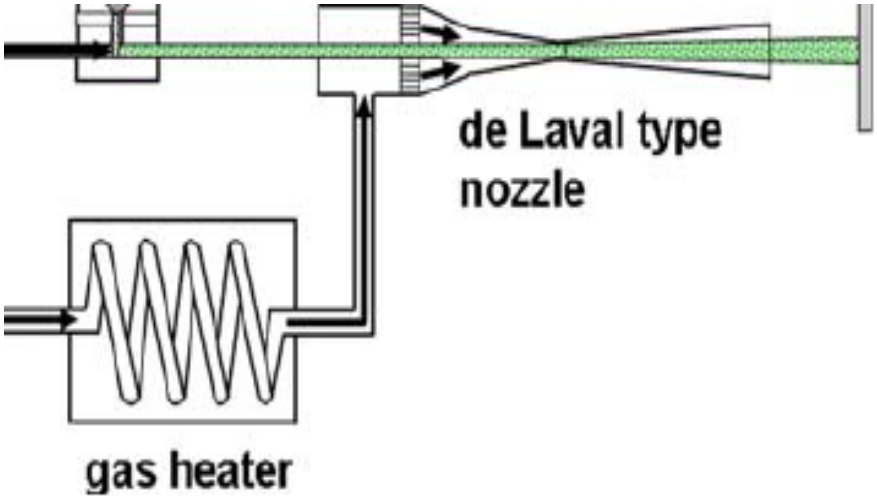

Figure 2.9: Schematic of a typical CGDS system [61].

The gas stagnation temperature increases the gas flow velocity and in consequence increases the particle velocity. Moreover, the heat transfer between the gas and particles not only increases the particle temperature but also their plasticity, which augments their deformability during impact [62]. Higher gas velocities and particle velocities can be reached in the nozzle by preheating particles up to a temperature as high as 900K. However, since the preheat softens the particles, clogging during spraying may occur in the nozzle [63]. Since the gas cools down during the expansion in the diverging part of the nozzle and the spray particles are only in short contact with the hot gas, the temperature of the particles are below the initial gas preheat temperature and thus below their melting temperature.

The fluidized powder feedstock is fed through a dedicated gas line and delivered at the spray nozzle throat or in the diverging section in a high pressure cold spray (HPCS) and low pressure cold spray (LPCS) process respectively [60], [61]. The powder injection can be performed coaxially or radially [62]. Typical exit diameters of the asymmetric nozzle range from 4 to 10 mm, their throat diameter ranges from 1.5 to 3mm and the overall length ranges from 100

to 200 mm [62]. The ballistic impingement of the particles is characterized with speeds ranging between 300 m/s and 1400 m/s.

In comparison to conventional thermal spray methods, the CGDS process avoids oxidation and retains the powder feedstock microstructure with some properties that can reach values comparable to the bulk material [61]. The deposition of oxygen-free coatings decreases the crack nucleation and propagation and thus the process enhances the fatigue life of the coated part [61].

2.3.3. Flow Analysis and Model Equations in CGDS

The current section will deal with the fluid dynamics fundamental theories and principles that govern the motion and state of compressible fluids. Understanding the compressible fluid dynamics and thermodynamics involved in the CGSD process is critical for proper nozzle design and effective CGDS system operation. This section will examine the basic compressible flow concepts, different flow regimes in variable area nozzles, the governing equations and their appropriate simplifications and assumptions, the nature of fluid discontinuities and the flow and boundary conditions at the exit of the nozzle.

2.3.3.1. Introductory concepts to Compressible flow

A compressible flow implies a change in density ($\partial\rho$) due to a variation in pressure (∂P). The rate of change of density with respect to pressure is an important parameter related to the speed of sound. Sound is an infinitesimal pressure wave that propagates steadily creating changes in pressure dP, density dρ and velocity dV. Applying and simplifying the continuity and the conservation of momentum equations to a control surface surrounding the pressure wave front leads to the following relations [64]:

$$\frac{d\rho}{\rho} = \frac{dV}{c} \qquad \text{Eq. 1}$$

and

$$c^2 = \left(\frac{\partial P}{\partial \rho}\right)_s . \quad \text{Eq. 2}$$

For a perfect gas undergoing an isentropic process, the latter equation can be simplified to yield

$$c = \sqrt{\gamma RT}. \quad \text{Eq. 3}$$

Hence, gases with small molecular weights are characterized by large sound velocities. The higher the c, greater is the change in pressure (∂P) required to produce a certain variation in density ($\partial \rho$). From fluid mechanics theories, since dP is proportional to the velocity, a fluid presenting a low speed of sound needs a lower change in pressure to produce a certain change in density and is thus more compressible than a fluid having higher speed of sound. The speed of sound in fluid mediums, used generally as a relative measure of speed itself, is characterized by molecular weight and atomic nature. The speed of sound of different fluids at standard conditions is presented in Table 2.1.

Table 2.1: Speed of Sound of Various Fluids

Fluid Medium	Speed of Sound
Air	343 m/s
Helium	927 m/s
Nitrogen	353 m/s

Its level of influence over the compressibility and pressure pulse patterns is described by the Mach number,

$$M = \frac{V}{c} . \quad \text{Eq. 4}$$

As such, the flow characteristics depend on the ratio of flow velocity over the local speed of sound. A flow with a low Mach number ($M < 0.3$) is considered incompressible. Compressibility effects start to emanate at subsonic ($0.3 < M < 1$) speeds and become even more important with Mach > 1.

2.3.3.2. Gas Dynamic Principles Applied to Converging/Diverging Nozzles

Equations describing the nozzle shape and the optimal conditions for the powder flow can be expressed analytically. An isentropic gas flow model is used to analyze the cold spray converging/diverging nozzle flow and involves numerous simplifications and assumptions;

1. The gas flow is assumed to be one-dimensional. In such flow, all fluid properties are uniform over the entire cross section of the nozzle [64].
2. The gas flow is assumed to be isentropic. The flow in nozzles, which are considered to be short in length, are very often adiabatic and the frictional effects can be assumed very small. Therefore, the gas stream can also be considered reversible and thus isentropic.
3. The gases are treated as ideal (perfect) gases.
4. The constant-pressure and constant-volume specific heats of the carrier and driving gases are considered to be constant and therefore, a calorically perfect gas is assumed.

The driving gas is assumed to initiate from a large section where the velocity is zero and the pressure, P_0, and temperature, T_0, are referred to as stagnation pressure and temperature respectively. At the smallest cross-sectional area, referred to as the nozzle throat, when the Mach number reaches unity, the flow is sonic and the states are noted by the superscript $*$. It is to note that the sonic state at the throat is only reached for specific combinations of stagnation pressure and back pressure, as described in more details further in the text. The stagnation temperature, T_0, and the mass flow rate of the gas, $\dot{m}$, are set, then the corresponding stagnation pressure, P_0, and the properties at the throat can be calculated by the following procedure:

The gas velocity at the throat is equal to the corresponding speed of sound at the throat and is defined as

$$V^* = \sqrt{\gamma R T^*}\,, \qquad \text{Eq. 5}$$

where R is the gas constant described as the universal gas constant (8.3144 J/mol·K) divided by the gas molecular weight, W.

The temperature at the throat, T^*, is given by

$$T^* = \frac{T_0}{1 + (\gamma - 1)/2} \,. \qquad \text{Eq. 6}$$

Therefore, a low molecular weight gas (i.e. having a larger R), monoatomic (i.e having a larger γ and therefore a larger T^*) can reach higher speeds for the same stagnation temperature than a diatomic gas having a high molecular weight. Thus, helium would be more applicable and effective gas to be used in the cold spray process.

From the mass flow rate, $\dot{m}$, selected, the sonic gas density is calculated by;

$$\rho^* = \frac{\dot{m}}{V^* A^*} \qquad \text{Eq. 7}$$

where A^* is the cross-sectional area of the throat.
Using the ideal gas law, the gas pressure at the nozzle throat can be determined by;

$$P^* = \rho^* R T^*. \qquad \text{Eq. 8}$$

As the throat pressure is defined, the stagnation pressure can be computed from the following;

$$P_0 = P^* \left(\frac{T_0}{T^*}\right)^{\gamma/\gamma-1} = P^* \left(1 + \frac{(\gamma - 1)}{2}\right)^{\gamma/(\gamma-1)} . \qquad \text{Eq. 9}$$

It is also possible to determine the gas properties at any section along the diverging and converging parts of the nozzle. It is to note that the cross-sectional area, the Mach number or one of the properties at that specific section must be determined in order to calculate and describe the total state of the gas flow at that specific section. The following isentropic relationships are used to determine the necessary gas property:

$$\frac{A}{A^*} = \frac{1}{M}\left[\frac{1}{(\gamma + 1)}\left(1 + \frac{(\gamma + 1)}{2} M^2\right)\right]^{(\gamma+1)/2(\gamma-1)} , \qquad \text{Eq. 10}$$

$$\frac{P}{P^*} = \left(\frac{(\gamma+1)}{2+(\gamma-1)M^2}\right)^{\gamma/(\gamma-1)}, \qquad \text{Eq. 11}$$

$$\frac{T}{T_0} = \frac{1}{\left(1+(\frac{\gamma-1}{2})M^2\right)}, \qquad \text{Eq. 12}$$

$$c = \sqrt{\gamma RT}, \qquad \text{Eq. 13}$$

$$\rho = \frac{\rho_0}{(1+(\gamma-1)/2)M^2)^{1/(\gamma-1)}}. \qquad \text{Eq. 14}$$

The previous equations can be used to calculate the nozzle exit conditions only if the gas flow stays isentropic throughout the nozzle. However, for certain combination of initial pressures (stagnation pressure) and final pressures (back pressures) there is no possible isentropic solution to the one-dimensional converging/diverging flow situation. Figure 2.10a summarizes the possible gas pressure profiles in a converging/diverging nozzle. Figure 2.10b is an example of the temperature and velocity profile through a CGDS nozzle for a given stagnation temperature and pressure.

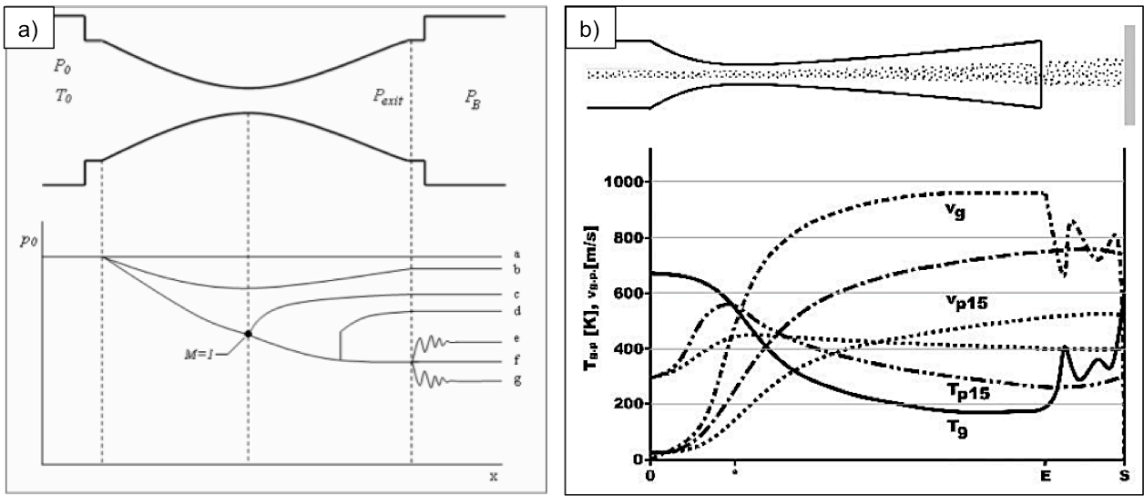

Figure 2.10: a) Flow behavior along the converging/diverging nozzle axis as a function of the pressure ratio P_o/P_B [65] and b) temperature and velocity profile through a nozzle for (g) nitrogen gas and (p15) 15 μm copper particles with T_o=593 K and P_o=2.5 MPa [66].

Thus, during the expansion of the gas within the diverging section, the internal energy (enthalpy) of the system provided by the pressure and temperature is converted to kinetic energy. Accordingly, the pressure and temperature decreases as depicted in the previous figure.

In a), the back pressure and stagnation pressures are identical, which creates a constant pressure state throughout the nozzle and no flow is generated. Reducing the back pressure to a slightly lower value than P_o creates a constantly decreasing pressure through the converging part of the nozzle. The pressure ratio is insufficient to choke the nozzle and the resulting flow is subsonic ($M<1$) at all locations. Under these conditions, the flow is accelerating in the converging nozzle until a maximum velocity and minimum pressure are reached at the throat, and then decelerating in the diverging section. If P_B is further decreased, the flow rate increases but it remains subsonic and decelerates in the diverging section. A larger decrease in P_B generates the flow characterized by curve c). In this situation, the flow in the section of minimum area, the throat, reaches $M=1$ and the nozzle is choked. However, the pressure ratio is still insufficient to create a supersonic state and the flow decelerates in the diverging section of the nozzle and exit at a pressure equal to P_B. In the following situations illustrated by curves e), f) and g), the pressure ratio is decreased enough to keep the supersonic regime in the diverging section of the nozzle. For case e) and g), the flows are said to be over-expanded and under-expanded respectively. For an over-expanded flow, the exhaust pressure is lower than the back pressure and in order for the jet to adapt to the back pressure it must encounter a series of irreversible oblique shocks and expansion waves. For an under-expanded flow, the exit pressure at the nozzle is higher than the outside pressure. In order, to readjust the stream, the additional expansion is generated though expansion waves and oblique shocks. Finally, case f) represents an ideal isentropic evolution characterized by an absence of strong disturbance inside and outside of the nozzle and a supersonic velocity at the exit of the diverging section. In the CGDS process, the nozzles are designed to operate as close as possible to this scenario in order to avoid disturbance in the particle flow by shockwaves.

Figure 2.11 summarizes the variation in flow properties for different flow regime in diverging and converging sections.

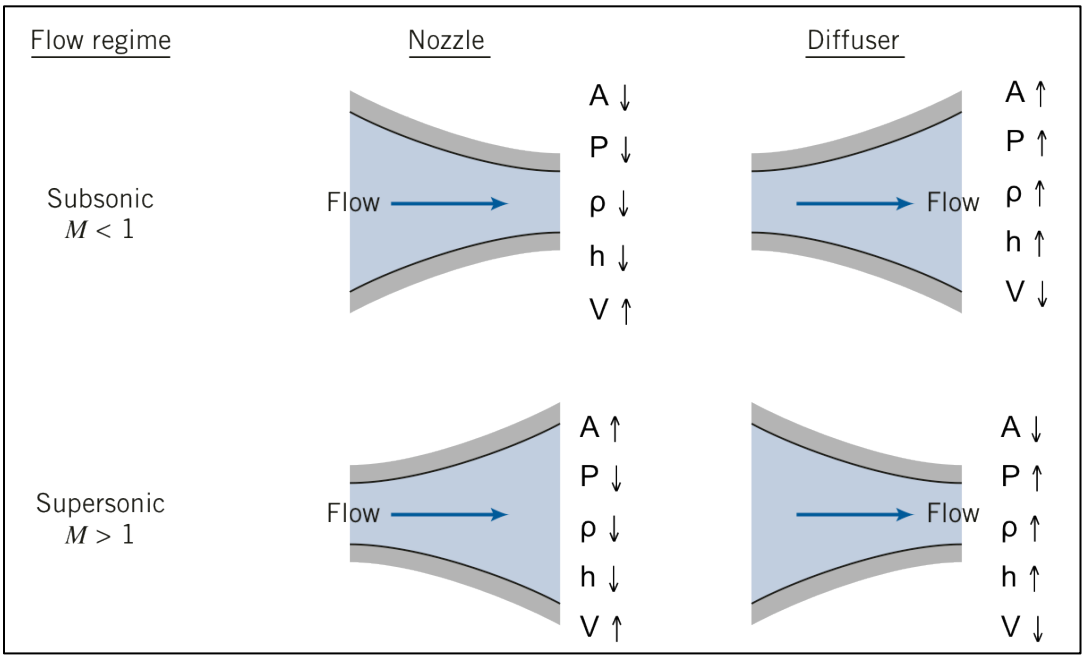

Figure 2.11: Flow properties for converging and diverging parts as a function of initial Mach number (Adapted from [67]).

2.3.3.3. Particle Acceleration

In the CGDS process, specific impact velocities of the powder particles must be achieved in order to produce a coating. The particles within the high-velocity flow are accelerated through the drag force acting upon them. The drag force, F_D, can be expressed by the following relation:

$$F_D = \frac{1}{2} C_D A_{pr} \rho (u - u_p)^2 , \qquad \text{Eq. 15}$$

where C_D is the drag coefficient, A_{pr} represents the projected area of the powder particle, ρ is the density of the flow and the term $(u - u_p)$ is the relative velocity of the flow with respect to the particle. Using Newton's second law of motion, the acceleration, a_p, of the particle is calculated

$$a_p = \frac{1}{2} C_D \frac{A_p}{m_p} \rho (u - u_p)^2 , \qquad \text{Eq. 16}$$

where m_p is the mass of the particle.

From the above equation, the acceleration of the particles is influenced by the drag coefficient, which is characterized by the particles morphology. Jodoin et al. [68] have observed that irregularly shaped particles are affected by a larger drag force due to the negative pressure gradient that is imparted on their surface. As a result, higher particle velocities are reached for non-spherical particles. Moreover, the acceleration is inversely proportional to the particles mass, which is influenced by the particles diameter to the cube. As a result, it will be more difficult to accelerate larger particles.

The flow dynamics at the exit of the nozzle drastically change during the impact process with a substrate surface. As shown in Figure 2.12, shockwaves are created at the substrate surface in order to readjust the supersonic flow to the presence of the substrate and to the conditions and changes it produces. Thus, the shock wave decelerates the flow to subsonic velocities and consequently produces stagnation conditions on the substrate.

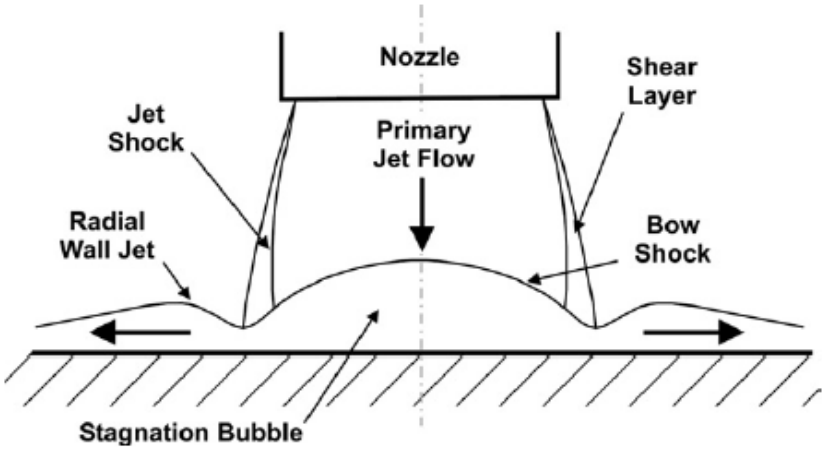

Figure 2.12: Illustration of the supersonic particle/substrate impact zone [69].

For the flow to be able to circumvent the substrate, a curved and detached shock is created, known as 'bow shock'. The bow shock is characterized by a region of high density, recirculating, low velocity fluid [69] that encloses strong gradients and variations in the flow properties. The particles that are going through the bow shock have their velocity and trajectory drastically altered. For a circular nozzle, the thickness of the region after the bow shock can reach 1.37 mm and 1.07 mm when nitrogen and helium gas are used respectively [69]. Likewise, the width of the bow shock region produced using nitrogen is 6.32 mm, while for helium it

corresponds to 4.15 mm [69]. Different spray beam dimensions and thinner bow shock layers can be obtained with the use of distinctive nozzle geometry such as rectangular nozzles [70]. Varying the nozzle length and size can also alter the deposition process and the gas flow characteristics.

In the work conducted by Jodoin et al. [68], it was proven that the bow shock wave (or more precisely the low velocity high density zone that follows the wave) has enough strength to decelerate particles with low momentum such that the deposition of the particle onto the substrate would be affected. The abrupt changes in the flow expose the particles to enormous increases in drag force, up to 70 times their original value [69], such that the velocity of the small and lightweight particles are drastically decreased.

2.3.4. Deposition Efficiency and Particle Critical Velocity

An important parameter in the cold spray process is the deposition efficiency (DE) of the powder, which represents the mass fraction of the deposited particles on the overall mass of sprayed particles [71]. The most critical criterion affecting the material deposition is the impact velocity. For deposition to occur, the particles must exceed a so-called critical velocity. Figure 2.13 shows the deposition efficiency of ductile material as a function of impact velocity for a certain impact temperature.

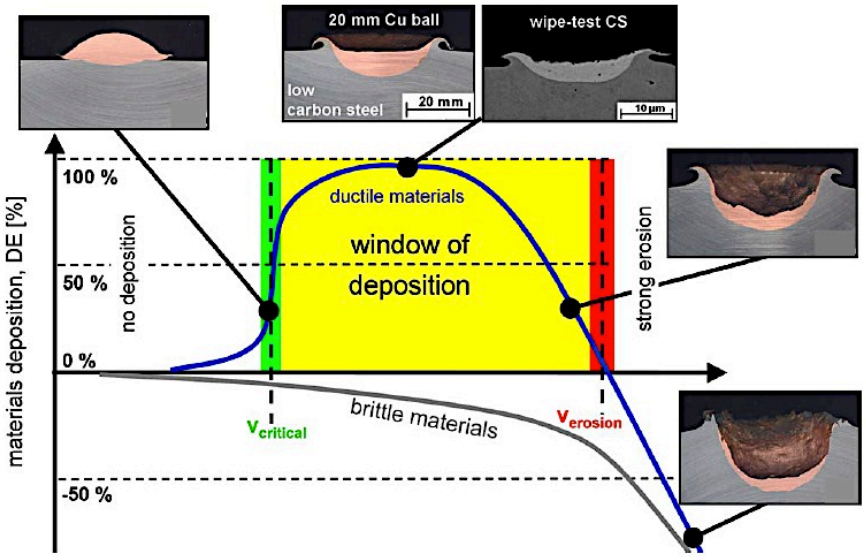

Figure 2.13: Representation of the correlation between particle velocities, deposition efficiency (DE) and impact effect [61]. Inserts of images from the deposition of copper onto low carbon steel are given.

The critical velocity ($V_{critical}$) is defined when a 50% DE is achieved. When the velocity is increased further, the DE reaches saturation and the characteristics of coating deposition conditions are said to be optimal [18]. A supplementary increase in velocity triggers the erosion regime ($V_{erosion}$), which is characterized by hydrodynamic penetration of the particles into the substrate surface and a DE of 0%. For brittle particle materials heated below their melting temperatures, the abrasion of the substrate occurs at every velocity. The critical velocity depends on various factors such as the material, particle impact temperature, particle size and shape and substrate temperature. Figure 2.14 shows the effect of impact temperature and particle size on the deposition.

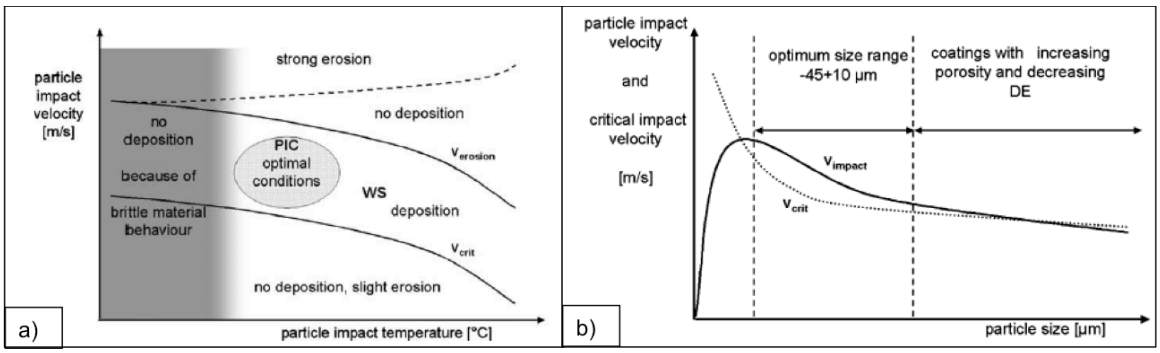

Figure 2.14: a) Particle impact velocity versus particle impact temperature and b) Particle impact and critical velocity as a function of particles size [72].

For a particle size of 20 µm, the critical velocity for aluminum is 620-660 m/s, for copper it corresponds to 460-500 m/s, for nickel the velocity is at 610-680m/s and for titanium it is found to be at 800-890m/s [18]. The oxide layer formed on the specific particle influences the critical velocities required for bonding [73]. Thus, a higher kinetic energy will be required to break a thicker oxide layer and provide sufficient particle plastic deformation.

2.3.5. Bonding Mechanisms

For a particle to achieve deposition it requires a minimum velocity, as noted in the previous section. This suggests that sufficient kinetic energy must be available at impact to deform and bond the particle to the substrate surface. The energy is used to disrupt the thin oxide layer surrounding all surfaces involved, to deform the particle and generate heat. Bonding and adherence of the particle to the substrate surface are affected by various factors. Different

mechanisms responsible for particle adhesion have been analyzed. The level of adhesion depends on the attractive and repulsive forces of the atomic interaction. The impact pressure and the presence of oxide free surface contact control the adhesion phenomenon of the particles. The binary diagram of the materials involved during the cold spray process gives an indication on the possible atomic interactions [74]. The existence of a solubility limit gives rise to repulsive atomic interactions, while complete mutual solubility and the development of an intermediate intermetallic compound is indicative of attractive atomic interactions. The effect of shear instability, metallurgical bonding, interfacial interlocking and mechanical anchoring on the adhesion strength will be presented in the following subsections. Currently, research is conducted to fully understand the bonding mechanisms and their effect on the adhesion of various types of particle/substrate material combinations.

2.3.5.1. Adiabatic Shear Instability

Similarly as in the explosive welding of materials, the adiabatic shear localization caused by the instability of strain softening induces localized particle deformation and heating. A large portion of the particle energy at impact is converted into heat and the rest into deformation. The particle softening, deformation, temperature increase and high contact pressure during the impact process create an intimate contact between clean surfaces, which promotes the bonding between the particles and substrate. In a work-hardening material under non-adiabatic conditions, the flow stress increases with plastic strain. However, in an adiabatic condition, material softening is generated by the increase in temperature caused by the heat input from the dissipation of plastic strain energy. Thus, the strain hardening of the material decreases and the flow stress reaches a maximum before decreasing with plastic strain. Furthermore, since the stress, strain, temperature and inherent instability of strain softening are not uniform within the material and are known to fluctuate, the straining and heating become highly localized and the flow stress rapidly drops to zero. Figure 2.15 illustrates the concepts of isothermal, adiabatic and adiabatic shear localization material deformation processes. The CGDS process is assumed to be adiabatic since the short impact time limits the thermal diffusion distance into the respective materials.

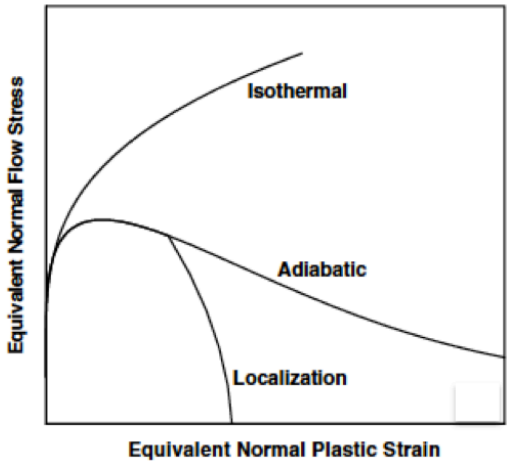

Figure 2.15: Stress-strain curves for a) isothermal, b) adiabatic and c) adiabatic shear localization processes [75].

In the CGDS process, the particles experience strong localized plastic shear deformation during impact. Since the deformation occurs within 50 ns, the heat generation associated with the particle impact cannot be dissipated, highly localized shear instability takes place [60], [61], [75]. The high strain rate plastic deformation along with the adiabatic shear instability leads to jet formation. Moreover, during the particle impact, at very localized regions in the range of few nanometers, the temperature reaches high values and facilitates metallurgical bonding. Figure 2.16 shows the presence of jetting of different particle materials, namely steel, titanium and aluminum on impact with various substrate surface materials.

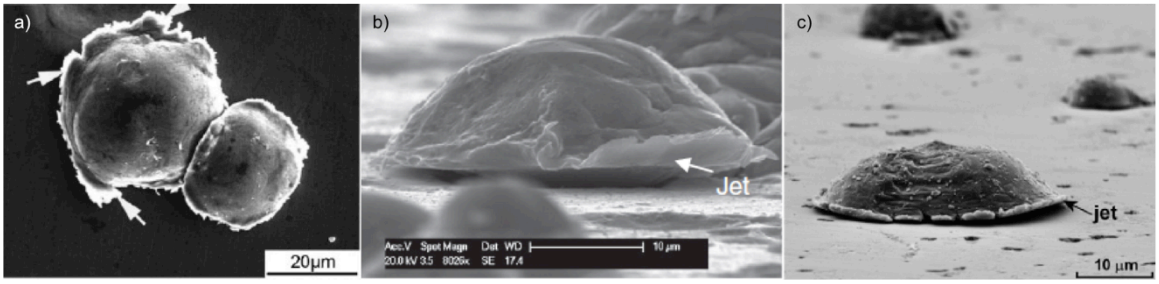

Figure 2.16: a) Morphology of impacted 3014 stainless steel particles on a low carbon steel substrate. White arrows showing jetting around the particles [76]. b) Titanium particle deformation when sprayed on Armco iron substrate [77]. c) Aluminum particle adherence to a PZT surface [78].

Therefore, the solid-state jets extruded at the interface are indicative of a successful surface oxide layer removal and a metal-to-metal contact situation, which can enable the

formation of intimate metallic bonds as shown in Figure 2.17. Oxide inclusions resulting from high oxide content can impede on the final bonding strength.

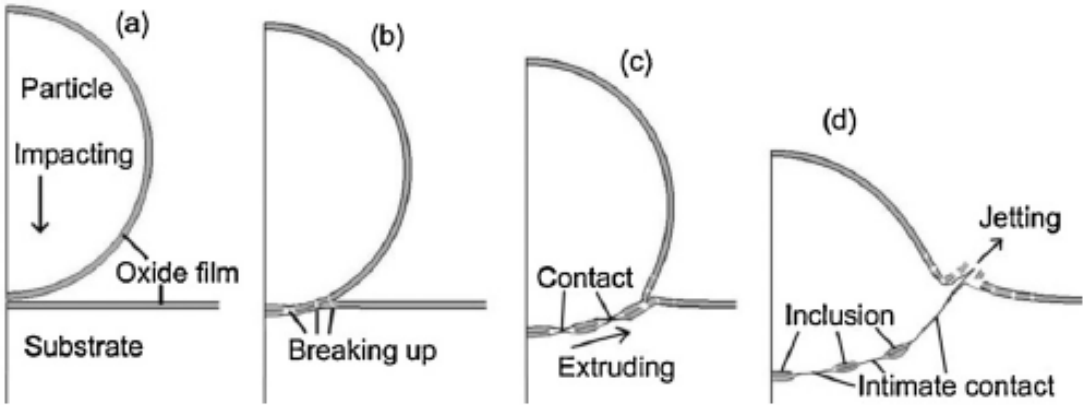

Figure 2.17: Schematic representation of the bonding and jetting process during impact [73].

For a particle to experience optimal bonding the kinetic energy dissipated into heat and plastic deformation must overcome the stored elastic energy. The elastic recovery can generate a repulsive force capable of detaching the particle from the substrate in any stage of the coating formation [74], [79].

2.3.5.2. Metallurgical Bonding

The intimate contact between the metallic lattices can lead to metallurgical bonding at the particle/substrate interface. Figure 2.18 shows examples of intermixed regions at the impact interface. However, due to short impact times, the atomic interdiffusion is limited and its formation into the respective materials is restricted. The interdiffusion distance for many paired materials is found to be less than 0.1 nm [74], [80]. The strength of the interdiffusion is dictated by the nature of the bonds (metallic, ionic or covalent). Based on the distance of the intermixed region, it was found that, the atomic interdiffusion was also complemented with the solid state amorphization of incident metals [80], [81]. It was found through numerous studies that the amorphization process is related to the plastic deformation induced melting followed by a rapid quenching process for materials characterized by low melting points. Whether or not the sprayed particles experience melting during the impact process is still argued. Some have reported that the melting point of FCC metals decreases with increased strains, which might explain their

amorphous structure after impact [80]. Amorphization has also been seen for materials characterized by high melting points, e.g., Ni, Ni alloys and Co alloys [81]. Thus, some claim that the high plastic deformation resulting from high strain-rates develops vacancies and interstitials, which encourage the formation of an amorphous phase during the short duration period of the impact process.

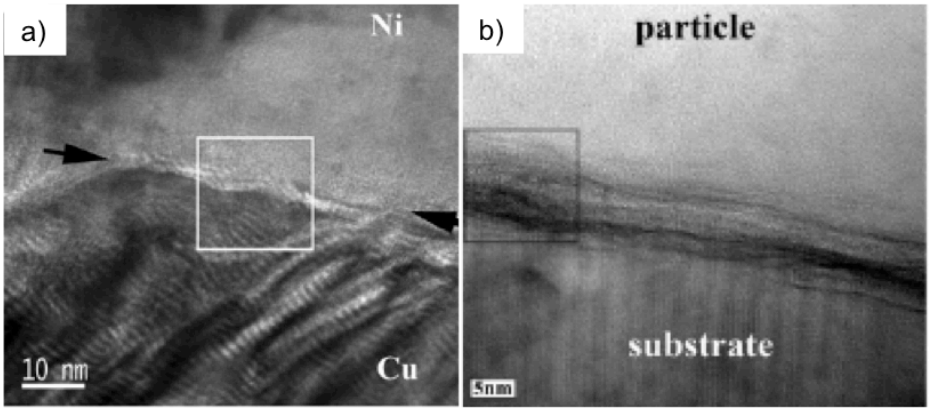

Figure 2.18: HREM of a) Ni particle after impact of Cu substrate [80] and b) Al amorphization [82].

Severe plastic deformation along with high temperature also leads to dynamic recrystallization (static recrystallization refers to heating and cooling processes) at the inter-particle interface through lattice and subgrain rotation. Grain refinement is thus frequently observed at the interface as shown in Figure 2.19.

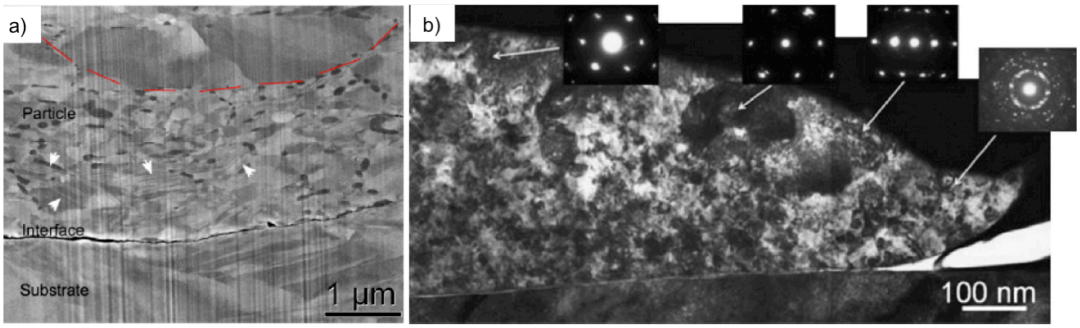

Figure 2.19: a) FESEM image of copper particle-substrate showing refined grains at the boundary and b) TEM single titanium splat grain microstructure [81].

Figure 2.20 also shows the presence of recrystallization at the particle/particle bonding boundaries. Ultrafine grains of 100-200 nm in size can be observed at the particle boundaries. The

rotation (misorientation of adjacent grains) is developed through the increase of dislocation density accumulated in a short period of time.

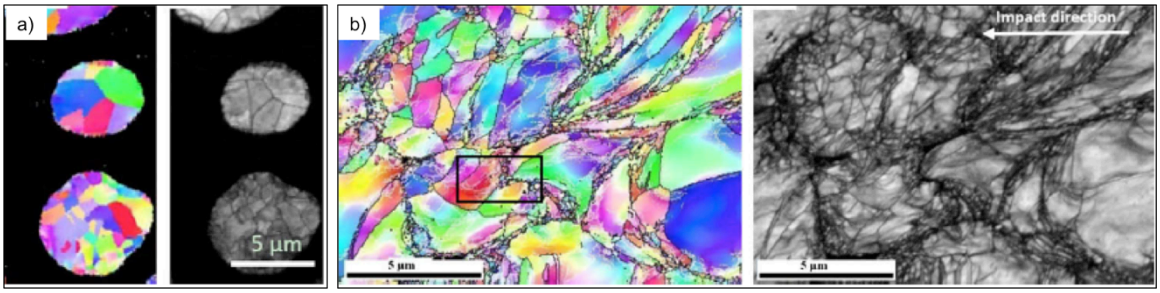

Figure 2.20: Ultrafine grains situated at the nickel particles bonding region, showing a) angle and quality map of as received-powder and b) characterization of as deposited coating (Adapted from [83]).

Moreover, the bonding can be increased as weak Van der Waals forces can develop between the molecules, which are closely spaced [84]. Therefore, the dynamic recrystallization, dynamic amorphization and jetting processes play major roles in the effective bonding of coatings. Their occurrence is proof that the particle impact process is complex and involves non-equilibrium states. The structural and chemical defects that occur after impact can play major roles in the atomic diffusion process and thus the bonding of the particles. Smaller grain size in the range of nanometers and microstructural defects created through the cold working process have been found to increase the atomic diffusion.

2.3.5.3. Interfacial Interlocking

Interfacial perturbations can arise from extremely high pressure and stress levels resulting in interfacial roll-ups and vortices, which promote material mixing, mechanical interlocking and increase the interfacial area. This phenomenon is based on interfacial instability and the surfaces involved can be assumed to behave as viscous 'fluid-like' materials due to the localized heat dissipation and thermal softening. In such situations, the formation of roll-ups, vortices and interfacial waves is seen at the particles/substrate interface as shown in Figure 2.21 [74], [85]. In the situation depicted below, the copper particles were traveling at velocities of 500 m/s in order to achieve such interfacial instability.

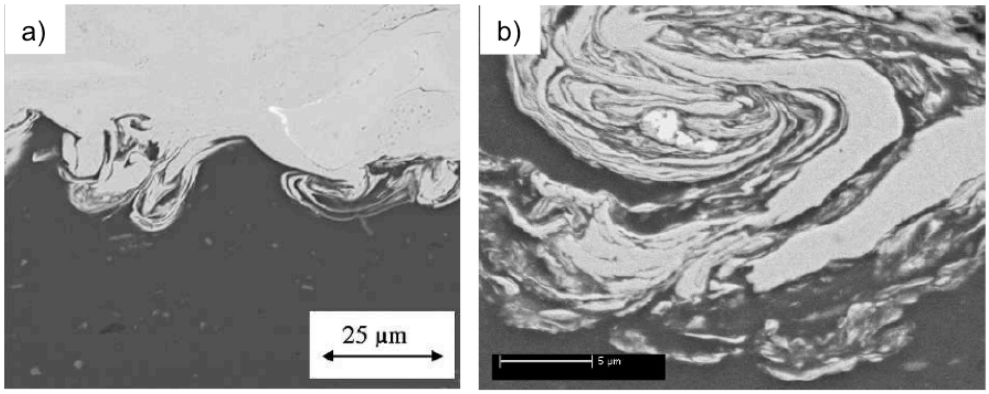

Figure 2.21: Creation of interface vortices during a) copper particle impact on an aluminum 6061 surface [85] and b) nickel powder onto an aluminum substrate [86].

2.3.5.4. Mechanical Anchoring

The topography of a rough substrate surface can influence the deposition of the particles at impact and affect the final coating adhesion. During impact, the pressure increases at the peaks of the substrate, which can lead to high particle deformation. Due to the presence of a surface profile, the particles can become locked at the crevices and mechanical anchoring can significantly increase, as shown in Figure 2.22.

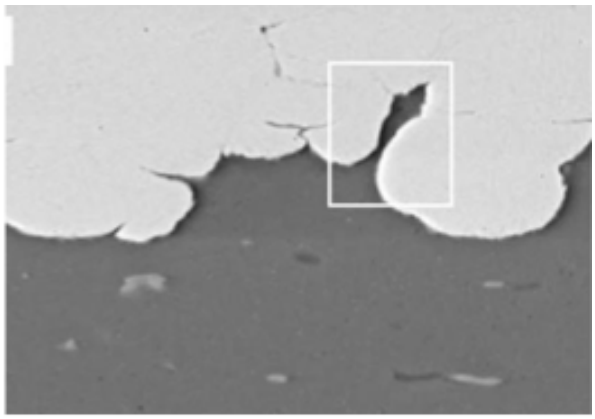

Figure 2.22: Copper coating on an aluminum substrate [87].

As the effective contact interface is increased, the probability for metallurgical bonding increases as well. The size of the particles relative to the size of the substrate crevices is another important factor to take into consideration during the evaluation of surface bonding. In order to

optimize the anchoring and wedging process of the particles, their size must be similar to the dimensions of the substrate profile gaps. Figure 2.23 shows a Ti-6Al-4V substrate laser treated surface upon which small and large titanium particles have been deposited. The small particles are entirely wedged into the substrate craters while the large titanium particles are limited to anchoring at their impact surface only across numerous ridges and valleys. Stronger adhesion values were obtained in the case of the smaller particles due to their specific fit within the substrate surface voids [88].

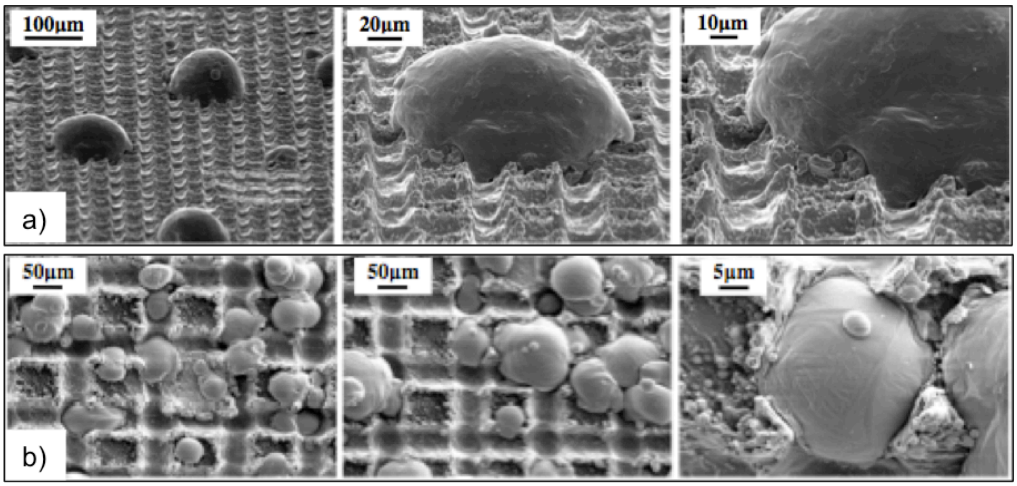

Figure 2.23: Laser roughened TIA6 substrate. a) Large titanium particles deposition and b) small titanium particles [88].

Roughening the substrate surface prior to spraying is a common practice for the cold spray procedure [89]. It has also been suggested that the main purpose of the very first particles hitting the substrate during cold spray is to activate its surface by roughening it in order to enable coating growth and optimize deposition [84], [90].

Marrocco et al. [91] have correlated the adhesion strength of titanium coatings on Ti-6Al- 4V (Ti-6wt.%Al-4wt.%V) substrates with the substrate surface preparation procedures, which have been categorized based on the resulting roughness of the substrate surface. Their results show bond strength of 22 MPa for polished and ground surfaces and a high decrease in adhesion to 8 MPa for the grit blasted surface. They claim that the grit blasting procedure has created a work-hardened substrate surface that is unable to deform upon impact, thus limiting the

formation of primary bonds. The surface roughness also reduces the level of particle jetting, which restricts the removal of particle oxide and gives rise to weak bonds.

Ziemian et al. [92] compared a glass-bead and grit blast surface procedure by measuring the cycles to failure of coated circular substrates. They concluded by stating that the glass-bead prepared substrates sustained more cycles to failure since the preparation procedure produced less surface damage, a higher substrate roughness and a lower percentage of embedded grit as compared to the grit blasting procedure. Similarly, González-Hermosilla et al. [93] have observed that the grit blasting procedure using alumina grit produces a highly deformed SAE 1045 steel substrate characterized by deep notches that act as stress concentrators and influence the fatigue crack nucleation in Wc-10Co-4Cr cermet coating. Moreover, as shown in Figure 2.24, the presence of embedded alumina grit at the substrate surface act as flaws and are defined as crack initiators. Any embedded media at the substrate surface will decrease the number of bonding locations and proper mechanical anchoring. However, various grit blasting parameters such as blast pressure and angle, grit size and material, blasting time and stand-off distance can be modified to avoid substrate contamination. Grit residue has been found to increase with increased blasting angle, pressure, grit size and decreased stand-off distance [94].

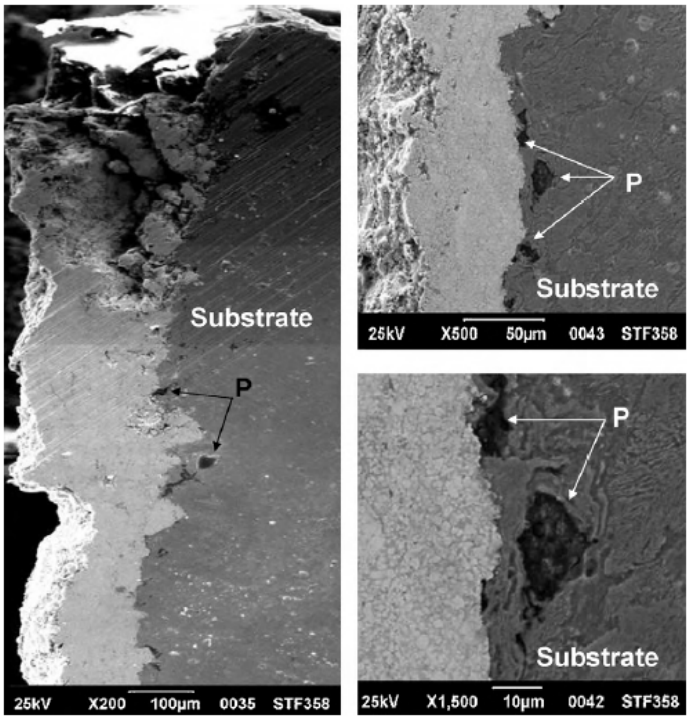

Figure 2.24: Embedded alumina grit media at the substrate surface [93].

Sen et al. [95] have evaluated that a minimum of 4 μm in surface roughness, obtained using an alumina grit of 40 and 60 mesh size, is needed to achieve the highest bond strength for their Cu, Al_2O_3 and WC-Co coatings sprayed using a detonation spray process on mild steel substrates. Likewise, Bahnou et al. [94] observed an increase in Tibaloy 800 coating (with nominal chemical composition of Co-28Mo-17Cr-3Si) adhesion strength as they increased the Ti-6Al-4V substrate roughness by grit blasting their surface with alumina media at angle of 90° prior to the plasma spray process.

2.3.6. Residual Stress

The residual stress profile in the coating/substrate assembly is caused by the plastic deformation encountered during the impact of high velocity particles. The final state of stress is affected by the successive impingement of particles and plastic deformation of the underlaying layers during the formation of the coating. For dissimilar materials characterized by different thermal expansion coefficients, in the coating/substrate assembly, an additional effect from the thermal misfit can influence the residual stress state [9], [96]–[99]. Compressive residual stresses at the surface can increase the fatigue life of a component [9], [92] but decrease the adhesion strength by initiating buckling in the coating. However, some argue that the roughness of the substrate after cold spraying act as stress raiser and facilitate the crack initiation and propagation regardless of the presence of compressive stresses [99], [100]. Compressive stresses are formed in the coating but various parameters that will be discussed in the following subsections can influence the final stress state and induce tensile stresses.

In previous studies, compressive stresses in copper coatings were measured to be in the range of 40 to 85 MPa, while for aluminum coatings inferior values of 9 MPa were obtained [97], [101]. A compressive residual stress of 253.7 MPa has been measured for a titanium coating deposited onto an aluminum substrate [81].

2.3.6.1. Effect of Process Temperature on Residual Stress

When high process temperatures are used, quenching stresses can develop after the spray procedure and diminish the influence of the compressive peening stresses, which can result in a tensile residual stress state [100]. Depending on the coating/substrate material combination and

based on their specific CTE's, the resulting residual stress can be compressive or tensile. Moreover, the thermal input dictated by the process temperature promotes the residual stress relaxation at the coating/substrate interface [9].

2.3.6.2. Effect of Coating Thickness on Residual Stress

An increase in the coating thickness, irrespective of the number of passes used to build the thickness, can decrease the compressive stress state at the coating/substrate interface through a stress relief annealing process [88], [96], [102], [103]. Larger coating thicknesses consequently increase the duration of spray and heat input, which allows the stress relief process to initiate. A lower residual stress state induces less stress on the coating at the coating/substrate interface and has less negative impact on its adhesion. However, decreasing the compressive residual stress at the interface can loosen the mechanical anchoring formed between the particles and the substrate, which can decrease the coating bonding strength [105]. Finally, the increasing impingement of particles with larger coating thicknesses increases the final compressive residual stress state in the coating, which may induce sufficient stresses at the interface to cause de-bonding failure. As depicted in Figure 2.25, Giraud [88] has shown that, besides the influence of coating thickness on the delamination, the dimensions of the coated surface also plays a major role in the coating adhesion and final residual stress state.

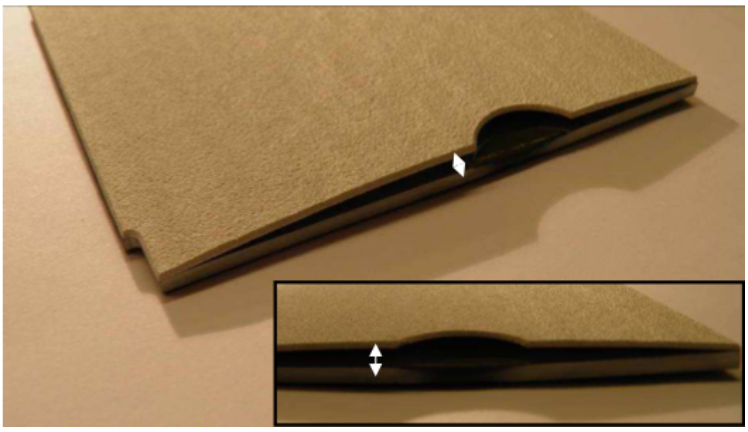

Figure 2.25:Thick aluminum coating delamination due to the presence of residual stresses [88].

Residual stresses are of self-equilibrating nature (zero net internal forces) for systems free of external forces and constraints [104], [105]. These stresses are induced by the elastic response

of the material to the non-uniform distribution of different factors such as plastic strains, thermal expansion and misfit [106]. Due to the self-equilibrating nature of residual stresses, an increase in coating thickness can vary the nature of the resulting stress at the interface and across the coating and substrate thickness.

Many factors influence the distribution, magnitude and sign of the residual stresses in coatings but their individual contribution to the overall state is still difficult to analyze.

2.3.7. Influence of CGDS Process Parameters on Deposition

This subsection will cover some important parameters that affect particle deposition and coating formation.

2.3.7.1. Process Pressure and Temperature Influence on Deposition

An increase in stagnation pressure increases the gas density, which increases the drag force acting on the particles [107]–[109] and consequently the particles are able to reach higher exit velocities. The stagnation temperature is more influent on the particle exit velocity than the stagnation pressure. That is because higher process temperatures increase the velocity of the gas flow, thus increasing particle velocity, and allow particle thermal softening, which decreases the particle critical velocity required to properly deposit, deform and bond [109]. Higher material ductility signifies that less kinetic energy is needed to plastically deform the particles during impact. Larger jetting and flattening ratios are more prone to happen during impact for particles of high temperature. Higher deposition efficiencies are obtained for higher gas pressure and temperature [110]. Therefore, the spraying traces increase in dimension with larger process temperatures and pressures as shown in Figure 2.26 for the case of an increase in temperature from 300 °C to 500 °C [110] during the deposition of Al-Si on mild steel substrates.

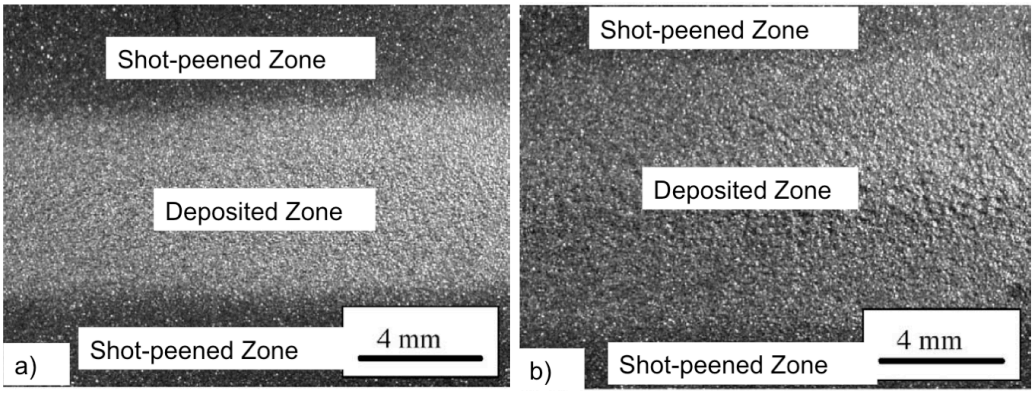

Figure 2.26: Al12-Si powder single pass deposition onto a mild steel substrate at 2.9 MPa and a) 300 °C and b) 500 °C (Adapted from [110]).

Furthermore, since the process temperature affects the particle stress-strain behavior by decreasing its shear resistance, the particles are able to undergo excessive deformation, which can significantly eliminate the porosity content in the coating [111]. Zahiri et al. [111] have discovered that the porosity in pure Cu coatings sprayed on aluminum substrates decreases from 0.7% to 0.005% when the process temperature is increased from 300 °C to 630 °C respectively.

2.3.7.2. Traverse Velocity

At lower nozzle traverse speed, the exposure time of the substrate surface to the cold spray gas flow increases. Thus, the surface temperature and the amount of subsequent impinging particles increase [13]. Sufficient surface heating and particle impingement can promote particle bonding and particle deformation. Higher levels of impingement can decrease the coating porosity and ensure proper compaction between the particles in the coating.

2.3.7.1. Powder Feed Rate

The powder feeding rate influences the deposition rate and impingement level [112]. Generally, the coating thickness increases with an increased level of projected feedstock powder. Large feeding rates increase the number of particles impingement per unit area of the substrate surface. However, an excessive powder feeding rate can result in oversaturation of the flow, which will affect the flow dynamics and eventually the coating quality. A larger particle mass

requires more energy from the gas to be accelerated and thus individual particles may not reach their critical velocity for proper deposition.

2.3.7.2. Substrate Pre-Heating

Numerous studies have shown that the increase in substrate temperature lead to improved particle deposition efficiency [113]–[116]. Higher surface temperature increases the particle deformation and promotes the occurrence of metallurgical bonding through interfacial melting. The substrate deformation degree also increases with substrate temperature as shown in Figure 2.27, which promotes the removal of the oxides films and intimate contact between the particles and substrate. As a consequence, larger bonding areas are formed and the bonding strength can be improved and mechanical anchoring sites multiplied. Significant stress relief can also be achieved through high pre-heating temperatures [117]. Embedment of particles inside the substrate surface due to its softening process at high temperature provides higher coating adhesion strength.

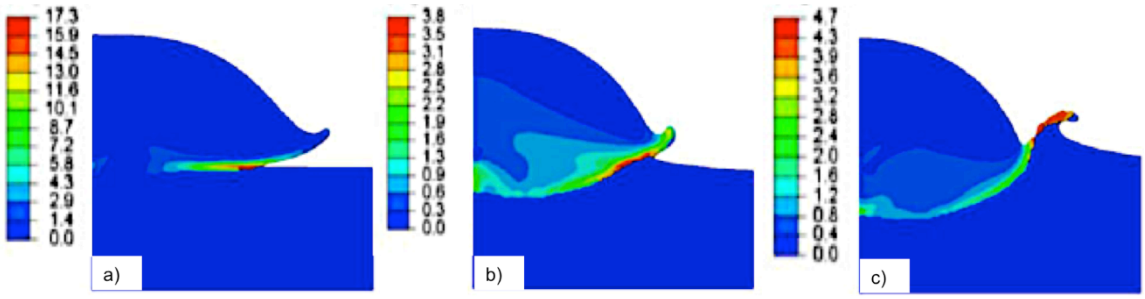

Figure 2.27: Simulations of Cu particles impacting In718 substrates heated at temperatures of a) 600°C, b) 950 °C and c) 1100 °C (Adapted from [118]).

Suo et al. [119] have discovered that preheating an aluminum substrate to 100 °C and 200 °C increased the bonding strength of the pure Mg coatings. A further increase in substrate temperature, up to 300 °C led to a decrease in bonding strength due to the excessive aluminum oxidation process encountered at that temperature.

2.3.7.3. Spray angle

During spray, the magnitude of the particle velocity normal to the surface is the main factor influencing the bonding and deformation process of particles during their impact. When the

powder flow impacts the substrate at off-normal angles, as shown in Figure 2.28, the normal velocity component decreases. As a consequence, if the effective velocity is less than the critical velocity, the deposition efficiency drastically decreases [120].

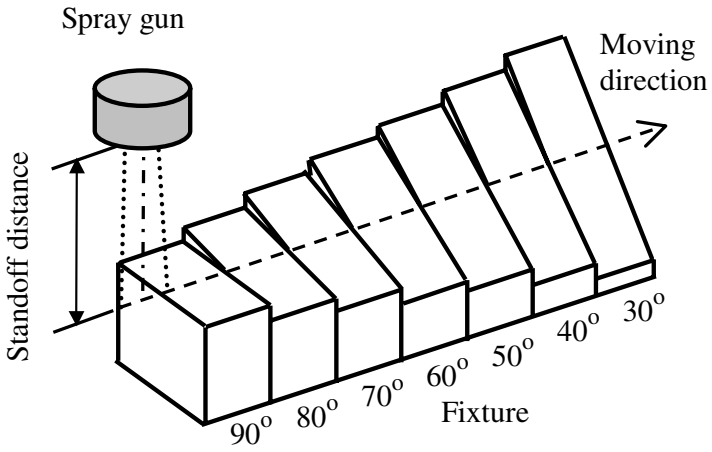

Figure 2.28: Illustration of angular deposition [120].

For angular spraying, a tangential momentum parallel to the substrate surface is also generated. Moreover, a gap between the particle and substrate is developed [121]. As the angle between the particle and the substrate decreases, the localization of the impact increases and thus the interfacial contact area decreases as shown in Figure 2.29. Wang et al. [122] have discovered that the bonding strength of Al6061-T6 particles with Al6061-T6 substrate increases with decreasing incident angles from 90 ° to 45 °. An increase in particle tangential movement across the substrate surface increases the friction dissipation energy and consequently increases the temperature of the particle at the impact zone and decreases the contact area between substrate and particles. Despite showing an increase in bonding strength, the coatings sprayed at shallow angles were characterized by low deposition efficiencies and low bulk material strengths.

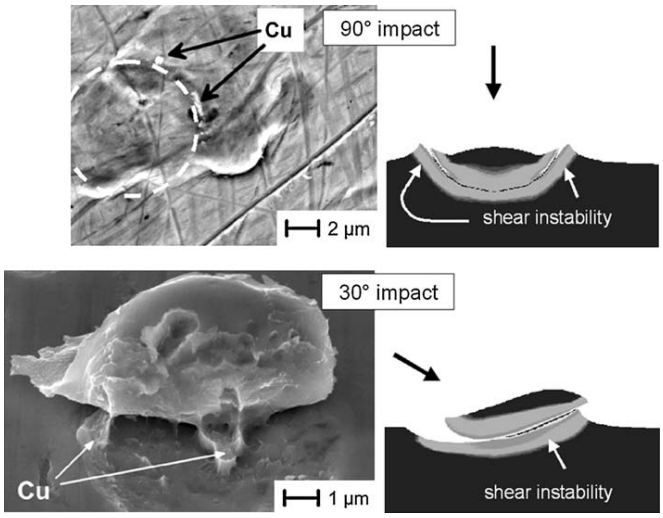

Figure 2.29: Impact area for perpendicular and angular deposition [61].

Moreover, the tangential velocity tends to separate the impacted particles from the substrate surface [121] as shown in Figure 2.29 and Figure 2.30. Dimple-like features seen on one side of the particle support the presence of tangential momentum and particle separation from the substrate surface.

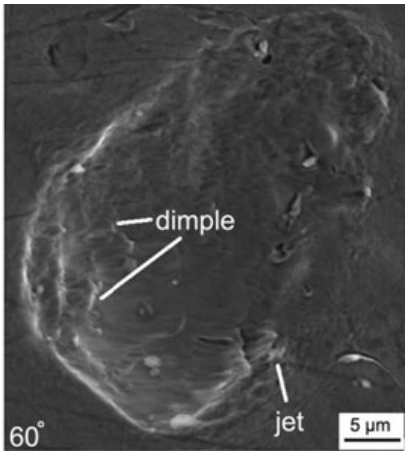

Figure 2.30: Dimple-like features supporting the evidence of tangential momentum in angular deposition [121].

In addition, the spray angle influences the temperature gas distribution on the substrate surface. As the angle is increased, the high temperature zone size decreases and the low temperature zones induced by the oblique shock increase at the uperhill direction as depicted in Figure 2.31.

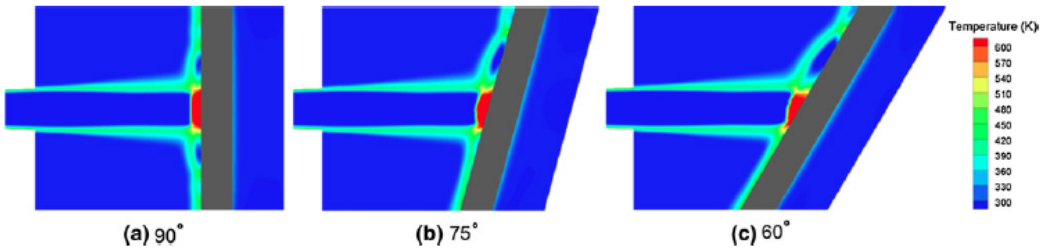

Figure 2.31: Temperature contours for varying substrate angles [123].

Thus, the spray angle affects the radial temperature distribution. For non-perpendicular spraying, the temperature contours are asymmetrical to the axis of spray.

2.3.7.4. Standoff Distance (SOD)

Pattison et al. [69] have shown a direct correlation between nozzle standoff distance and deposition efficiency, as shown in Figure 2.32. At small SODs, the bow shock created at the substrate surface is strong enough to affect and reduce the particles velocity and deposition efficiency strongly to reduce it. At high SODs, the bow shock disappears but the particle velocity decreases during their flight in air environment due to a negative drag force (slowing down the particles rather than accelerating them) created by the lower atmospheric gas velocity. Thus, for optimal deposition, the SOD must be evaluated so that the effect of the bow shock, at the substrate surface, and air, at the exit of the nozzle, on the particle velocity is limited.

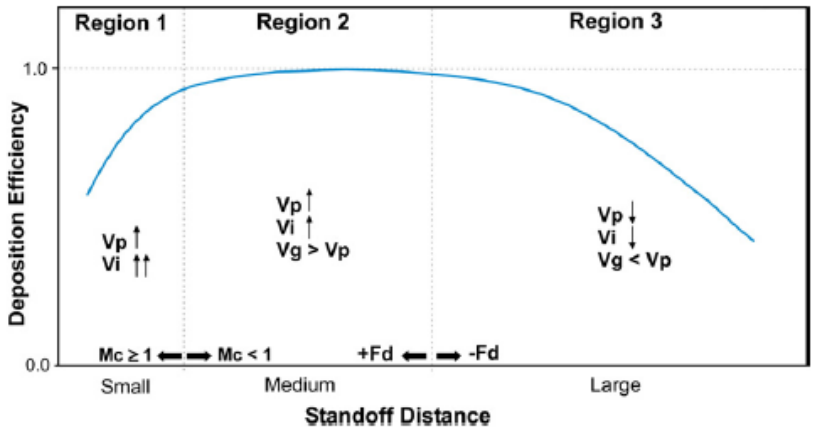

Figure 2.32: Illustration showing the effect of standoff distance on deposition efficiency. F_d represents the drag force, M_c is the axis Mach number, V_g is the gas velocity, V_p id the particle velocity before impact and V_i is the velocity at impact [69].

The standoff distance at which maximum particle velocity is achieved must be known in order to optimize deposition. Saden et al [126] have observed that an increase in temperature and pressure result in an increase of the jet length and maximal velocity is thus achieved further away from the nozzle exit.

2.4 Non-Structural Repair by Cold Spray

The cold spray technology is currently being used to repair damaged zones on various metallic structures. It is primarily used as a dimensional restoration process. In many cases, such as repair of corrosion damage, a different material is sprayed to improve the properties of the damaged component. The successful repairs must usually meet specific service requirements regarding porosity, corrosion resistance, adhesion strength and dimensional integrity. As such, the military standard, MIL-STD-3021, revised in 2011 has been approved by the US department of Defense for use in repair of military components to control the cold spray process and property testing procedures.

Figure 2.33 shows the use of the cold spray process to restore the dimensions of cam bearing mounting pads on a cast iron engine using nickel alloy material.

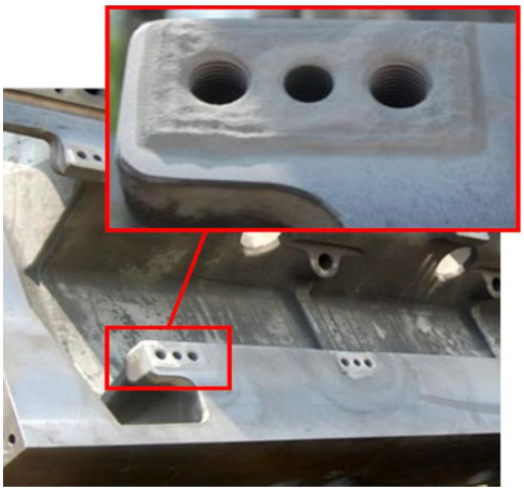

Figure 2.33: Restoration of iron engine block mount [27].

A low temperature repair process had to be used in order to avoid distortion of the pads. Figure 2.34 shows the repair of Al7149 Apache Helicopter mast supports by LPCS process using

a mixture of aluminum-alumina powder. The damaged area is re-build and re-machined to its initial dimensions.

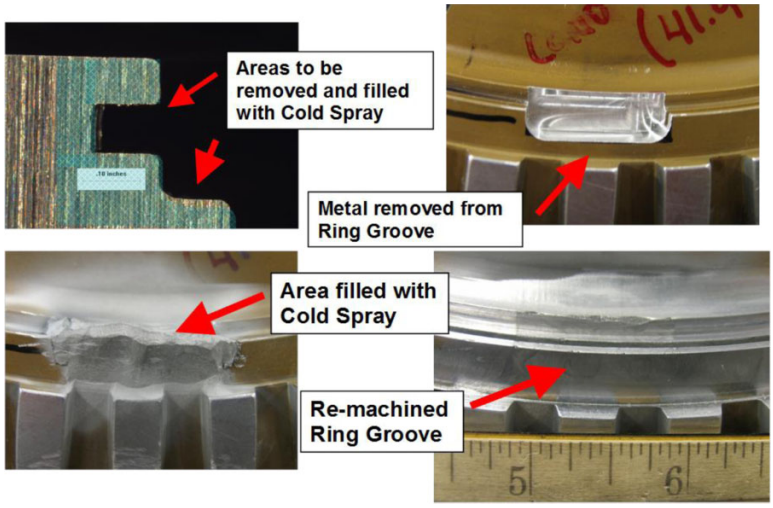

Figure 2.34: Repair of aluminum mast support in helicopter [27].

Figure 2.35 shows the repair of corrosion damaged ZE41 magnesium gearbox housing using cold sprayed Al6061 material. Aluminum has been used based on its availability and its capacity to reduce corrosion recurrence.

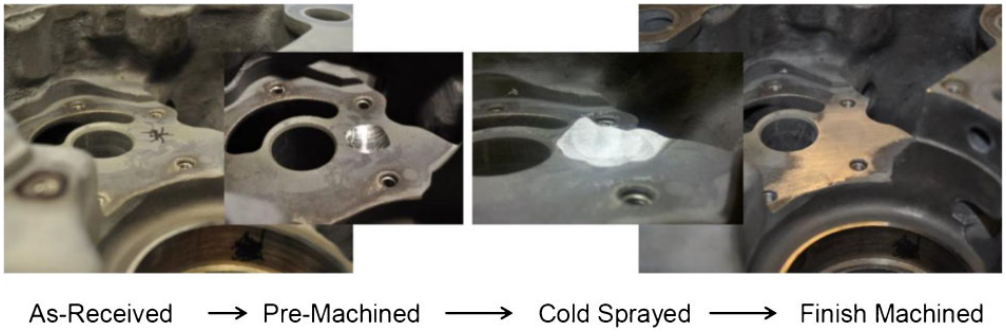

Figure 2.35: Magnesium gearbox repair [27].

Figure 2.36 shows the B1 bomber skin panel repair using the CGDS process. The repairs have been tested in shear and fatigue for which they have shown no delamination or degradation. The repair process is currently being used on the B1 aircraft.

Figure 2.36: Skin panel repair using the cold gas dynamic spray process [125].

2.5 Summary and Comparison of the Thermal Spray Processes

Figure 2.37 depicts the operating window of various thermal spray processes based on their operating gas temperatures and resulting particle velocities. As seen in the figure, the cold spray process occupies a distinct operating window that is characterized by low process temperatures and high particle velocities.

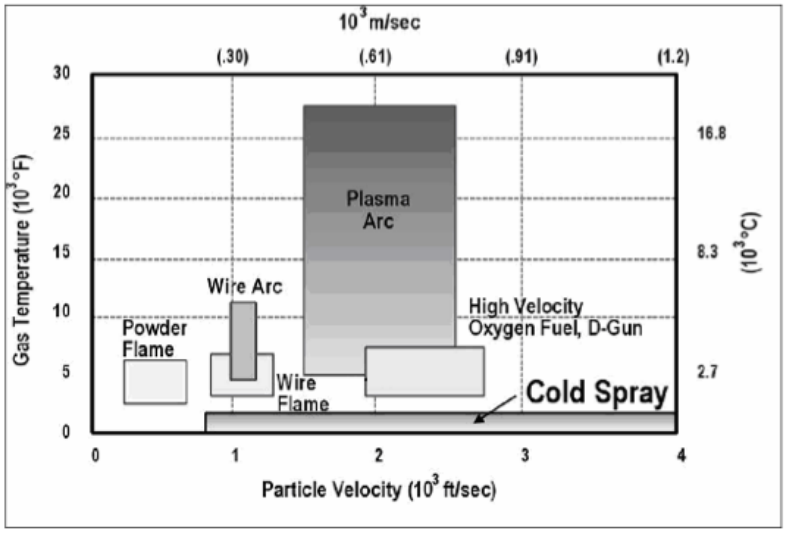

Figure 2.37: Particle velocity and gas temperature for various thermal spray processes [126].

The plasma arc spray defines itself with the highest spraying temperatures and reasonable particle velocities. Similarly, the HVOF operates at higher temperatures than the cold spray process but as described in section 2.2.1.3, is capable of depositing material using only a fraction of the temperature used by the plasma arc spray. The wire arc process operates at both low temperature and particle velocities. Thus, unlike the other thermal spray processes, the thermal energy in the CGDS process is used primarily to accelerate the particles instead of heating them to their melting point. Table 2.2 gives a summary of the typical spraying features and coating characteristics for different thermal spray processes.

Table 2.2: Characteristic of Different Spray Processes [40], [48], [127], [128]

Spray Process	Electric Arc	Plasma Spray	HVOF	CGDS
Process Parameters				
Gas Temperature (°C)	5500	>20000	3000 to 4500	20 to1100
Particle velocity	50 to 100	200 to 800	200 to1000	200 to 1200
Coating Characteristics				
Porosity (%)	10 to 20	APS: 1 to 40 LLPS: 1 to 10	0.5 to 5	< 5
Oxide Content	Moderate to high	Moderate to low	Moderate to Disperse	Minimal
Residual Stress	Tensile	Tensile	Compressive	Compressive
Adhesion Strength (MPa)	10 to 40	15 to 25	90	70

Figure 2.38 shows the cross sectional microstructure of Ni–5 wt.%Al coatings on steel substrates obtained using thermal and kinetic (CGDS) spray processes. As shown, the coating deposited using the APS presents the highest amount of porosity due to the use of high process gas temperatures. The expansion of the air trapped between the molten particles creates voids within the deposited coatings. The level of porosity is thus reduced for coatings obtained during HVOF deposition. For the cold spray process, very dense coatings are created as the particles undergo a high level of plastic deformation at very low processing temperatures and high particle velocities. The kinetic energy also promotes interaction between particles and thus improves the interparticulate bonding.

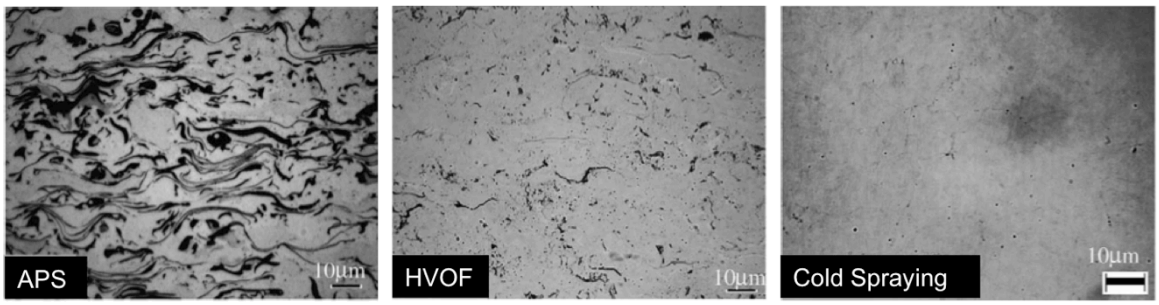

Figure 2.38: Cross sections of Ni-Al coatings deposited using different spraying processes (Adapted from [128]).

The amount and distribution of oxide content in the coating is also dependent of the spray process. Notable oxide inclusions are seen in various coatings sprayed with molten particles. Moreover, the final residual stress state in the coating is a function of the kinetic energy, such that the HVOF and CGDS processes lead to compressive residual stresses.

2.6 CGDS Advantages and Disadvantages

This section will list the main advantages and disadvantages of the CGDS process.

2.6.1. Advantages

- Increased area deposition rate and narrow spray beam, which allows controlled deposition in near-net-shape features [40].
- Unlike the other thermal spray processes, overspray is limited and no masking is needed.
- High density coatings can be achieved due to the peening effect that allows additional deformation processes from subsequent impact particles.
- Due to the low process temperatures, the thermal input to the substrate is limited to the stagnation temperature of the impacting gas flow and thus CGDS process can be used to repair temperature-sensitive materials.
- Due to the high particle plastic deformation during impact, a compressive residual stress state is formed within the coating, which disables crack initiation and propagation and improves fatigue performance.
- Compressive residual stresses inherently generated in the CS coatings increase the fatigue life of components. The compressive residual state can also provide sufficient pressure to

keep the particles mechanically attached to the substrate surface. In typical thermal spray processes, the residual tensile stress increases with thickness up to a critical value described by coating spallation.

- During the CGDS process, the particles remain near ambient temperature and therefore oxidation, decomposition, formation of metastable phases and grain growths are avoided.
- Due to the high interparticulate bonding caused by high particle plastic deformation, limited amount of oxide and inclusions and restricted formation of pores, the CGDS coatings exhibits high thermal and electrical conductivity.

2.6.2. Disadvantages

- Similarly to the other line-of-sight thermal spray processes, the spray of complex internal surfaces difficult of reach is impossible.
- Ceramics are hard to deposit due to the low processing temperatures.
- Due to the CGDS process assembly and equipment, high powder feeding rates and elevated stagnation temperatures can lead to nozzle clogging.

2.7 Previous Research on Coating Deposition

The following section will discuss the results obtained in various studies found in the literature for the deposition of Al2024 and pure aluminum particles. The purpose is to obtain a general overview of the process parameters required to obtain proper deposition and list the mechanical and microstructural properties of the specific coatings.

2.7.1. Al2024 Deposition

A limited amount of published research was available on the CS of Al2024 coatings. Sprays conducted on Al2024-T3 substrates using a commercially available Centerline (Windsor) Ltd. SST Low Pressure Cold Spray system from Centerline (Windsor) Ltd, a steel nozzle and process pressures and temperatures ranging between 400 °C and 500 °C and 1.4 MPa to 1.7 MPa respectively have resulted in no deposition and severe nozzle clogging issues [129]. To prevent clogging, preliminary sprays using a polymer nozzle (Centerline (Windsor) Ltd.) limited to a working temperature of 350 °C was used to produce Al2024 coatings. The process temperatures

tested are 300 °C and 350 °C along with 1.4 MPa and 1.7 MPa of stagnation pressure. Despite solving the clogging issues, no deposition was obtained due to the powder low exit velocity [129].

2.7.2. Pure Aluminum Deposition

Numerous published papers regarding the pure aluminum powder deposition ability and coating quality are available in the literature. In the study conducted by Hall et al. [130], dense pure aluminum coatings were obtained at a process temperature and pressure of 350 °C and 1.7 MPa respectively, as shown in Figure 2.39.

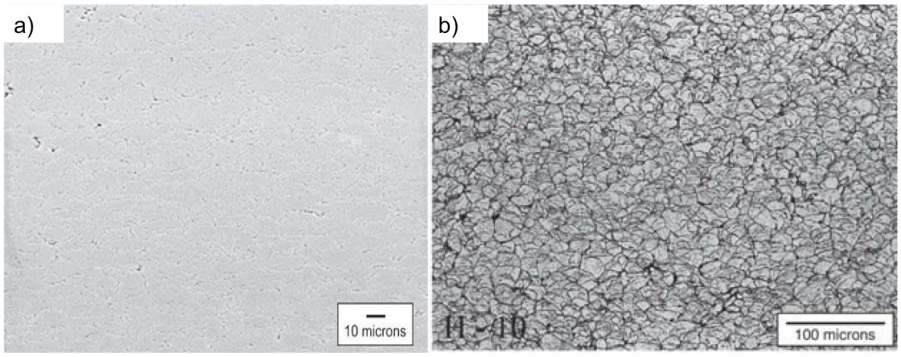

Figure 2.39: As sprayed pure aluminum coatings [130].

The obtained coatings exhibited a brittle behavior characterized by 1% strain to failure. Finer aluminum particles were able to reach higher exit velocity and yield coatings with higher ductility and lower porosity. Van Steenkiste et al. [131] have deposited 1.19 mm and 3.30 mm thick pure aluminum coatings using large aluminum particles (>50 μm) and process temperatures of 204 °C and 315 °C respectively. Figure 2.40 shows the coating microstructure obtained after the CS deposition process. Besides obtaining larger depositions at higher process temperatures, the number of passes required to build the thickness was decreased from 10 passes to 5 passes. An increase of the powder feeding rate from 13.1 g/min to 39.4 g/min led to a decrease in deposition efficiency from 26 % to 7 %.

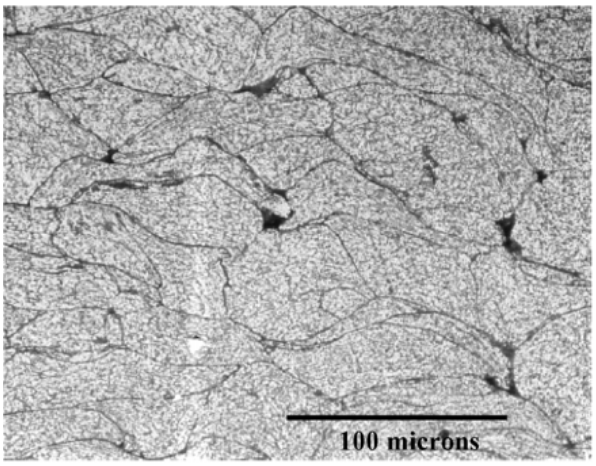

Figure 2.40: Pure aluminum coating microstructure at the as-sprayed state [131].

Champagne et al. [132] were also able to produce dense aluminum coatings as shown in Figure 2.41 at higher spraying parameters of 4 MPa and 400 °C. The cold working involved in the CS process resulted in an increase in hardness from the virgin aluminum powder hardness value of 36HV to 68 HV after spray.

Luzin et al. [97] have studied the residual stress profile in pure aluminum coatings deposited at 0.62 MPa and nozzle temperature of 140 °C on aluminum substrates. The obtained coating presented a low amount of porosity and a residual stress of less than 10 MPa. Stress relaxation processes caused by the process gas temperature may have had an influenced on the finals residual stress state.

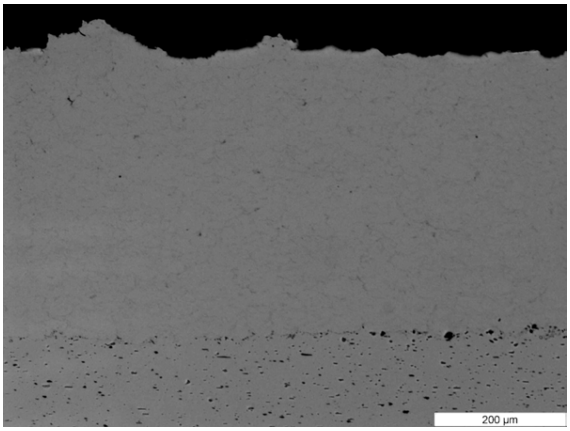

Figure 2.41: Pure aluminum coating microstructure sprayed on Al6061 [132].

Table 2.3 presents a summary of the pure aluminum coating properties obtained at various system parameters through different studies. A large amount of literature is available on the use of the CGDS process to deposit pure aluminum powder on various substrate materials, however, only five have been selected and presented below to provide a general idea of the coating properties obtained at different spray parameters. Generally, very dense coatings were produced at various process parameters, which indicates that the deposition of the pure aluminum powder requires a low amount of energy. The high ductility and low-density of the pure aluminum powder facilitates its deformation process upon impact and consequently increases its bonding to the substrate surface. Higher stagnation temperatures lead to an increase in coating ductility and decrease in residual stresses.

Table 2.3: System Parameters and Coating Properties for the Cold Spray of Pure Aluminum

Parameters	K. Balani et al. [133]	A.C Hall et al. [130]	C.W. Ziemian [92]	T.H. Van Steenkiste et al. [131]	V. K. Champagne et al. [132]
Gas Type	He and N_2	He	N_2	Air	N_2
Powder Type	1100 Al	Pure Al	CP* Al	Pure Al	Pure Al
Powder Size (μm)	1-30	Average 11.8	5-50	65-105	Average 15
Powder Morphology	Spherical	GA**	GA**	Spherical	N/A
Process Pressure (MPa)	2.1	1.7	3.45	2	3-4
Process Temperature (°C)	227-527	350	230	204-371	350-400
Standoff Distance (mm)	N/A	38	25	20	N/A
Nozzle Area Ratio	N/A	2.5	3.77	2.83	N/A
Nozzle Length (mm)	N/A	100	168	80	N/A
Substrate Material	Aluminum alloy	N/A	AA2024-T351	Brass	Al6061
Substrate Preparation	None	N/A	Shot peened or glass-bead	Sand blasted	N/A
Coating Porosity (%)	Dense	<0.1	0.4	1.75-4.51	N/A
Coating Hardness	128-275 VHN	N/A	34-70VHN	0.38-0.513 MPa	60 HV

* Commercially pure

**Gas atomized powder

2.8 Particle in Flight Velocity and Distribution Measurements

The current section aims to report the results found by many researchers regarding the cold spray free jet dimensions and the parameters influencing the powder velocity and distribution field. The trajectory of the powder at the exit of the nozzle influences its deposition

efficiency and deformation process. Therefore, to optimize the coating quality and reduce the spray time, many researchers have studied the general stream behaviour at the nozzle exit.

Zahiri et al. [124] have used a PIV system to illustrate the effect of pressure and temperature on the particle velocity pattern at the exit of the nozzle for CP titanium particles. The results are presented in Figure 2.42 for different combinations of process parameters. As shown, an increase in both the pressure and temperature leads to an increase in particle velocity at the center of the jet and in stream length. The length of the high velocity stream increases from 7 cm to 13 cm under an increase in stagnation parameters. The velocity reduces radially from the center to the flow boundaries. The uniformity of the particle velocity across the obtained profile is affected by the process parameters. As seen in Figure 2.42, an increase in stagnation temperature from 550 °C to 750 °C produces an unequal distribution of velocity from the center to the jet boundaries. The velocity increases at the core of the flow at the cost of reducing the particle in-flight velocity near the edges. An uneven distribution leads to an unequal deposition of powder and to a reduced coating quality. An increase in pressure shifts the velocity distribution and disturbs its uniformity.

Gilmore et al. [134] have measured the in-flight copper particle velocity using a laser two-focus system. Their results indicate that the velocity remains relatively constant within a portion of 6 mm of the stream width and decreases by 11% near the flow edges. It was also found that the mass loading of particles inside the nozzle had an important influence on the resulting mean particle velocity. An increase in feeding from 0.5 g/s to 1.5 g/s decreased the velocity from 360 m/s to 347 m/s.

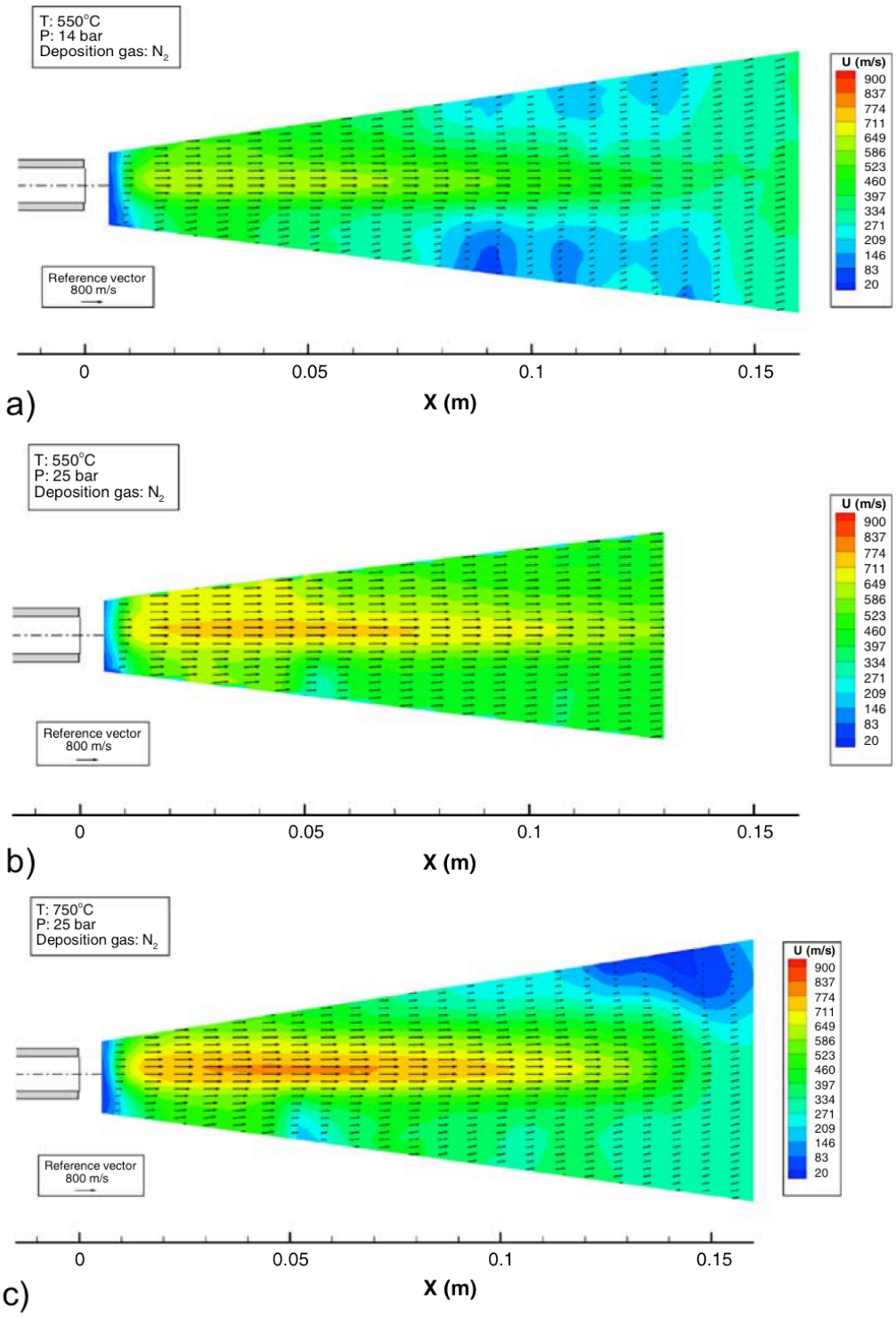

Figure 2.42: PIV representations of the velocity field at the exit of the nozzle for cold sprayed CP titanium supersonic jet at a) 550 °C and 1.4 MPa, b) 550 °C and 2.5 MPa and c) 750 °C and 2.5 MPa [124].

Patisson et al. [69] have explained that the viscous effects of the environment decrease the gas velocity that is at the jet edges and leaves a supersonic core at the center of the flow. The length of the supersonic core affected by the process parameters as shown previously, changes the bow shock dimensions with the standoff distance. If the SOD is larger than the supersonic core length, the bow shock size is drastically reduced as it only arises due to the impact of supersonic gas velocities.

Figure 2.43 depicts the influence of particle size (15 μm and 150 μm) on their spreading in the gas flow. Larger particles are subjected to higher inertia forces such that their path undergoes only small deviations relative to the center of the nozzle, which creates a conical type of flow distribution [88], [135]. Thus, the highest flow rate is located in the center of the jet and decreases radially.

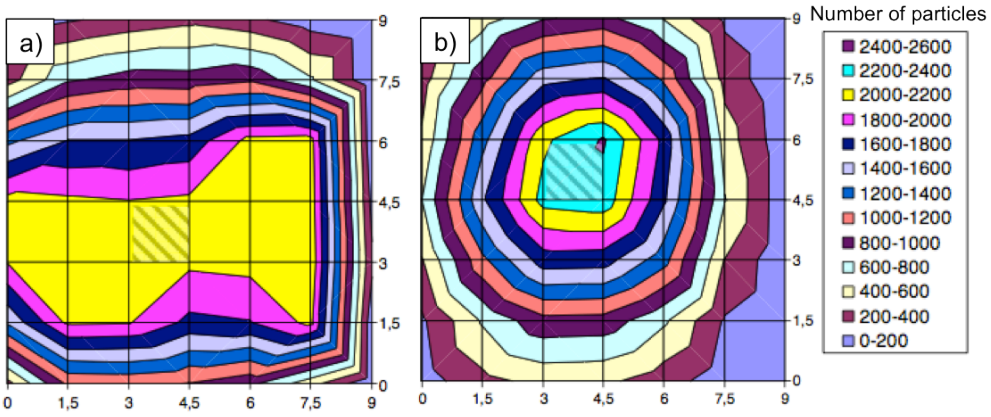

Figure 2.43: Mapping of titanium particle distribution in the exit gas jet for a) small particles and b) large particles (Adapted from [88]).

The gas pressure affects the radial particle flow distribution in a similar manner. The width of the particle spray jet increases with decrease in propellant gas pressure as shown in Figure 2.44. The particles characterized by low velocity situated away from the center will bounce off the substrate during impact [108], [136]. To improve homogeneity in material deposition, a symmetrical and uniform particle flow distribution is thus preferred over a highly dispersed spray jet.

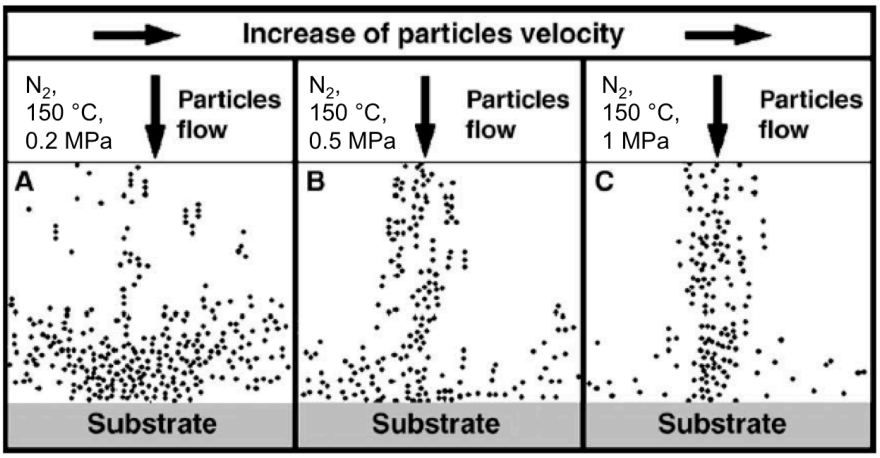

Figure 2.44: Influence of gas pressure on the radial copper particle distribution [136].

In parallel to the results shown previously, smaller particles are accelerated to higher velocities as shown in Figure 2.45. Particles of 15 μm in diameter are accelerated up to 728 m/s while particles having a diameter of 150 μm reach only 557 m/s.

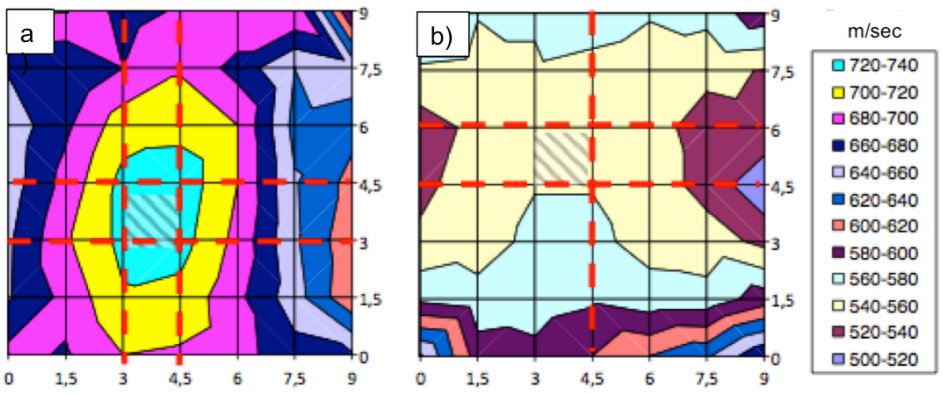

Figure 2.45: Mapping of titanium particle velocity for a) small particles and b) large particles (Adapted from [88]).

Moreover, irregularly shaped particles tend to have a higher drag coefficient and therefore tend to be accelerated to higher velocities than spherical particles [137], [138].

CHAPTER 3

Research Objectives

The previous chapter has discussed the importance of developing technologies related to the additive manufacturing sector. The ability to repair worn areas on damaged parts by rebuilding their initial dimensions, restoring an acceptable fraction of their initial load carrying capacity and performance and ensuring to protect the original properties of the substrate component is crucial to extend, upgrade and restore the life of the damaged component. Numerous industries can benefit from the advantages of a well-structured, understood and researched repair process. Fixing damaged components allows industries to mainly save on the costs of replacement, labour and time. In the aerospace field, being able to repair a deteriorated part results in putting an aircraft in service with minimal delay.

The study of the relevant literature has suggested that the current repair processes present numerous disadvantages associated to the inherent properties of the repair and the extrinsic properties of the component. These drawbacks are mainly associated to the high processing temperatures of the traditional repair technologies. Challenges encountered during the use of a high temperature process are related to the reduction of mechanical properties caused by the oxide content, the thermal degradation of the base material, the development of residual stress from high cooling rates, poor versatility linked to a limited amount of material that are unaffected by high temperature exposure and the mechanical distortion of the component.

To address these issues, this research focuses on the study of using the CGDS process as an alternative solution for the repair of damaged components. The general objective of this project **is to develop a procedure for the repair of threads found on the nose landing gear steering actuator from the 757 Boeing aircraft model**. Pure aluminum powder is to be deposited on

Al6061-T6 and Al7075-T6 circular components. It will attempt to validate the ability of threads, cut into cold sprayed material of over 6 mm in thickness, to withstand loads usually found on the actuator component during normal service. The repair process must ensure good material deposition efficiency, low porosity content, good adhesion to the base substrate, suitable repair machinability and low component surface temperature during the repair procedure. Once repaired, the cold sprayed material will be evaluated on its ability to withstand a torque ranging between 169 N·m and 203 N·m. To further improve on the repair process, additional aspects regarding the CGDS process, component preparation procedure and repair properties will be analyzed. Thus, included is the study of the effect of nozzle movement relative to the substrate rotation on the repair quality, the influence of substrate roughness on the deposition adhesion strength, the effect of gas temperature on the coating hardness and the influence of powder mass feeding rate on the coating characteristics.

The second goal of this research is **to study the ability of the CGDS process to deposit Al2024 thick coatings onto Al2024-T351 flat and circular substrates**. Results from literature have shown that clogging of the steel nozzle during spray is the main limiting factor in the deposition process of Al2024 powder. Moreover, only low process parameters have been tested using a Centerline (Windsor) Ltd. polymer nozzle due to the temperature and pressure limitations of the SST Low Pressure Cold Spray system from Centerline (Windsor) Ltd. In the current study, the Al2024 deposition will be attempted using a different polymer nozzle from Centerline (Windsor) Ltd. and with the use of a SST High Pressure Cold Spray system from Centerline (Windsor) Ltd, which can reach 500 °C and 3.45 MPa. Also covered are the influences of the nozzle material and internal geometry on the spray process.

The following section presents in details each of the separate specific steps that will be completed in order to achieve the objectives described previously.

3.1 General Test Plan

For reasons reviewed in CHAPTER 2, the aluminum 7075 and aluminum 2024 have been chosen to be the focus aerospace component materials in this project. Therefore, the main repair objective is to restore the aluminum 7075 parts using pure aluminum powder. In this context, the pure aluminum powder is used to restore the dimensions of the damaged components, reinstate acceptable mechanical properties and provide a protection against corrosion of the aluminum 7075 base material. The pure aluminum powder has been selected due to its known inherent corrosion resistance and well-researched deposition properties and coating quality.

Aluminum 2024 powder has also been studied in this research for the repair of aluminum 2024-T351 components. The purpose of this part of the work is to study the deposition ability of the Al2024 powder with a commercially available SST High Pressure CGDS system from Centerline (Windsor) Ltd. and through the use of a polymer material nozzle, both limited to a spray temperature of 500 °C.

3.2 Thick Dense Coating Development and Spraying Parameters Selection

The first step in evaluating the use of the CGDS process for the repair of aluminum alloy components resides in finding the spraying parameters that will produce satisfactory material deposition and eventual repair. A series of cold spray trials will be produced on small flat coupons using different combination of spraying pressures and temperatures. Influence on the coating properties of other system parameters such as powder feeding rate and nozzle standoff distance will be examined. This thorough investigation will be applied to the aluminum 2024 powder only. The deposition of the pure aluminum powder using the CGDS process to deposit thin and thick coatings on aluminum alloy substrates has been considerably documented and researched as presented in section 2.7.2. To produce large repairs, only high spraying parameters will be evaluated in this project due to their improved deposition efficiency over low process parameters. As opposed to thin coatings, in order to economically, efficiently and with minimal time deposit thick pure aluminum coatings for repair purposes, high powder deposition efficiencies are mandatory. Such depositions are possible at high spraying parameters only. The Centerline (Windsor) Ltd. SST-EP system was used such that the maximum allowable pressures and temperatures were limited to 3.45 MPa and 500 °C. For both powders, suitable spraying

parameters for repair purposes will be selected based on coating density, material deposition efficiency and particle apparent deformation. The hardness obtained at different spraying parameters will also be evaluated.

3.3 Influence of Spray Parameters on Coating Roughness

In order to deposit the necessary amount of material for the repair of damaged components, it is essential to account for the final coating surface roughness. The surface profile affects the effective coating thickness and is accounted for as material loss. As the outer layer of the repair must be machined down to a smooth surface prior to the machining of threads, larger surface roughnesses require the removal of a greater portion of sprayed material. The influence of the spray parameters on the coating surface profile will be studied.

3.4 Procedure for Thread Repair

Once the system parameters have been adapted for the deposition of thick coatings on flat substrates, the spraying parameters will be used for the repair of large circular components. The Boeing Company has imposed the following repair criteria:

- The component has to be machined to 0.875% of its external diameter prior to repair in order to maintain the part structural integrity and repair capability.
- Pure aluminum powder must be used to repair aluminum 7075-T6 components and aluminum 2024 powder to repair aluminum 2024-T351 parts, as mentioned in Section 3.1.
- The component surface temperature must be kept under 93 °C during the repair process to avoid reaching the Al7075 artificial aging temperature of 121 °C. This ensures that the initial properties and heat treatments of the base material are not altered.
- 3.75-12UNJ-3A threads must be machined into the CS repair following the military MIL-S-8879 standard. The machinability of the repair will be analyzed.

Besides the general requirements set by the Boeing Company, other specific aspects of the repair process will be studied:

- The influence of the nozzle movement relative to the rotation of the component on the repair properties.
- The influence of the component edge angle on the powder deposition. The edges of the damaged component have been machined to different angles (45°, 60°, 90° and curved) and the deposition has been evaluated.
- The effect of cooling rates on the repair adhesion.

Smaller scale repairs will be included in this study in order to extend the developed repair procedure to various substrate sizes for the deposition of Al2024. They consist of repairing 1.5-12UNJ-3A threads. Those depositions will allow to produce a larger amount of Al2024 repairs for statistical purposes.

3.5 Coating Adhesion

At the start of the project, limited to no literature was available on the effect of substrate surface roughness on the coating properties and adhesion. It was also reported that grit blasting the surface using hard media would result in grit embedment. No further analyses were made and an 80 grit blasting procedure was evaluated as suitable for CGDS processes. Therefore, in this project, the repairs and initial sprays will be produced using the 80 grit surface preparation procedure.

The influence of the substrate roughness on the coating to substrate adhesion will be studied for both powders and substrates materials. The bond strength of the coating is a major factor influencing the repairs performance. Three grit blasting media will be used at various grit blasting pressures to produce different substrate surface profiles. The adhesion will be evaluated using the ASTM C633 standard. With the use of microscopy and imaging techniques, the mechanisms (physical, mechanical and metallic interactions) controlling the adhesion of the coating will be linked to the obtained adhesion strength values.

The impact of the temperature, coating thickness and component geometry on the repair adhesion will be studied. Explanations based on measured repair adhesion values and theories from literature will be used to explain the relations between those properties.

3.6 Mechanical Properties and Performance of the CGDS Repairs

After the 3.75-12UNJ-3A threads have been machined into the pure aluminum repair, their load carrying capacity will be analyzed. The Boeing Company has requested a torque verification on the threads ranging between 169 N·m and 203 N·m. Moreover, the smaller scale Al2024 repairs will be tested in shear using a compressive load test. The main objectives of these tests will be to analyze the adhesion strength of the repairs made on circular components and analyze the cause of failure.

3.7 Influence of the CGDS Repair Process on the Polymer Nozzle

Because the production of repairs using the CGDS process is novel, the influence of the spray time and powder material on the polymer nozzle will be studied. In order to efficiently deposit material onto the damaged components, it is imperative to reduce any external deficiencies that may affect the material deposition during spray.

3.7.1. Material Removal Rate

The effect of time and powder feeding rate on the polymer nozzle material removal rate will be studied.

3.7.2. Polymer Nozzle Internal Geometry Alteration and its Influence on the Spray Dynamics

A cold spray meter (CSM) will be used to study the influence of the nozzle wear on the powder deposition at a standoff distance of 25 mm from the exit. A mapping of the flow rate, particle diameter and particle velocity distribution will be produced for a worn and unworn nozzle. The differences between the obtained results will be linked to the modification of the internal nozzle geometry caused by wear during the spray of aluminum powders.

3.7.3. Ceramic Nozzle

To possibly improve the current repair procedure and reduce the influence of polymer nozzle wear on the powder deposition, a Mica ceramic nozzle will be machined. Tests on deposition efficiency using different spraying pressures and temperatures will be produced on small flat coupons with the aluminum 2024 powder only. Porosity levels and coating thickness will be evaluated for each produced coating and compared with those obtained with the polymer nozzle (as presented in Section 3.2). The ceramic nozzle performance will be evaluated in terms of powder deposition efficiency and the presence of clogging, powder internal deposition and wear issues.

CHAPTER 4

Experimental Research Method

The following chapter will present the material, equipment and procedures used in the repair and general cold spray investigation process. First, the powders and substrates materials will be described. The methods used to characterize the substrate properties during and after cold gas dynamic spraying will be explained in details. The equipment and steps used in sample preparation for efficient material deposition prior to spraying and subsequent microstructural analysis will be explained. The Cold Gas Dynamic Spray equipment will also be presented. Following will be a description of the methodology used to map the flow distribution and velocity of the powder using different nozzles. Finally, the chapter concludes with a demonstration of the various test procedures used for the evaluation of the mechanical performance of the obtained coatings and repairs.

4.1 Feedstock Powder Material

Two commercially available aluminum powders have been used and compared in parallel throughout this study. Both powders have been evaluated based on their deposition efficiency using different spraying parameters. The microstructure and properties of the obtained coatings and repairs produced using both powders have been investigated. The following subsection will present the powders morphology, composition and size distribution.

4.1.1. Pure Aluminum

The SST-A5001 pure aluminum powder (Centerline (Windsor) Ltd.) was used in this study. Its morphology can be deduced from Figure 4.1. A Keller's etchant (190 ml distilled water, 5 ml nitric acid, 3 ml hydrochloric acid and 2 ml hydrofluoric acid) has been used to reveal the powder grain size. The surface was covered with the etchant for approximately 40 seconds. As depicted in the figure below, the grains have an elongated shape and are approximately less than 8 μm in size. The powder is composed of distorted teardrop and oval shaped particles, which is uncommon for gas atomized powders (generally of a perfectly spherical shape).

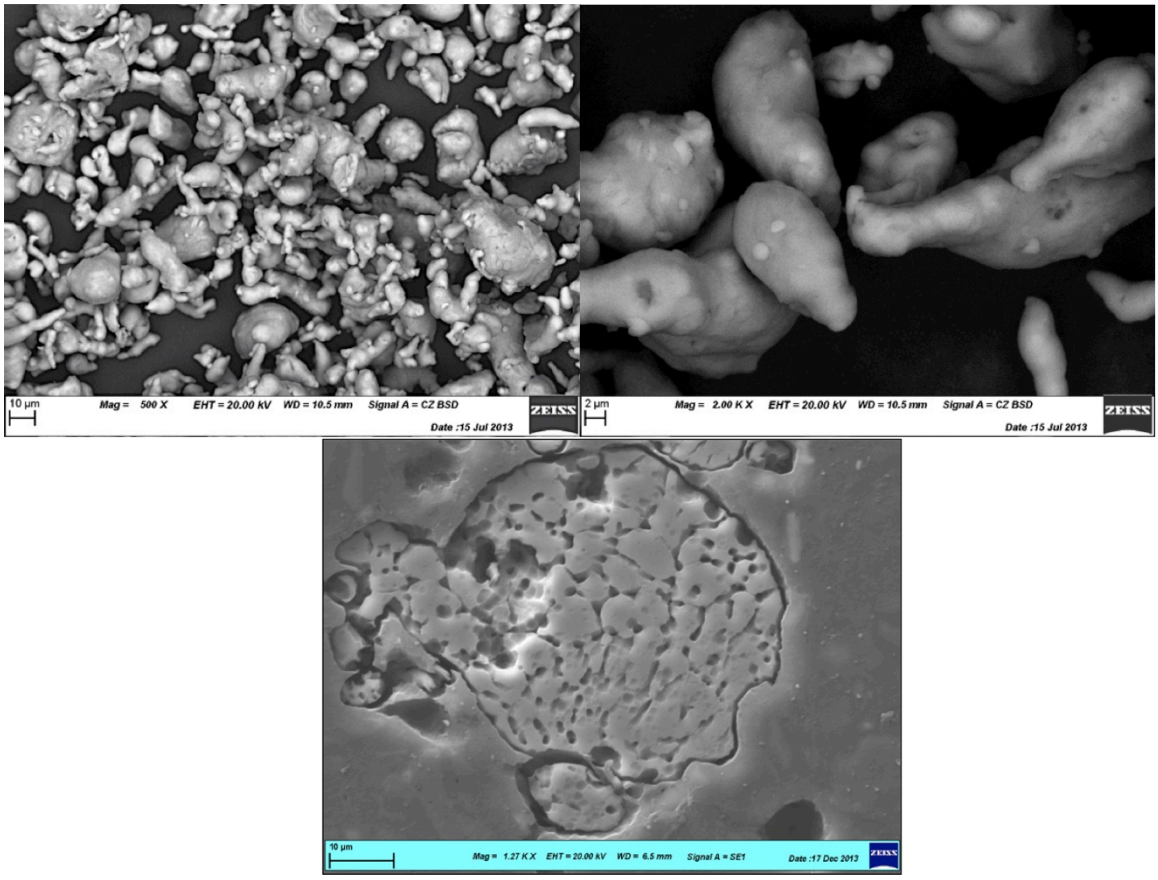

Figure 4.1: Powder morphology of SST-A5001 pure aluminum powder from CenterLine (Windsor) Ltd.

The composition of the powder was obtained through the energy dispersive X-ray spectroscopy method. The result from the analysis, shown in Figure 4.2, indicates a 98.12% and 1.88% in weight of aluminum and oxygen respectively.

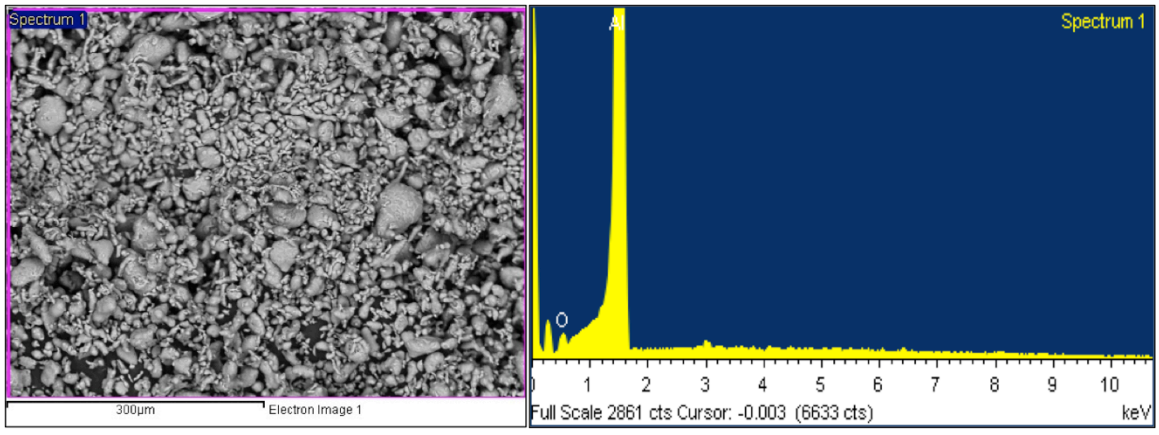

Figure 4.2: EDS analysis of the SST-A5001 pure aluminum powder.

According to the manufacturer, the SST-A5001 powder has a hardness of 25-30 HB. In the aerospace repair technology, the pure aluminum powder offers great corrosion resistance, which explains its use in the current project.

The powder particle-size distribution was characterized and analyzed using laser diffraction instruments (Microtrac Particle Size Analyzer S3500, Nikkiso, Japan) shown in Figure 4.3. The system is able to analyse particles size ranging between 0.024 μm to 2800 μm. To disperse the powder and avoid agglomeration, the powder was placed in a liquid suspension state using an organic solvent into the sample delivery controller. The powder was then directed to the dynamic image analyser, which houses the optical and detection components. Microtrac FLEX software was then used to retrieve the results of the particle size distribution analysis.

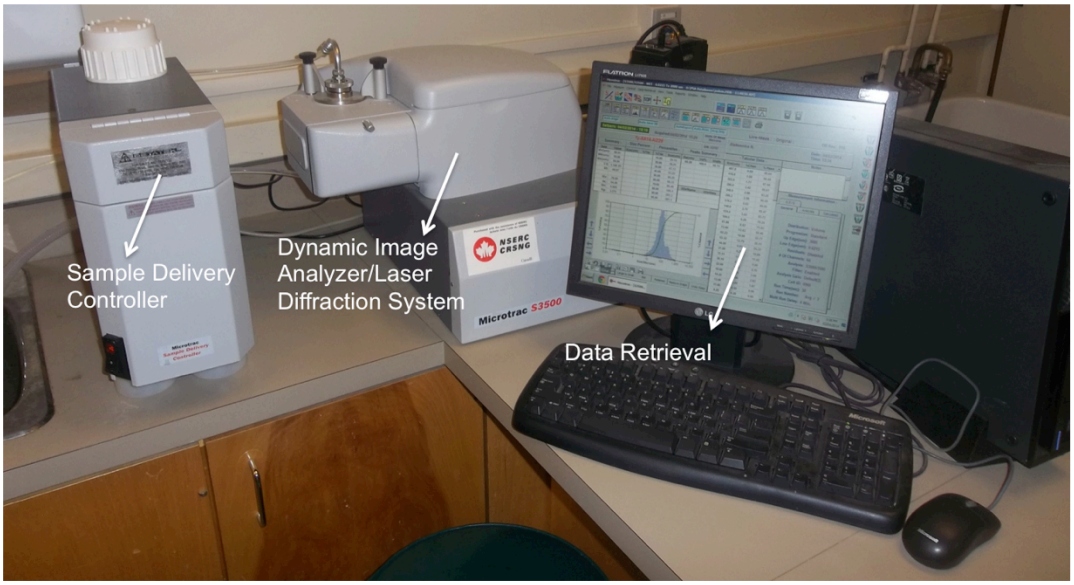

Figure 4.3: Microtrac particle analyzer S3500.

The results from the analysis are depicted in Figure 4.4, which shows the differential and cumulative particle size. The 90th percentile is underlined at a particle size of 47.39 μm.

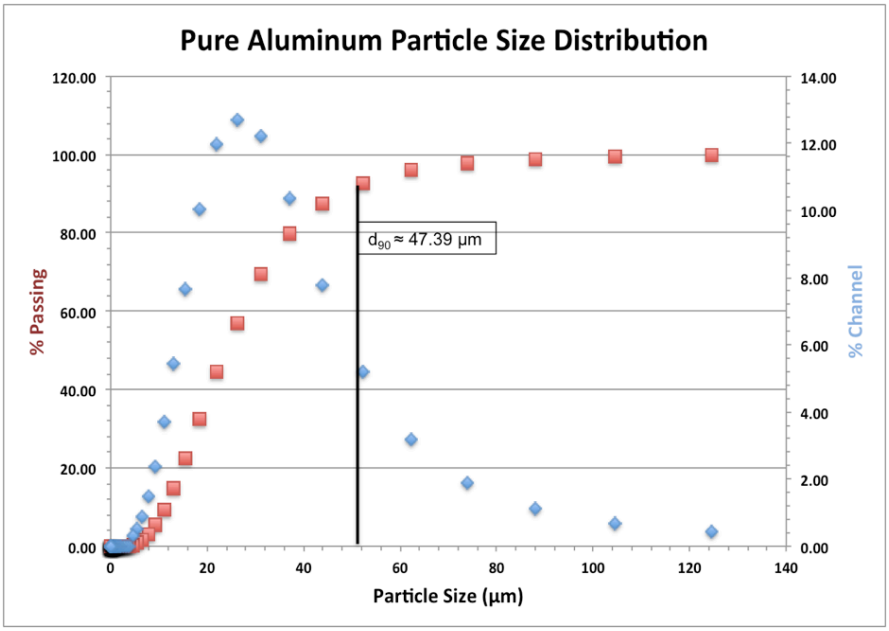

Figure 4.4: Differential and cumulative particle size analysis of the pure aluminum powder.

Table 4.1 presents the particle size distribution d_{10}, d_{50} and d_{90}, which correspond to the 10^{th}, 50^{th} and 90^{th} percentile of the particle size distribution respectively.

Table 4.1: Pure Aluminum Particle Size Distribution Percentiles

	Pure Aluminum-SST-A5001.		
	d_{10}	d_{50}	d_{90}
Particle diameter (µm)	11.29	23.75	47.39

4.1.2. Al2024 Aluminum Alloy

The second type of powder that was analyzed is the MIM 2024 Al2024 powder (Ampal Inc), shown in Figure 4.5. The powder is constituted of small spherical and of large slightly deformed shaped particles. The powder seems to have been obtained through gas atomization based on its spherical shape. The hardness of the powder was measured to be 75.18 ± 5.7 $HV_{0.01}$ by averaging a total of twenty indentations made through different powder batches. The Vickers indentations were made at the lowest load of 0.01 kg using a Struers Duramin-1microhardness tester, which is presented in more details in Section 4.6.3. Only particles with large diameters have been used for proper hardness assessment.

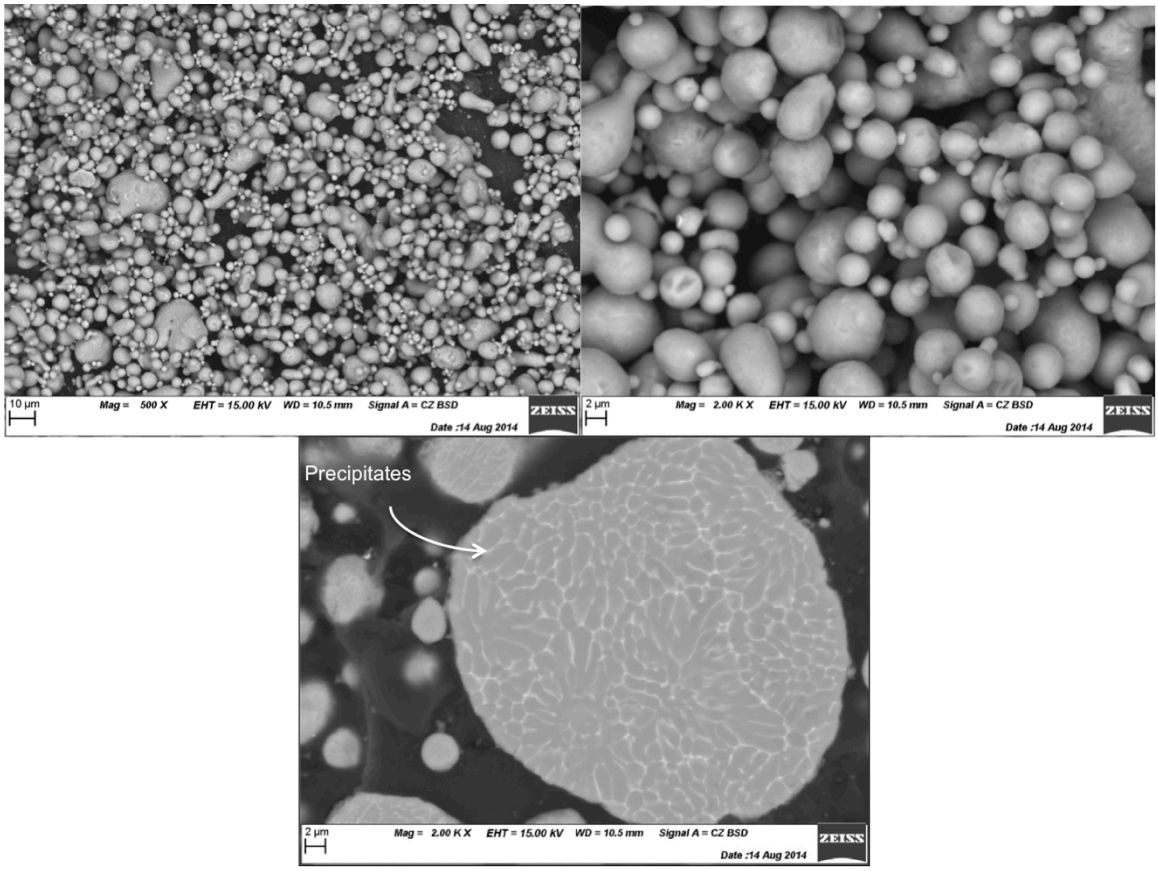

Figure 4.5: Morphology of theAl2024 powder from Ampal Inc.

The elongated grains in the powder have been exposed after polishing and precipitates are seen at the grain boundaries; an approximate size of less than 2 µm was recorded. The powder's composition has been analysed using the energy dispersive X-ray spectroscopy method, as shown in Figure 4.6. The obtained atomic percentage is 93.95% Al, 0.99% Mg, 4.46% Cu and 0.60% Mn in weight percentage. The single polished powder particle, shown in the previous figure, has been analysed using the backscattered electron detector (BSD), which allowed distinguishing the location of elements having a different average atomic number. It displays atomic number contrast by generating a brighter color for elements having a higher average atomic number. Therefore, the precipitates found at the grain boundaries using the backscattered electron detector are most likely Al_2CuMg or Al_2Cu due to their high concentration of Cu, which has the highest average atomic number of all of the Al2024 elements.

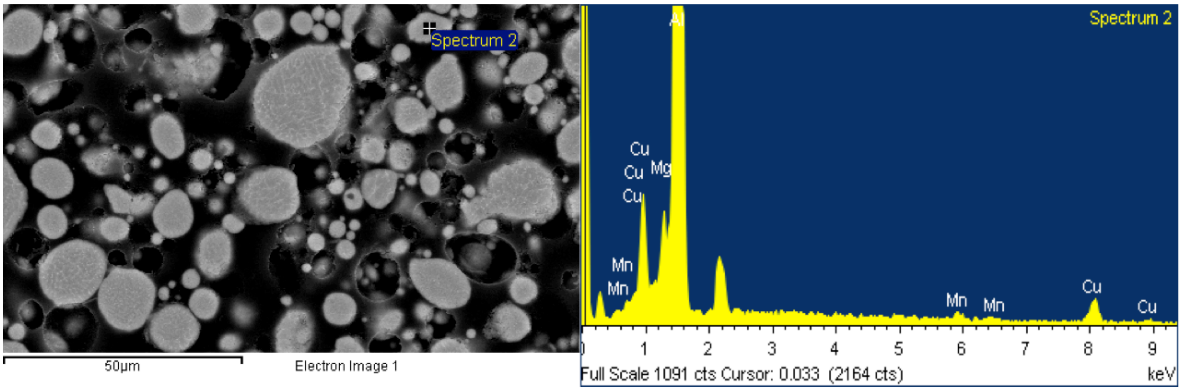

Figure 4.6:EDS analysis of the Al2024 powder.

The results from the powder particle size distribution analysis are depicted in the Figure 4.7. The 90th percentile is shown on the graphic at a particle diameter of approximately 37 µm.

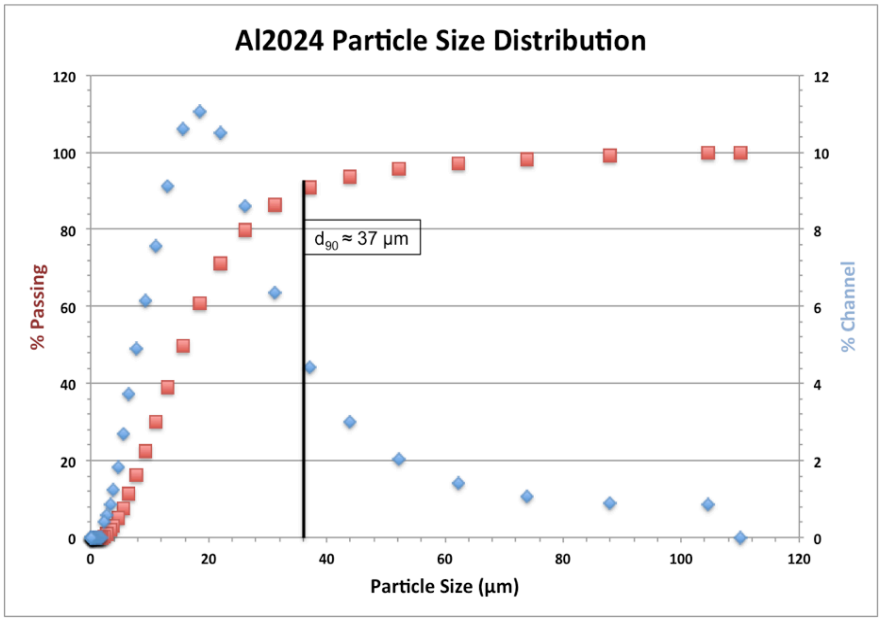

Figure 4.7: Differential and cumulative particle size analysis of the Al2024 powder.

Table 4.2 summarises the particle size distribution by presenting the 10th, 50th and 90th percentile values.

Table 4.2: Particle Size Distribution Percentiles

	Al2024-Ampal Inc.		
	d_{10}	d_{50}	d_{90}
Particle diameter (μm)	6.54	15.55	37

4.2 Substrates Characteristics and Properties

Al2024-T351, Al7075-T6 and Al6061-T6 have been used as substrate materials to test the repair capability of the cold spray technology. Table 4.3 summarizes the size and type of aluminum alloy used as base material in various tests and analyses conducted in this study.

The deposition efficiency and process parameters influence on coating microstructure of both pure aluminum and Al2024 powders have first been tested through preliminary tests on small coupons. The type of aluminum alloy substrate material does not have any influence on the coating growth process as it only affects the first coating layer adhesion strength and bonding process, which was not the objective of the preliminary analyses. Thus, the choice of the substrate aluminum alloy type was arbitrarily chosen for all preliminary tests including all tests of comparative nature such as the analysis conducted to understand the influence of substrate surface angle on the deposition process. Al6061-T6 was used for the deposition of pure aluminum powder, as it was more accessible than Al7075-T6 plates. Al2024-T351 substrate material has been selected for the deposition of Al2024 powder, as it was available at the time of testing.

Table 4.3: Summary of Substrate Material and Geometry Selection for Different Tests

Substrate Material and Dimension Selection Matrix for Different Tests and Repairs		
Objective	**Preliminary Analysis**	**Final Analysis**
Repair of 3.75-12UNJ-3A Threads (Al7075-T6 and Al6061-T6 substrates)	***Pure Aluminum Powder***	88.9 mm diameter Al7075-T6 (***section 6.1.3)***
	1. Powder Deposition Ability	
	Small 25.4 mm by 19.05 mm Al6061-T6 ***(section 5.2)***	
	2. Powder Repair Ability	
	88.9 mm diameter Al6061-T6 (***section 6.1.1 and 6.1.2)***	
Deposition on Various Substrate Angles	***Pure Aluminum Powder***	38.1 mm diameter Al6061-T6 (***section 6.2)***
	Small 25.4 mm by 19.05 mm Al6061-T6 ***(section 5.2)***	
Repair of 1.5-12UNJ-3A Threads (Al2024-T351)	***Al2024 Powder***	
	1. Powder Deposition Ability	2. Powder Repair Ability
	Small 25.4 mm by 19.05 mm Al2024-T351 (***section 5.1)***	33 mm Al2024-T351 ***(section 6.3)***
Bond Plugs Adhesion Tests	***Pure Aluminum Powder***	***Pure Aluminum Powder***
	Small 25.4 mm by 19.05 mm Al6061-T6 ***(section 5.2)***	Al7075-T6 Bond Plugs (***section 7.2)***
	Al2024 Powder	***Al2024 Powder***
	Small 25.4 mm by 19.05 mm Al2024-T351 (***section 5.1)***	Al2024-T351 Bond Plugs (***section 7.1)***

Once the proper spraying parameters were found, the repairs have been produced on substrates having the same size as the actual specific component and the proper substrate material.

For final repairs and adhesion tests, the Al2024-T351 and Al7075-T6 as substrate materials were selected due to their use in the aerospace field. Only for the repair of 3.75-12UNJ-3A threads case has the complete repair process been initially tested on Al6061-T6 material, as its main purpose was to analyse the effect of coating thickness and spraying procedure on the repair quality. The subsections below will also present the substrate surface preparation and characterization processes.

4.2.1. Aluminum Alloy Coupons

Small 25.4 mm by 19.05 mm aluminum alloy coupons have been used to test and map the deposition efficiency of the powders for different spraying pressures and temperatures, as shown in Figure 4.8. A vise was used to hold the substrate in place during the cold spray process. Carbon fibre plates were placed between the coupon and the vise to prevent heat transfer between the steel vise and the substrate. Without the proper insulation, a decrease in coating reproducibility would arise due to the temperature variation of the vise during spraying. Therefore, proper insulation ensures that the equipment surrounding the substrate material does not affect and influence the results.

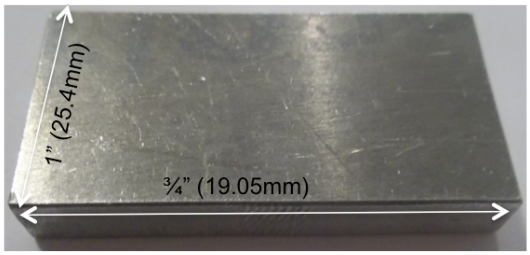

Figure 4.8: Aluminum alloy coupon substrate size and geometry.

4.2.1. Substrate Surface Angle Influence on Coating Deposition and Characteristics

For the following series of tests, the Al6061-T6 aluminum alloy has been selected as the substrate material. As mentioned previously, since this test only compares the coating quality obtained using different substrate surface angles, it only requires the use of the same substrate material throughout the test, irrespective of its type. Figure 4.9 shows the 38.1 mm diameter

substrates used to achieve that objective. Besides the influence of the substrate surface angle on the coating deposition process, the coating growth procedure on the inclined substrate surfaces through time has also been analysed. To do so, both fine and coarse 1.5 UNJ threads have been machined on the cylindrical substrates. As illustrated in Figure 4.9, four different substrate surface angles (45°, 60°, 90° and curved) have been machined to test the influence of the direction of impact of the powder on its adhesion to the substrate.

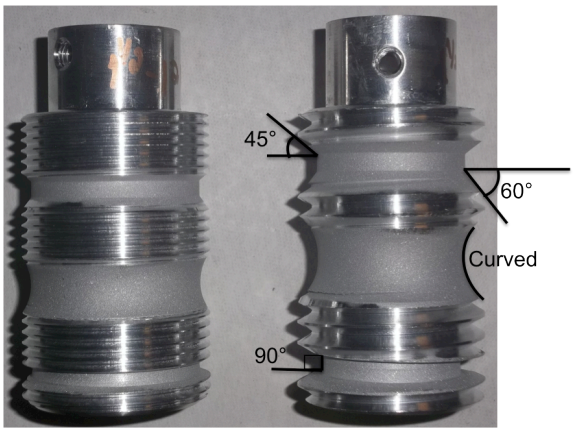

Figure 4.9: Fine (1.5-12UNF-3A) (left) and coarse (1.5-6UNC-3A) (right) threads machined in Al6061-T6. Threaded sections have been machined down to produce surfaces with angles of 45°, 60°, 90° and curved. These specific regions have been grit blasted prior to the dimensional restoration procedure.

The results from this section will guide the machining process of the partial repairs presented in the previous subsection. It will provide the optimal angle at which the exterior surface of the remaining undamaged threads should be machined for improved particle/substrate contact. Thus, the microstructure or any other substrate material property evaluation prior to spraying was considered unnecessary.

4.2.2. Thread Repair of Nose Landing Gear Steering Actuator

In order to reproduce the 3.75-12UNJ-3A threads from the landing gear actuator found on the Boeing 757 models (Figure 4.10), a portion of 25.4 mm (1”) in length of a 101.6 mm (4”) aluminum alloy diameter bar was machined down to 88.9 mm (3.5”) to simulate a damaged area. Initial tests were made on Al6061-T6 components and the final repair was produced on Al7075-T6 alloy material. The UNJ threads are used in highly stressed applications that require high

fatigue strength. The UNJ thread profile has a controlled root radius and an increased minor diameter. Thus, specific tooling was used in order to correctly produce the threads dimensions while accounting for the tight and close tolerances of the 3A clearance fit.

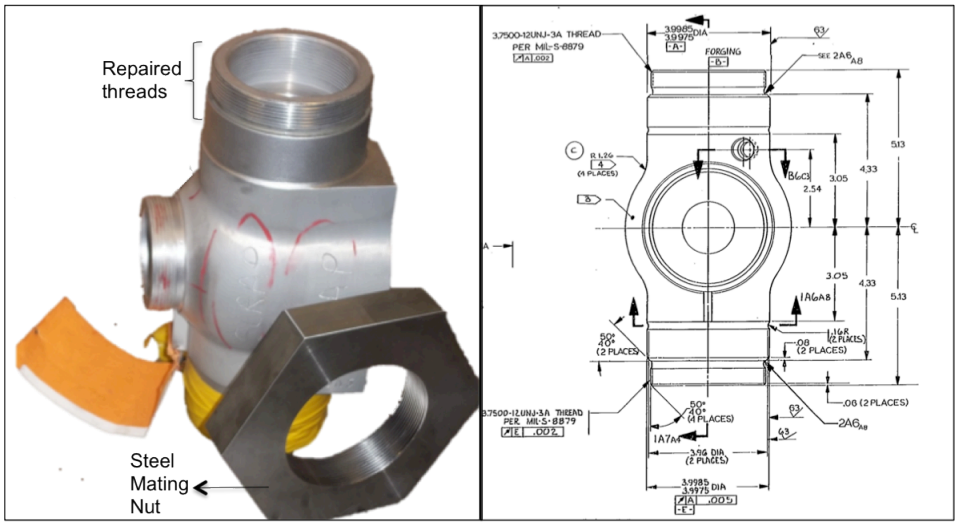

Figure 4.10: Dimensions of the nose landing gear steering actuator found on the Boeing 757 models[2].

To test the performance of the repaired threads, a mating steel nut has been machined. Its hexagonal exterior shape has been produced using wire electrical discharge machining (WEDM) and a lathe was used to machine the internal 3.75-12UNJ-3B threads. Figure 4.11 shows the aluminum alloy substrate size and dimensions after machining and prior to spraying. Only the 88.9 mm diameter portion was sprayed in its full length up to its initial diameter of 101.6 mm. After repair, eight threads have been machined into the cold sprayed material as per the MIL-S-8879 military standard. A tapped hole was drilled through the substrate center from which it was held during the repairing process. Details on the threads and dimensions of the center hole will be given in section 4.2.5.

[2] Credits to The Boeing Company.

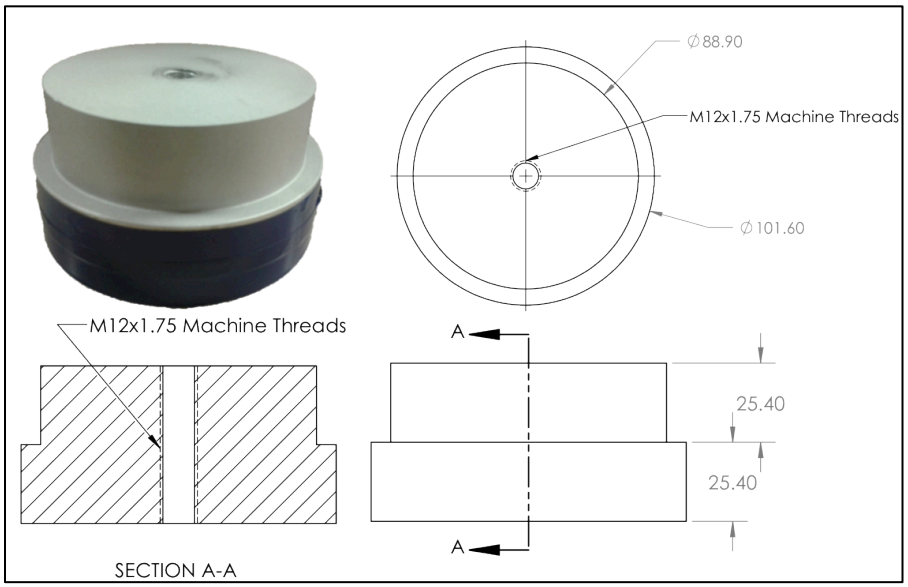

Figure 4.11: Aluminum alloy substrate dimensions for the repair of threads on the nose landing gear steering actuator (dimensions are in mm).

4.2.3. Thread Repair for Compression Tests

Coating adherence on circular substrates has been investigated through the characterization and mechanical testing of 1.5-12UNJ-3A threads repair. Figure 4.12 shows the 38.1mm (1.5") Al2024-T351 substrates dimensions after machining prior to the cold spray repair process. Partial and full repair of the threads have been tested in order to verify the influence of the area and substrate angle on the coating final adherence and characteristics. For the full repairs, shown in Figure 4.12a, the complete set of initial threads have been machined out as they will all be restored to their dimensions through the cold spray process. Figure 4.12b shows the component used for the partial repairs where only half of the initial threads have been removed. Thus the 33 mm diameter area has been sprayed on a 23 mm and 10 mm length for the full and partial repair respectively.

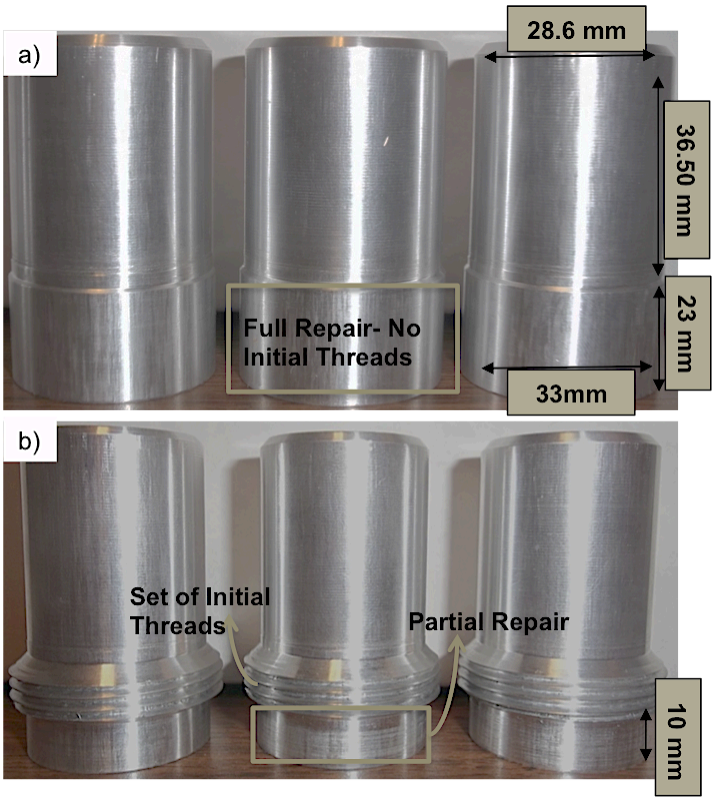

Figure 4.12: Al2024-T351 substrates for small scale repair. a) Full repair of damaged area and b) Repair of the damaged area only (partial repair).

4.2.4. Substrate Surface Preparation

Prior to deposition, the substrate surfaces underwent a grit blasting process. The hand held gravity fed grit blasting unit used during this process is shown in Figure 4.13. The grits were fed through a steel nozzle having a 5.2 mm (13/64”) internal diameter with an average air consumption of 6 CFM (170 l/min) (20 CFM continuous) at a pressure of 621 kPa (90 psi) (Princess Auto SKU: 8140709).

Figure 4.13: Grit blasting unit.

During the grit blasting procedure, the gun was held at an approximate 45° angle and at a standoff distance of approximately 50.8 mm (2”) from the substrate surface. Three types of abrasives were used in this study to examine their effects on the adhesion of the coating to the substrate surface. Figure 4.14 shows the different grit blasting medium used during the surface preparation procedure. An 80 mesh (178 μm) aluminum oxide (Opta Minerals Inc.), 20 mesh (853 μm) ferrosilicate (Ebonygrit from Opta Minerals Inc.) and 25-40 mesh (700 μm–420 μm) steel abrasive (McMaster-Carr steel abrasive blasting media) were used.

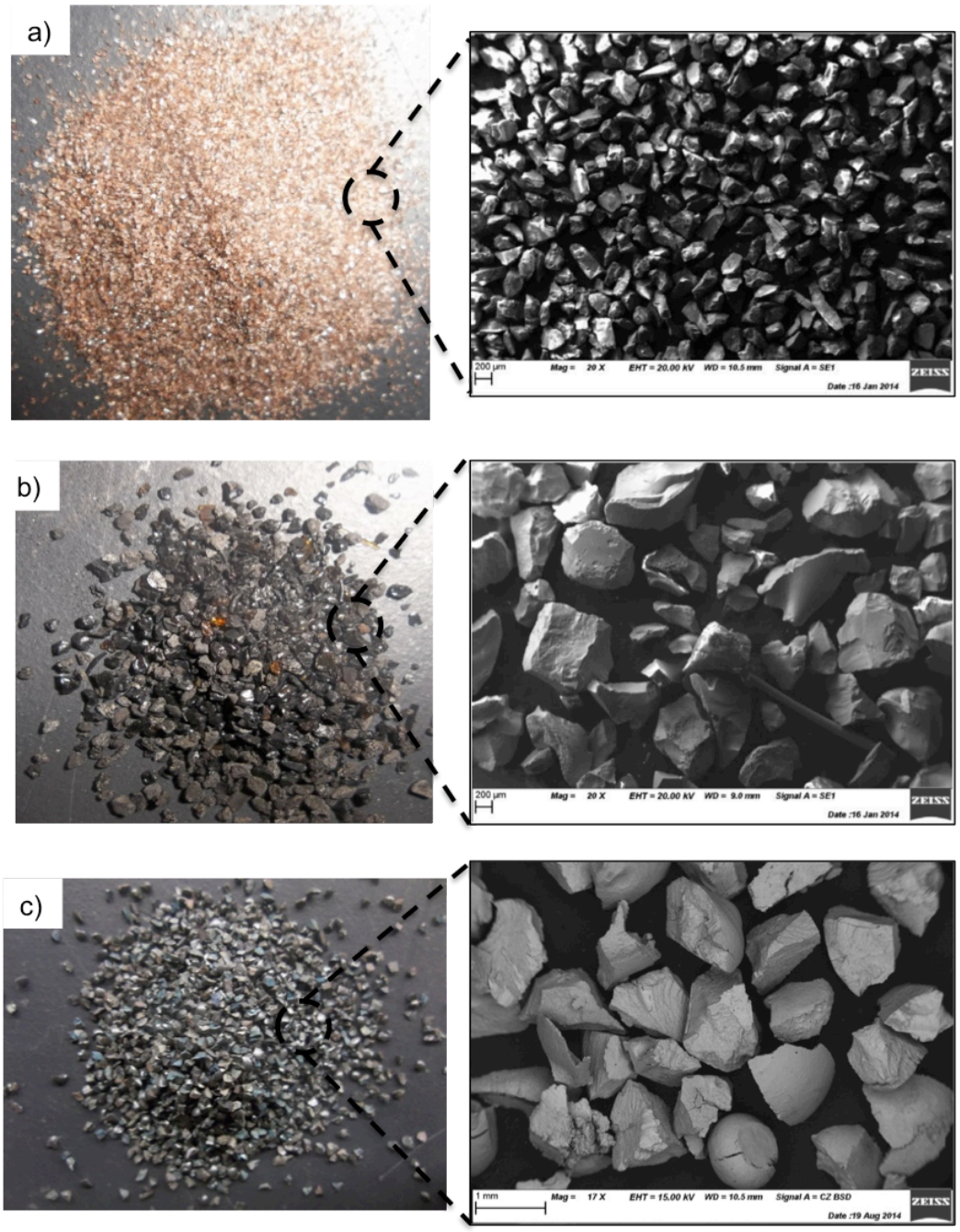

Figure 4.14: Grit medias used during the surface preparation procedure. a) 80 alumina grit; b) 20 ferrosilicate grit and c) steel abrasive.

The surface topography created using the various grits are shown in Figure 4.15. Pressures ranging between 0.4 to 1.4 MPa were used to propel the grit into the substrate surface.

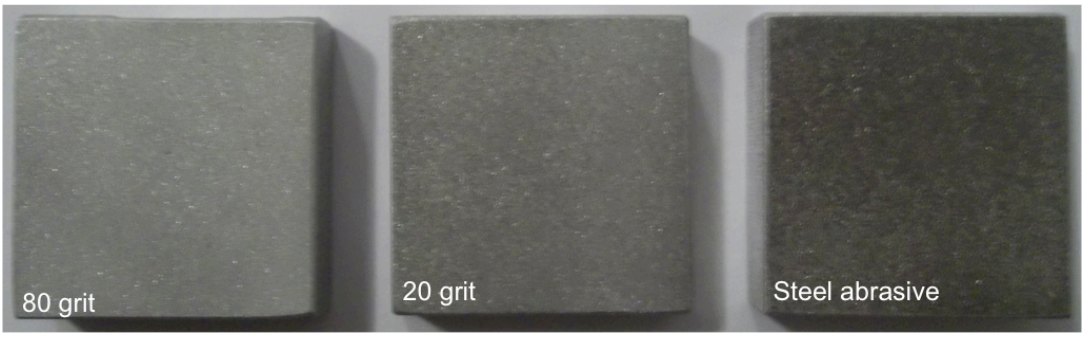

Figure 4.15: Aluminum alloy substrate surface after a grit blasting process.

The pressure, grit type and exposure time are important parameters affecting the final substrate surface roughness. After the grit blasting procedure, the substrates were immersed in an ultrasonic bath for approximately 3 minutes to clean the surface from any environmental debris or loose grits.

4.2.5. Equipment and Set-Up During Thread Repair

A 24 V, 1800 rpm and 17.5 torque Leeson permanent magnet motor (Regal Beloit Company), shown in Figure 4.16, was used to hold and turn the substrates during their repair for the restoration of threads as presented in Subsection 4.2.2 up to Subsection 4.2.3. The motor was attached to a metallic structure designed with four long threaded bolts at its four corners. The bolts were used to adjust the distance between the cold spray nozzle and the substrate surface by raising or lowering the entire metallic structure along with the motor.

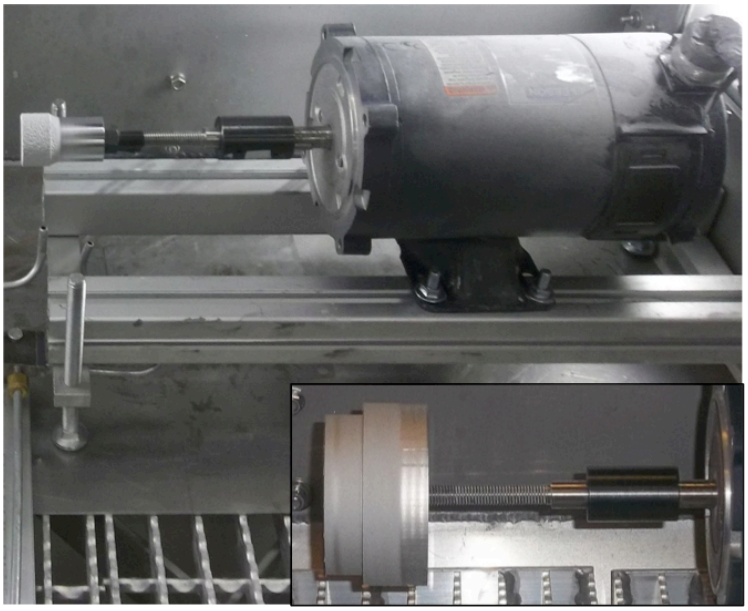

Figure 4.16: Leeson motor used to rotate the component during repair.

A steel threaded rod was inserted into the shaft coupling of the motor and held in place by a set screw. An M12x1.75 tapped hole was machined into the center of the circular substrates and tightly fastened into the threaded mating rod. Figure 4.17 illustrates the location and depth of the holes machined in the specific substrates used for thread restoration. In order to avoid vibration and ensure proper alignment and rigidity of the 88.9 mm diameter substrates, the component was completely fastened through its entire length onto the threaded shaft during spray.

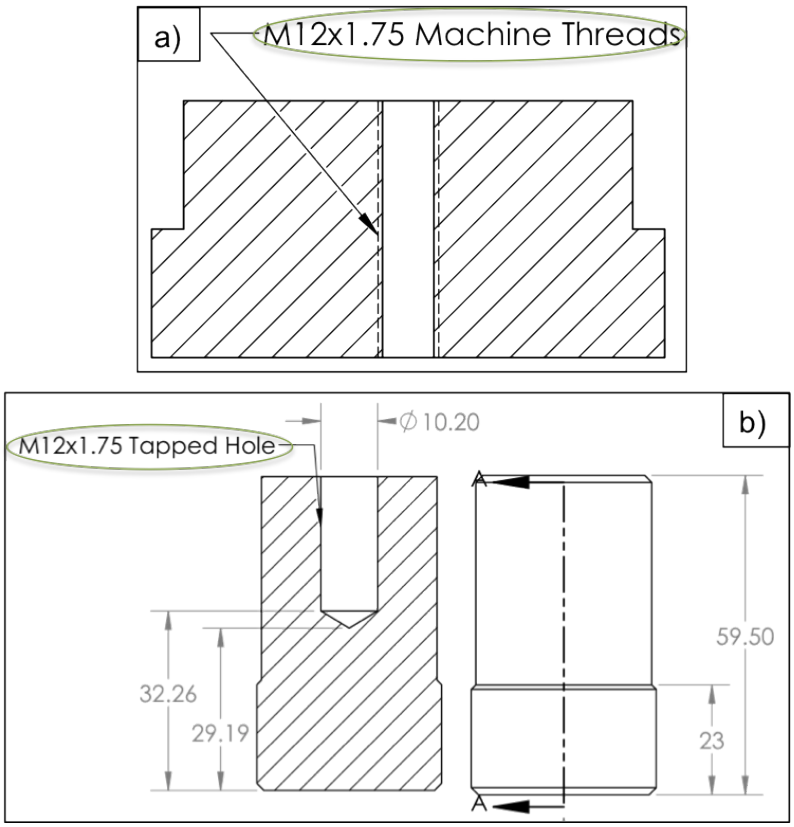

Figure 4.17: Substrate center drilled hole used for attachment to the motor. Substrates for the repair of a) 3.75-12UNJ-3A threads and b) 1.5-12UNF-3A threads (dimensions are in mm).

4.2.6. Substrate Temperature Monitoring

During the repair process, the surface temperature of the damaged components was monitored using a thermal infrared sensor (Raytek, Thermalert GP Series), shown in Figure 4.18. A monitor was used along with the fixed infrared sensor to provide direct reading of the current substrate surface temperature.

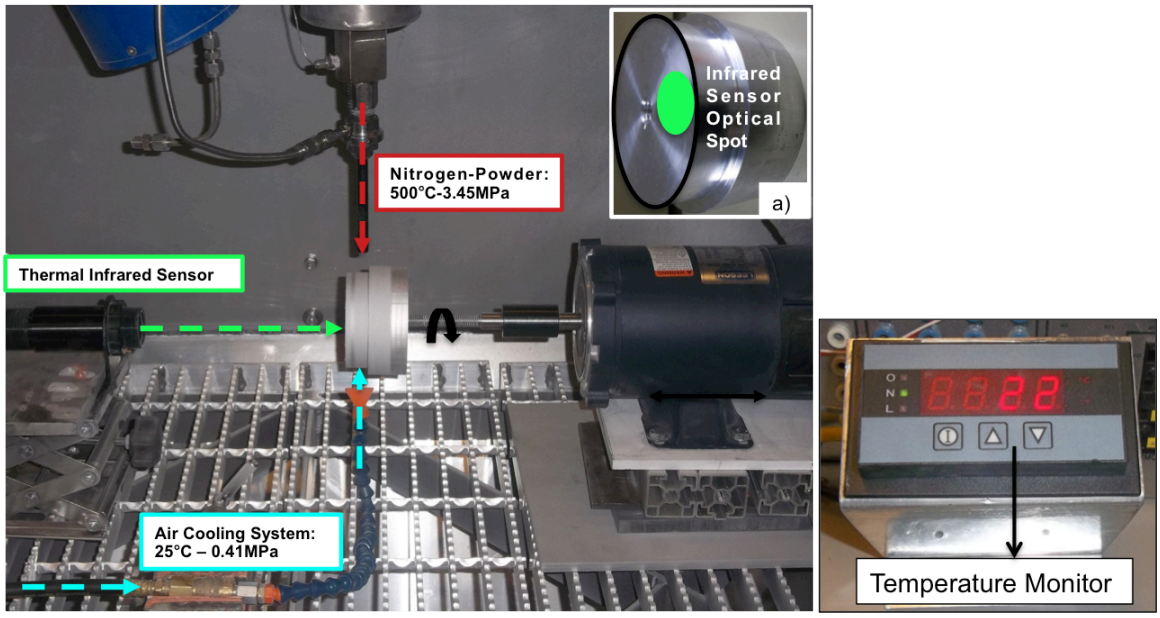

Figure 4.18: General set-up for temperature monitoring during repair. a) Optical spot site.

The emissivity of the aluminum material was set to 0.33. This value was found by verifying the obtained temperature with the temperature measured using a conventional K-type thermocouple (-40 °C to 1250 °C) when the aluminum material was heated up to 50 °C using an industrial heat gun. The sensing head of the thermal infrared sensor uses a 1 mW laser with an output wavelength of 630-670 nm. At a distance of 50 cm from the aluminum part, the infrared sensor optical spot diameter was of 2.5 cm. The surface temperature variation of the aluminum part was recorded, at a sampling time of 1 s, during the entire repairing process through a LabView program having as input the readings of the laser sensing head.

4.2.7. Substrate Surface Cooling System

In order to ensure that the substrate undergoing repair does not experience any material properties changes, its surface temperature was kept under 93°C (200°F). To maintain that temperature during the cold spray process, which was done at a main gas temperature higher than 100°C, an air cooling system placed under the substrate was assessed most practical. Figure 4.19 shows the position, the set-up and the equipment used to construct the cooling system for the repairs of small (33 mm diameter part) and large (88.9 mm diameter part) substrates.

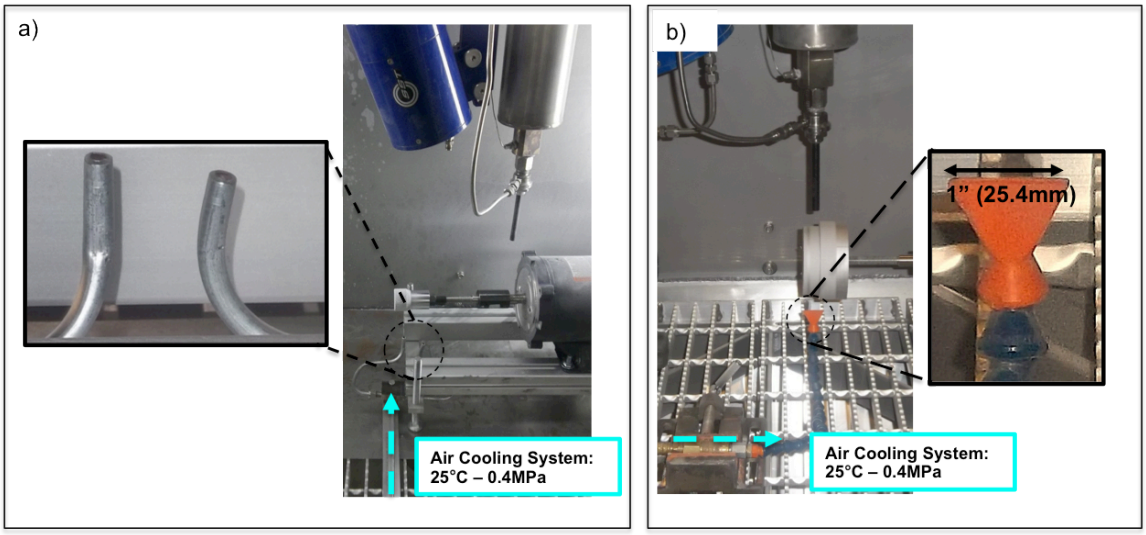

Figure 4.19: Air cooling system set-up used during repairs.

For the cooling of small substrates, two precision aluminum tubing (capillary tubing) with 2.9 mm (0.115") ID were used to conduct the cooling air at 25 °C and 0.4 MPa. Metallic tubing in the cooling system was required during repair of small substrate since the streamlines of the main flow were affecting the stability of any other type of tubing. Figure 4.20 shows the entire assembly of the air cooling tubing system.

Figure 4.20: Aluminum tubing used to conduct air to the substrate surface for cooling purposes.

A flat nozzle flexible pipe hose was used to direct the cooling air during the repair of large substrates. The flat nozzle has a 25.4 mm rectangular exit that overlaps the substrate surface to be sprayed. A clamp was also placed between the pressure hose and flexible pipe in order to ensure stability of the cooling pipe system.

4.3 Surface Roughness Measurements

The surface roughness of the coatings and the substrates after the grit blasting procedures was measured using a portable profilometer, shown in Figure 4.21. The instrument uses a 5 μm diamond stylus to scan the height of the surface profile. It has a depth measuring limit range of 0.005 μm ~ 16 μm and a corresponding display resolution of 0.001 μm. The arithmetic average of the absolute values obtained through the profile height variation was used to express the roughness, known as Ra.

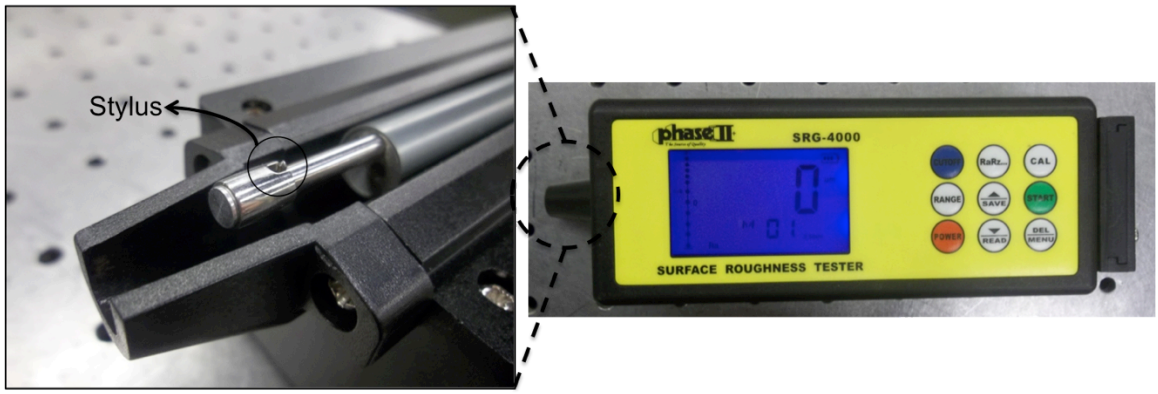

Figure 4.21: Surface roughness measurement equipment (PHASE II, SRG-4000).

The calculation principle of the arithmetic average height obtained through the scan of the surface irregularities and the definition of the Ra is shown in Figure 4.22.

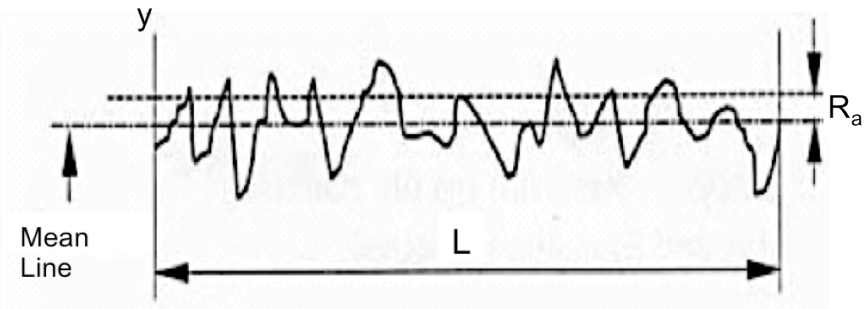

$$R_a = \frac{1}{L}\int |y| dx \approx \frac{1}{L}\sum_{i=1}^{L} |y_i|$$

Figure 4.22: Ra definition and calculation.

Moreover, profiles having a surface roughness exceeding the 16 μm limit of the profilometer have been analyzed using a 3D microscope, which will be presented in Subsection 0.

4.4 EP-CGSD System and Equipment

In order to produce a repair or any coatings, a commercially available CGDS system (Centerline SST-EP system, Windsor Centerline Ltd.) was used. The cold spray system is composed of a control cabinet, a spray chamber, a robotic spray gun, a heater, a powder feeder, a ventilation unit, a water based filter and a nozzle assembly. An overview of the entire system is shown in Figure 4.23. The following subsections will explain specific features of the different components found in the CGDS system.

Figure 4.23: CGDS system overview (Centerline (Windsor) Ltd. SST-EP system).

4.4.1. Control Cabinet and Nitrogen Gas Supply

The control cabinet depicted in Figure 4.24 was used to control and monitor the inlet pressure from the bottle packs and the temperature of the heater. The temperature was set digitally through a touch screen on the control panel, while the pressure was controlled through a pressure regulator found on the side of the control cabinet as shown below. Also attached to the control unit is the powder feeder flow meter, which adjusts the volumetric flow of gas from the nitrogen bottle to the powder feeder.

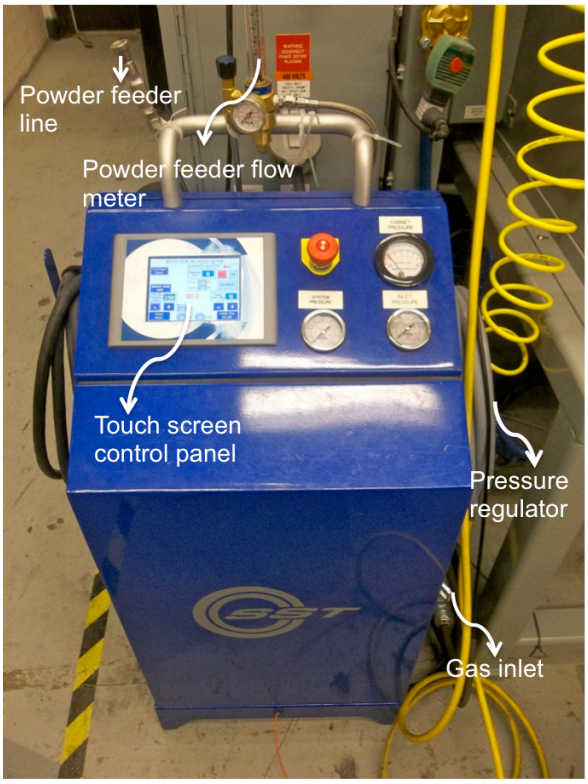

Figure 4.24:Centerline (Windsor) Ltd. SST-EP control unit.

The nitrogen bottle pack unit used to provide the carrier gas pressure is shown in Figure 4.25. The nitrogen gas is thus supplied through 11 industrial high pressure cylinders connected together and fed to the system through a main gas valve. At full parameters, one unit of 18 MPa is able to provide nitrogen gas for spray times up to 2 hours.

Figure 4.25: Seven units of nitrogen bottle pack (11 bottles/unit).

Two pressures gauges were installed to control and monitor the nitrogen flow rate to the system and consumption during spray. The pressure regulators limited the nitrogen inlet to the system to 4.48 MPa (650 psi).

4.4.2. Spray Gun, Heater and Robotized Traverse System

The CGDS system is equipped with a 15KW, 480 Volt and 3PH heater, which is able to provide a maximum of 500 °C at 3.45 MPa (500 psi). The driving gas is heated to the desired stagnation temperature using electrical resistance placed in an insulated frame. The spray gun assembly, which includes the main heater, powder preheater and the nozzle, is shown in Figure 4.26. It is to note that the powder preheater was not used in this study.

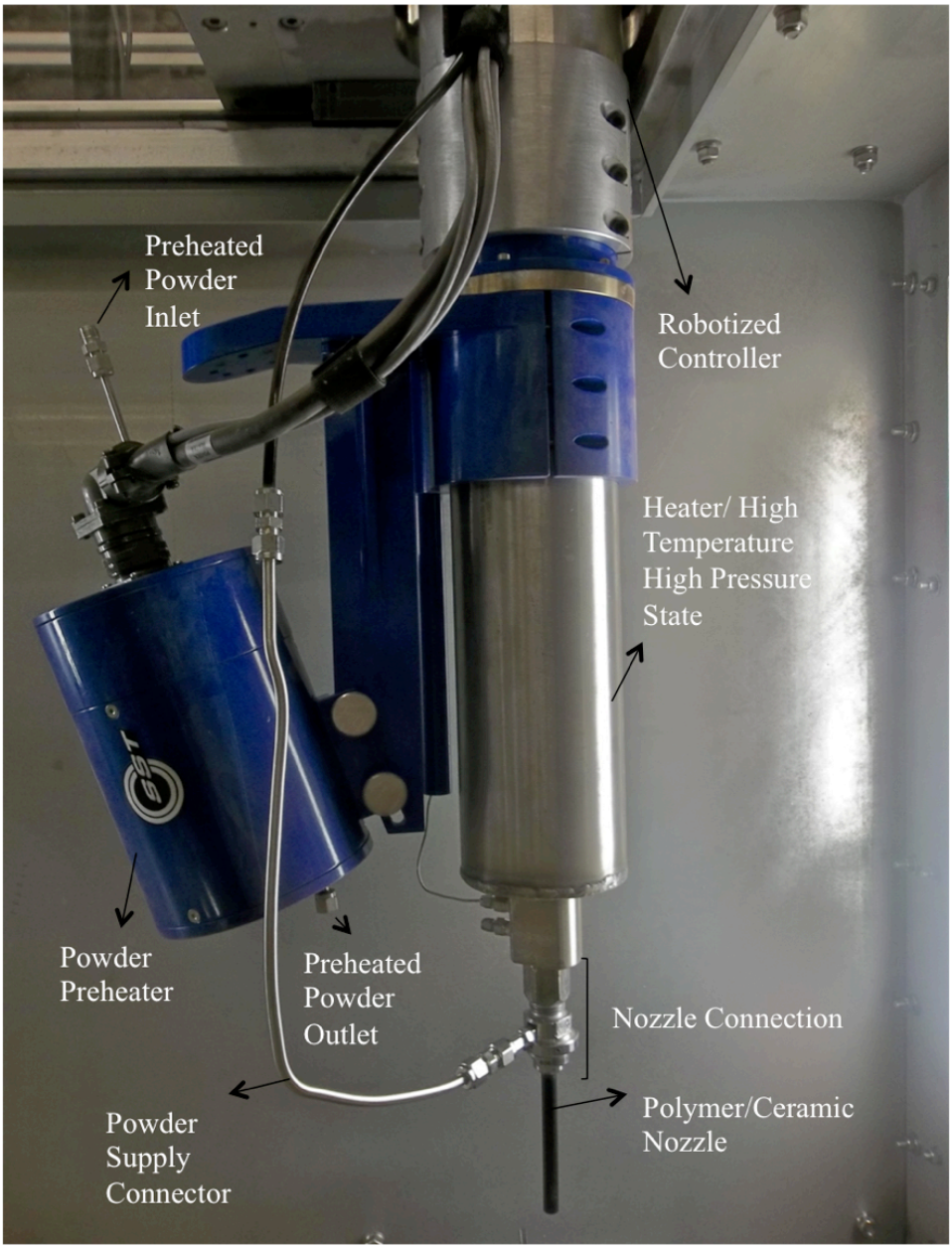

Figure 4.26: Spray gun.

The entire equipment is mounted on a stepper motor controlling the acceleration, velocity and X-Y displacement of the gun. Its movement and other characteristics were coordinated through PC Interface Software for X-SEL program. Prior to spraying, the user implements the velocity, acceleration, X distance, Y distance, step size, total displacement and number of cycles into the program.

4.4.3. Spray Chamber, Ventilation and Water Based Filter

During the use of the cold spray system, all samples were placed within the spraying area inside the spray chamber as shown in Figure 4.27. The non-deposited powders were pulled by a ventilation system out of the chamber up to a water filtering system. The powder was then caught by the water and the air was filtered through a HEPA filter before being discharged to the working area.

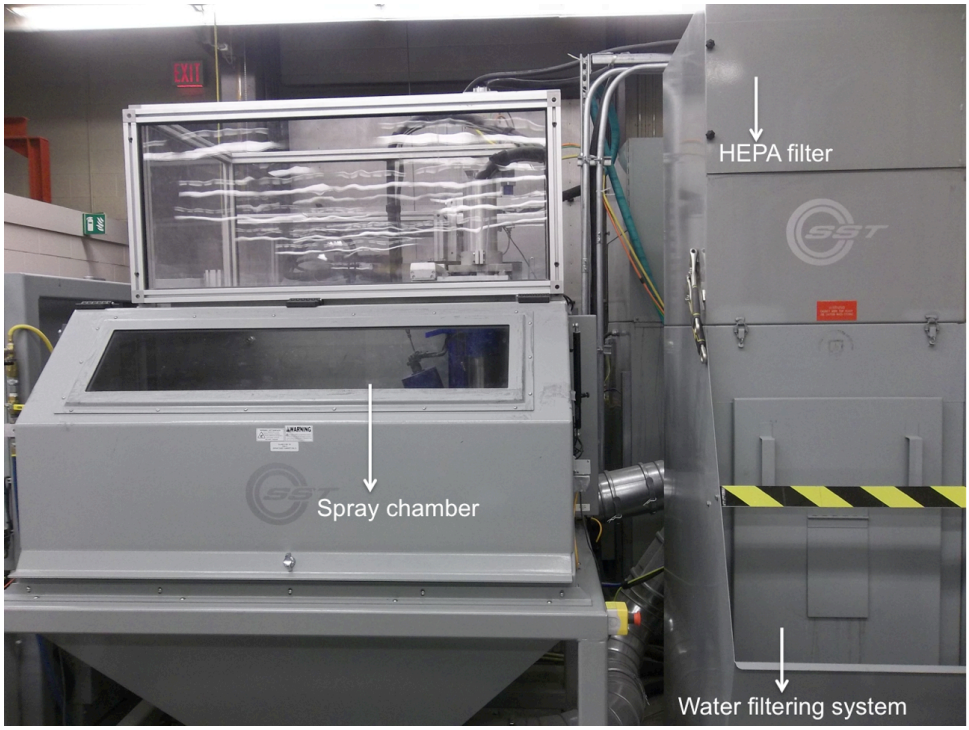

Figure 4.27: Centerline Ltd cold spray chamber.

4.4.4. Powder Feeder

A Thermach powder feeder (Model AT-1200, Thermach Inc. Thermal Spray and Machining, Appleton, WI, USA) was used in this study. The powder canister, the control panel and the gas carrier flow rate pressure gauge are its main components, as shown in Figure 4.28.

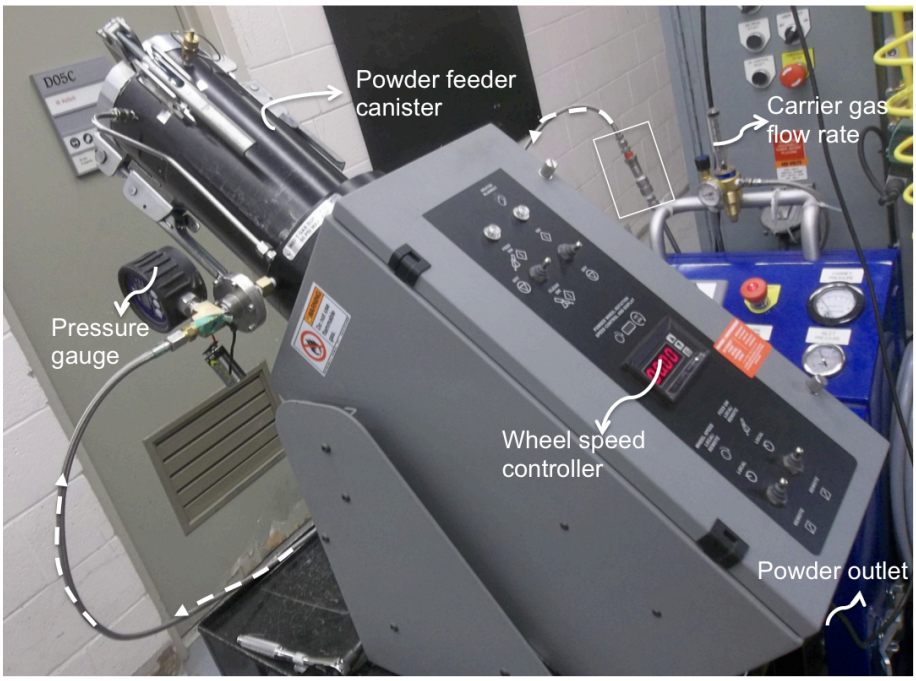

Figure 4.28: Termach powder feeder.

The powder is placed inside the canister and tightly sealed using a cover. The sealing permits to keep the powder away from the atmosphere and allows a pressure buildup to properly propel the powder through the feeder outlet. The figure above also shows the flow meter used to adjust the gas powder carrier pressure inside the canister. The volumetric flow of nitrogen from the bottle packs to the powder feeder canister was set for all tests to 30 SCFH (standard cubic feet per hour), which is equivalent to 1.16 NCMH (normal cubic meters per hour).

In this study, a small wheel (320 holes) has been used for all tests to obtain the required coatings and repairs, as shown in Figure 4.29. As the wheel rotates, the holes align with the powder feeder outlet passageway, which enables the carrier gas stream to carry the powder up to the nozzle inlet. The powder feeding rate can be controlled through the speed of the powder feeder wheel. The fluidity of the powder and its flow rate consistency through the feeder outlet up to the nozzle inlet is assisted with a tapping movement of the hammer shown in the following figure.

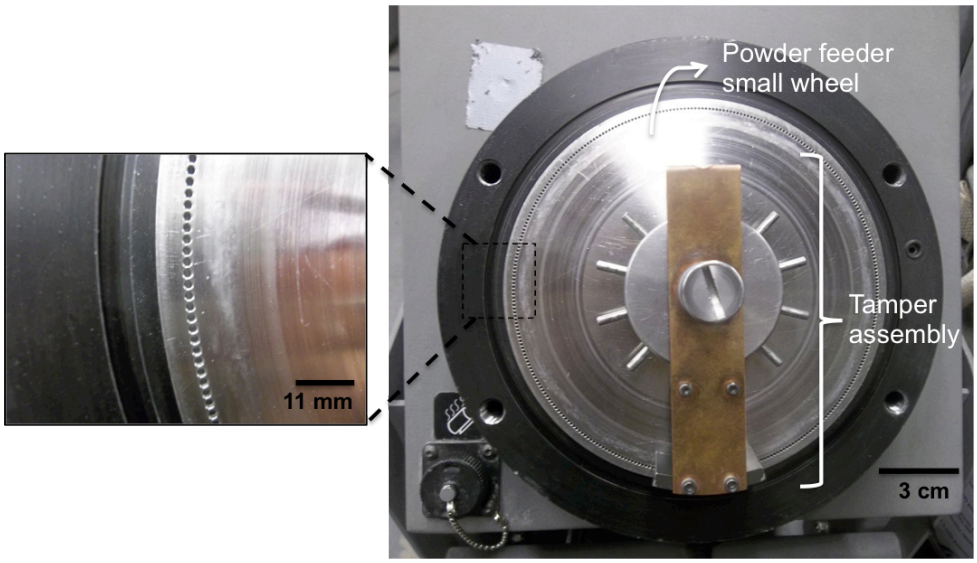

Figure 4.29: Powder feeder small wheel (320 holes).

4.4.5. Nozzles

In this research, the influence of the nozzle material and its internal geometry on the deposition efficiency and the flow distribution of the powder have been studied. Moreover, the material removal rate of the nozzles during spray has been investigated.

4.4.5.1. Nozzle Material

Centerline SST-Ultiflow polymer nozzles with a 2 mm orifice, 6.5 mm exit diameter and 120 mm in length have been used in this study. Figure 4.30 shows the internal dimensions of the Ultiflow nozzle. Manufactured out of Polybenzimidazole (PBI) the nozzle is able to withstand high spraying parameters such as 500 °C and 3.45 MPa without clogging. The clog-resistant PBI material has a thermal conductivity of 0.41 W/m·K [139].

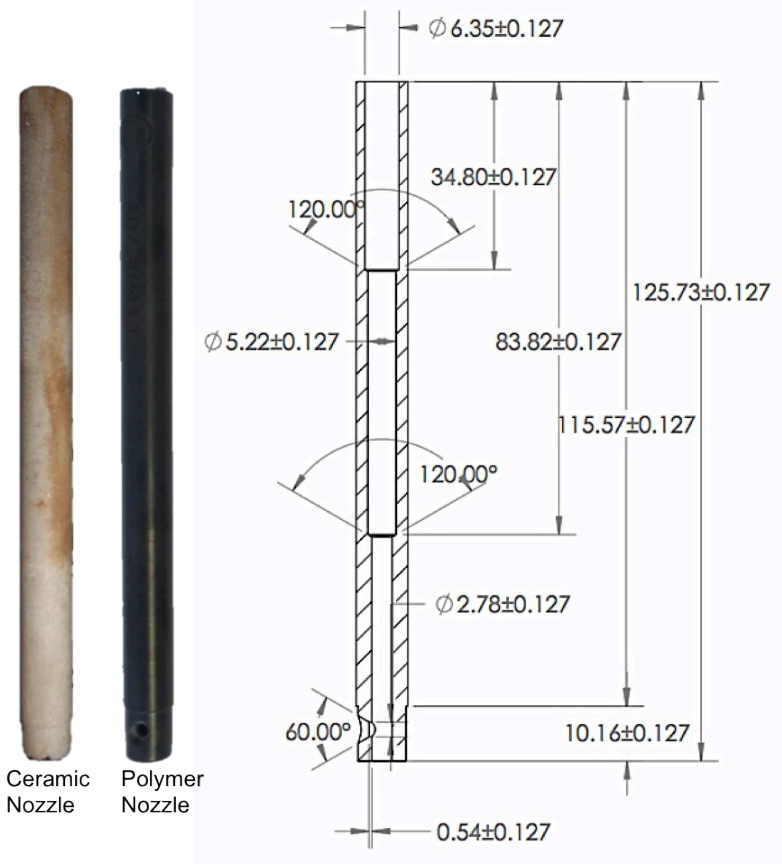

Figure 4.30: Centerline (Windsor) Ltd. SST-Ultiflow polymer nozzle and Mica ceramic nozzle internal dimensions (mm).

Easy-to-machine glass-mica ceramic material (McMaster-Carr) has been used to manufacture a ceramic nozzle at the University of Ottawa machine shop. Also known as Mykroy, this material is able to withstand a maximal temperature of 500 °C. The material is characterized by a high hardness value and a thermal conductivity of 1.02 W/m·K [140].

4.4.5.2. Nozzle Assembly

In order for the driving gas to achieve a supersonic speed, the nozzle was assembled to the spray gun using specific connectors as shown in Figure 4.31. A stainless steel nut screwed into the spray gun exit was used to attach the converging part of the nozzle assembly. The nozzle was fitted after the 2 mm throat using a spring and a quick connect cap. Therefore, the powder entry to the nozzle is made after the throat. Once the powder enters the main stream, 11 mm after

the throat, it travels through the nozzle in the diverging part of the assembly. At that stage, the gas is expanding, cooling down and accelerating to supersonic speeds.

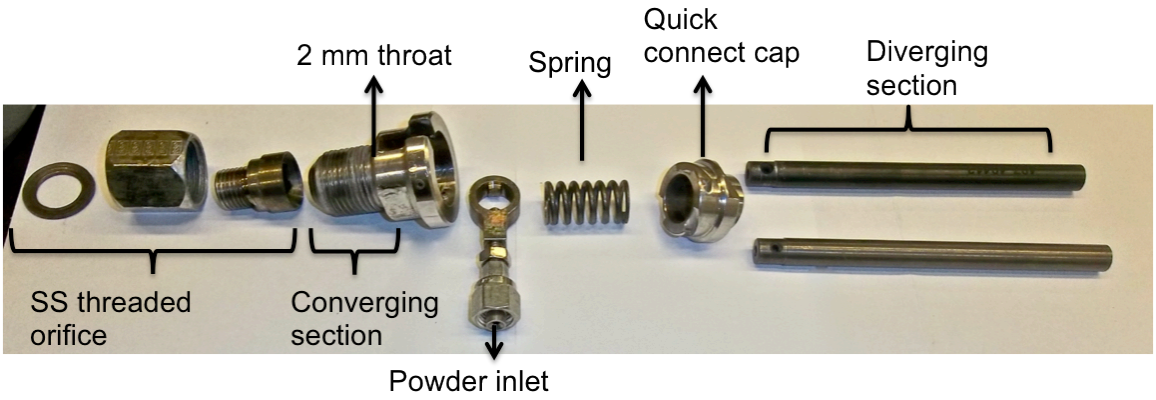

Figure 4.31: Nozzle assembly to the EP system

4.5 In-flight Particle Properties Measurement: Cold Spray Meter

To allow a better understanding of the impact and bonding process of the particles, it is important to examine the velocity of the particles when achieving deposition. Sufficient kinetic energy must be available in order to break the oxide layer and to plastically deform the particles at impact. Therefore, the particles velocity, flow rate and approximate diameter distribution within the flow at a standoff distance of 25 mm from the exit were measured using a laser in-flight analytical system known as the Cold Spray Meter (CMS) (Tecnar Automation Ltd, St-Bruno, Québec, Canada) shown in Figure 4.32.

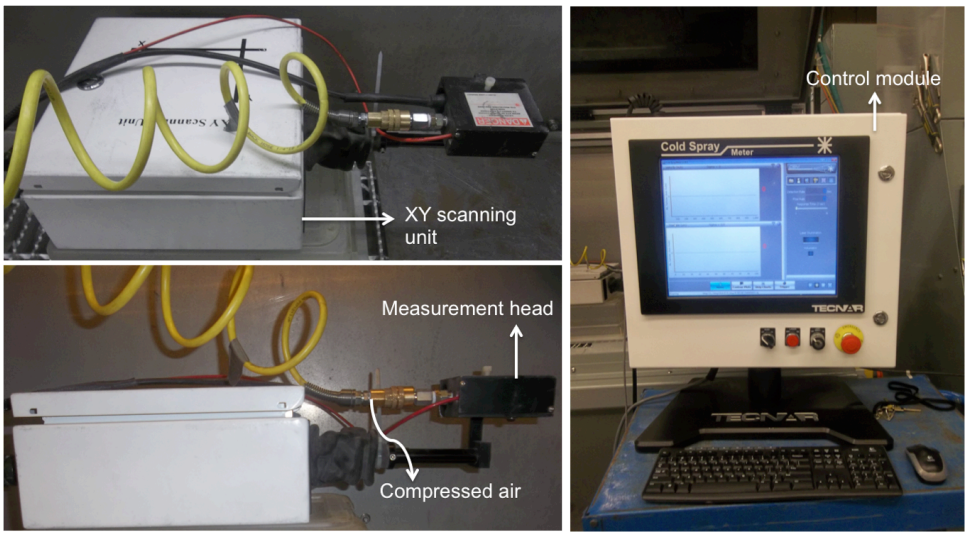

Figure 4.32: Cold spray meter equipment and set-up.

The CSM is equipped with a control unit, an XY scanning unit and a measurement head. A compressed air line was connected to the head to avoid powder entry in the system.

4.5.1. Principle

The continuous laser that illuminates the particles at the exit of the nozzle has a power density of 6.57 W/cm^2 and a 2.4 W power at the exit of the optical fiber. The laser has a wavelength of 810 nm and its spot diameter at the 10 cm focal point is 8 mm. The diffracted light from each individual particle is captured by a dual-slit photomask, which transfers all signals to the internal interpreting system. The distance between the slits and the time required to obtain the second signal provides the velocity at which individual particles are travelling through the flow. Figure 4.33 illustrates the operating principle of the CSM.

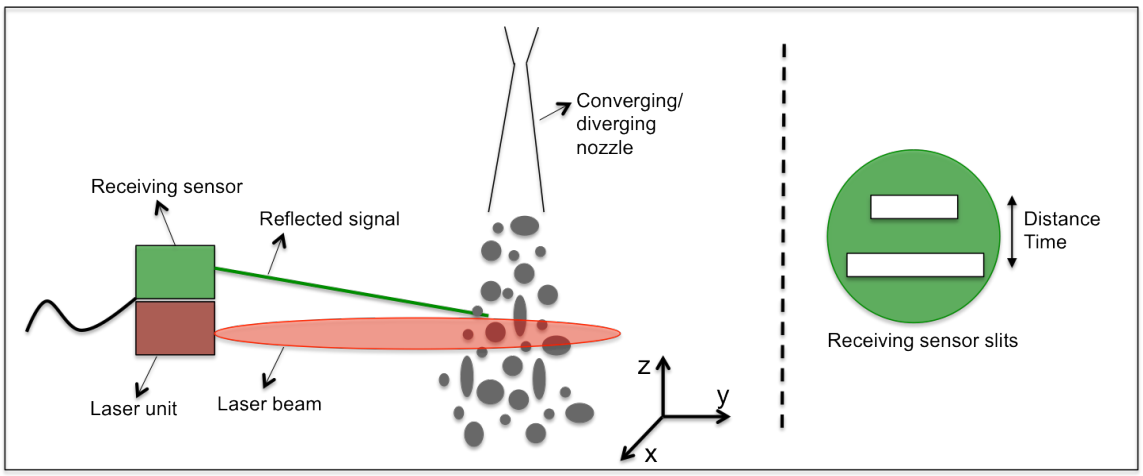

Figure 4.33: Illustration of the CSM working principle (Adapted from [88]).

4.5.2. Data Acquisition and Interpretation

In order to link the signals obtained at both slits to the same particle, the system relates the intensity of the diffracted signal to the diameter of the traveling particle. A larger particle reflects a signal of higher intensity than a smaller particle. Therefore, if identical intensities are acquired through both slits, the system measures and gives the velocity of that specific particle. A difficulty in linking a signal to the same particle arises when the particles used in cold spray are not spherical; as particles rotate in-flight, the projection of the diameter changes and therefore leads to erroneous data due to false link between signals and particles. However, due to a high flow rate, a large number of data can be obtained and the results are then statistically assessed. The statistical evaluation permits to obtain averages and standard deviations leading to results that are within the margin of error.

In this research, two types of analysis have been conducted using the CSM;

1. A measurement of velocity at specific single locations (away from the center or/and at the center) inside the flow at a standoff distance of 25mm.
2. A cross-sectional mapping of the flow in terms of particle velocity, flow rate and particle diameter in a (x, y) plane covering the entire flow area. A 9x9 grid having a total of 81 data acquisition points was used to produce the mapping. For statistical purposes, the acquisition time was set to 5 to10 seconds per position.

The purpose of the mapping is to characterize the particle properties inside the jet stream and to analyze the influence of nozzle wear on the cold spray plume. To verify the effect of nozzle erosion, the flow distribution has been analysed for worn and unworn PBI nozzles. Consequently, the variation in powder deposition and coating development due to the presence of nozzle material removal process has been studied.

4.6 Material Characterization Equipment

This section will discuss the approach taken to analyze the coatings obtained in terms of thickness, roughness, porosity, hardness and microstructure. These coating evaluation procedures are important because they associate the coatings specific characteristics and intrinsic properties to the coating performance.

4.6.1. Cut, Mount and Polish Procedures

The cutting process was essential in obtaining a representative section from the coating in order to simplify its characterization and further preparation. The samples were cut using a precision saw (Secotom-10, Struers) equipped with a silicon carbide cut-off wheel of 203 mm in diameter (10S20) as shown in Figure 4.34a. During sectioning, the wheel speed and feed rate were set at 2200 rpm and 0.075 mm/s respectively.

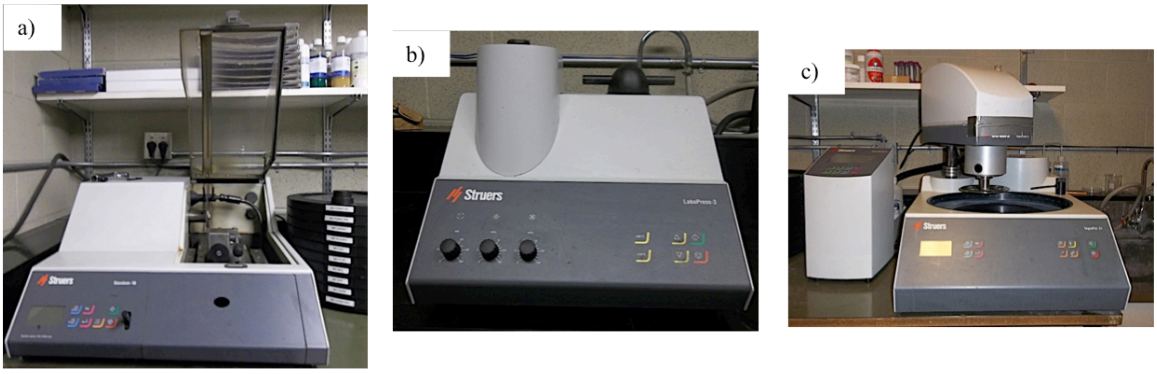

Figure 4.34: Sample preparation equipment. a) High speed cutting machine (Struers Sectom-10); b) Automatic hot mounting with thermosetting resin (Struers LaboPress-3/Phenolic powder) and c) Automatic grinder/polisher (Tegrapol-31, TegraForce-5 and TegraDoser-5).

Following the cutting was the mounting process, which main purpose was to facilitate the subsequent material characterization preparation steps. A phenolic plastic powder was used as the mounting media inside an automatic hot mounting press (LaboPress-3, Struers) as depicted in Figure 4.34b. The selected settings for the hot press were 20 KN uniaxial compressive force, 6 minutes of heating at 150 °C and 3 minutes of cooling.

The grinding and polishing process was performed using an automatic grinder/polisher (Tegrapol, Struers). The surfaces of the sample (coating and substrate) were polished down to 0.04 μm using a colloidal silica suspension. All surface preparation procedures followed the polishing routine presented in Table 4.4, applicable to pure aluminum and aluminum alloy coatings. Between each steps of grinding/polishing, the samples were cleaned using tap water. Once the polishing procedure was completed, the surface of the samples was dried using compressed air.

Table 4.4:Grinding and polishing method

Steps	Surface	Abrasive	Lubricant	Time
Plane Grinding	MD-Piano 220 (Struers)	None	Water	2 min
Fine Grinding	MD-Largo (Struers)	None	Water	2 min
Intermediate Polishing	MD-Mol (Struers)	9 μm diamond suspension	None	4 min
Final Polishing	MD-Chem (Struers)	0.04 μm diamond suspensions	None	1 min

4.6.2. Imaging and Microstructural Analysis

The obtained coatings were observed and analyzed using optical microscopy (OM) and various microscopic imaging techniques. As shown in Figure 4.35a, a 3D digital microscope was utilized to produce 3D images of the coatings as-sprayed and as-machined surface profiles and to verify the accuracy of the repairs. It works by generating images at various focus depths, which once accumulated create a 3D profile.

Moreover, it was used as a tool along with the optical microscope, shown in Figure 4.35b, to qualitatively and quantitatively characterize the coatings porosity level, particle deformation level and to observe and report any deposition anomalies. The images taken were analyzed using the Clemex Vision Lite and VHX-200 Communication analysis software. The metallurgical microscope shown in Figure 4.35c was used to briefly verify if the polishing steps produced a surface free from scratches and marks.

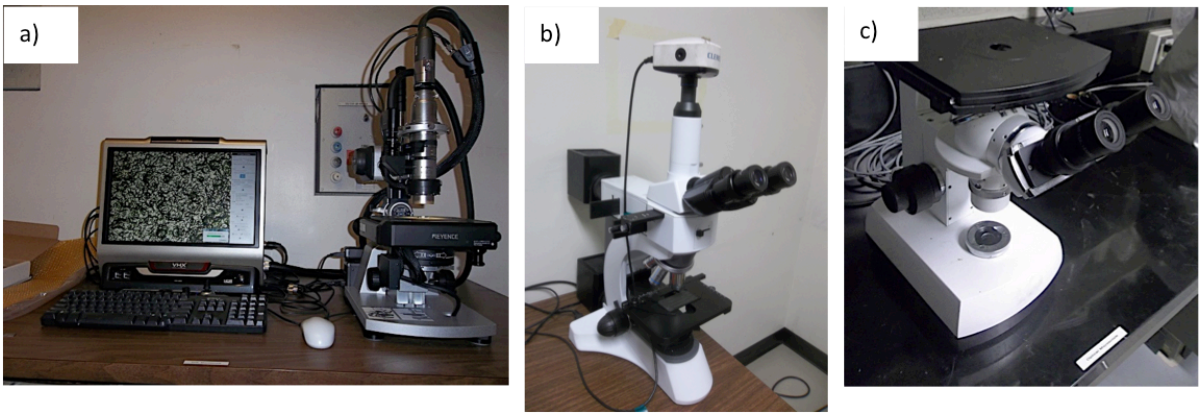

Figure 4.35: Metallurgical analysis optical equipment. a) 3D digital microscope with image analysis software (VHX-2000 Keyence); b) Optical microscope equipped with digital camera for surface analysis (Clemex Vision Lite Software) and c) Metallurgical optical microscope (XJP-3A).

Since the optical microscopes are limited to a magnification of 1000X, a scanning electron microscope (SEM) (Zeiss, EVO-MA10) was used to examine the cross-sections and surfaces of the coatings in order to provide information on their composition and topography. The SEM in Figure 4.36 is equipped with secondary electron (SE), backscattered electron (BSE), energy dispersive X-ray spectrometer (EDS), electron backscatter diffraction (EBSD) and X-ray computed tomography (CT) detectors. In this research, other than the standard SE analysis, the BSE and EDS examinations were also produced.

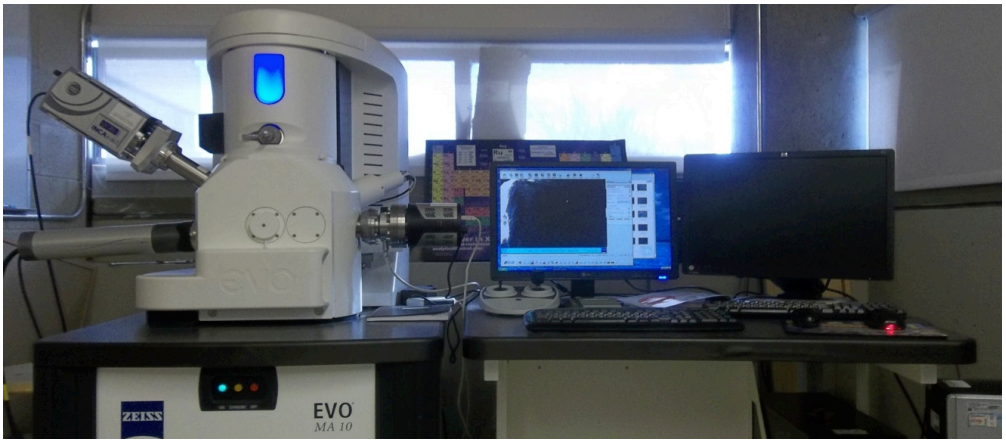

Figure 4.36: Scanning electron microscope (University of Ottawa, Oxford Instrument, EVO-MA10, Zeiss, UK).

Prior to analyzing the coatings using the SEM, the polished samples surfaces have been covered with a thin conductive gold layer using a cold gold sputtered device (Denton Vaccum) shown in Figure 4.37. The gold conductive layer prevents charging of the mounted specimen once bombarded by electrons inside the SEM, which otherwise would accumulate on the surface. This thin electrically conducting coating also reduces thermal damage and improves the signal to noise ratio (amount of detected SE).

Figure 4.37: Gold sputtering equipment.

4.6.3. Microhardness Measurements

A diamond indenter having an angle of 136° between its opposite faces was used to perform the Vickers indentation test. Figure 4.38 presents both of the Vickers hardness testers used in this study. The test was produced to evaluate the coating microhardness and to verify the

properties of the substrate prior and after spraying, according to the ASTM E92-82R03 standard. As noted in a previous section, the substrate hardness was tracked in order to ensure that the cold spray process didn't induce any property changes. An average of 5 to 10 indentations were used for every test to cover the statistical requirements. A load of 0.3 kg was used, as suggested in the literature for cold sprayed materials [141], [142], along with a 10 seconds dwell time. The hardness value was obtained automatically through the internal software of the hardness machine by using the following relation:

$$HV = \frac{1.8544F}{d^2} \qquad \text{Eq. 17}$$

Where F is the load (kg) and d is the average of the diagonal lengths (mm).

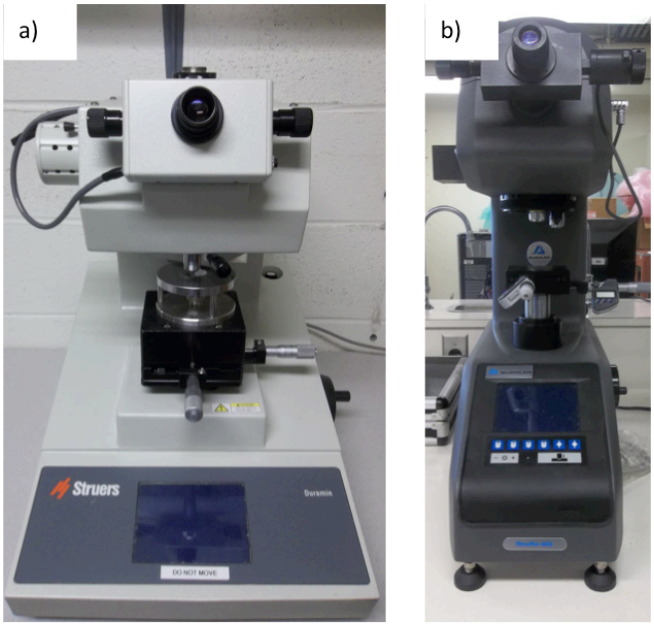

Figure 4.38: Vickers microhardness tester. a) Struers Duramin-1 and b) Buehler Micromet 6030.

4.7 Adhesion/Cohesion Strength

In order to understand the influence of the substrate surface preparation and final roughness on the pure aluminum and Al2024 coatings adhesion strength to the substrate surface, the coatings were tested in tension according to the ASTM C633 standard. For this test, the

surface of 25.4 mm diameter rods (bond plugs) was prepared using different procedures as presented in Subsection 4.2.4 to create various surface conditions as shown in Figure 4.39.

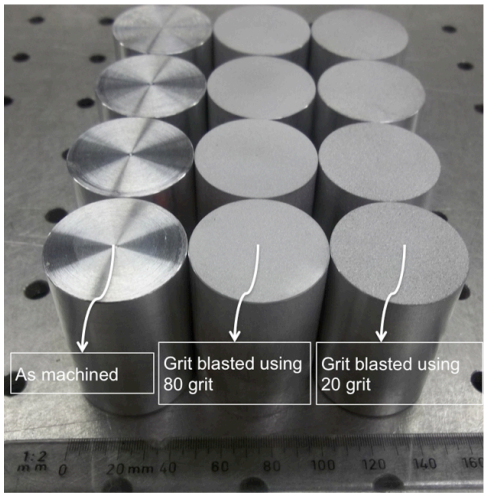

Figure 4.39: Bond plugs surface roughness.

To eliminate any discrepancies created by the external environment, the surface of the bond plugs need to be cold sprayed immediately after the substrate surface has been prepared and subsequently cleaned. The bond plug holder and the spaying pattern used during the deposition of the powders are shown in Figure 4.40.

Figure 4.40: Set-up for the adhesion test during spray and spraying pattern (carbon fibre plates omitted in figure).

As depicted in the previous picture, five bond plugs can be sprayed at once. However, in this study, only one bond plug was installed on the holder and sprayed at a time. By using this technique, the heat exchange between the holder and bond plugs was limited, which ensured that all coated bond plugs had the same initial surface temperature. Moreover, if five bond plugs were

sprayed at once, the first deposited layer would be cooling down while the second up to the fifth bond plugs were being sprayed. This would lead to inconsistencies in the deposition of subsequent layers.

Once sprayed, the coating surfaces are slightly machined down to a flat surface using a lathe. The bond plugs assembling fixture and set-up are shown in Figure 4.41. The pull-off and substrate bars are glued together using a FM-1000 elastomeric adhesive glue (Cytec Engineering Materials). The pull-off bar and the substrate material were made out of the same aluminum alloy either Al2024 or A7075 for the Al2024 and pure aluminum coatings respectively. The complete set-up procedure and details regarding the preparation process is presented in Appendix II.

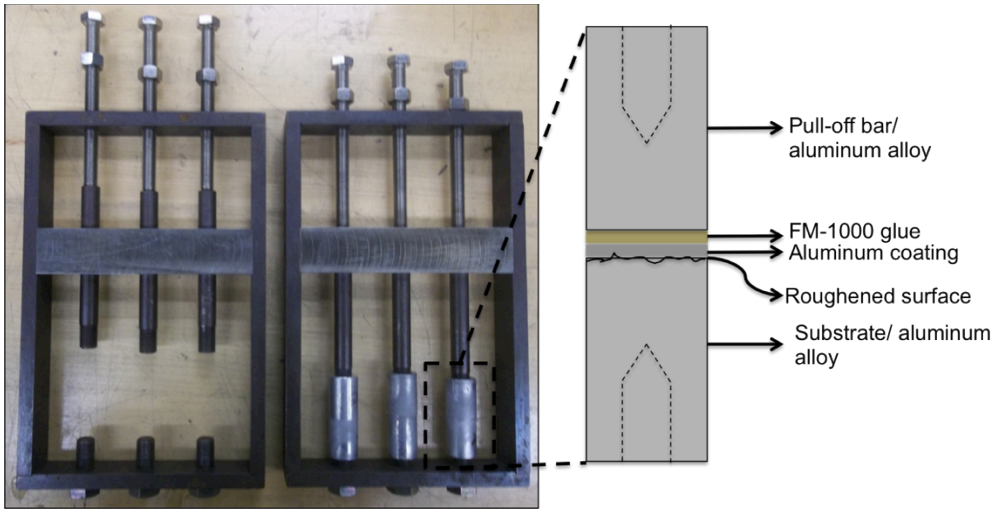

Figure 4.41: Bond plugs assembly structure.

Finally, the bond plugs are tested in tension using an Instron Universal Tensile Testing Machine (Instron Series 4482) shown in Figure 4.42. More than five adhesion tests were completed for each different set of surface preparation procedures. The complete bond plug preparation procedure can be found in Appendix II. The pressure, P, required to delaminate the coating, either through a cohesive or adhesive failure, was calculated using the following equation;

$$P = \frac{F}{A} \qquad \text{Eq. 18}$$

Where F is the force at failure (N) and A is the bond plug substrate area (m^2).

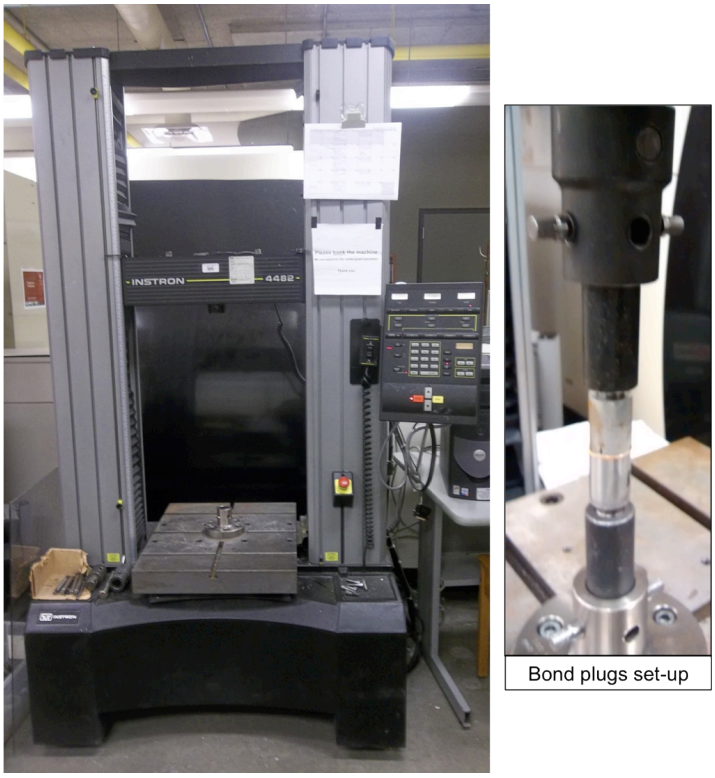

Figure 4.42: Instron Series 4482 tensile testing machine.

4.8 Cold Sprayed Threads Properties

To characterize the load carrying capacity of the repaired threads, both the 3.75-12UNJ-3A and 1.5-12UNF-3A threads were tested in shear. The following subsections describe the procedures used to quantify the structural performance of the repairs.

4.8.1. Torque Resistance Requirement

To test the performance level of the 3.75-12UNJ-3A threads, a dry torque test (no lubricant) was completed using a deflecting beam torque wrench as shown in Figure 4.43. The hexagonal mating nut was machined out of 15-5 PH steel material to replicate the components used in the aerospace application. A stainless steel crowfoot wrench was designed to connect the wrench to the nut through a 19.05 mm (¾") to 25.4 mm (1") square socket adapter. Once

assembled, the maximal achievable torque was of 303 N·m (2683 inch·lbs), which accounts for the additional crowfoot length.

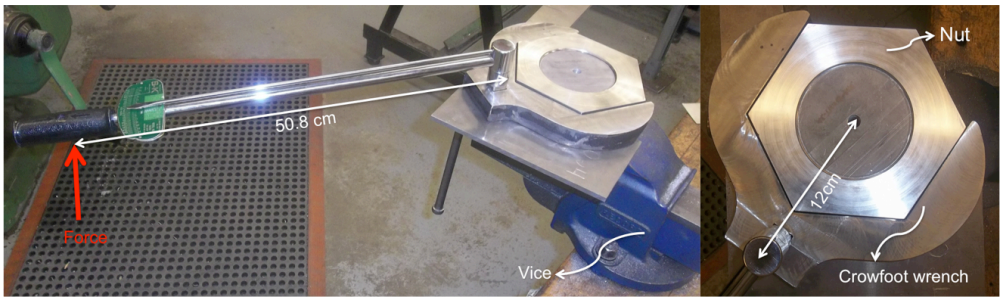

Figure 4.43:Torque test set-up.

4.8.2. Threads Shear Resistance at the Coating/Substrate Interface

The load capacity of the 1.5-12UNF-3A threads has been tested through a compressive load test using a Series 4482 Instron machine. Figure 4.44 illustrates how the repaired component was fastened into a mating steel nut of matching internal threads during the test. Eight threads in total have been repaired and all threads were engaged during the compressive test. The compressive force was applied directly to the component and a shear force was induced at the coating/substrate interface.

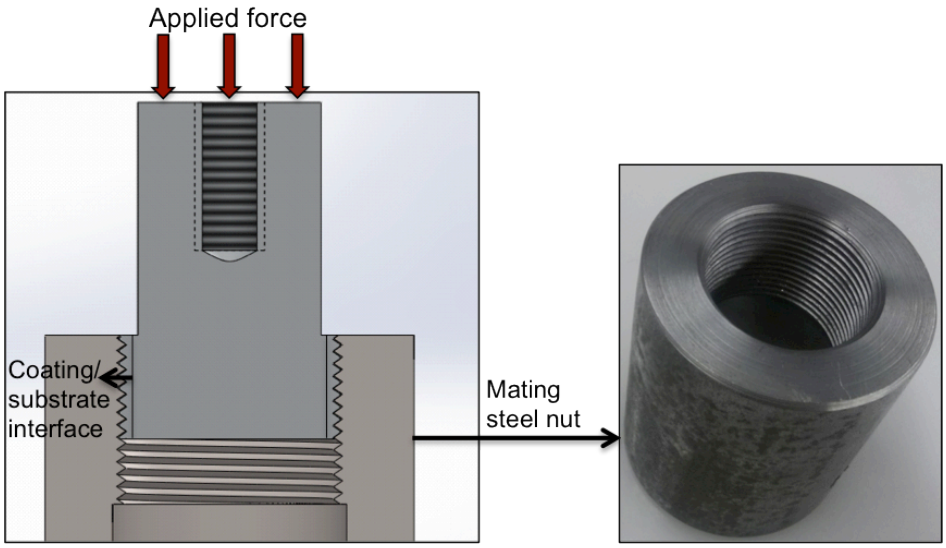

Figure 4.44: Compressive load test.

In this test, the following equation was used to calculate the shear stress, τ, level at failure;

$$\tau = \frac{F}{2\pi r h} \quad \text{Eq. 19}$$

Where F is the load at failure (N), r is the radius of the substrate (m) before repair and h is the total length of the repaired area (m).

CHAPTER 5

Feasibility and Coating Development

The current chapter describes the approach that was taken to develop and achieve proper material deposition for repair and restoration of aluminum parts. Numerous experimental trials have been produced to test the influence of process pressure and temperature on the coating quality. The results are separated into two distinct sections according to the sprayed material. Due to a lack of existing research data on the Al2024 deposition, an extensive study has been made to describe its potential use in the cold spray process. Mapping of the coating thickness, porosity and microhardness as a function of process pressure and temperature has been performed. Other spraying aspects such as the powder feeding rate and stand off distance have been analysed.

Only high spraying parameters have been tested and studied for the pure aluminum powder. The production of thick dense pure aluminum repairs has been achieved through the adjustment of the powder feeding rate. The study of the influence of other parameters (T°C and P) on the pure aluminum coating quality was not necessary as the main goal was to achieve low porosity at high deposition efficiencies.

5.1 Development of Al2024 Coatings on Al2024-T351 Substrates

To investigate the effect of an individual spraying parameter on the coating deposition rate and properties, all influencing parameters were held constant while the parameter of interest was varied. The coatings were produced on small 25.4 mm by 19.05 mm Al2024-T351 coupons. The substrate surface preparation procedure was the same for all produced coatings and is presented in Table 5.1. The resulting substrate surface roughness after the grit blasting procedure was 1.47 ± 0.20 μm.

Table 5.1: Substrate Surface Preparation Procedure for the Development of Al2024 Coatings on Al2024-T351 Substrates

Parameters	Values
Abrasive	Aluminum Oxide
Size	80 Mesh
Process Gas	Compressed Air
Pressure	0.55 MPa
Grit Blasting Angle	45°
Standoff Distance	51 mm
Post Treatment	Acetone (Ultrasonic bath)

In order to quantify the amount of powder that is injected into the nozzle based on the powder feeder wheel speed and powder feeder gas rate, the powder mass was measure before its entry into the nozzle for a feeding time of 2 minutes. The purpose of this test was to obtain a general mass/min value representative of the physical conditions, which can be used to repeat these tests while using different equipment. The tests were performed using the small 320 holes powder feeder wheel and a 30 SCFH powder feeder gas rate and the results are shown in Figure 5.1. The powder feeding flow rates in g/min are linearly related to the revolution per minute of the powder feeder wheel. Based on the results, the powder mass flow rate (g/min) is approximately equal to the number of revolution per minute of the wheel.

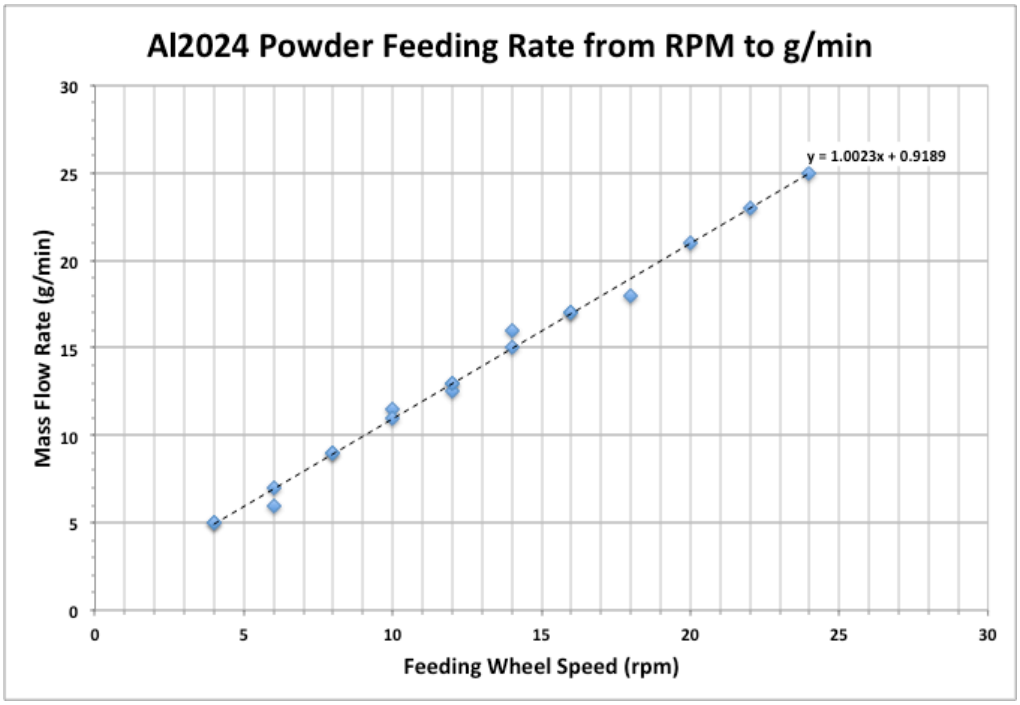

Figure 5.1: Powder feeding rates using the Al2024 powder.

5.1.1. Influence of Pressure and Temperature on Coating Quality

Coatings have been produced using different combinations of process gas pressure and temperature. The purpose of this test was to identify the limits of proper deposition of the Al2024 powder. As stated in Section 2.3.4, the ability of the sprayed material to deposit and build a coating is related to the critical velocity. The CGDS parameters that were kept constant during these tests are shown in Table 5.2.

Table 5.2: CGDS Parameters Held Constant During the Initial Development of Al2024 Deposition Ability Matrix

Parameters	Values
Nozzle Type	Ultiflow
Increment Size	2 mm
Number of Passes	5
Nozzle Traverse Velocity	15 mm/s
Powder Feeder Wheel	320 Small Wheel
Powder Feeder Gas Rate	30 SCFH
Powder Feeder Rate	11.25 g/min
Standoff Distance	25 mm

Figure 5.2 shows the obtained deposition matrix based on the process gas pressure and temperature used. As stated in section 2.3.7.1, a decrease in stagnation pressure and temperature decreases the particle kinetic energy and its ability to deposit. At a process temperature of 150 °C, the Al2024 particles tend to bounce off due to a lack of ductility and impact energy, which only leaves an eroded substrate surface. Similarly, at a pressure of 1.38 MPa, the particles do not have sufficient kinetic energy to adhere to the substrate surface and therefore reflect away from the substrate surface after impact without undergoing any metallurgical or mechanical bonding.

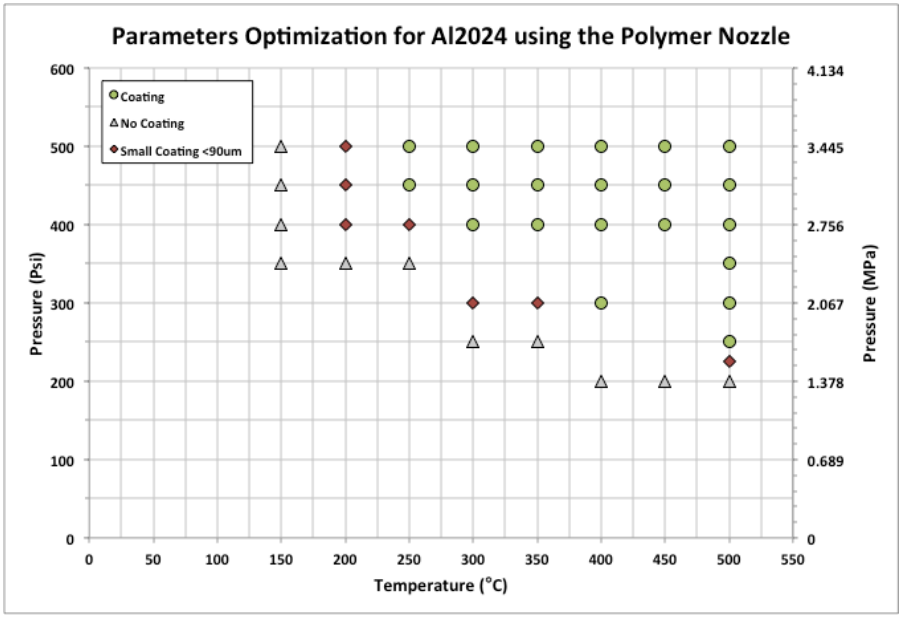

Figure 5.2: Pressure and temperature qualification map for the spray of Al2024 powder.

For all successfully deposited coatings, metallographic examination was performed and the coating thickness, porosity, roughness and Vickers microhardness were evaluated. Figure 5.3 shows the coating thickness obtained for different process pressure and temperature. Thickness error bars have been omitted, as the coating surface roughness will be given further in this subsection. The deposition efficiency of the powder can be related to the relative final coating thickness. As the same amount of powder was sprayed per unit area, an increase in thickness is representative of an increase in the percentage of deposited powder. As such, high spraying parameters of 500 °C and 3.45 MPa generate the highest deposition efficiency with a coating thickness of 1004 μm. As stated in the literature review, the process gas temperature has a higher influence on the particle exit velocity and deformation process than the pressure. A higher gas temperature increases the gas velocity and consequently the particle kinetic energy. Moreover, it induces a higher particle thermal energy, which lowers the required critical velocity for bonding and increases particle ductility during the deformation process. As such, as shown in Figure 5.3, an increase in gas temperature drastically increases the coating thickness. A jump in deposition efficiency is seen around 2.07 MPa and 2.42 MPa. At this pressure, the gas density and drag force applied to the particles during their trajectory is sufficiently increased allowing larger particles to reach the critical velocity. The overall effect is a growth in the number of particles reaching the critical velocity for appropriate deposition and bonding, which increases the deposition efficiency and consequently the coating thickness.

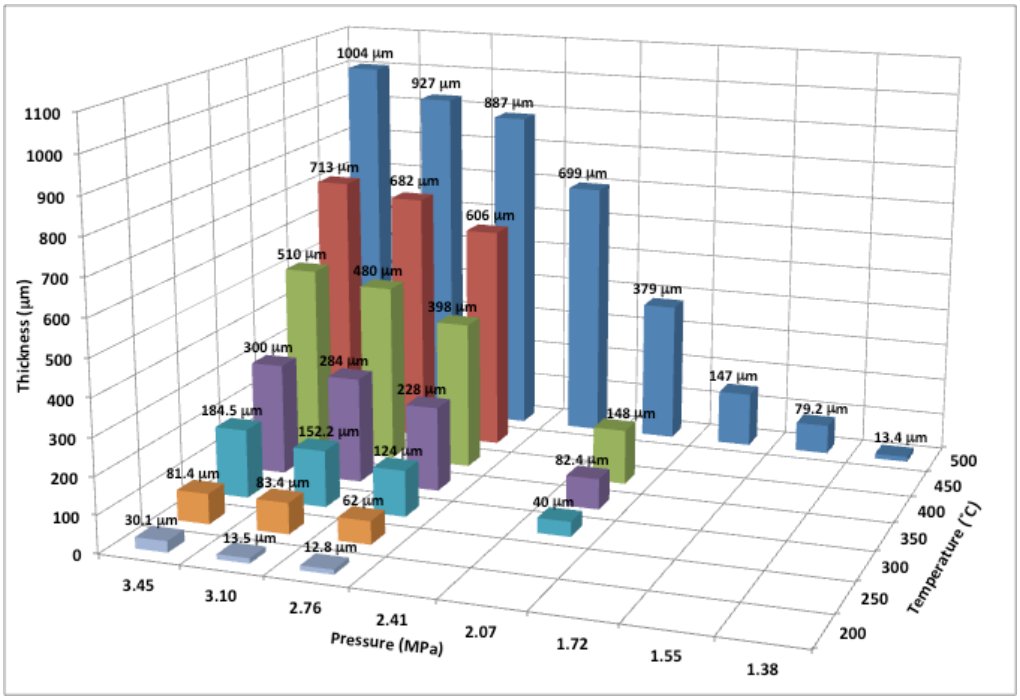

Figure 5.3:Al2024 coating thickness based on the process temperature and pressure. Obtained thickness values are shown above each corresponding combination of parameters.

Independent of the process gas pressure and temperature, all obtained coatings were dense, as shown in Figure 5.4 through Figure 5.9, as no porosity could be detected. The adiabatic regime of the CGDS process can induce thermal softening during particle impact, which can facilitate the plastic deformation and assist in inducing proper particle interlocking and stacking. At high parameters, adequate kinetic energy promotes particle plastic deformation and close contact deposition, which results in dense coatings while at lower parameters, high tamping and impinging effects of the non-deposited particles increases the coating density at the expense of a lower deposition efficiency.

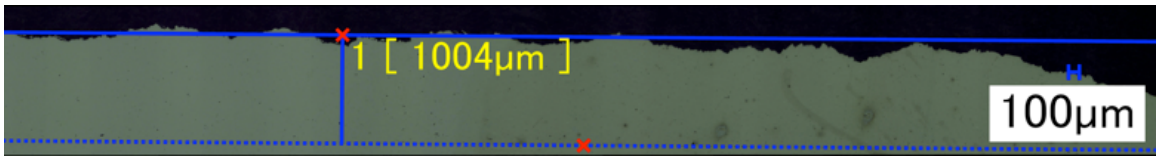

Figure 5.4: Al2024 coating on Al2024-T351 substrate obtained at 500 °C and 3.45 MPa.

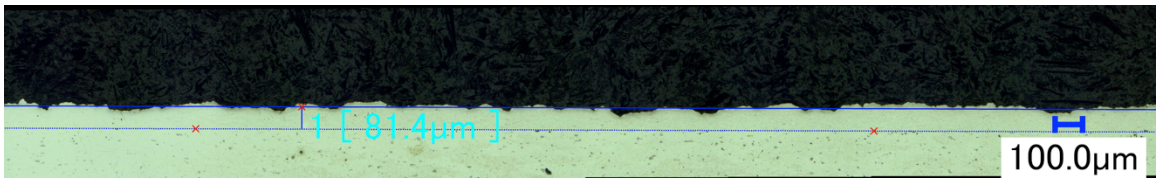

Figure 5.5: Al2024 coating on Al2024-T351 substrate obtained at 250 °C and 3.45 MPa.

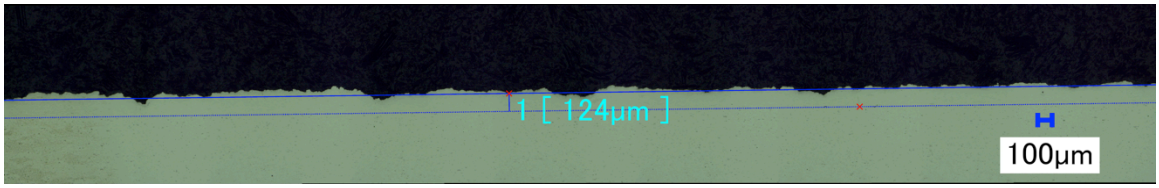

Figure 5.6: Al2024 coating on Al2024-T351 substrate obtained at 300 °C and 2.76 MPa.

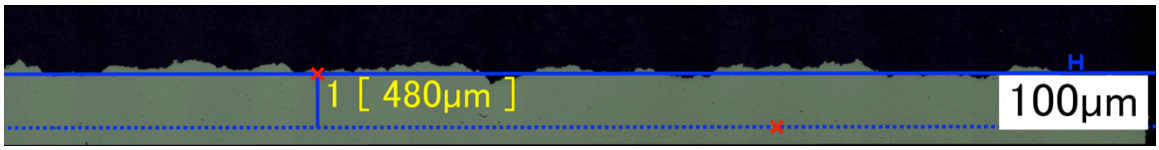

Figure 5.7: Al2024 coating on Al2024-T351 substrate obtained at 400 °C and 3.10 MPa

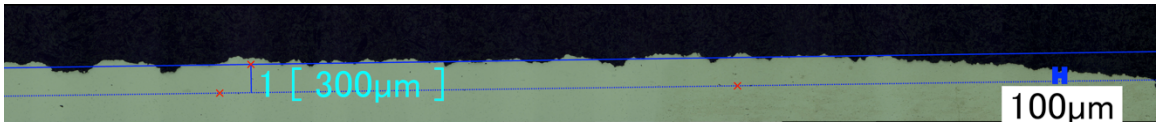

Figure 5.8: Al2024 coating on Al2024-T351 substrate obtained at 350 °C and 3.45 MPa

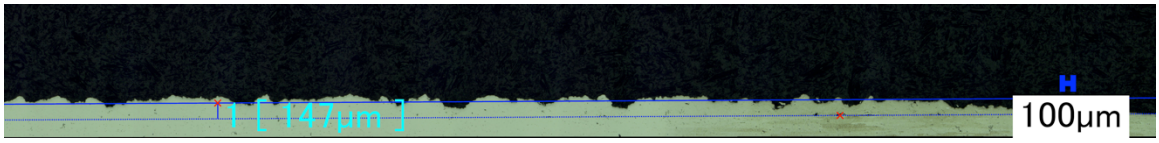

Figure 5.9: Al2024 coating on Al2024-T351 substrate obtained at 500 °C and 1.72 MPa.

Figure 5.10 shows high magnification micrographs of coatings shown above and obtained at different parameters.

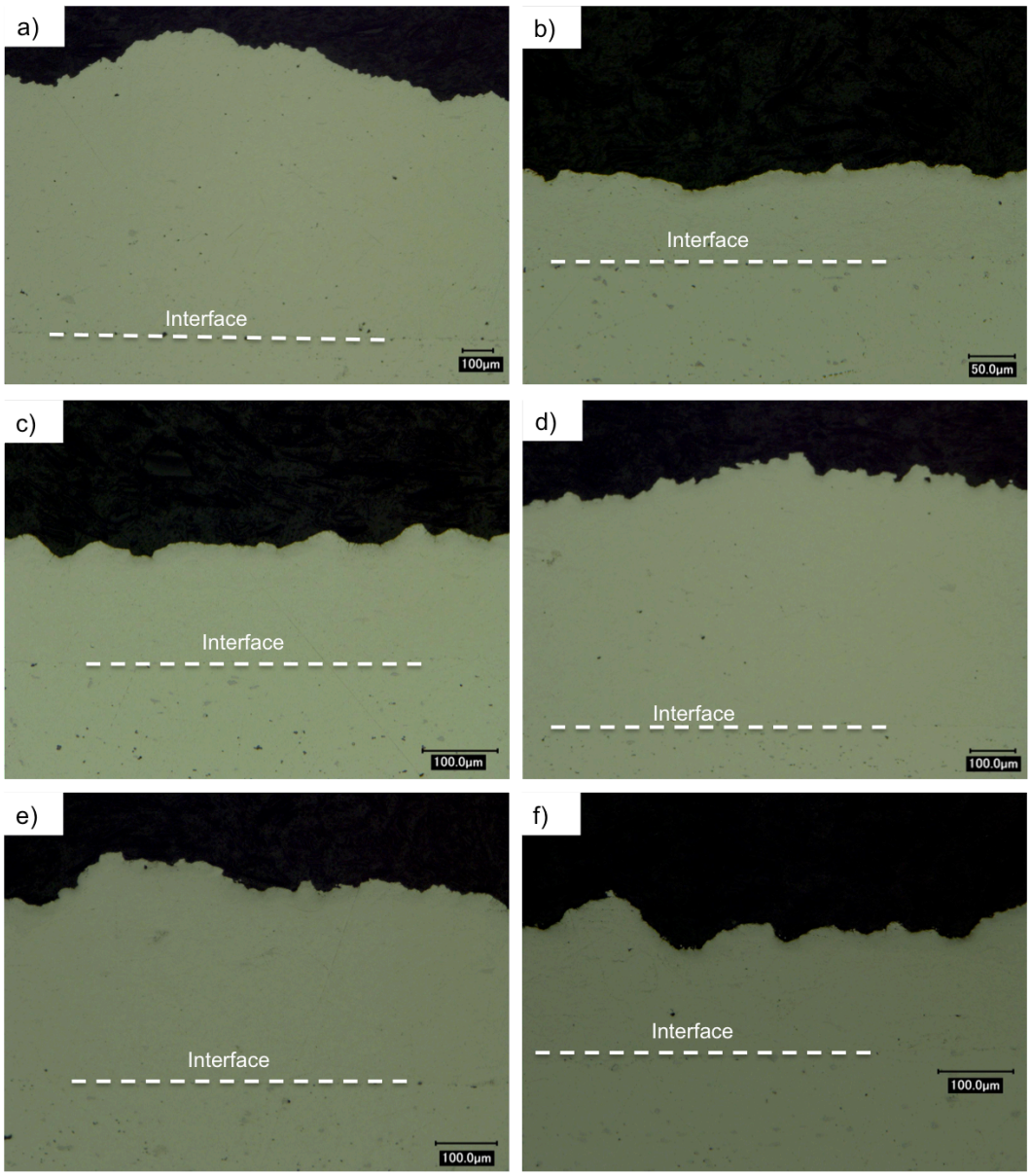

Figure 5.10: Zoom of the Al2024 coatings sprayed at a) 500 °C – 3.45 MPa, b) 250 °C-3.45 MPa, c) 300 °C- 2.76 MPa, d) 400 °C- 3.10 MPa, e) 350 °C- 3.45 MPa and f) 500 °C- 1.72 MPa.

Figure 5.11 illustrates the coating roughness based on the process gas temperature and pressure. The coating surface roughness measurements were taken perpendicular and parallel to the gun travel direction. As expected, the roughness increases with coating thickness as more particles are being deposited. However, the coating roughness plateaus at approximately 20 µm and does not increase for higher spraying parameters and larger depositions. Higher particle impact velocities are obtained at higher parameters, which generates higher particle deformation,

packing and contact. As a consequent result, the roughness does not increase gradually with deposition and smooth coatings are obtained at high process parameters [143].

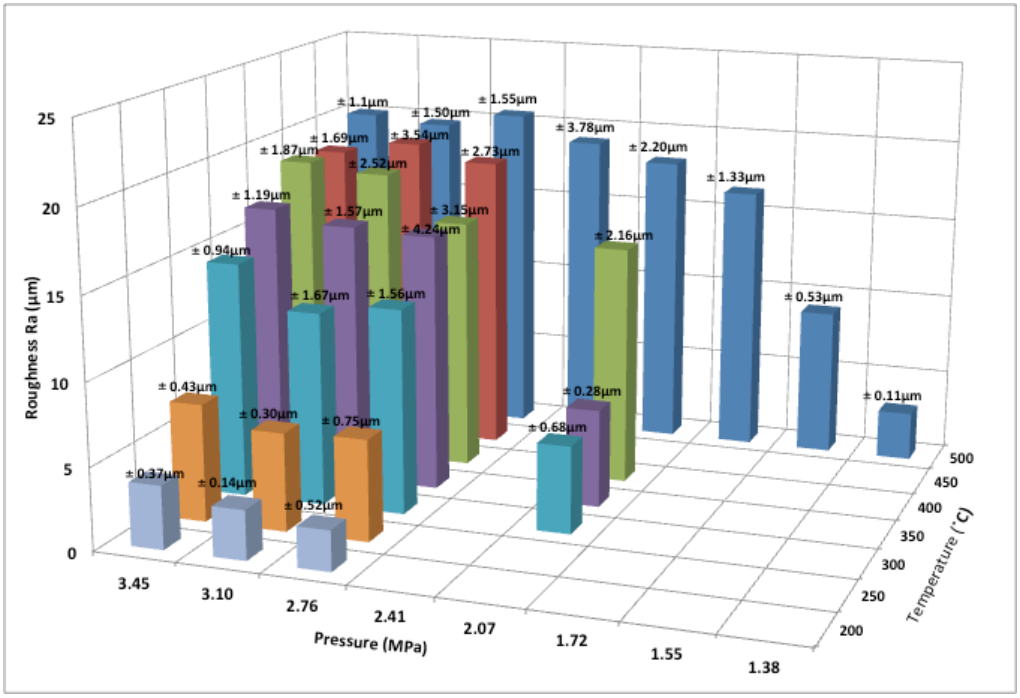

Figure 5.11: Al2024 coating surface roughness based on the process temperature and pressure. Standard deviation values are given above each result.

Figure 5.12 illustrates the coatings Vickers microhardness ($HV_{0.3}$) values taken at the center of the deposition. The ASTM E92-82R03 standard requires that the distance between the center of the indentation and the edge be at least 2.5 times the length of the impression diagonal. Therefore, only coatings with sufficient thick deposition have been tested. Dense Al2024 coatings with higher hardness are obtained at lower gas pressures and temperatures due to the larger peening effect created by the non-deposited particles involved in the coating production at these parameters. Severe deformation resulting from the work hardening process involved in the cold spray process induces strengthening by plastic deformation. In consequence, higher hardness is obtained with lower deposition efficiencies. The characteristic coating hardness is related to the plastic strain through the Holloman and Tabor relationship [132]. At lower pressures, the hardness of the Al2024 coating is 15% superior to the 137 HV hardness of the cold worked Al2024-T3 material. Similar results and conclusion were found by Champagne et al. [132] for cold sprayed pure aluminum powder.

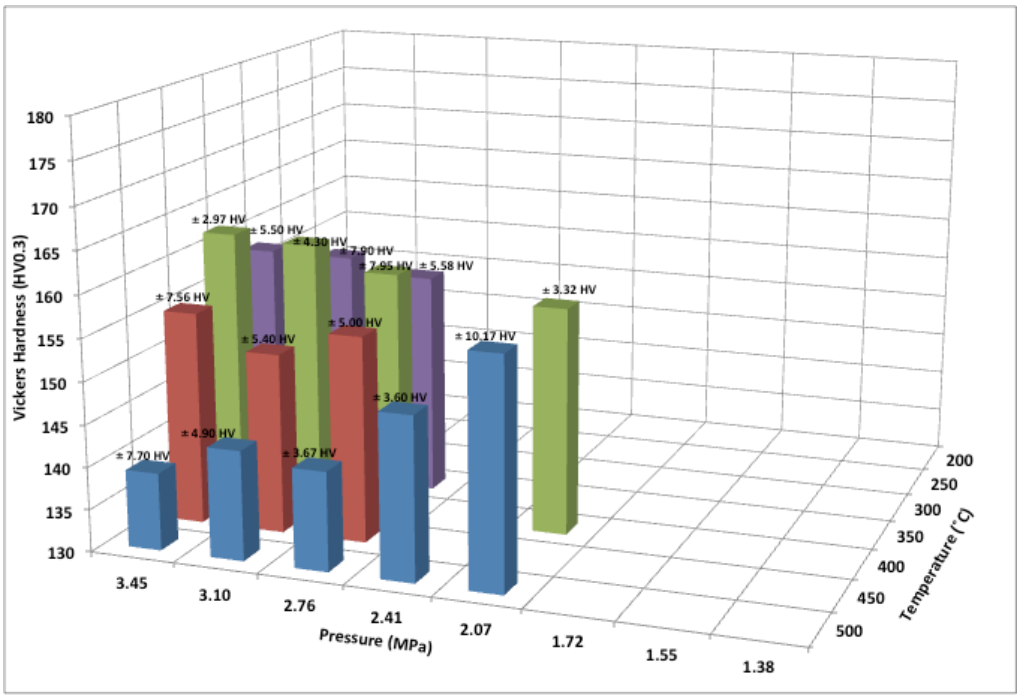

Figure 5.12: Al2024 coating Vickers microhardness based on the process temperature and pressure. Standard deviation values are given above each result. (The temperature axis label order has been reversed to allow proper view of low hardness values.)

As noted in section 2.3.5, grain refinement and increased dislocation density resulting from severe plastic deformation influences the coating hardness obtained through the cold spray process. Moreover, the compressive residual stress accumulation in the coating arising from the peening effect and high strain plastic deformation might affect to a certain degree the coating's resistance to micro-plastic deformation induced during the hardness measurements. The compressive residual stresses in the coating are superimposed on the applied indentation stress field and affect the overall plastic deformation. Thus, larger compressive residual stresses can possibly limit the zone of plastic deformation and increase the elastic recovery upon unloading, which would result in larger apparent hardness. Although, residual stresses can affect the hardness evaluation process, whether or not the influence is large enough to produce noticeable effect during microindentations tests needs to be further studied.

The coating hardness sprayed at the highest parameters is of 139 ± 7.7 $HV_{0.3}$, which corresponds to the lowest measured hardness. High process temperatures promote the occurrence of residual stress relaxation in the coating. General heat treatment for stress relief is performed at

190 °C for the aluminum 2024 alloy [37]. This temperature is easily attained during the spray at 500 °C [103]. The stress relief annealing effect on the residual stress is also dependent on the coating exposure time to the high gas stream temperature.

Moreover, exposure to high gas temperatures can induce thermal softening of the particles. Softer particles are easily experiencing higher degrees of plastic deformations during impact than harder particles, which limits their peening process and their influence on the cold working process and resulting compressive residual stresses in the coating.

5.1.2. Parameters Selection for Al2024

To repair aluminum 2024 alloy components with Al2024 powder, spraying temperature and pressure of 500 °C and 3.45 MPa have been chosen respectively. These parameters provide the highest particle deposition efficiency, which will limit the time of repair and use of resources. Moreover, due to the high gas stream temperature, stress relief annealing effects reduce the coating brittleness, which will make the repair less susceptible to cracking and warping during the machining process. In addition, particle thermal softening decreases the amount of cold work and impingement effects of individual particles. As dense coating were obtained at highest parameters, less peening effects will only result in higher coating ductility and softness and lower compressive residual stress.

5.1.3. Influence of the Standoff Distance (SOD)

In the production of thick coatings using the CGDS process, the standoff distance changes according to the thickness of the deposited material. In this study, coatings of 7 mm in thickness needed to be deposited for proper restoration and repair of the aluminum nose landing gear steering actuator threads. Therefore, the goal of this subsection is to evaluate the effect of the standoff distance on the deposition efficiency and coating quality and find the standoff distance that is best suited for the repair of large components. During this test, only the SOD distance was varied while all other influencing parameters were kept constant as presented in Table 5.3.

Table 5.3: CGDS Parameters Held Constant During the Evaluation of the Effect of Standoff Distance on Coating Deposition

Parameters	Values
Gas Nature	Nitrogen
Gas Pressure	3.25 MPa
Gas Temperature	500 °C
Nozzle Type	Polymer
Increment Size	2 mm
Number of Passes	5
Nozzle Traverse Velocity	15 mm/s
Powder Feeder Wheel	320 Small Wheel
Powder Feeder Gas Rate	30 SCFH
Powder Feeder Rate	11.25 g/min

In total, seven SODs have been tested ranging between 10 mm and 40 mm. Figure 5.13 shows the average thicknesses obtained at different SODs.

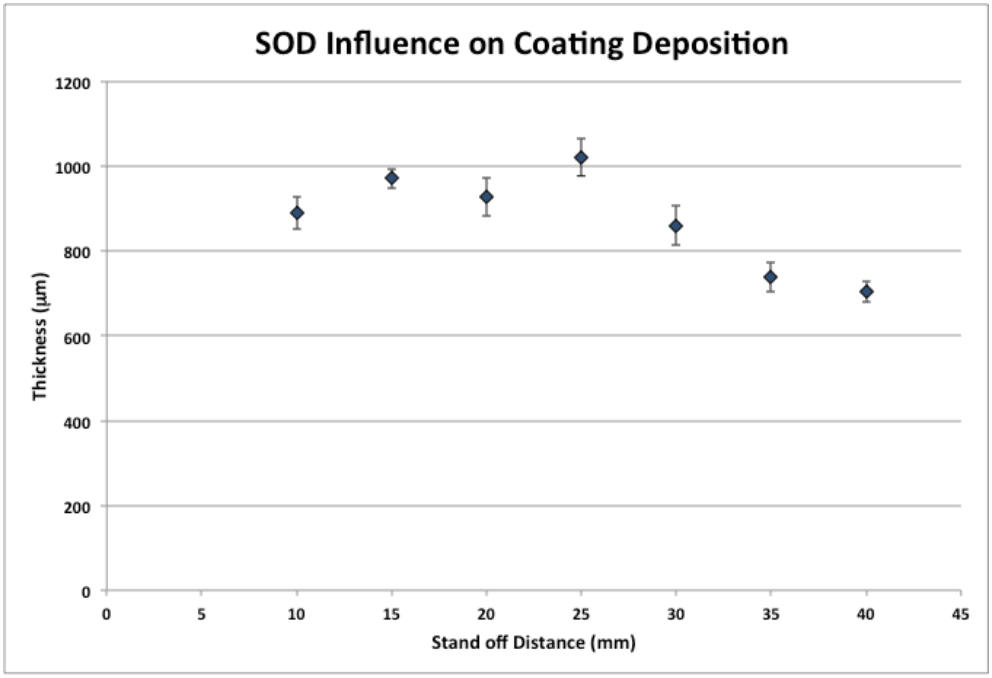

Figure 5.13: Influence of the standoff distance on the Al2024 coating thickness.

Based on the results, the highest deposition is obtained for standoff distances ranging between 15 mm to 25 mm. As stated in section 2.3.7.4, for small standoff distances (<15 mm), the bow shock generated at the substrate surface deviates the particles trajectory and lowers their impact velocity. For large standoff distances (>25 mm), the particles flow is affected by the low gas velocity and negative drag force produced by the ambient atmosphere, which decrease the particles velocity at impact. However, despite the influence of the standoff distance on the deposition efficiency, all deposited coatings were still dense as shown in Figure 5.16 for standoff distances of 10 mm, 20 mm and 40 mm. Needless to say that sufficient particle deformation and stacking was achieved through the impingement effect of subsequent deposited and non-deposited particles for 25 mm<SOD< 15 mm. To accommodate for the repair thickness and to avoid obtaining SODs lower than 15 mm during the dimensional restoration process, a SOD of 25 mm was estimated appropriate for this work.

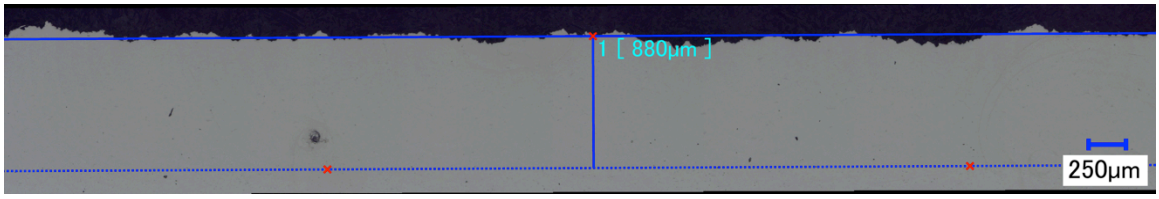

Figure 5.14: Al2024 coating deposited at a standoff distance of 10 mm

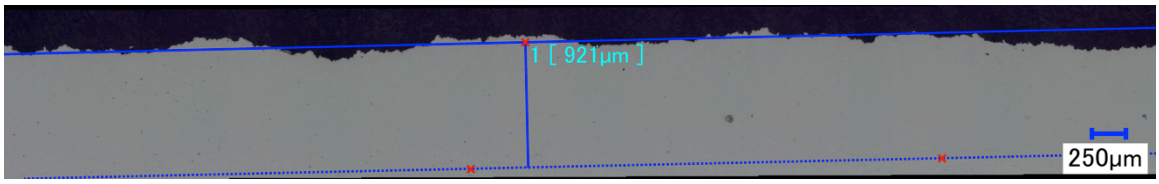

Figure 5.15: Al2024 coating deposited at a standoff distance of 20 mm.

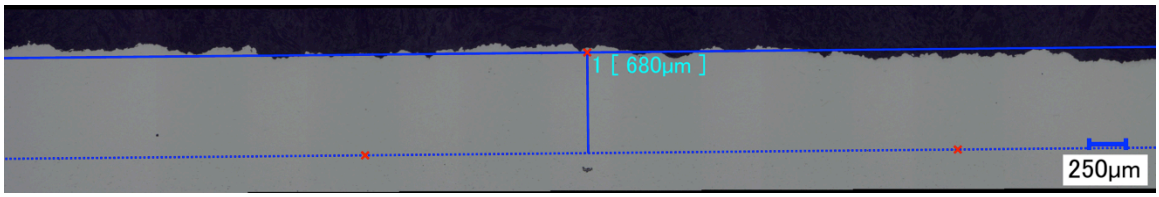

Figure 5.16: Al2024 coating deposited at a standoff distance of 40 mm.

5.1.4. Influence of Powder Feeding Rate and Nozzle Traverse Velocity

In order to reduce the repair time, the CGDS parameters must be adjusted to produce the highest deposition rate of the powder material. In this subsection, the powder feeding rate influence on coating quality and growth is analyzed. The relation between different nozzle traverse velocities is also investigated.

Figure 5.17 depicts the obtained average coating thicknesses for feeding rates varying from 5 g/min to 17 g/min and for two nozzle velocities (15 mm/s and 50 mm/s). These two nozzle traverse speeds have been chosen arbitrarily to provide a preliminary understanding on the influence of nozzle velocity on coating growth process. The other parameters that were kept constant are the same as in Table 5.3.

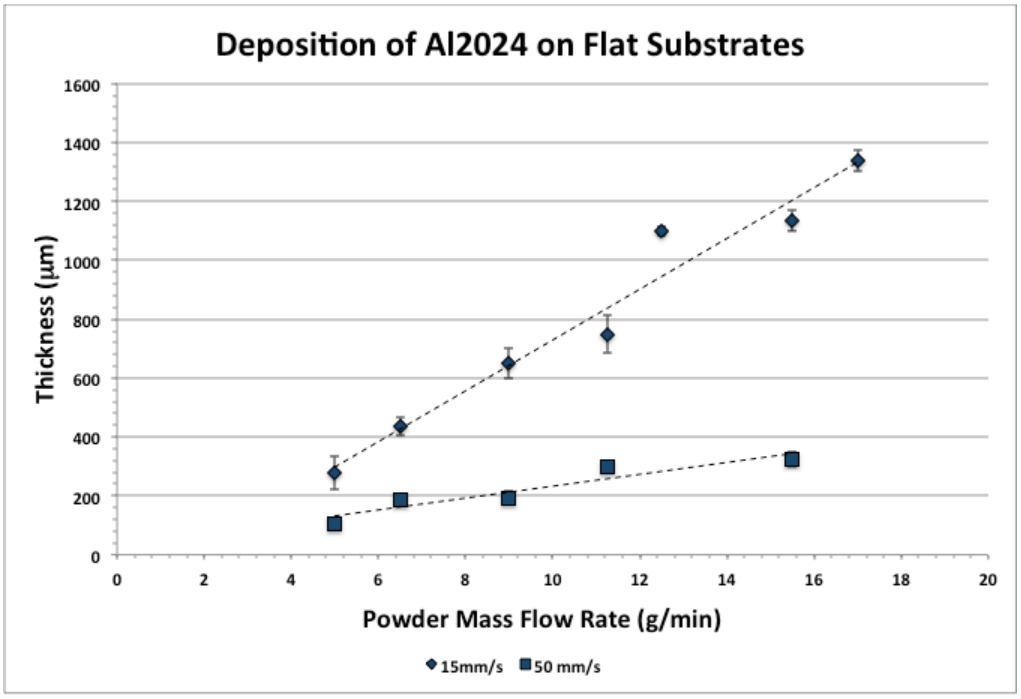

Figure 5.17: Influence of the nozzle traverse speed and powder feeding rate on the deposition of Al2024 powder. Different slopes are obtained for different nozzle traverse speeds, which indicates that the nozzle velocity influences the coating growth process.

Based on the obtained results, higher feeding rates linearly increase the number of deposited particles. As expected, for the same mass feeding rate, the coating thickness varies with

the nozzle traverse speed. Lower traverse speeds enable larger amount of particles to hit the substrate surface per unit area. Based on that statement, at 50 mm/s, 3.33 times less particles should hit the surface per unit area than at 15 mm/s. However, the results show that at a nozzle speed of 15 mm/s, the coating thickness is inferior to 3.33 times the coatings produced at 15 mm/s for all mass feeding rates exclusively lower than 15.5 g/min as shown in Figure 5.18. The overall heat input from the hot gas flow to the substrate/coating increases with decreasing nozzle speeds.

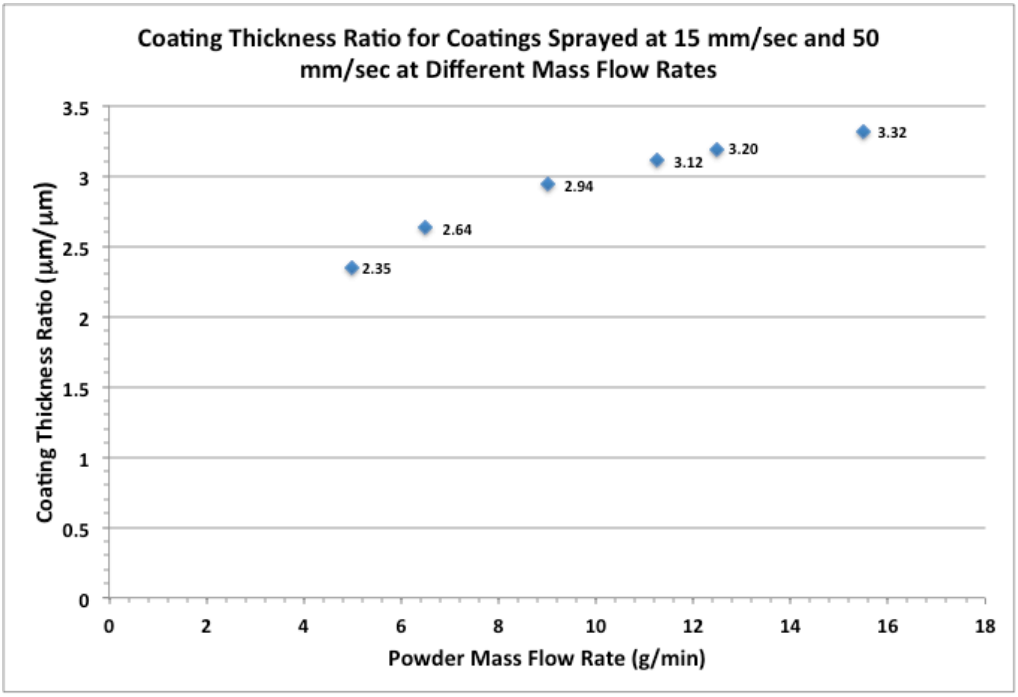

Figure 5.18: Ratio of coatings thickness sprayed at 15 mm/s and 50 mm/s at different mass feeding rates.

At a nozzle speed of 50 mm/s, the coatings thickness appears to slowly increase with the powder mass flow rate and as a consequence, feeding double the powder mass does not constantly double the coating thickness. One of the main differences when spraying at high and low gun velocities is the achieved substrate/deposited coating surface temperature. The substrate temperature mainly affects the coating first layer adhesion but its effect on coating growth process may also be influenced through the heat exchange experienced between the substrate and coating. Moreover, the coating heat input from the subsequently deposited CS material layers also influence the overall coating and substrate temperature. At lower gun speeds and consequently lager heat inputs, the embedment and deposition of subsequent particles is facilitated due to the

softening process. Thus, the nozzle speed of 50 mm/s might be too fast to heat the substrate surface to temperatures high enough to influence the coating growth.

The effect of nozzle traverse speed on the particle velocity is believed to be limited as the particles achieve a great amount of kinetic energy before impact. It is highly unlikely that the nozzle velocity of 50 mm/s can affect particles velocities that are more than a magnitude larger at approximately 600 m/s.

Once again, all coatings produced during these tests were dense as shown in Figure 5.19 and Figure 5.20 for a nozzle traverse speed of 15 mm/s and 50 mm/s respectively at different mass feeding rates.

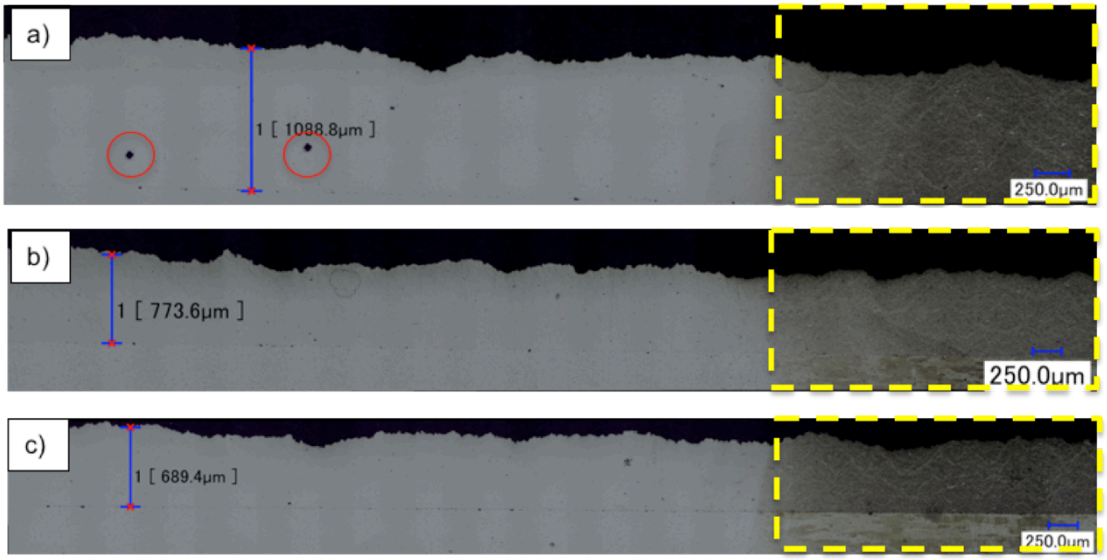

Figure 5.19: Cold sprayed coating of Al2024 on Al2024 substrate at 500 °C and 3.45 MPa at a feeding rate of a) 15.5 g/min b) 11.25 g/min and c) 9 g/min and a traverse speed of 15 mm/s. The yellow sections of the coating have been etched and the red circles are Vickers indentations.

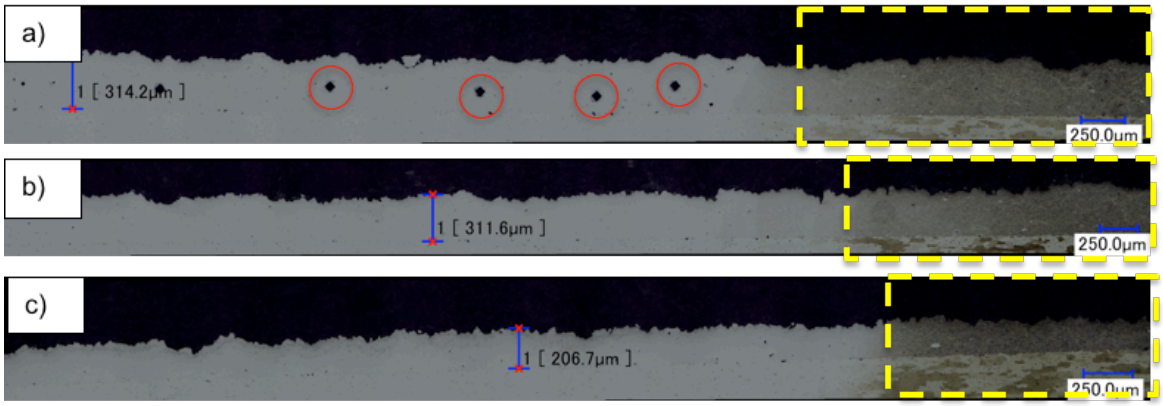

Figure 5.20: : Cold sprayed coating of Al2024 on Al2024 substrate at 500 °C and 3.45 MPa at a feeding rate of a) 15g/min b) 11.25 g/min and c) 9 g/min and a traverse speed of 50 mm/s. The yellow sections of the coating have been etched and the red circles are Vickers indentations locations.

Following was the investigation of the powder feeding rate effect on the coating hardness for the coatings obtained using a 15 mm/s nozzle traverse speed. Coatings obtained at 50 mm/s were too thin for hardness measurements, based on the ASTM E92-82R03 standard requirements. $HV_{0.3}$ measurements were taken approximately in the center of the coating cross-section and the results are shown in Figure 5.21. At least five microhardness readings have been taken for each sample to obtain an average value and standard deviation.

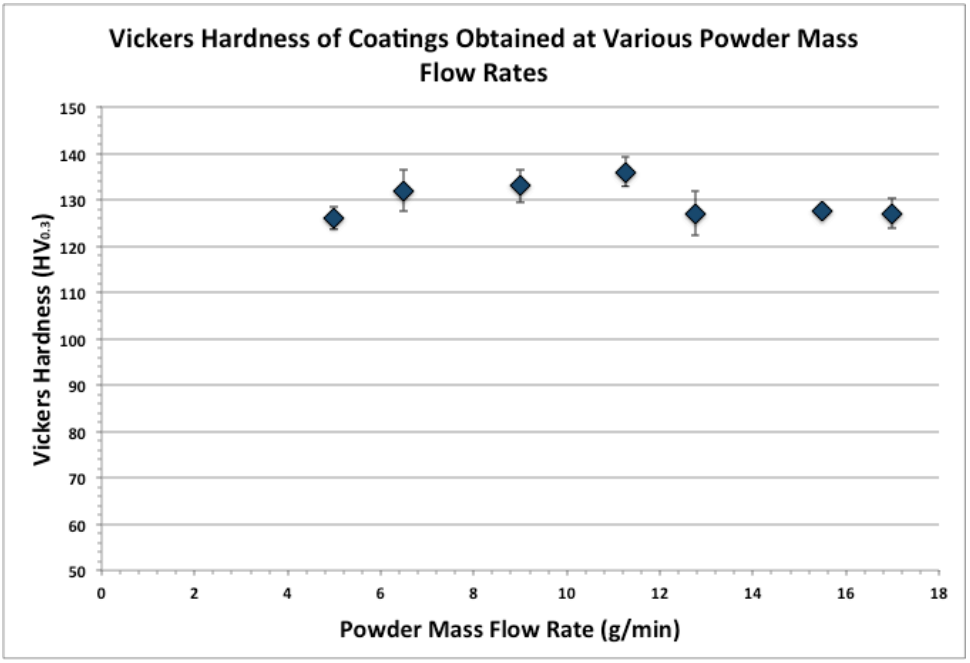

Figure 5.21: Al2024 coating microhardness based on the powder feeding rate.

For feeding rates ranging between 5 g/min and 11.25 g/min, the microhardness slightly increases from an average of 126 ± 2.39 $HV_{0.3}$ to 136 ± 2.24 $HV_{0.3}$. A larger powder feeding rate increases the level of impingement the coating sustains. Therefore, as the mass loading rate is increased so is the peening effect on the coating and resulting hardness. However, based on the obtained results, increasing the mass flow rate over 11.25 g/min results in lower coating hardness. A possible explanation is that at high powder mass flow rates, the gas flow must accelerate a larger mass. As a consequent result, lower particle velocities are reached when the gas flow is saturated with powder [134]. The final particle velocities are large enough to generate deposition but insufficient to provide proper strain hardening to the deposited particles.

5.1.5. Hardness Progression Through Coating Thickness

Figure 5.22 shows the reduction in hardness, at the substrate/coating interface, with progressive coating thickness growth. Thicker coatings have been obtained by increasing the number of passes for the same 11.25 g/min powder feeding rate. A. Moridi et al. [79] have reported that for the same coating thickness, the number of passes has very low influence on the coating inherent properties.

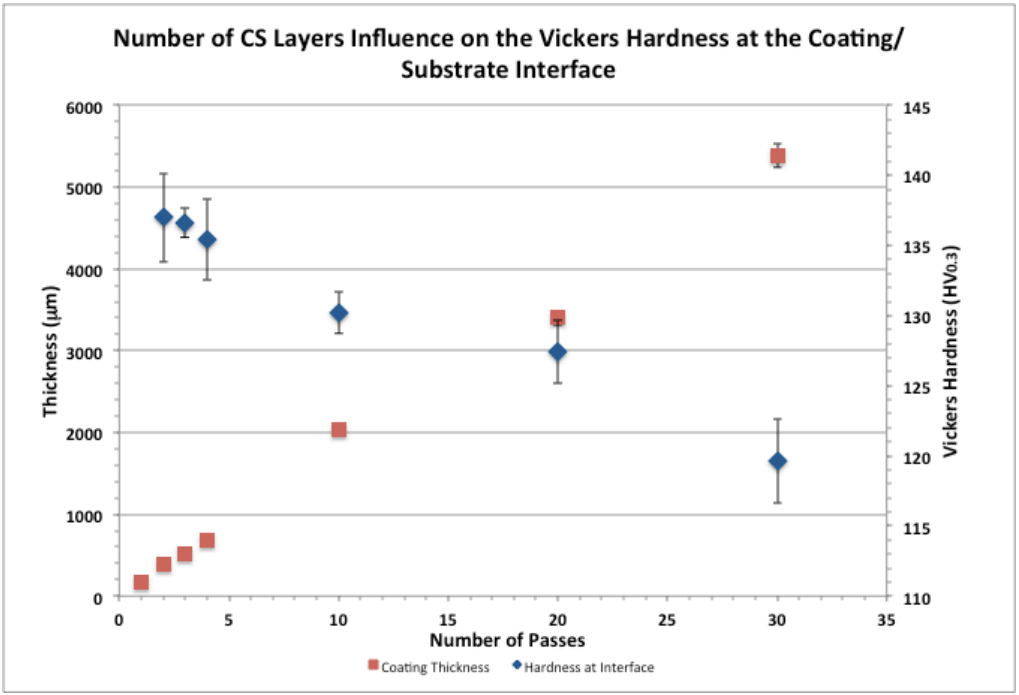

Figure 5.22: Influence of coating thickness on the interface microhardness.

The above analysis underlines the importance of the influence of number of passes on the annealing processes at the coating/substrate interface. The microhardness at the interface decreases from 137 ± 3.16 $HV_{0.3}$ to 119.6 ± 3.00 $HV_{0.3}$ for coatings produced using 2 passes (thickness of 389 ± 35.88 μm) and 30 passes (thickness of 5382.61 ± 141.38 μm) respectively. As longer spraying times are needed to produce thicker coatings, the coating heat input from the hot gas stream increases with coating thickness. The thermal input could induce various annealing conditions, which can partially eliminate cold working coating structure and properties. Recovery annealing in aluminum alloys material can be detected at temperatures as low as 90 °C to 120 °C. Softening of the material is achieved through the decrease in dislocation density initially introduced in the coating by the cold working process and consequently less plastic work is needed for the particle deformation process. Moreover, if thermal softening influence on particle properties is more important than the induced cold working effects, the plastic strain proceeds as the plastic flow stresses become steady and no longer increase. Various annealing processes can be introduced in the coating as their occurrence and influence is dependent on time and temperature. Thus, longer spraying times increase the annealing effect and decrease the material hardness.

Figure 5.23 presents the evolution of microhardness across the 5382 μm coating thickness. At least five measurements have been produced at each analyzed region.

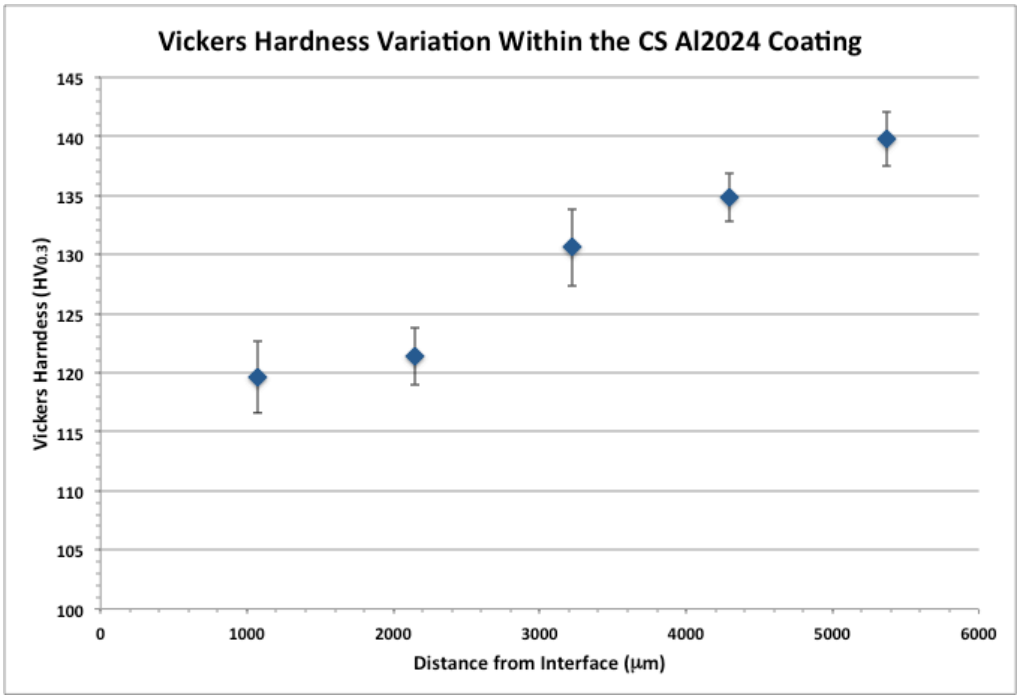

Figure 5.23: Stress relaxation and coating thickness influence on the evolution of coating microhardness.

High plastic deformation along with enhanced peening effects is expected to increase the hardness of the coating lower layers. However, despite the tamping effects, the coating hardness seems to be highly influenced by the coating thickness. The cold hardening (i.e. strain hardening or work hardening) increases the dislocation density in the coating through particle plastic deformation, which decreases the distance between dislocations and impedes their relative motion. After the cold spray process is completed, the dislocation strain field and the grain distortion level obtained through plastic deformation are retained [144], [145]. As a consequence, the microhardness of the material is expected to increase as the material resistance to plastic deformation is increased. However, as high spraying temperatures can initiate stress relief in the material, the cold hardening induced internal strain energy can be released and the ductility enhanced. Based on the measurements presented above, the microhardness increases from 120 ±3.0 $HV_{0.3}$ to 140 ± 2.3 $HV_{0.3}$ at 1789 μm and 5368 μm from the coating/substrate interface respectively.

As previously stated, the compressive residual stresses near the interface decrease with coating thickness. The compressive residual stress influence the deformation process such that it might also obstruct the penetration of the microhardness indenter by limiting the coating plastic

deformation and applied effective stress. As a consequence, larger microhardness values might be related to larger compressive residual stresses. However, the sensitivity of the microindentation process to stress and the relation between the involved mechanisms needs to be further studied in order to accurately state any dependency and correlation between the two global material properties.

Moreover, the compressive residual stress at the interface affects the coating final adhesion strength. Depending on the nature and degree of the bonding, the reduction in interface stress relaxation can be beneficial or destructive to the adhesion strength of thick coatings. If the particles are mechanically anchored into the substrate surface, the decrease in stress may loosen and relax the connections, which would lower the coating adhesion. However, if the bond is also metallurgical, a decrease in compressive stress will decrease the coating buckling and delamination tendency, which would result in an increase in adhesion strength.

In conclusion, a powder feeding rate of 11.25 g/min will be used in this research to produce the required repairs. This mass flow rate ensures suitable particle deposition, avoids obstructing and oversaturating the gas stream and has no apparent undesirable influence on the coating microstructure.

5.1.6. Reverse Indentation Size Effect (RISE) in CGDS Coatings

This subsection evaluates the suitability of using a 0.3 kg to evaluate the hardness of cold gas dynamic sprayed aluminum alloy coatings. Figure 5.24 shows the obtained hardness values approximately at the center of the coating for indentations loads of 0.01 kg, 0.025 kg, 0.05 kg, 0.1 kg, 0.2 kg, 0.3 kg, 0.5 kg and 1 kg. At least five indentations have been produced at each load and all measurements have been made through the 3D digital microscope for increased precision.

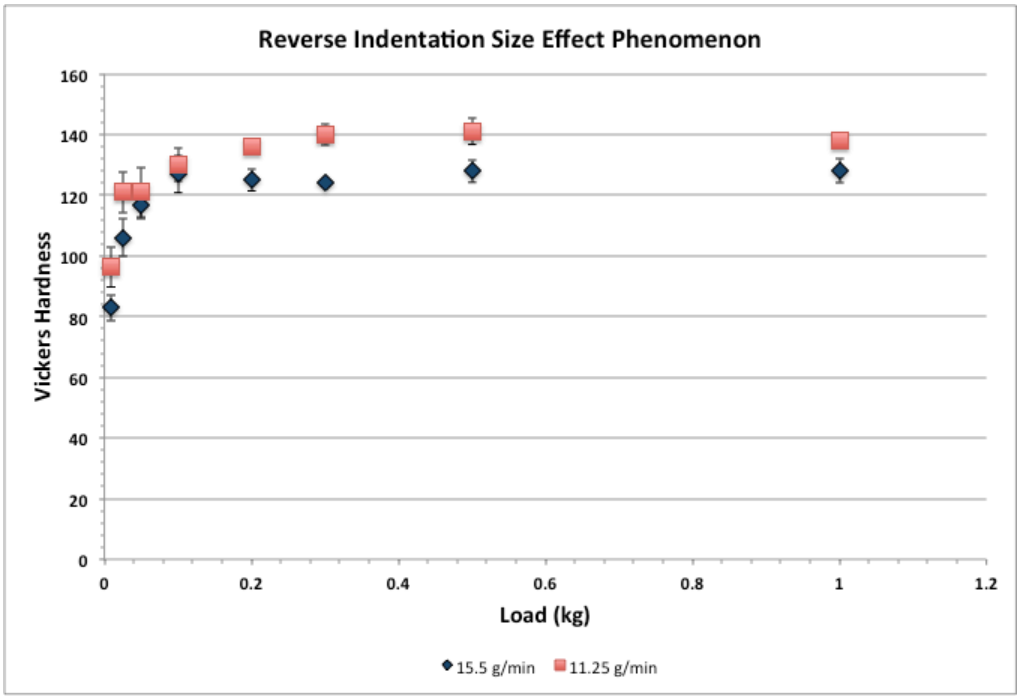

Figure 5.24: Indentation load effect on coating microhardness measurements.

The hardness value increases from 82.9 ± 4.23 $HV_{0.01}$ to a load independent hardness value of 125 ± 0.89 $HV_{0.3}$ for coatings sprayed with a powder feeding rate of 15.5 g/min. A similar trend is seen for the coating sprayed at 11.25 g/min, where the hardness increases from 96.4 ± 6.64 $HV_{0.01}$ before it plateaus to 140 ±3.44 $HV_{0.3}$. The load dependency of the hardness value, as shown in the previous figure, is commonly referred to as the reversed indentation size effect (RISE) phenomenon [146]–[151]. The RISE is dependent on the material response to deformation and yielding. The nucleation and multiplication process of the dislocation system inside the coating also affects the residual plastic contact impression size. The strain-hardened state of the cold sprayed deposits can significantly influence the apparent hardness at low loads. The level of elastic recovery, material yielding continuity and uniformity, plastic zone evolution, strain gradients, cracking and friction contributions (between indenter and coating surface) can affect the effective indentation energy and induce RISE. As the size and depth of the indention is reduced at low loads, the porosity and defect content can significantly affect the apparent hardness at low penetrating stresses. Needless to say that the influence of the interaction and bonding between the particles on the indentation size is amplified at low indentation loads. Other causes that are not related to material properties can induce RISE such as, coating cross section roughness and vibration of the equipment [151].

This test provides evidence that a minimal mass of 0.3 kg must be used in order to obtain a hardness reading that is representative of the coating structure.

5.2 Development of Pure Aluminum Coatings on Al6061-T6 Substrates

To produce proper and efficient deposition for the repair process of aluminum components, high spraying parameters have been analysed as they facilitate and enhance the particle deposition process [81], [109], [152], [153] by increasing particle temperature and velocity. The obtained coatings have been examined in terms of structure, microstructure and hardness to evaluate their suitability for the repair process. Subsequently, the powder feeding rate has been varied to ensure high quality of the coating.

The influence of the process pressure, temperature and powder feeding rate alone on the coating quality and deposition efficiency has been studied by holding all other parameters constant. The specific coatings were produced on small 25.4 mm by 19.05 mm Al6061-T6 coupons. The substrate surface preparation procedure was the same for all produced coatings and is presented in Table 5.4. The resulting substrate surface roughness was 2.04 ± 0.38 μm.

Table 5.4: Substrate Surface Preparation Procedure for the Development of Pure Aluminum Coatings on Al6061-T6 Substrates

Parameters	Values
Abrasive	Aluminum Oxide
Size	80 Mesh
Process Gas	Compressed Air
Pressure	80 psi
Grit Blasting Angle	45°
Standoff Distance	51 mm
Post Treatment	Acetone (Ultrasonic bath)

The powder mass flow rate (g/min) was calculated for different powder feeding wheel speeds. The powder mass was measured before the nozzle inlet for a feeding time of 2 minutes. A small 320 holes wheel and a 30 SCFH feeder gas flow rate were used to perform the test. Figure

5.25 presents the obtained results and shows that the mass flow rate is approximately equal to the powder feeding wheel speed.

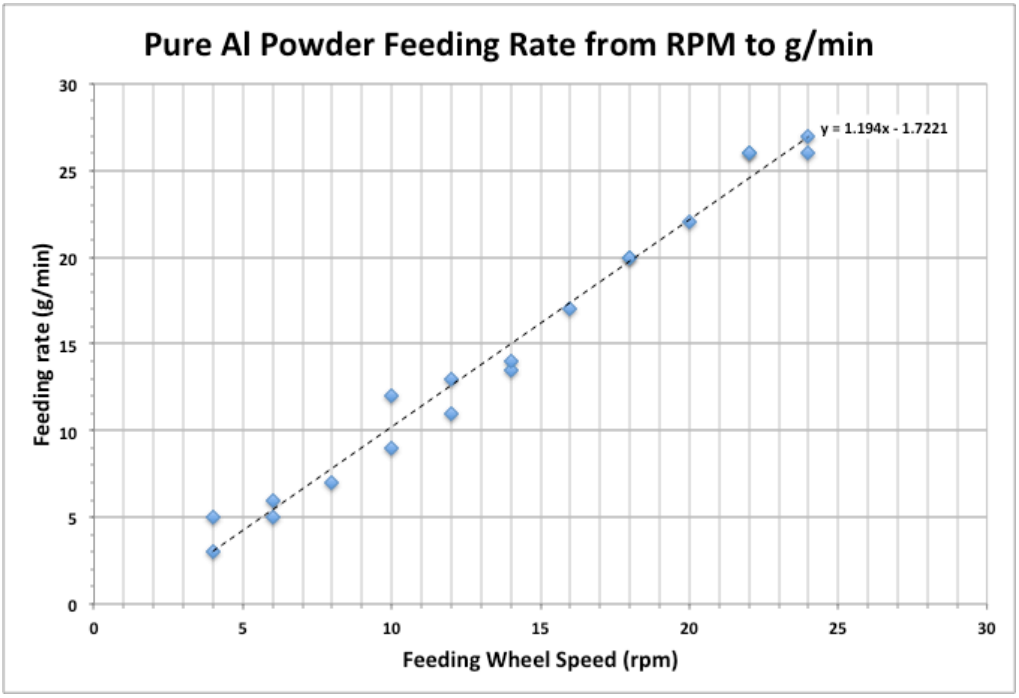

Figure 5.25: Powder feeding rates using the pure aluminum powder.

5.2.1. Influence of Pressure and Temperature on Coating Quality

Preliminary sprays have been produced on small Al6061-T6 coupons. As the pressure and temperature are known to be the most significant processing parameters, their influence on the coating quality has been examined through the coating thickness, roughness, porosity and Vickers hardness. The CGDS parameters that were kept constant during these tests are shown in Table 5.5.

Table 5.5: CGDS Parameters Held Constant During the Initial Development of Pure Aluminum Deposition Ability Matrix

Parameters	Values
Nozzle Type	Polymer
Increment Size	2 mm
Number of Passes	5
Nozzle Traverse Velocity	15 mm/s
Powder Feeder Wheel	320 Small Wheel
Powder Feeder Gas Rate	30 SCFH
Powder Feeder Rate	4 g/min
Standoff Distance	25 mm

Figure 5.26 shows the coating average thickness obtained for different combinations of high gas process pressures and temperatures. Standard variation of the coating thickness has not been included in the figure below as the coating roughness values will be given subsequently.

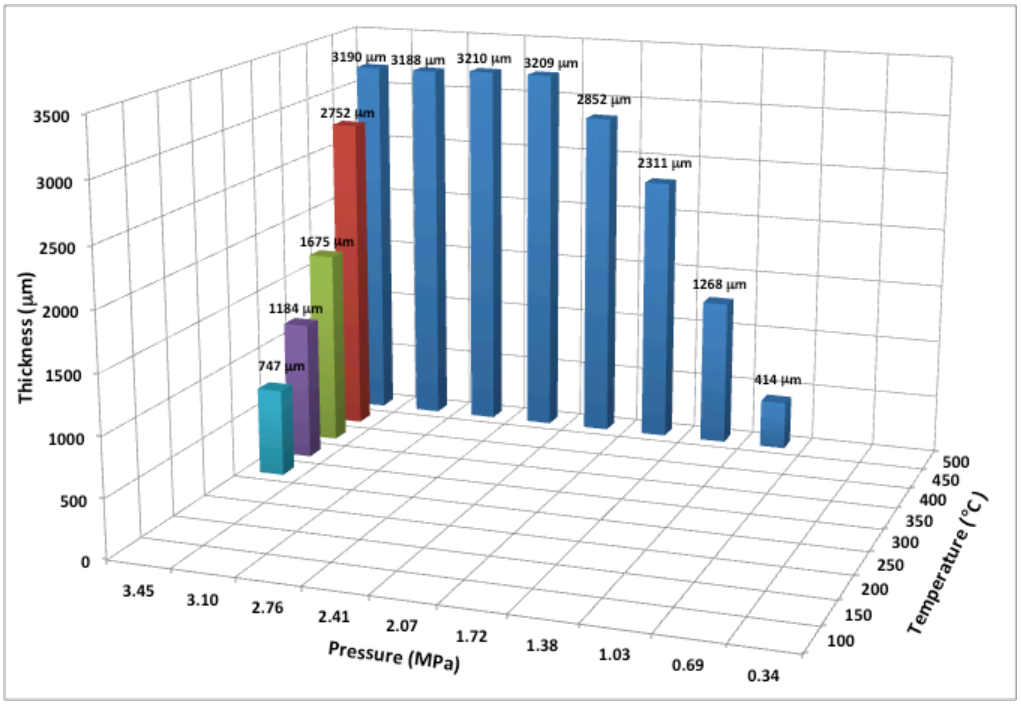

Figure 5.26: Pure aluminum coating thickness based on the process temperature and pressure. Obtained thickness values are shown above each corresponding combination of parameters.

Similarly as in the Al2024 tests, an increase in pressure or temperature has the effect of increasing the particle deposition efficiency. However, when reaching a pressure of 2.07 MPa at 500 °C, the coating thickness remains constant for any further increase in pressure up to 3.45 MPa. This indicates that between 2.07 MPa and 3.45 MPa the supplementary increase in drag force and particle kinetic energy is not primarily used to deposit additional particles. An increase in pressure from 2.41 MPa to 3.45 MPa at 500 °C increases the coating thickness by approximately 19 μm. When increasing the temperature from 300 °C to 500 °C at 3.45 MPa, the coating thickness gradually increases without reaching a plateau. An increase in temperature from 350 °C to 500 °C increases the coating thickness by 2 mm. An increase in the main gas temperature leads to an increase of the pure aluminum particles velocity, which enhances their energy at impact and subsequently the deposition process. An increase in particle acceleration permits large particles to achieve the critical velocity necessary for particle deposition. It can be seen that maximal deposition efficiency is achieved at 500 °C and 2.41 MPa. An increase in gas temperature concomitantly increases the particle temperature, which can soften the aluminum particles and improve their deposition efficiency by facilitating the plastic deformation process. Severe plastic deformation enhanced by the adiabatic shear effects leads to higher strains and ultimately to increased formation of metallic jetting and proper oxide layer removal.

Figure 5.27 shows the effect of the process parameters on the coating porosity. It is seen from the results shown below, that the coating porosity slightly increases from 1.70 ± 0.25% to 3.27 ± 0.45% as the process temperature increases from 300 °C to 500 °C at 3.45 MPa. This seems to be counterintuitive based on the fact that higher particle velocity and deformation are obtained at higher temperatures. However, the particles with insufficient energy to properly deform gain sufficient energy to deposit rather than to rebound, which leads to an increase in voids between adjacent particles. At low gas pressures, the coating porosity is low due to the accumulative deformation resulting from the repeating impingement of non-deposited low velocity particles. As the pressure increases up to 2.41 MPa, the coating porosity reaches 7.98 ± 1.05% with an increase in coating thickness and poorly deformed particles. Further increase in pressure results in a decrease in coating porosity. As noted previously, a further increase in pressure from 2.41 MPa leads to no increase in coating thickness, which indicates that the supplementary increase in drag force enables higher particle deformation leading to proper particle stacking and decrease in voids.

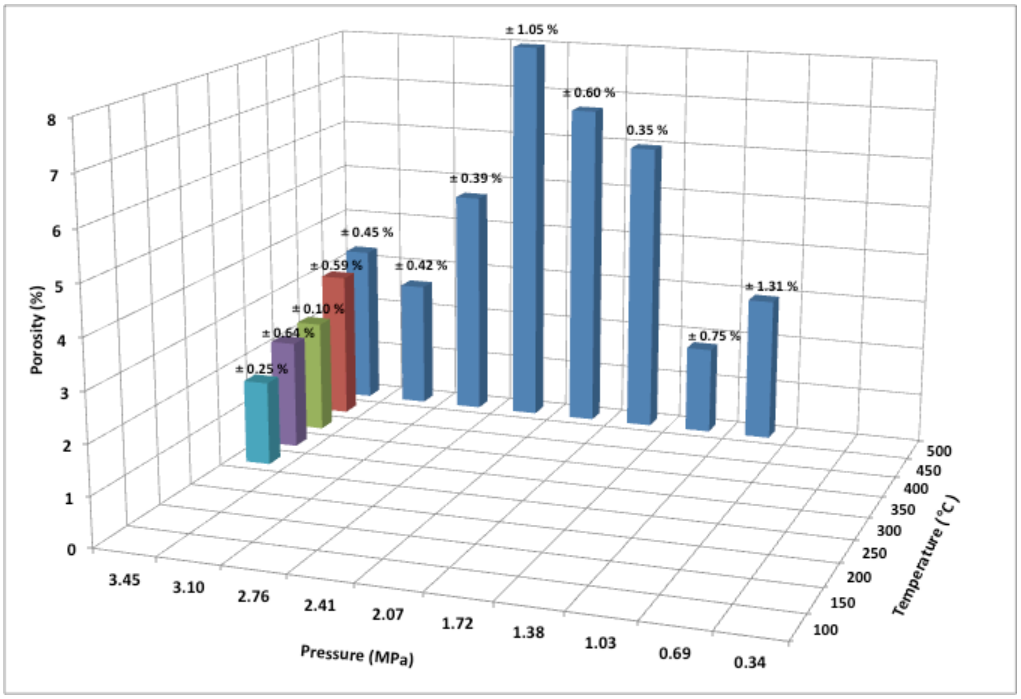

Figure 5.27: Pure aluminum coating porosity based on the process temperature and pressure. Standard deviation values are given above each result.

Figure 5.28 shows the resulting coating surface roughness obtained when sprayed at high pressures and temperatures. The CGDS coating surface profile measurements were taken parallel and perpendicular to the gun travel direction. The coating roughness gradually decreases from 31.34 ± 3.27 μm and 23.43 ± 2.49 μm to 14.05 ± 1.14 μm with increasing gas pressure and temperature respectively. At low process parameters, the particles stored energy is sufficient to produce proper deposition of only a limited number of particles (i.e small diameter particles) but insufficient to allow proper large particle deformation, which leads to high surface roughness. Additionally, the non-deposited particles tend to deform the coating surface, which can either flatten or roughen the coating surface profile depending on the impingement homogeneity across the coating surface. Increasing the powder deposition efficiency increases the coating roughness as more particles are being deposited but the level of particle deformation and stacking process contributes in decreasing the surface profile.

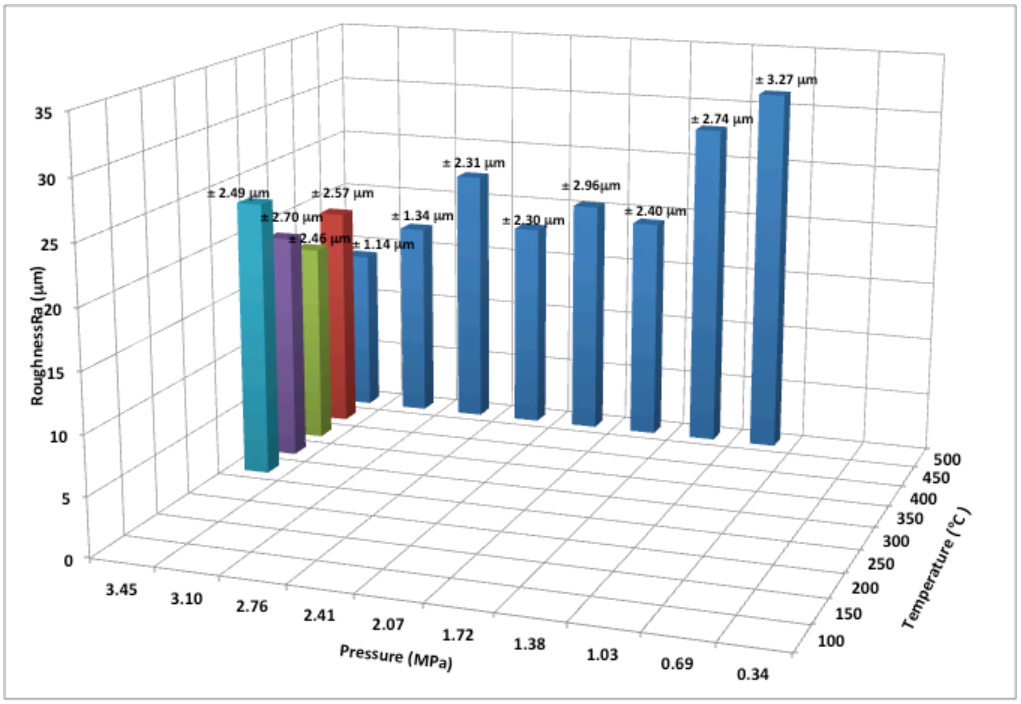

Figure 5.28:Pure aluminum coating roughness based on the process temperature and pressure. Standard deviation values are given above each result.

Coatings with low deposition efficiencies exhibit large surface roughness as depicted in Figure 5.29 due to the large peening effects.

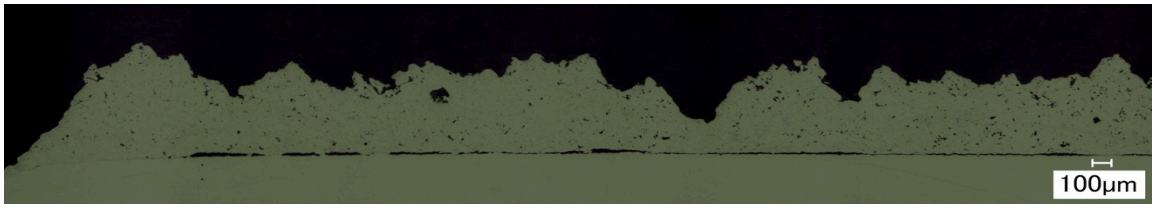

Figure 5.29: Coating obtained at 500 °C and 1.03 MPa.

Vickers microhardness tests were performed on polished cross sections. Figure 5.30 shows the hardness of the pure aluminum coatings obtained using high spraying parameters.

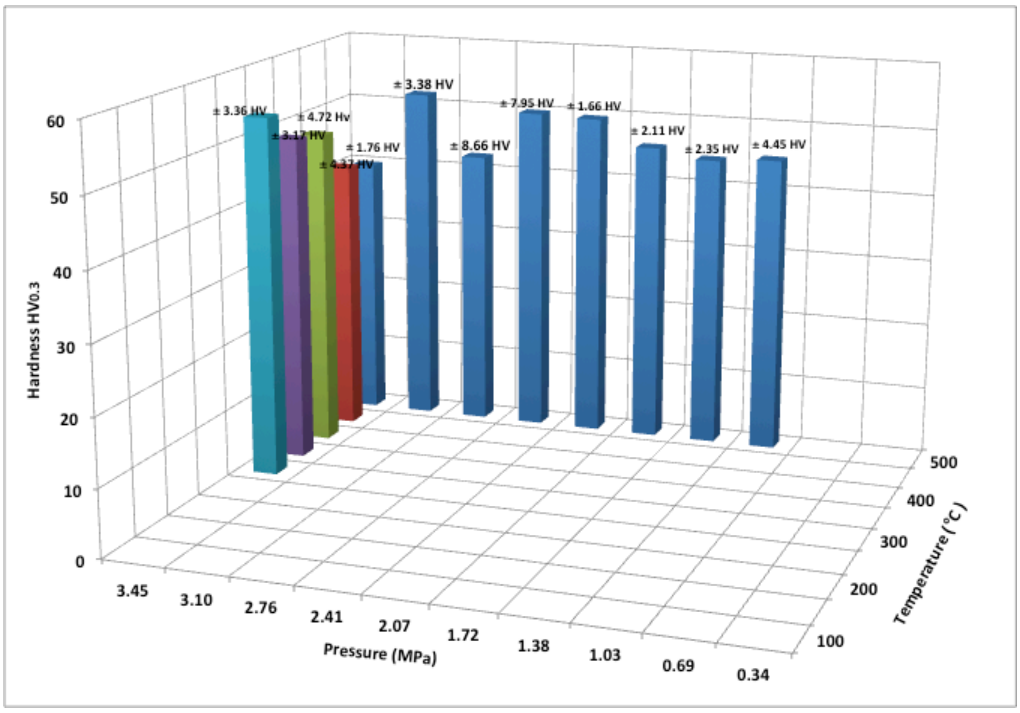

Figure 5.30: Pure aluminum coating Vickers hardness ($HV_{0.3}$) based on the process temperature and pressure. Standard deviation values are given above each result.

The hardness of the coating sprayed at maximal parameters is 39.78 ±1.76 $HV_{0.3}$, which also corresponds to the lowest obtained hardness. As noted in the Al2024 tests, at high gas temperatures, the coating may undergo a stress annealing process and the particles can experience thermal softening, which can lower the coating hardness. Low inter-particle bonding and limited particle deformation can decrease the coating hardness. A cold sprayed coating exhibiting low hardness can show high ductility, which would limit its brittleness and increase its formability. At the lowest accelerating gas pressure and temperature the coating hardness is of 44.94 ± 4.45 $HV_{0.3}$ and 53.78 ± 3.36 $HV_{0.3}$ respectively. Despite the high coating porosity, a relatively high hardness is obtained due to the presence of strong impingement effect and particle deformation.

The level of influence of the particle deposition, deformation and impingement on the properties presented previously is only qualitatively defined in this study, such that further research is needed to precisely understand the contribution of each of these mechanisms on the specific coating properties.

5.2.2. Parameter Selection for Pure Aluminum

A gas temperature and pressure of 500 °C and 3.45 MPa respectively have been chosen to produce pure aluminum repairs. At elevated parameters, high powder deposition efficiency and low coating surface roughness are obtained, which will reduce the repair time and limit additional spraying as to account for surface unevenness. Low coating hardness and increased coating ductility and softness are expected to improve repair machinability.

5.2.3. Effect of Powder Feeding Rate on Coating Quality

This section presents the influence of the powder feeding rate on the microstructural properties and porosity content of pure aluminum coatings. Parameters presented in Table 5.5 along with feeding rates varying from 4 g/min to 13.75 g/min have been used. Moreover, different numbers of passes have been used for each analyzed powder feeding rate in order to produce coatings with thicknesses larger than 3 mm. As such, proper estimation of the thick repair properties will be made and the influence of coating thickness on the resulting microstructure will be evaluated.

Table 5.6 presents the number of passes and coating thicknesses obtained using different powder feeding rates. As expected, the number of passes required to achieve the necessary thickness increases with decreasing powder feeding rates. Delamination at the coating/substrate boundary has not been observed in any of the sprayed material despite the large thickness of the deposited coatings. The probability of coating delamination through buckling increases with increasing coating thickness due to the development of high compressive residual stresses. However, longer spray times have led to increased heat input from the hot gas stream, which might have lowered the residual stress at the interface through a stress relief annealing process [79].

Table 5.6: Pure aluminum powder feeding rates, number of passes and resulting coating thicknesses

Feeding Rate	Number of Passes	Coating Thickness
13.75 g/min	4	4720 ± 33.95 µm
12 g/min	8	5425 ± 55.92 µm
10.5 g/min	8	4740 ± 37.08 µm
7 g/min	9	4237 ± 40.07 µm
5.5 g/min	10	3480 ± 44.91 µm
4 g/min	16	3810 ± 48.27 µm

Figure 5.31 depicts the microstructure across the thickness of the coating sprayed at 13.75 g/min. Only four passes were necessary to reach a thickness of 4.7 mm but a high amount of porosity was detected across the entire coating. The thickness of each deposited layer is seen to increase with coating thickness to the exception of the last layer.

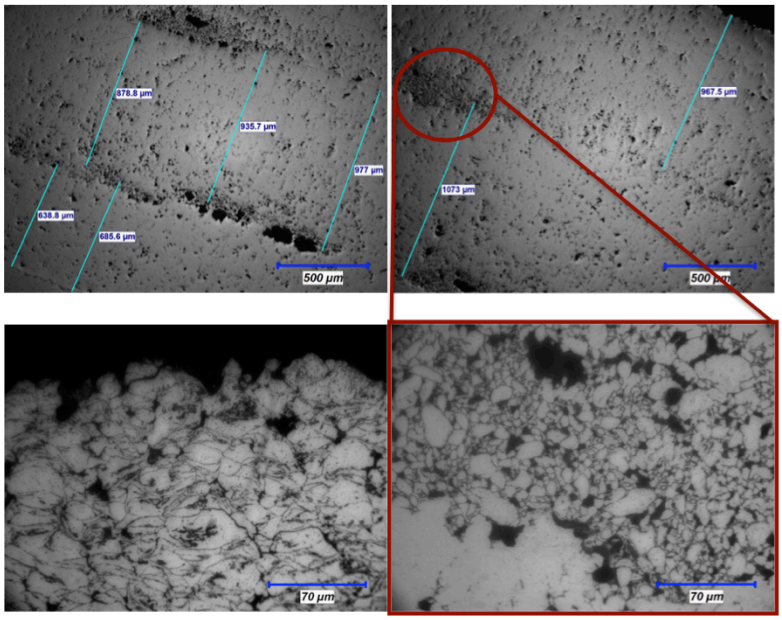

Figure 5.31: Microstructure of coating sprayed at maximal spraying parameters and 13.75 g/min feeding rate. Etched cross-section shows the intensity of particle deformation.

Discontinuity and inconsistency in deposition and particle deformation are observable between each deposited layer. From the previous figure, it is evident that particles at the interfaces between layers lack in deformation, such that the porosity content at those locations is

the highest. This phenomenon is however not observable at the coating/substrate interface or top coating layer. Four possible explanations are used to justify the preferential occurrence of the sticking phenomenon and lack of particle deformation. The first reason is that the difference in elasticity (softness) between the pure aluminum particles and Al7075-T6 substrate unavoidably forces the soft particles to highly deform upon impact with the substrate, which makes it difficult to distinguish the presence of sticking as particle deformation is enhanced. Secondly, the thin oxide layer that surrounds the individual particles is removed during their high velocity impact with the substrate. The additional deformation and jetting of the particles results in increasing the particle surface area, which forces the oxide layer to crack exposing a larger free-oxide metal surface. As such, the subsequent deposition of particles is either made on an oxide free coating surface or on a newly grown weak thin oxide layer (i.e grown in a rich nitrogen stream). For the latter case, the oxide layer is believed to be easily disrupted during the high particle impact such that the deposition and bonding is considered unaffected. Sticking of singular interacting particles is enhanced as the metallurgical bonding process is facilitated in a true metal-to-metal contact situation. Pure metal-to-metal contact along with the presence of sufficient pressure and close contact enhances the electrostatic attractive forces between electrons and merges the atomic lattices at the surface. Consequently, the electrons at the interface are shared between different particles and a metallic bond is created similarly as in a cladding process. Thirdly, temperature differences and heat transfer between the involved surfaces plays a major role in the particle deformation process. Impacting a cold substrate surface or a hot coating affects the particle deposition and adherence process. Lastly, the occurrence of sticking (i.e. particle deposition characterized by low deformation) increases with increasing powder mass flow rate, as seen in the obtained coatings shown in Figure 5.31 and Figure 5.32. Larger mass flow rates require more energy to be accelerated, which consequently lowers the individual particle velocity. Sufficient energy for depositing is reached but not for proper deformation. The contribution fraction of each of these processes on the occurrence of sticking between the layers has not been analyzed in this study.

The coating porosity content decreases with decreasing powder mass flow rate and increasing number of CS layers as shown in Figure 5.32. A larger number of deposited layers increase the overall coating heat input and enhances individual particle deformation, which promotes close particle contact. In order to deposit a coating of approximately 3 mm in thickness

and limit the porosity content, a feeding rate of 4 g/min must be used. At higher feeding rates, the deposition per unit area is higher but so is the porosity level.

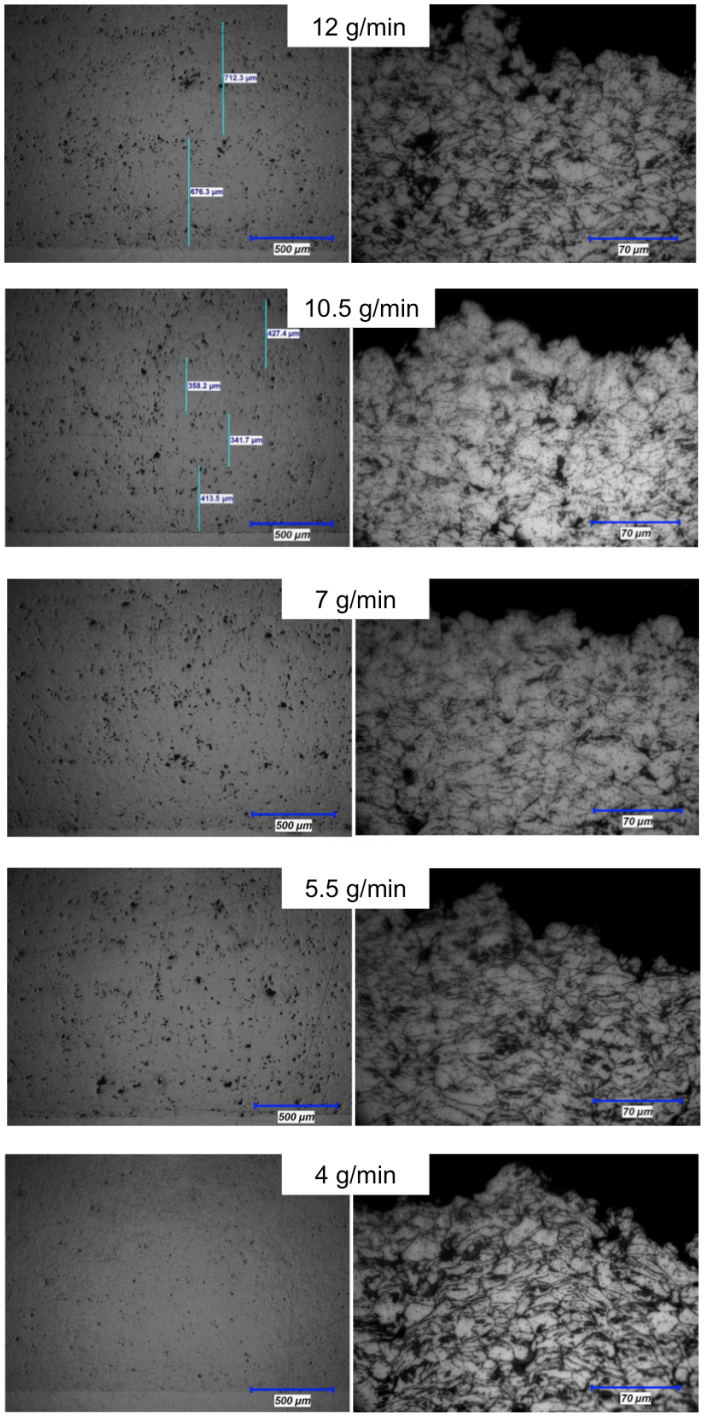

Figure 5.32: Microstructures of coatings sprayed at maximal spraying parameters using different feeding rates. Top coating section have been etched to demonstrate the particle deformation level under impact.

CHAPTER 6

Repair and Restoration of Threads

This chapter will present the repair procedure employed to rebuild pure aluminum threads on Al7075-T6 alloy substrates. The initial threads dimensions found on the Boeing 757 nose landing steering actuator component have been re-machined in the repair. The spraying parameters analyzed in the previous chapter have been used to restore the initial dimensions of the damaged component. The component surface angle influence on the coating properties has been investigated using small scale repairs. Two different nozzle movements relative to the circular substrate surface have been analyzed. These two techniques generate two different kinds of coatings, which have been characterized in terms of porosity and machinability. The restored threads have been tested in torque to characterize their mechanical behaviour and performance. The component surface temperature with and without the use of an air cooling system has been monitored and is presented in this chapter.

Despite exhibiting low deposition efficiencies at high spraying parameters, a single repair of a large component has been produced using Al2024 powder for which the main purpose was to analyze the effect of substrate dimensions and cooling on coating growth process and adhesion. The repair of small threaded components has been performed and their load carrying capacity has been tested through a compression test.

6.1 Repair of Nose Landing Gear Steering Actuator Threads Using Pure Aluminum

The following subsections present the procedure that was taken to restore an entire array of 3.75-12UNJ-3A threads, using pure aluminum powder, on an 88.9 mm diameter aluminum alloy substrate. It also demonstrates the influence of the nozzle travelling speed on the repair properties. The last subsection presents the repair obtained while using an air-cooling system to keep the substrate surface below 93 °C.

6.1.1. Stepped Repair Process

The first material restoration procedure was conducted on a commercial Al6061-T6 substrate. The substrate surface was manually grit blasted using the parameters presented in Table 5.1. After the surface preparation procedure, the component was soaked into an ethanol solution in an ultrasonic bath and subsequently dried using compressed air. The cleaning process removed the excess and loose grits that were trapped within the substrate surface. The spraying parameters used for the dimensional restoration step are shown in Table 6.1. As stated in the table, the nozzle was moved across the machined surface in a stepped manner using a “step time” of 11 to 12 seconds approximately.

Table 6.1: Spraying Parameters Used to Restore 3.75-12UNJ-3A threads using a stepped nozzle motion

Parameters	Values
Gas Nature	Nitrogen
Gas Pressure	3.25 MPa
Gas Temperature	500 °C
Standoff distance	25 mm
Nozzle Type	Polymer
Nozzle Traverse Velocity	50 mm/s
Powder Feeder Wheel	320 Holes Small Wheel
Powder Feeder Gas Rate	30 SCFH
Powder Feeder Rate	4 rpm
Step Time	11 to 12 seconds
Step Size	3 mm
Substrate Angular Velocity	6 rpm

Figure 6.1 illustrates the nozzle movement across the substrate surface and as such describes its stepped motion. The substrate angular velocity was arbitrarily set to 6 rpm. To ensure complete surface coverage of the substrate section under the nozzle, the nozzle had to be held stationary for 11 to 12 seconds. Once the substrate completed a full rotation, the nozzle moved by 3 mm to the adjacent location at a velocity of 50 mm/s. This was repeated until a full size coating was obtained.

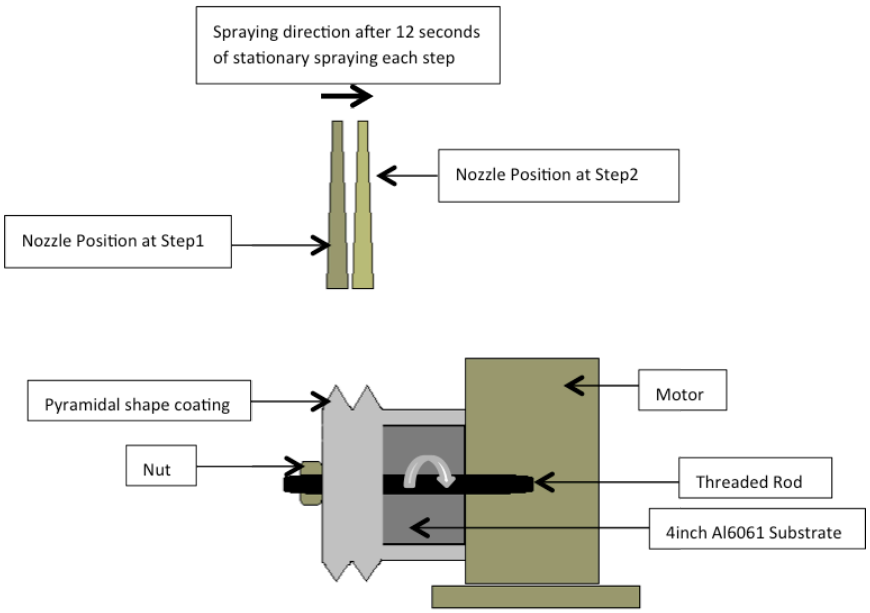

Figure 6.1: Step set-up for the repair of the 88.9 mm diameter Al6061-T6 bars.

Figure 6.2 summarizes the different steps used in the repair of pure aluminum threads, from the surface preparation to the recovery of original threads dimensions.

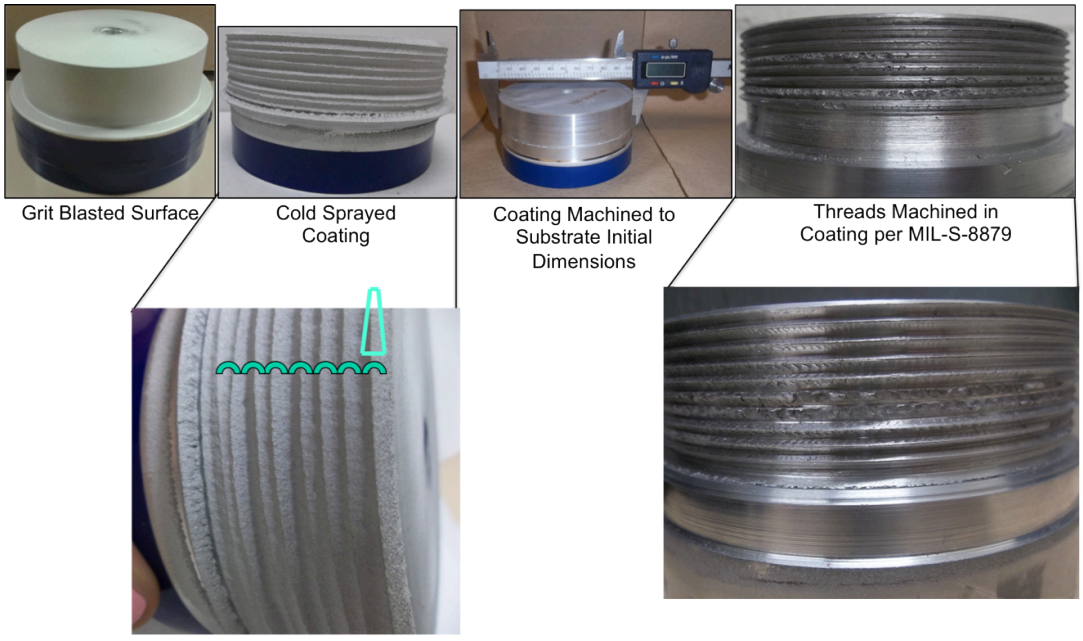

Figure 6.2: Summary of steps used during the repair procedure of pure aluminum 3.75-12UNJ-3A threads sprayed using a stepped nozzle motion.

The resulting top surface profile of the deposited coating suggests that the material deposits in a pyramidal like shape. This form is initially produced at the microscopic level and is caused by the difference in velocity and energy of particles traveling along the axis of the nozzle and the particles traveling away from the axis. The former easily deform and generate proper deposition as oppose to the latter, which stick or bounce off the substrate without deforming or adhering respectively. The difference in the particle effective impacting velocity is due to the boundary layer effects at the edge of the flow [154], [155] and the angle at which the particles hit the surface as illustrated in Figure 6.3.

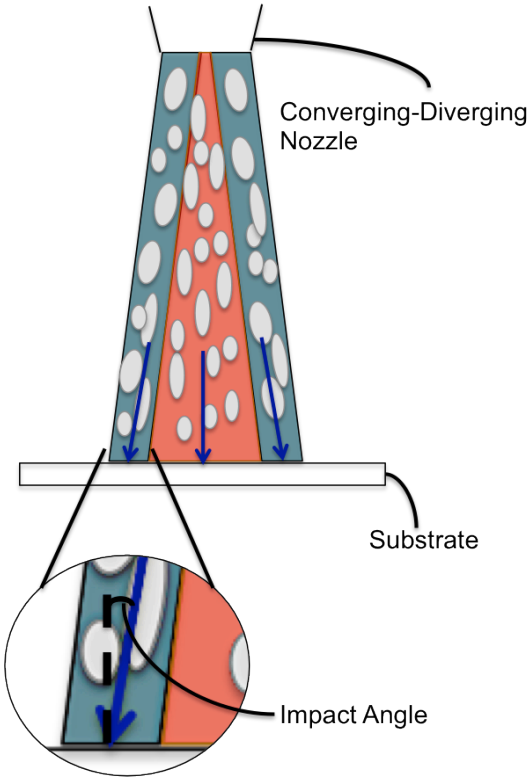

Figure 6.3: Illustration of the difference in particle impact angle.

The pyramidal shape is accentuated as more layers of material are deposited. In addition, the resulting coating pyramidal form increases the angle at which particles impact the surface as shown in Figure 6.4. As a consequent result, the normal velocity of the particles decreases while the tangential velocity V_t increases. However, the latter velocity vector is assumed to have no influence on the particle deposition efficiency [156]. Thus, for spray angles lower than 90°, the normal velocity component V_n is decreased. The deposition process and deformation process is

subsequently affected. Whether or not the friction dissipation energy encountered during the powder impact at an angle influences the deposition needs to be further analysed.

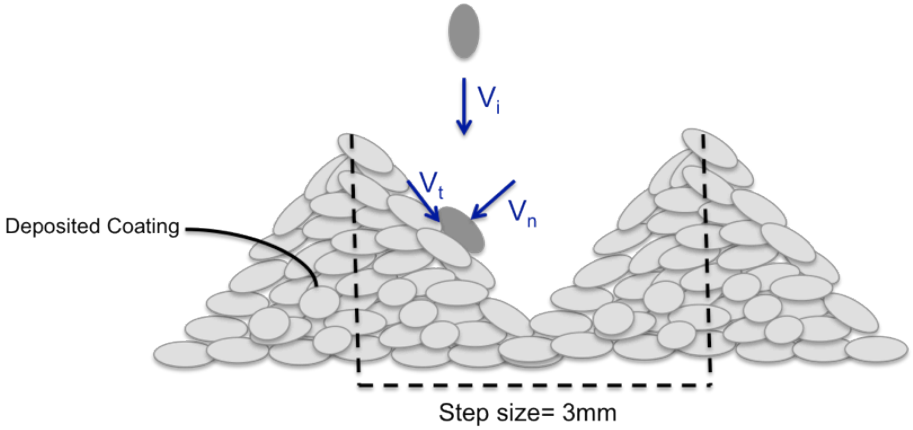

Figure 6.4: Schematic showing the velocity components during powder deposition on a pyramidal shaped material. V_i represents the initial velocity vector, V_n represents the normal velocity component of V_i and V_t represents the tangential of V_i. Where $V_i > V_t$.

Figure 6.5 depicts the cross-section of the obtained repair and provides the particle deformation, porosity level and Vickers microhardness at different locations away from the interface. The distribution of porosity in the coating is heterogeneous and mostly concentrated at the top layer where it reaches 13.5 ± 0.65%. The Vickers hardness is inversely proportional to the porosity level and reaches a minimum of 39.62 ±11.3 $HV_{0.3}$ at the top layer. The high standard deviation is caused by the elevated amount of porosity, which significantly lower the apparent hardness value as they enable and facilitate material deformation and compression during indentation. Despite the large coating thickness and consequent peening effect, the etched cross-sections of the repair, shown in Figure 6.5, reveal little difference in particle deformation across the coating. However, the 2D micrograph confines the analysis to a single plane, which disregards the possibility of particle rotation and Poisson's effect. Nevertheless, the peening effect is presumably the primary source of void and porosity reduction near the interface of the coating. The kinetic energy transferred at the impact to the coating from the subsequent impacting particles has the effect of further increasing the plastic deformation and decreasing the porosity.

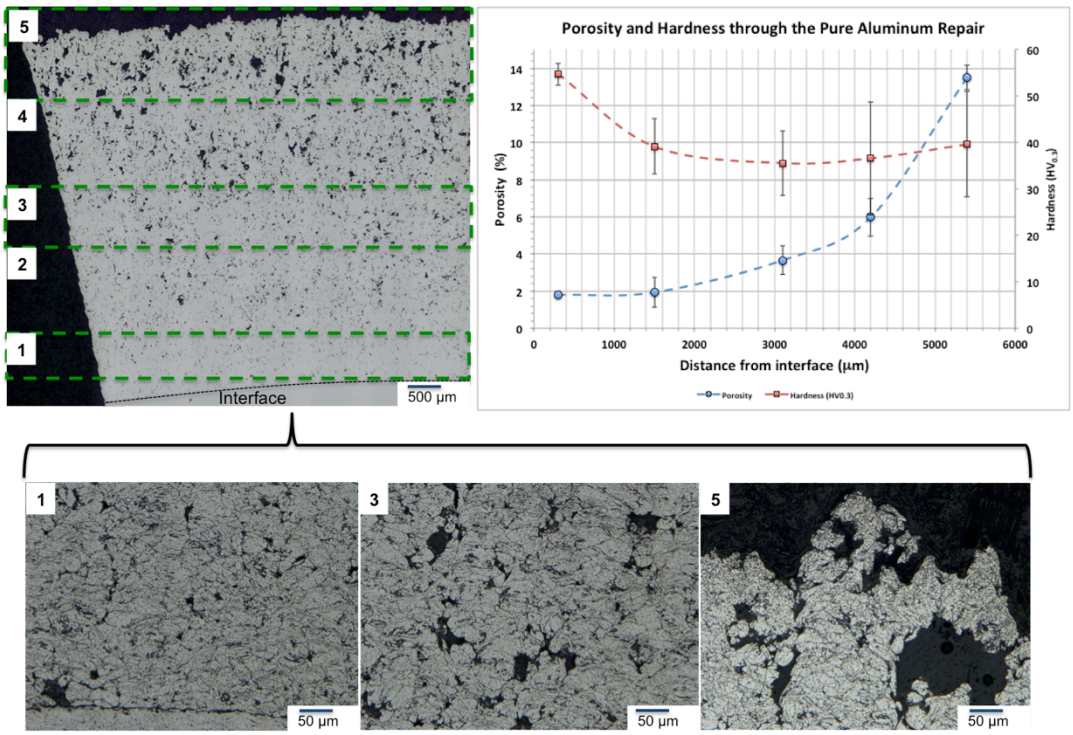

Figure 6.5: Porosity, particle deformation and Vickers hardness of a pure aluminum coating sprayed using a stepped nozzle motion.

The Vickers hardness is also largest closer to the substrate due to the increased work hardening process. However, longer spray times at high gas temperature can also induce stress relief annealing in the coating.

Figure 6.6 shows a 3D scan of the threads machined into the pure aluminum coating. Chipping of the material is seen at the crest and flanks of the threads. Severe coating disintegration is also observed. Both are described by surface powdering, which seems to be caused by coating porosity. It is therefore important to achieve good coating density in order to avoid tears in the sprayed material during machining.

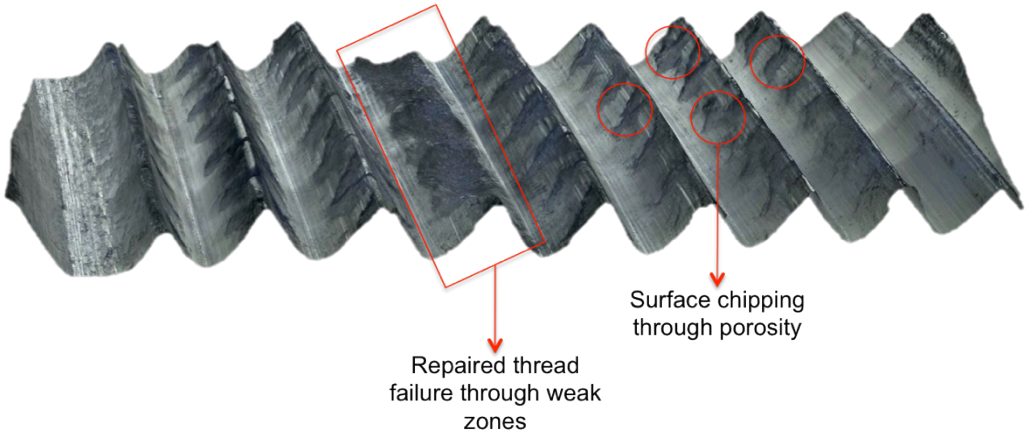

Figure 6.6: Pure aluminum threads machinability. Chipping of the coating is seen on the threads.

6.1.2. Continuous Repair Process

To rectify the porosity issue encountered in the previous repair and primarily caused by the nature of nozzle displacement, a different spraying technique has been used in the following repair. The schematic below represents the "continuous system" in which the nozzle moves continuously without intervals or steps, back and forth along the substrate surface. In this set-up, the coating has been produced seamlessly avoiding the build-up of pyramidal shaped coating layers.

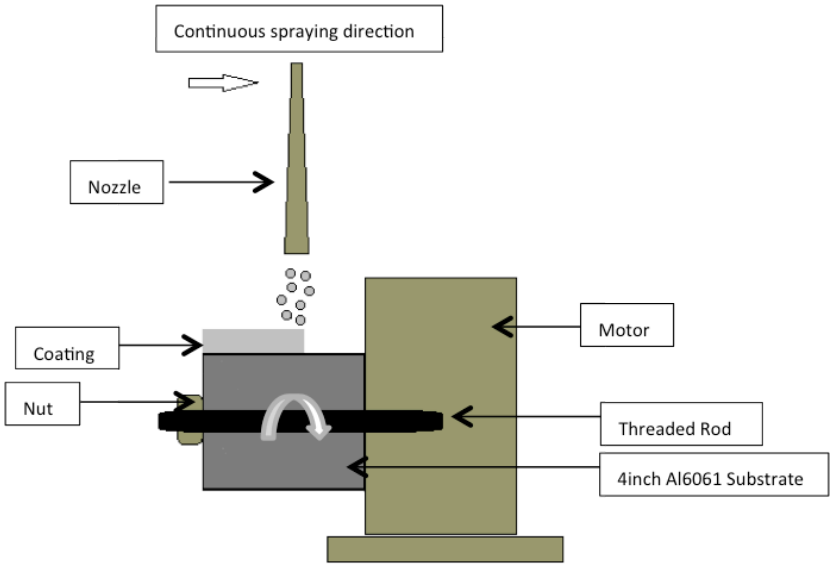

Figure 6.7: Continuous set-up for the spraying of the 88.9 mm diameter Al7075-T6 bars.

The same surface preparation procedure presented in the previous section has been used for the current repair. Table 6.2 shows the spraying parameters used to restore the dimensions of the 88.9 mm diameter Al6061-T6 substrate. The nozzle traverse speed has been set to 7 mm/s for a substrate angular velocity of approximately 300 rpm.

Table 6.2: Spraying Parameters Used to Restore 3.75-12UNJ-3A threads using a continuous nozzle motion

Parameters	**Values**
Gas Nature	Nitrogen
Gas Pressure	3.25 MPa
Gas Temperature	500 °C
Standoff distance	25 mm
Nozzle Type	Polymer
Nozzle Traverse Velocity	7 mm/s
Powder Feeder Wheel	320 Holes Small Wheel
Powder Feeder Gas Rate	30 SCFH
Powder Feeder Rate	4 rpm
Step Time	Continuous
Substrate Angular Velocity	~300 rpm

Figure 6.8 shows the various steps of the repair procedure, from the machined substrate to the restored threads. The obtained 5.9 mm thick coating has a high surface roughness but does not present any characteristics of preferential deposition. The spray time needed for the complete dimensional restoration of the component was approximately 1 hour.

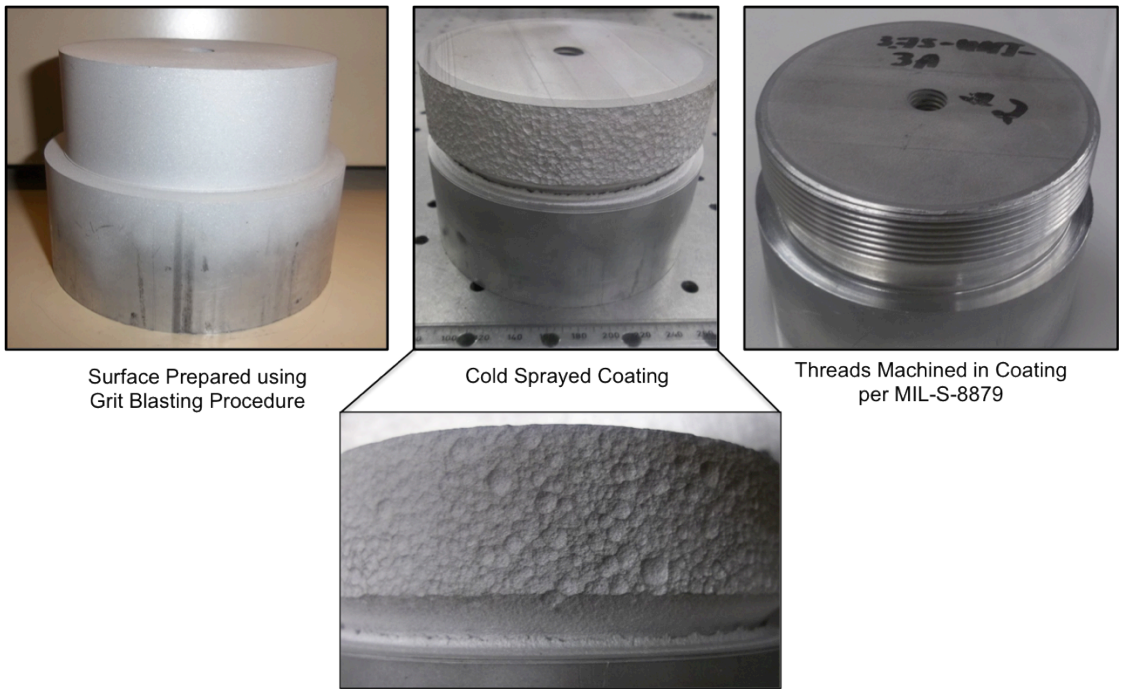

Figure 6.8: Summary of steps used during the repair procedure of pure aluminum 3.75-12UNJ-3A threads sprayed using a continuous nozzle motion.

As shown in Figure 6.9, the craters produced at the surface reach a depth of approximately 780 μm. The cavities are circular and distributed arbitrarily across the entire coating surface. The cavities proportions increase with coating thickness such that ticker coatings need to be sprayed in order to overcompensate for the consequent material loss.

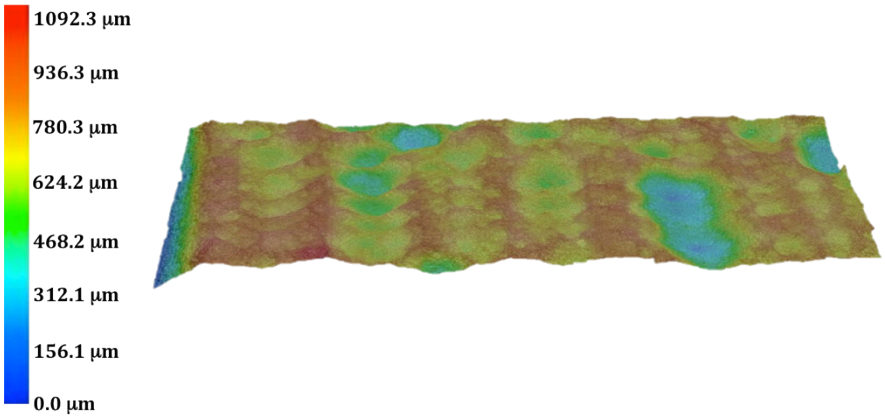

Figure 6.9: 3D scan of the cold sprayed repair coating.

Figure 6.10 depicts the microstructure of the obtained repair. The porosity content is constant up to 3.8 mm from the coating/substrate interface and its average value reaches 0.37 %. The porosity increases to 1.3% near the coating surface. As the top layer of the coating will be machined off during the restoration of the 3.75-12UNJ-3A threads, its porosity level is irrelevant to the final repair microstructure.

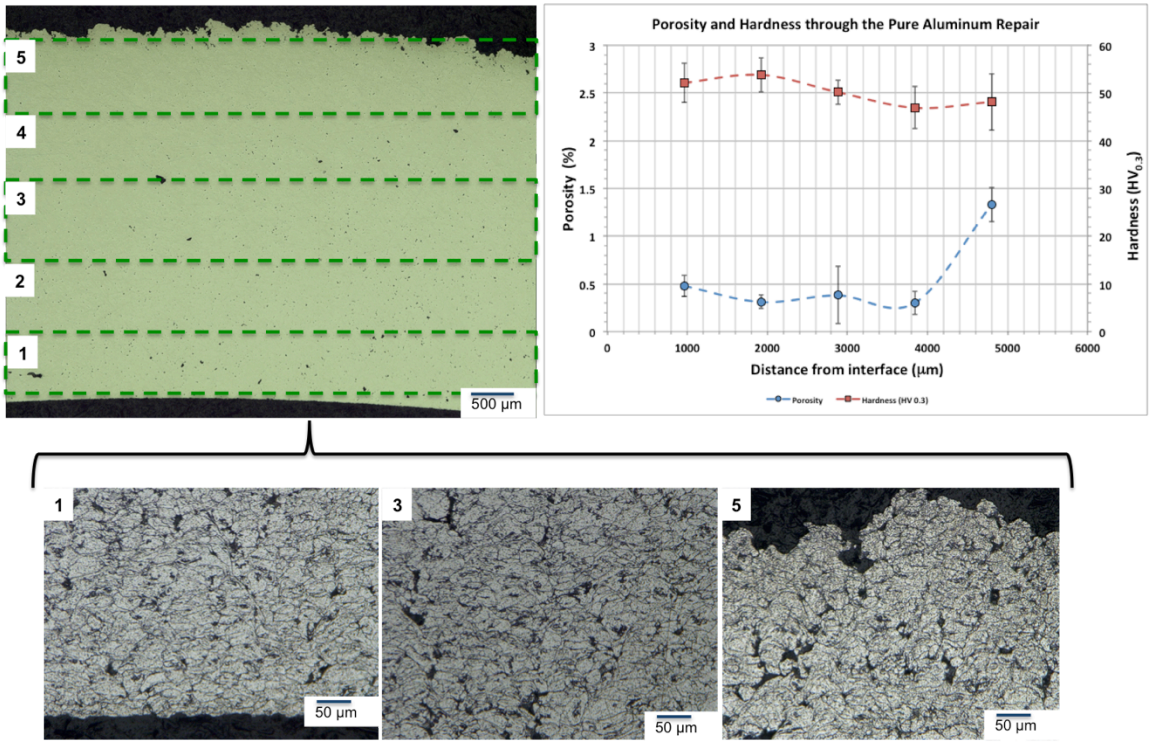

Figure 6.10: Porosity, particle deformation and Vickers hardness of a pure aluminum coating sprayed using a continuous nozzle motion.

The results presented in the previous figure indicate that the hardness value is highest near the substrate/coating interface and decreases slightly with the coating thickness. At 960 µm from the interface, the hardness reaches 52.18 ± 4.12 $HV_{0.3}$ and decreases to 48.13 ± 5.89 $HV_{0.3}$ near the coating surface. Despite using a different material deposition process than the previous stepped nozzle motion, the hardness is still affected by the peening process induced by the high impact velocity particles. The subsequent deformation of the coating leads to a decline in porosity. Moreover, since the nozzle displacement is consistent across the coating surface, it is possible that the increased coating temperature facilitated its deformation through the heat treatment process of thermal softening. Based on the micrographs presented in Figure 6.10, a

larger amount of particle deformation and flattening seems to be observed as we approach the substrate/coating interface, which supports the presence of the peening phenomenon.

Figure 6.11 shows a 3D scan of the 3.75-12UNJ-3A threads machined into the cold sprayed material. The smooth surface finish indicates that the repair has good machinability properties. As expected, a lower fraction of porosity increases the coating properties and quality.

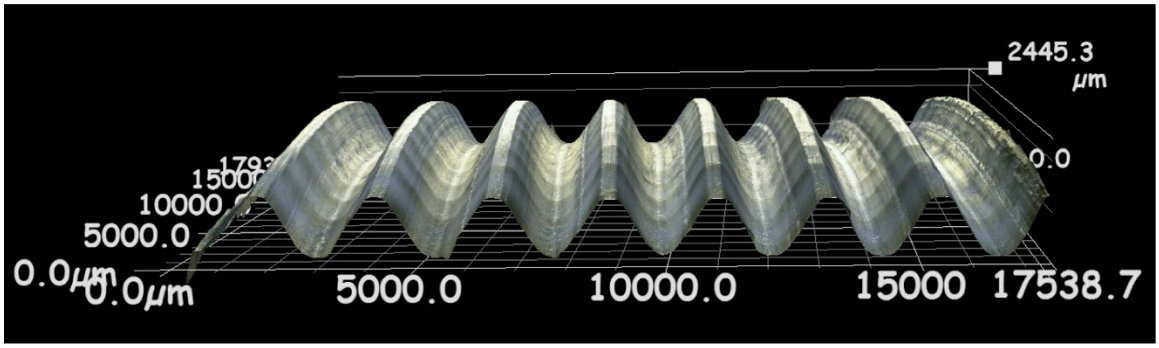

Figure 6.11: 3D scan of pure aluminum threads machined into the cold sprayed coating.

Once the machining process has been completed, the threads have been tested in torque with eight active non-lubricated threads. The repair was able to withstand the maximum torque applied, which corresponded to 303 N·m. This value is above the Boeing Company requirement of 203 N·m. After the test, the threads were intact as no sign of abrasion or material deterioration was observed.

6.1.3. Substrate Cooling During Repair

The repairs presented in the previous sections have been produced without the use of an external cooling system and temperature monitoring devices. Figure 6.12 shows the 88.9 mm substrate temperature during material deposition at maximum spraying parameters with and without the use of external cooling equipment. The first curve in the graphic shows the component surface temperature during spray without any use of external cooling systems. In this case, the test was stopped after 4 minutes once the temperature reached 120 °C. This confirms that the convective heat transfer between the rotating substrate and ambient air is insufficient to lower the component temperature. The conductive heat transfer within the large component is considered to only have a limited influence on the substrate surface temperature.

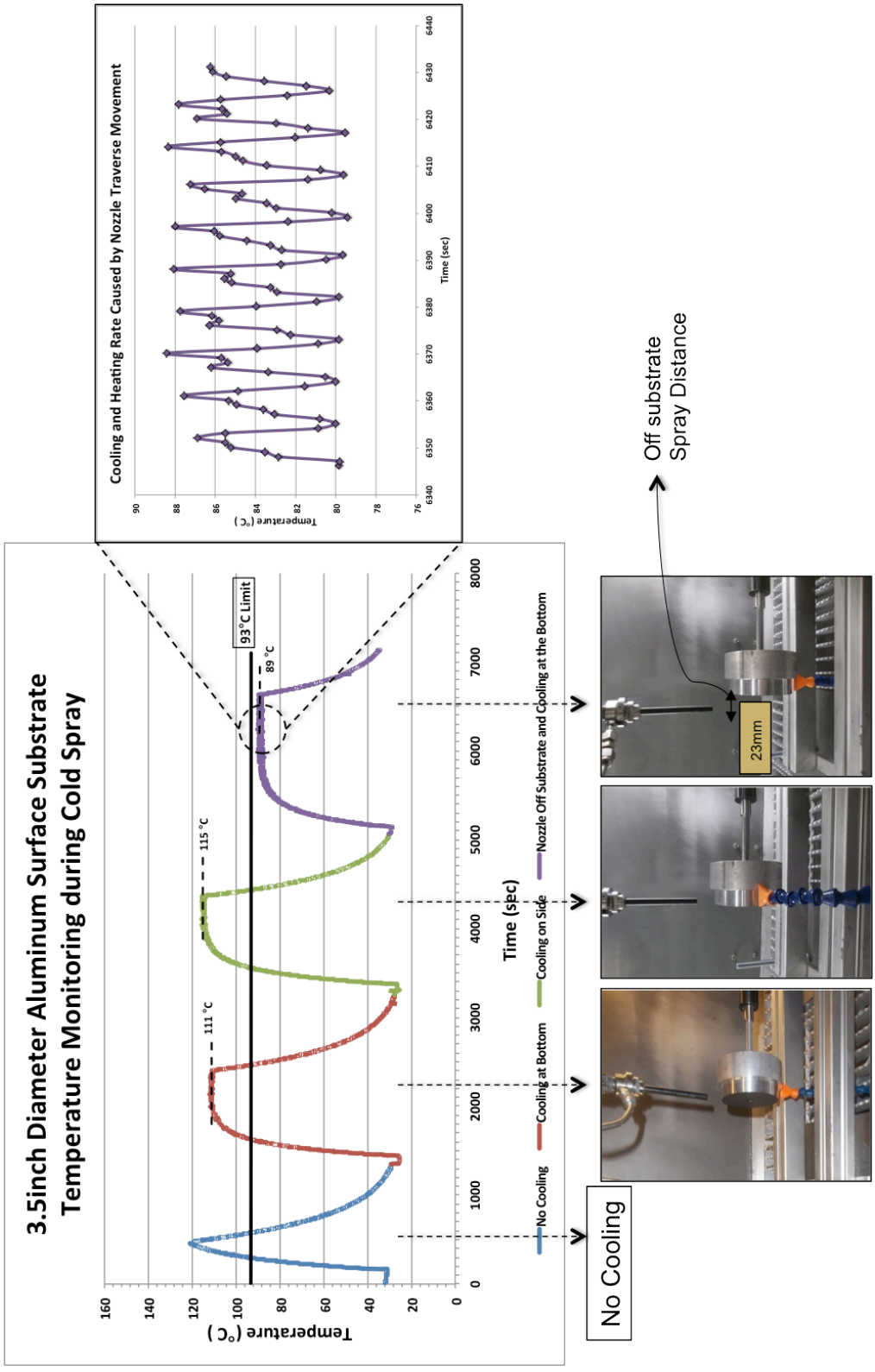

Figure 6.12: Substrate surface temperature monitoring during cold spray.

When the air cooling line is placed under the component, opposite to the cold spray flow, the surface temperature stagnates at 111 °C after 7 minutes as shown in Figure 6.12. As the cooling line is relocated to the side of the component, the substrate surface temperature stagnates to 115 °C after 9 minutes. The reduced efficiency of the cooling system as the line is placed closer to the cold spray flow is associated with the influence that the high pressure hot streamlines have on the nearby cooling flow. The last test studied the effect of having an additional nozzle displacement alongside the substrate surface that would allow further cooling of the component and consequently the coating, as illustrated in Figure 6.13. Using an off substrate spray distance of 23 mm and cooling system under the component decreased the substrate temperature to 89 °C. Since the obtained temperature is below the allowed limit, this set-up and nozzle displacement were used during the full dimensional restoration of the part. As the substrate temperature was kept below the 93 °C limit set by The Boeing Company, microstructural and mechanical variations in the Al7075-T6 commercial material were prevented.

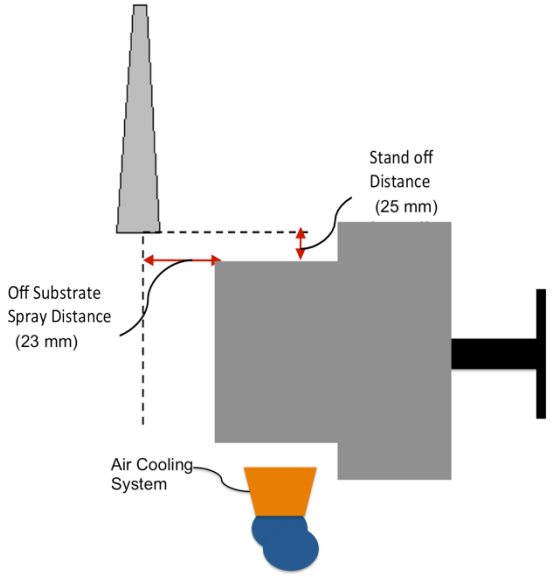

Figure 6.13: Illustration showing the off substrate spray distance added for cooling purposes.

The same sample preparation procedure and spray parameters used in the previous subsection have been used for the following repair. Figure 6.14 summarizes the repair process and shows the surface of the component, the as-sprayed coating and the restored threads. A 5.7 mm thick coating has been deposited onto the substrate surface. The time required to complete the dimensional restoration of the component was 1 hour.

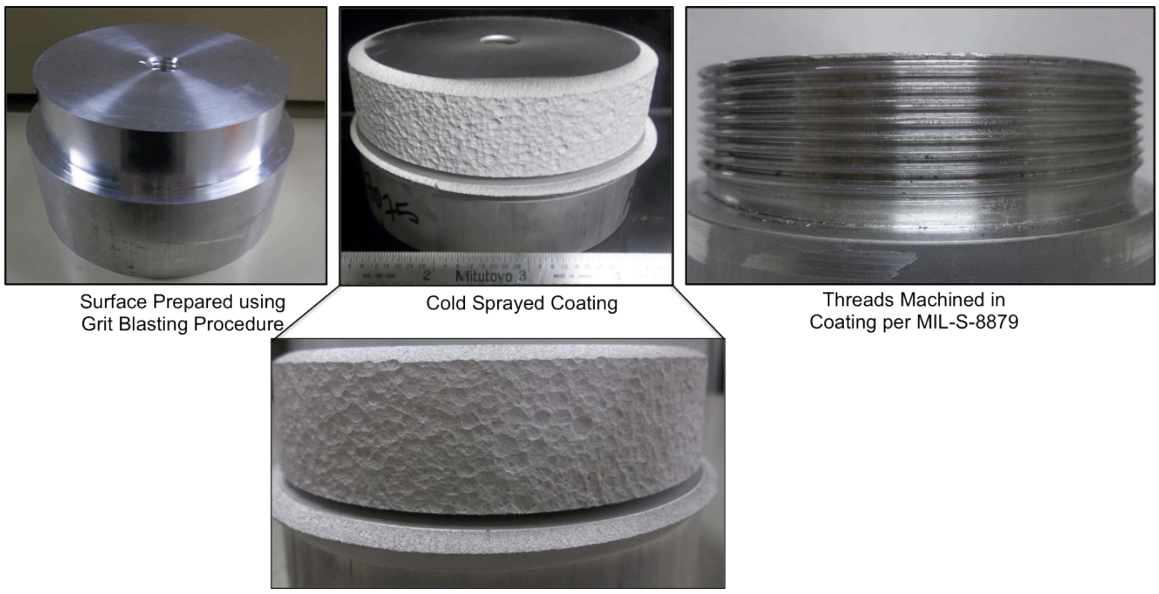

Figure 6.14: Summary of steps used during the repair procedure of pure aluminum 3.75-12UNJ-3A threads sprayed using a continuous nozzle motion and an air cooling system.

The coating surface is composed of 903.8 μm deep circular craters as shown in Figure 6.15. which are scattered across the entire coating surface.

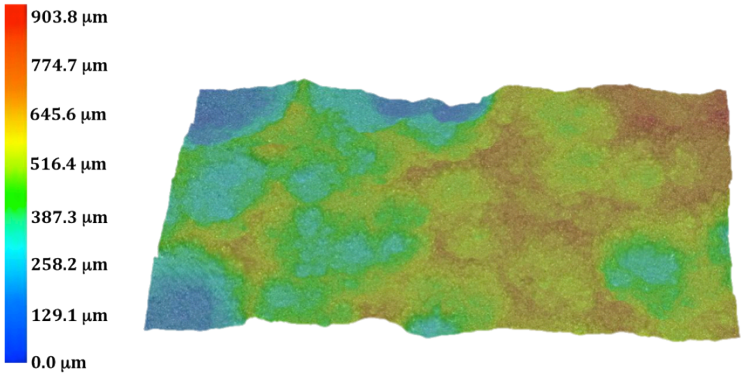

Figure 6.15: 3D scan of the as-sprayed coating surface.

Figure 6.16 shows the final microstructure of the repair and quantifies the porosity and Vickers hardness across the coating thickness.

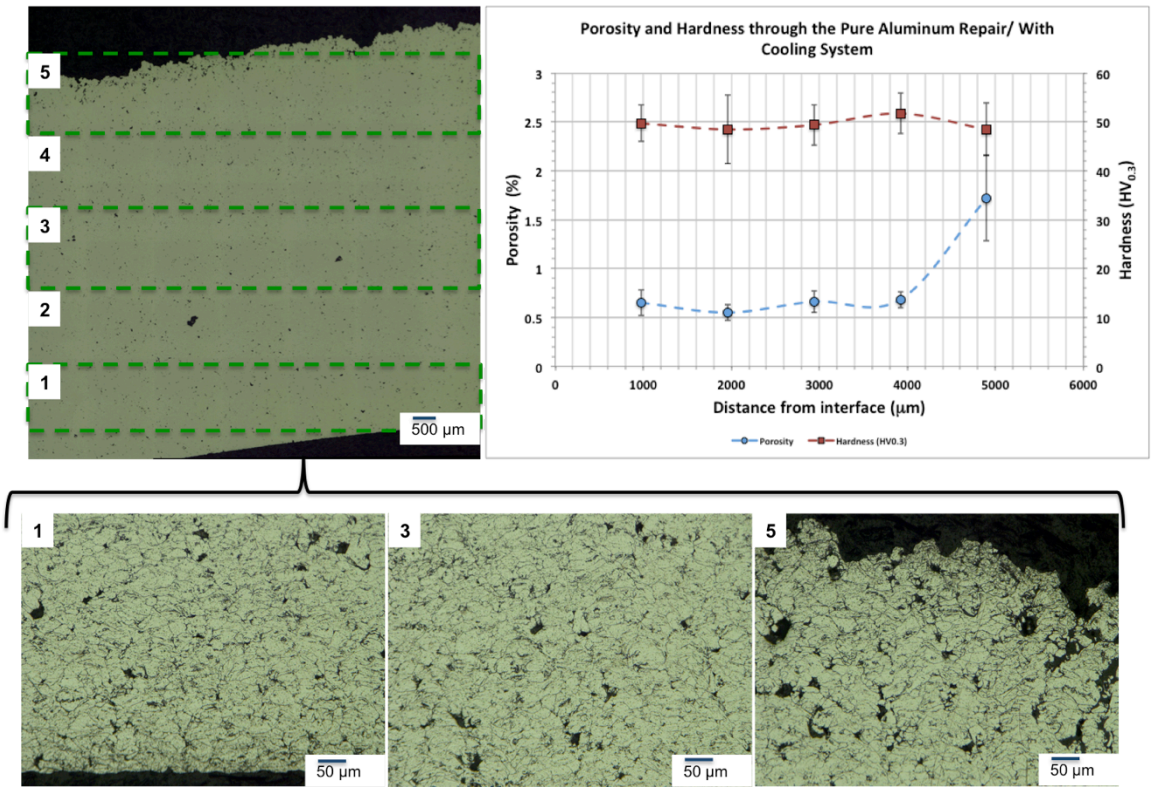

Figure 6.16: Porosity, particle deformation and Vickers hardness of a pure aluminum coating sprayed using a continuous nozzle motion. An air cooling system is used to lower the substrate surface temperature.

The porosity level in the coating is approximately 0.64 % and increases to 1.7 % in the last deposited layer. This confirms that the subsequent deposited particles compress and deform the coating during impact. As a result, the voids between particles are reduced in size and number in the coating. The etched cross-sections shown in Figure 6.16 also indicate that the particles comprised within the last layer have been subjected to a minimal amount of deformation. It is observed that the overall porosity in the repair is higher than in the coating obtained previously without a cooling system. This suggests that a higher coating temperature facilitates the deformation of previously deposited particles during subsequent particle impact. These results seem to indicate and confirm that the hot high velocity gas is able to partially induce thermal softening of the coating.

The obtained average hardness value is 49.75 ±3.75 $Hv_{0.3}$ and 48.45 ±5.37 $Hv_{0.3}$ near the substrate/coating interface and coating top layer respectively. Once again, the obtained Vickers harnesses are higher than the values presented in subsection 5.2.1 for thinner flat coatings. The

difference is caused by the presence of larger heat inputs, increased coating thickness and larger cold working process. Further research is needed to analyze the effect of the substrate thickness and geometry on the coating quality. Moreover, the cooling system involved in the current repair does not influence the cold working process as similar hardness values were obtained for the previous repair.

Figure 6.17 is a 3D scan of the threads machined into the coating. As expected, a smooth surface finish was obtained due to the dense properties of the coating. A torque test was performed on eight active threads and the repair was again able to withstand 303 N·m. After the test, the threads did not present any of sign of wear or deformation.

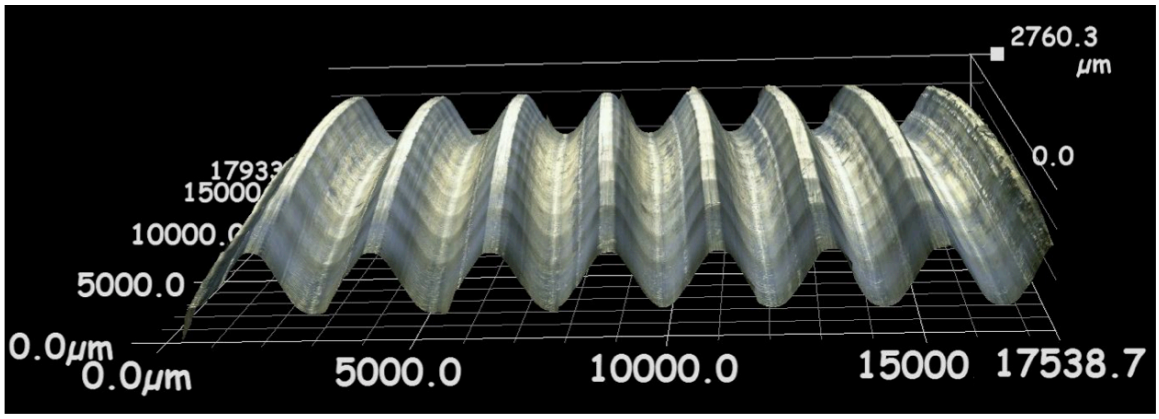

Figure 6.17: 3D scan of threads machined into the pure aluminum cold sprayed coating.

Figure 6.18 presents the Vickers hardness of the substrate material before and after repair. The results show that the repair process does not affect the properties and heat treatment of the base material. The Vickers hardness at 1mm under the substrate surface before and after repair is 182.7 ± 1.89 $HV_{0.3}$ and 181.9 ±2.36 $HV_{0.3}$ respectively.

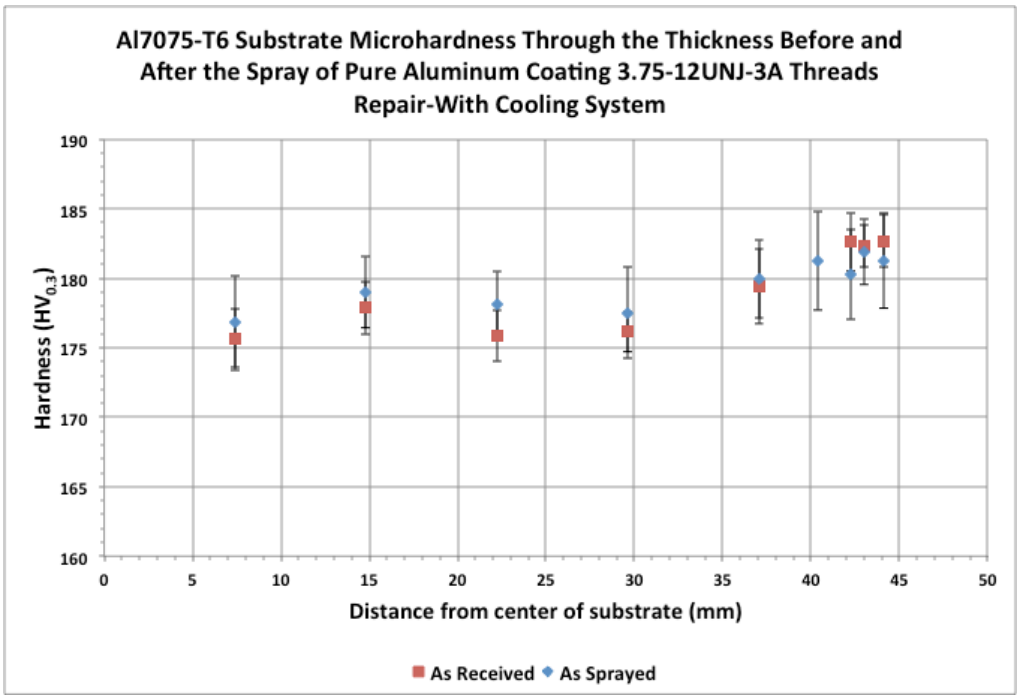

Figure 6.18: Vickers hardness of the 88.6 mm diameter Al7075-T6 substrate before and after the pure aluminum cold spray repair.

6.1.4. Influence of Thermal Gradients on the Coating Adhesion

An important factor to take into account when spraying thick coatings while using a cooling system is the temperature gradient in the component. If the coating is cooled down sharply (e.g. with the use of a cooling system) after a partial repair and then re-sprayed on, the coating risks to fail in adhesion due to induced high thermal stresses as shown in Figure 6.19. The 0.84 mm thick pure aluminum coating has detached in one piece from the substrate after being cooled down using the air cooling system and subsequently re-sprayed. The thermal contraction of the coating contributed to the creation of tensile stresses at the substrate interface, which reduced the adhesion strength of the coating to the substrate surface.

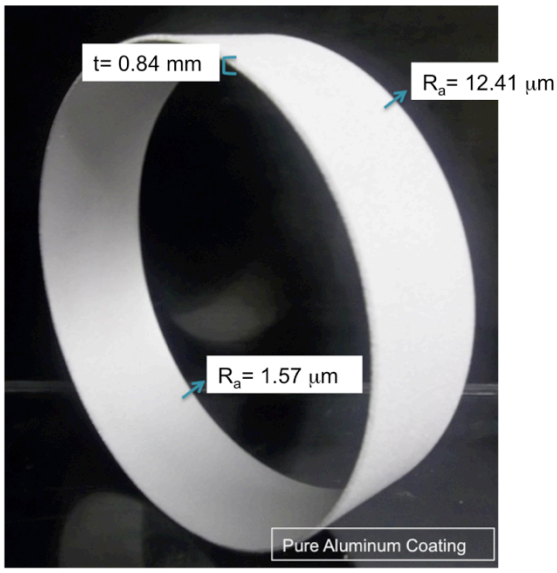

Figure 6.19: Pure aluminum coating failed during spray due to temperature gradient.

For that reason, it is highly recommended to spray thick coatings without interruption of the spray. If interruption of the spray is unavoidable, the coating should be left to cool down at ambient temperature before the spray is reinitiated to avoid large temperature drops across the coating surface.

6.2 Large Component Repair using Al2024 Powder

The parameters presented in Section 5.1.2, are suitable for the deposition of thin Al2024 coating layers but are however, not appropriate for the repair of large components. Do to the limited amount of resources, full repair can only be produced at an industrial level using the previously selected parameters. However, in this section, a thin Al2024 layer has been deposited on an 88.9 mm diameter component in order to study the coating growth process and the influence of the cooling system on the coating adhesion.

It has been noticed in multiple sprays that when Al2024 is used to repair a cooled part, the first coating layer deposits poorly and starts to lift at specific edges and chip at various locations during spray as depicted in Figure 6.20. Thus, the air flow from the air cooling system may affect the coating deposition during particle impact.

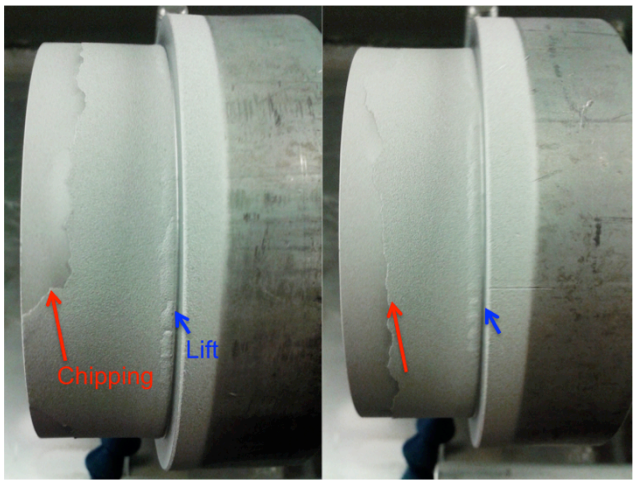

Figure 6.20: Al2024 coating chipping and lifting during spray.

In order to avoid an adhesion failure of the coating during spray, a substrate preheating temperature of 80 °C has been found to be appropriate. The preheated substrate temperature enables the particles to stick firmly to the substrate surface, thus avoiding any dislodging of the deposited powder from the impact of upcoming particles. As noted in section 2.3.7.2, pre-heating the substrate surface can increase the occurrence of metallurgical bonding [113]–[116] and consequently the adhesion strength of the first deposited layer. Due to the low deposition efficiency of the Al2024 powder, no complete repairs were attempted or produced.

6.3 Influence of Substrate Surface Angle on Pure Aluminum Deposition

The previous sections have presented the dimensional restoration and repair of a complete set of threads found on the nose landing gear steering actuator. The current section, however, concentrates on the repair process of single and multiple threads on smaller components. This will assist in understanding the requirements, in terms of substrate preparation procedures, needed to produce a suitable CS repair of only the worn and damages threads found within a set of threads. The goal of the current study is to identify the influence of the substrate angle on the pure aluminum particle deposition characteristics and coating features. The results obtained will provide the angle at which the aluminum component edges need to be machined during partial repair. Good transition in terms of material properties is mandatory between the repair material and the undamaged region of the component in order to ensure uniform distribution of properties along the interface and avoid stress concentration factors. Circular

coarse and fine threaded substrates of 38.1 mm in diameter have been machined on a lathe as shown in Figure 6.21. Threaded components have been used as substrate materials to facilitate the assessment of coating machinability. Different thread dimensions have been selected to cover the influence of deposition time and coating thickness on the coating porosity for different substrate angles.

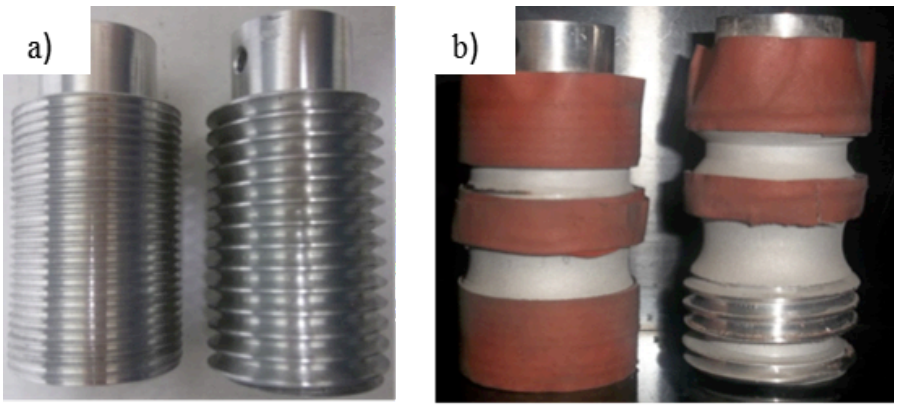

Figure 6.21: a) Threaded substrate dimensions and b) Machined and grit blasted repair locations. Fine (left) and coarse (right) threaded substrates machined down to produce variable substrate surface angles.

Figure 6.22 shows the dimensions of the machined surfaces. The substrates were cut at angles of 45°, 60° and 90°. A curved surface has also been included in this study to evaluate its benefits over the hard cut angles. For all substrate surface inclinations, the depth of the repairs is approximately 2 mm and 3 mm for the fine and coarse threads respectively.

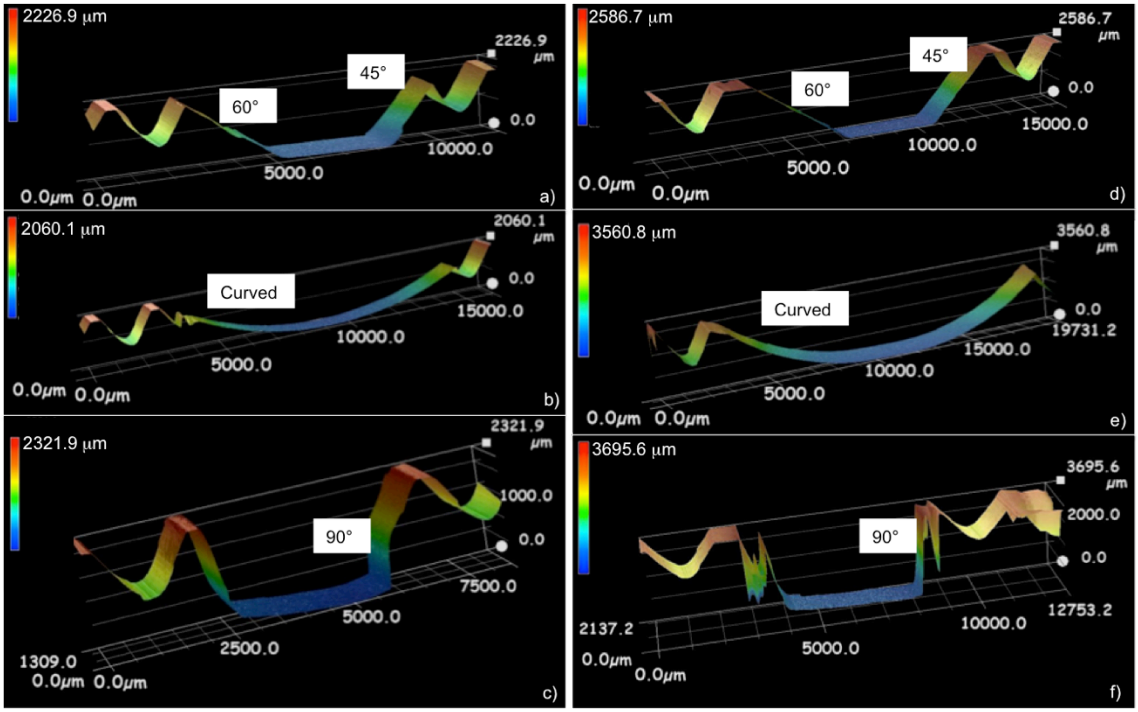

Figure 6.22: 3D digital images showing the dimensions and patterns of the machined surfaces. The influence of surface inclination on the deposition is analyzed for different angles. (Left) UNJF threads (Right) UNJC threads.

The machined surfaces were individually grit blasted using the parameters presented in Table 5.1 in Section 5.1. Masking tape was used to protect the adjacent surfaces from bouncing grits. The spraying parameters used for these tests are presented in Table 6.3. The nozzle displacement across the component surface was achieved through the stepped motion. Since only two steps were required to cover the machined portion of the component, issues previously related to the cooling process of the coating surface would be avoided in this case.

Table 6.3: Spraying Parameters Used to Restore Single Threads

Parameters	Values
Gas Nature	Nitrogen
Gas Pressure	3.25 MPa
Gas Temperature	500 °C
Standoff distance	25 mm
Nozzle Type	Polymer
Increment Size	3 mm
Nozzle Traverse Velocity	50 mm/s
Powder Feeder Wheel	320 Holes Small Wheel
Powder Feeder Gas Rate	30 SCFH
Powder Feeder Rate	2 rpm
Step Time	11 to 12 seconds
Angular Velocity of Substrate	6 rpm

Figure 6.23a shows the component after the deposition of pure aluminum powder. In Figure 6.23b, the threads have been machined to their initial dimension in the cold sprayed material.

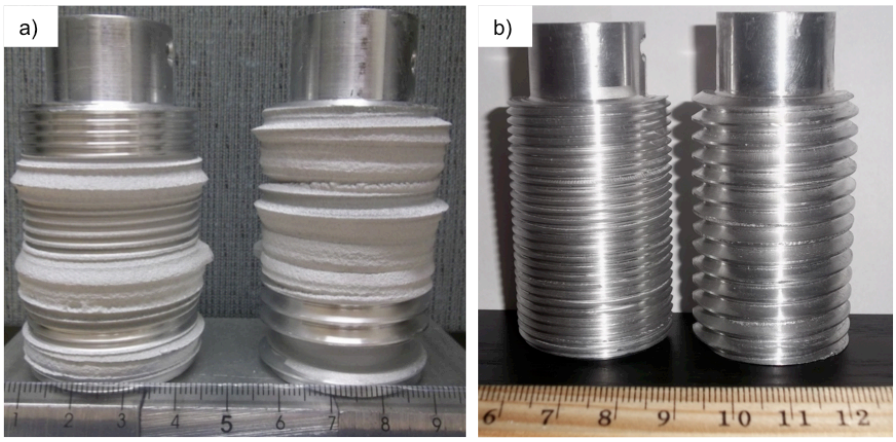

Figure 6.23: a) Pure aluminum material deposited onto the 38.1 mm diameter part and b) threads machined into the cold sprayed material.

Figure 6.24 and Figure 6.25 show the resulting microstructures of fine and coarse repaired threads respectively.

For fine threads, shown in Figure 6.24, the porosity level is at its lowest for powder sprayed at 45°, 60° and curved surfaces. For coarse threads, depicted in Figure 6.25 the porosity percentage is smallest at a 60° angle and for the curved profile. In terms of powder deformation, both coarse and fine threads show that at the 90° interface the powder does not deform nor does it bond in any way to the substrate despite showing a compact deposition. As expected, parallel particle impacts lead to poor mechanical properties and low coating adhesion. Moreover, in the case of both coarse and fine threads, decreasing the impact angle to 45° increased the presence of defects at the coating/substrate interface. Discontinuity in particle deposition along the 45° edges is observable. Therefore, based on the amount of porosity, particle deformation and coating quality, the ideal surface angle for partial repairs is 60° or a curved profile. The particle flattening ratio is largest for perpendicular impact and decreases with increasing surface angles. For angular deposition, the additional tangential momentum increases with increasing angles and as a consequence a decline in the normal momentum is expected. The reduction in the impact intensity reduces the particle deformation potential and bonding strength. Thus, the coating mechanical properties and microstructural characteristics are significantly affected in angular spraying.

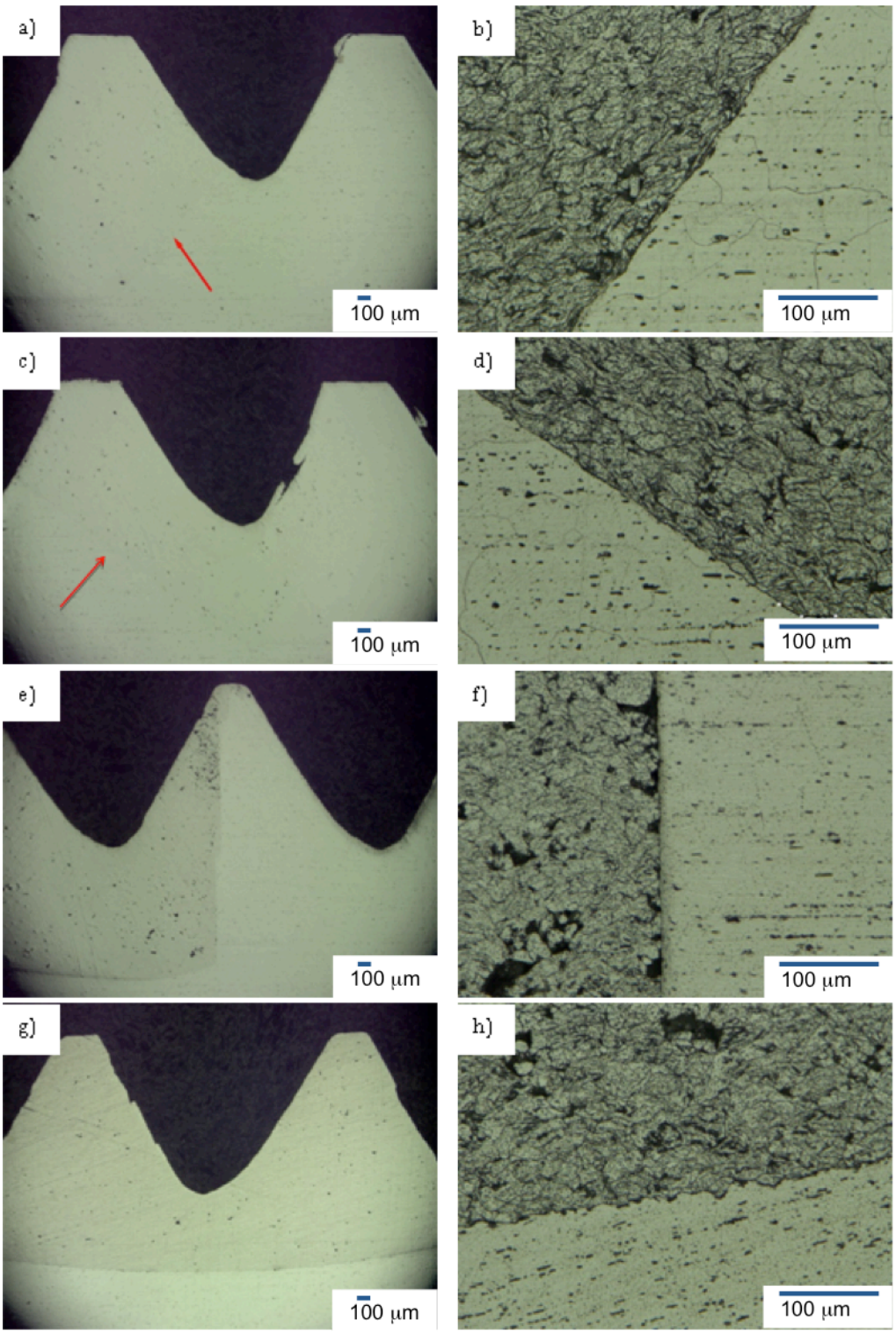

Figure 6.24: 3D Digital images showing the interface (arrows) at each angles for the 1.5-12UNJF threads; a) 45°; c) 60°; e) 90° and g) curved. Etching with Keller's etchant for 50 s illustrated the deformation of particles at the interfaces; b) 45°; d) 60°; f) 90° and h) curved surface.

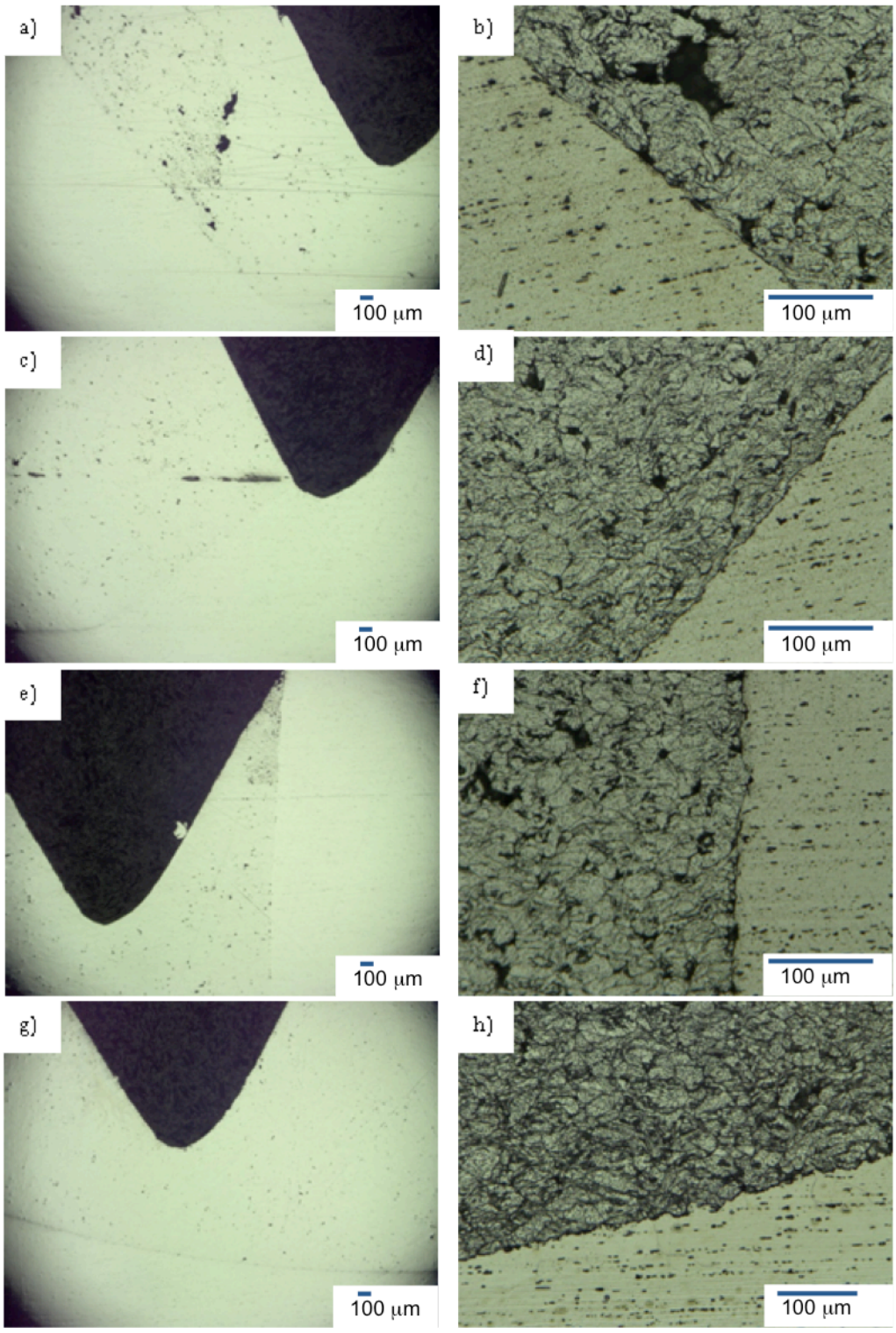

Figure 6.25: 3D Digital images showing the interface at each angles for the 1.5-6UNJC threads; a) 45°; c) 60°; e) 90° and g) curved. Etching with Keller's etchant for 50 s illustrated the deformation of particles at the interfaces; b) 45°; d) 60°; f) 90° and h) curved surface.

Figure 6.26 shows the state of the coating surface after the machining of threads. The location of flaws is near the curved root and on the crest of the threads. The former defect seems to have been caused by the machining itself. This can be corrected by adjusting few machining parameters such as the material removal rate (velocity). The latter flaw is described by surface powdering, which seems to be caused by coating porosity arising from poor bonding between particles in angular spray.

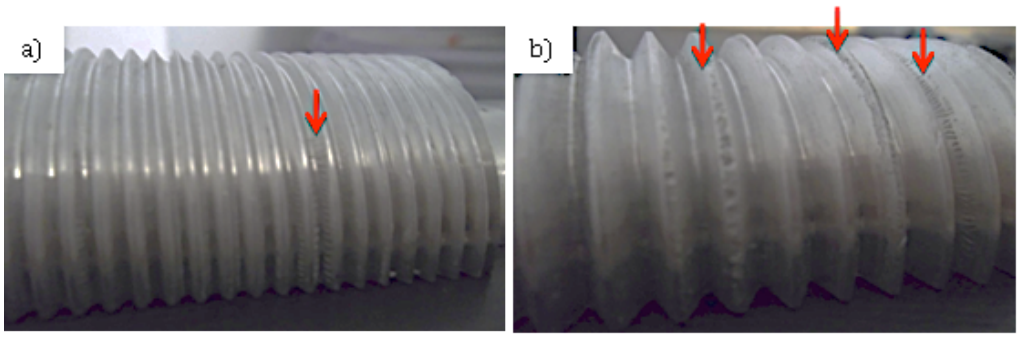

Figure 6.26: Threads machined on cold-spray showing a smooth surface with machining flaws; a) surface of 1.5-12UNJ and b) surface of 1.5-6UNJ. Arrows point to surface flaws after machining of cold sprayed pure Al.

6.4 Small Scale Repairs Using Al2024 Powder

Commercial 38.1 mm diameter Al2024-T351 bars have been machined down to a diameter of 33 mm to replicate the dimensions of a damaged component. Partial and full 1.5-12UNJ-3A thread repairs have been produced to analyze the adhesion of the coating on a 60° wall and to evaluate the load carrying capacity of a cold spray repair respectively. In the case of the partial repair, four out of eight threads have been restored, while all eight threads have been repaired for the full repair test. The machined surfaces have been grit blasted using the parameters listed in Table 6.4. All components have been soaked in ethanol in an ultrasonic bath after the grit blasting procedure.

Table 6.4: Grit Blasting Parameters Used During the Preparation of Partial and Full Al2024-T351 Repairs

Parameters	Values
Abrasive	Aluminum Oxide
Size	80 Mesh
Process Gas	Compressed Air
Pressure	551 kPa
Grit Blasting Angle	45°
Standoff Distance	51 mm

The spraying parameters used to produce the repairs are presented in Table 6.5. The substrate surface temperature of the partial and full repairs has been kept to 88 °C and 66 °C respectively as shown in Figure 6.27 during spray.

Table 6.5: Cold Spraying Parameters Used During the Partial and Full Repairs of Al2024-T351

Parameters	Values
Gas Nature	Nitrogen
Gas Pressure	3.25 MPa
Gas Temperature	500 °C
Standoff distance	25 mm
Nozzle Type	Polymer
Nozzle Traverse Velocity	5 mm/s
Powder Feeder Wheel	320 Holes Small Wheel
Powder Feeder Gas Rate	30 SCFH
Powder Feeder Rate	11.25 g/min
Step Size	Continuous
Angular Velocity of Substrate	350 rpm

The maximum surface temperature changes with respect to the amount of heat transferred from the main gas flow to the component surface. As a consequence, higher cooling rates are achieved for smaller repair areas.

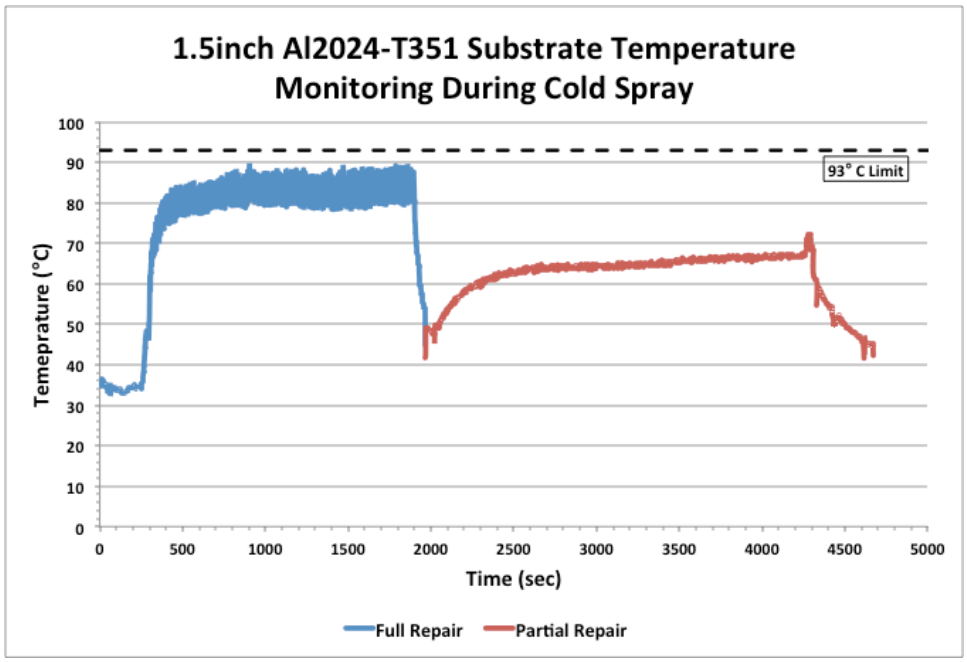

Figure 6.27: Al2024-T351 substrate surface temperature during full and partial 1.5-12UNJ-3A repairs.

Figure 6.28 shows the repair process of the partially damaged components. The 3.8 mm thick cold spray coating surface profile is characterized by the presence of statistically distributed craters. The depth of the cavities reached 1.2 mm in average. During the machining of the 1.5-12UNJ-3A threads process, all repairs failed in adhesion at the coating/substrate interfaces. The coatings abruptly slipped along the substrate surfaces without any friction or resistance. The failure process is characteristic of a poorly bonded coating.

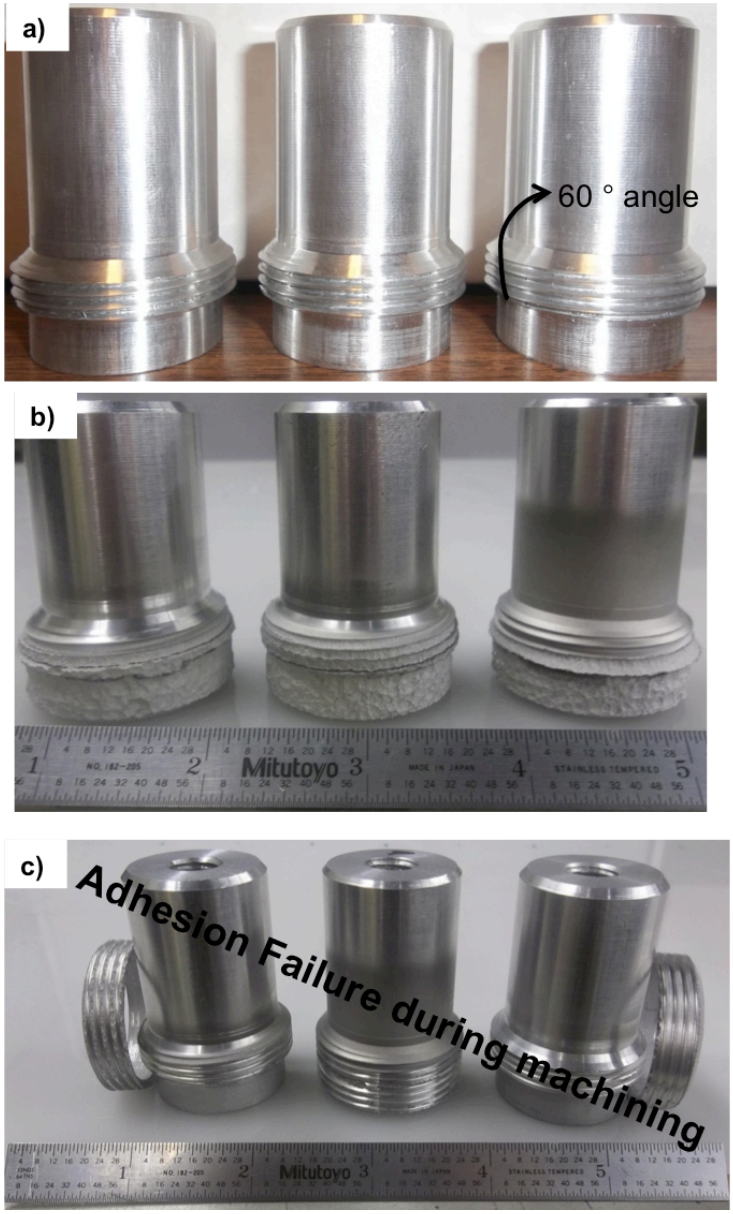

Figure 6.28: Al2024-T351 substrate partial repair using Al2024 powder. a) Substrate machined to proper dimensions, b) damaged area repaired using cold spray and c) coating failure during machining.

Figure 6.29 depicts the repair procedure for the full restoration of 1.5-12UNJ-3A threads. The 4 mm thick coatings surface roughness is characterized by 2 mm deep cavities distributed across the entire coated area. Smooth coating surfaces were obtained once the machining process has been completed. Chipping or fragmentation of the coating has not been observed during the cutting process.

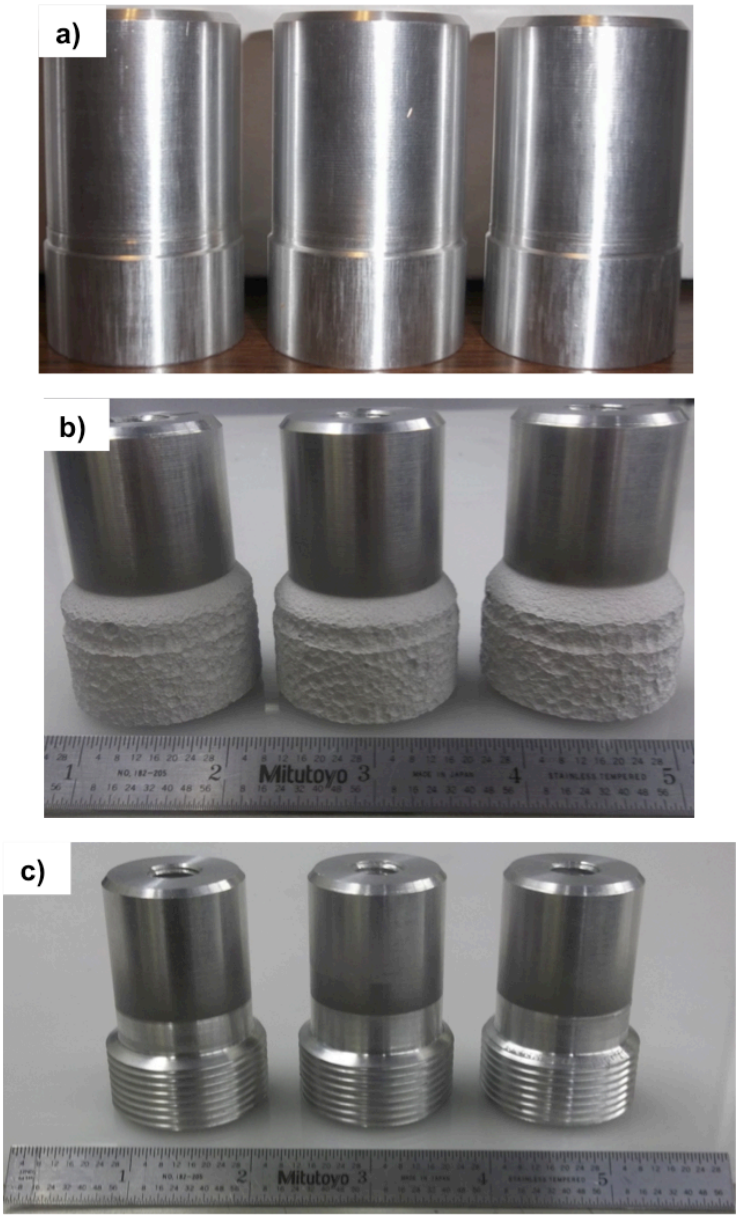

Figure 6.29: Al2024-T351 substrate full repair using Al2024 powder. a) Substrate machined to proper dimensions, b) cold spray material deposited onto the damaged area and c) threads machined into the cold spray.

The load carrying capacity of the full repairs has been tested through the compression test described in section 4.8.2. Figure 6.30 shows the state of the repairs after the test has been performed. One of the repairs has failed during its installation in the mating nut, which indicates that its adhesion strength to the substrate surface was very low and approaching its maximum even after the machining process. The second repair has also failed in adhesion at a stress of only

0.52 MPa. The last repair failed at 6.2 MPa at the substrate interface. As shown in Figure 6.30b, the coating surface at the interface is smooth and shows no apparent lines of deformation or smearing, which is characteristic of a slipping process and typical for surfaces exhibiting limited bonding mechanisms.

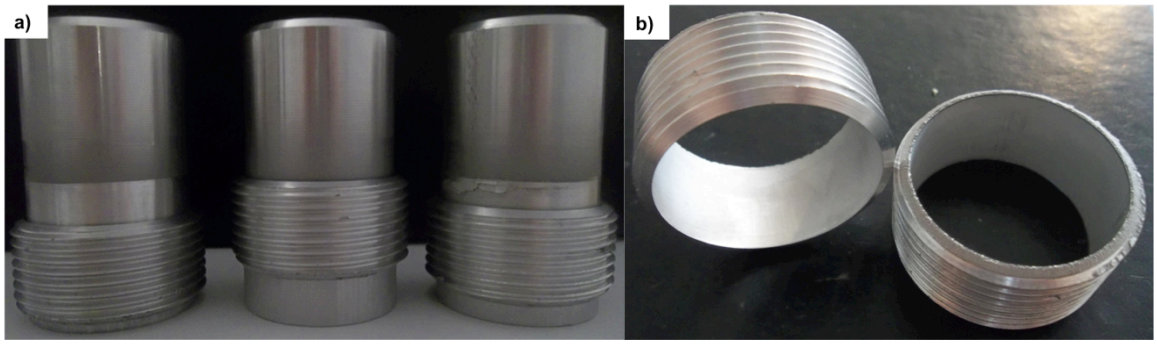

Figure 6.30: Al2024 coating failure in adhesion during the compression test.

The relatively weak adhesion of the obtained repairs is the main issue of thick cold sprayed coatings. Although the Al2024 particles are expected to deform plastically at the impact with the substrate surface and locally attain sufficiently high temperatures to undergo bonding, it appears from the obtained results that the metallurgical or mechanical adhesion strength is limited. The coating thickness has an important effect on the residual stress state and consequently the adhesion strength at the interface [102]. Based on the results, it is hypothesized that the increase in coating thickness led to a release of the compressive residual stress at the interface. As a consequence, the adhesion strength decreased to a point where only small stresses such as those experienced during machining could initiate failure.

CHAPTER 7

Influence of Substrate Surface Roughness on Coating Adhesion Strength

Based on the results from the previous chapter, one of the main limiting factors in the performance of the repairs produced using the CGDS process is the adhesion strength. Low coating adhesion strength induces premature failure of the repair through coating/substrate interface sliding. The current chapter includes the study of the effect of substrate surface roughness on the coating adhesion. The first two sections present the results of the adhesion tests performed on Al2024 coatings sprayed on Al2024-T351 substrates and pure aluminum coatings deposited on Al7075-T6 substrates respectively. The last section elaborates in more details on the mechanism responsible for the adhesion of Al2024 and pure aluminum powder. It gives insight into the possible causes that create different adhesion strengths for the Al2024 and pure aluminum repairs.

7.1 Adhesion/Cohesion Tensile Test for the Al2024 Powder on Al2024 Substrate

7.1.1. Al2024 Surface Preparation

A series of tests have been produced to identify the effect of various substrate surface preparation procedures on the Al2024-T351 surface profile. Different abrasive mediums have been used at different blasting pressures to obtain varying substrate surface profiles as shown in Figure 7.1. The grit blasting time and gun standoff distance were set to 5 seconds and 25.4 mm respectively.

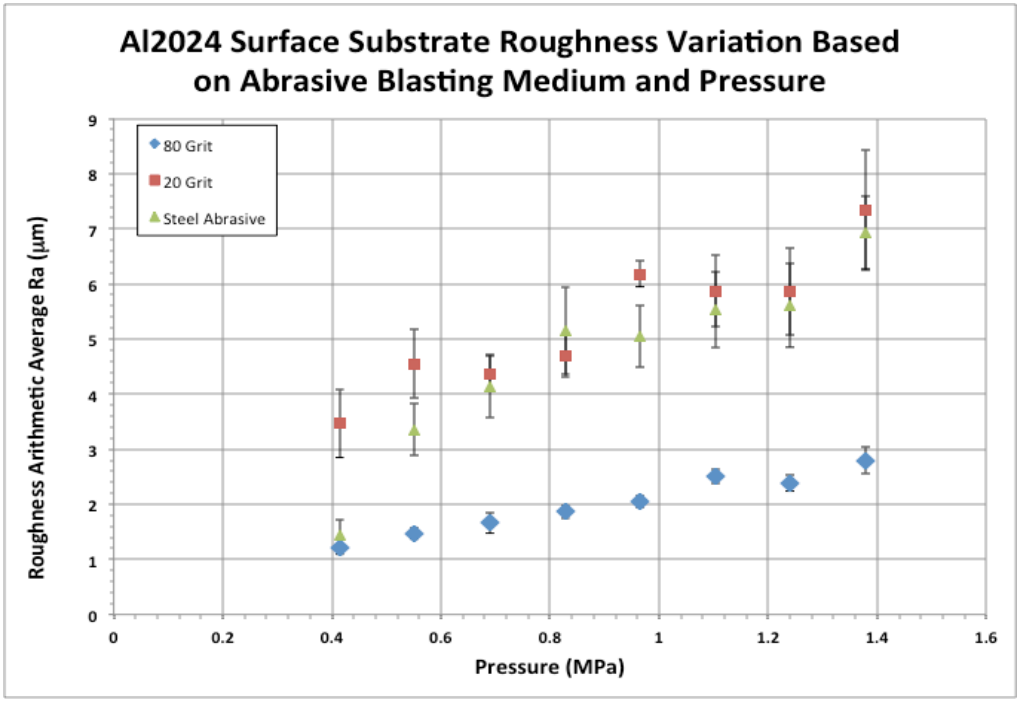

Figure 7.1: Al2024-T351 substrate surface roughness obtained through a grit blasting procedure using various abrasive medium and process pressures.

The substrate surface roughness varies linearly with the grit blasting pressure and augments for coarser abrasives. The roughness standard deviation increases as the amount of grit sprayed per surface area decreases with grit size. Coarser grit size induces larger plastic deformation of the substrate surface during every individual grit impact. Since the ferrosilicate 20 grit has a higher hardness than the steel grit, 7 and 4.36 respectively on the Mohs abrasive hardness scale, and a slightly larger grit size it will convert more energy into plastic deformation

during impact [157], [158]. As a consequence, higher roughnesses are obtained with the use of the ferrosilicate grit as opposed to the steel abrasive. Figure 7.2 depicts the obtained surface profiles after the grit blasting procedure at 0.55 MPa and 1.38 MPa using all three abrasive mediums. The waviness characterized by the valley to peak distance increases with grit blasting pressure and grit size. Moreover, intact portions on the surface grit blasted using the steel abrasive are seen mostly at lower pressure, which are caused by an observed decrease in grit flowability through the gun. Uniform coverage of the substrate surface is obtained when treated using ferrosilicate and aluminum oxide grits.

Substrate surface roughnesses ranging between 1.22 μm and 7.36 μm were obtained. Minimal grit embedment was observed during the high pressure grit blasting process using the ferrosilicate medium. Immersing the substrate into a vibratory bath dislodged most of the embedded grit from the surface.

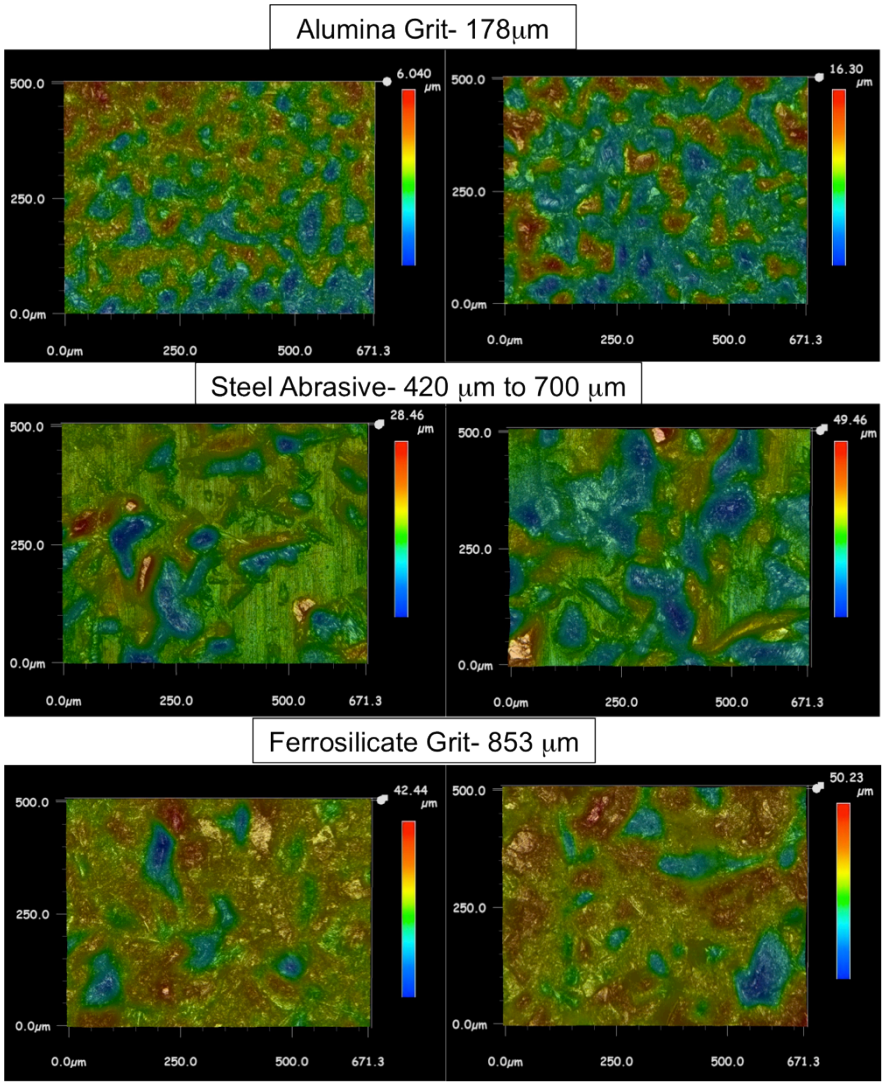

Figure 7.2: 3D scans of the Al2024-T351 surface profile grit blasted using different abrasive mediums at 0.55 MPa (left) and 1.38 MPa (right).

7.1.2. Adhesion Strength Test for the Al2024 Powder on Al2024-T351 Substrates

To analyze the influence of the substrate surface profile on the coating adhesion strength, four different substrate roughnesses have been tested. An as machined surface was produced to obtain the coating adhesion strength on a smooth Al2024-T351 substrate. Subsequently, three different substrate surface profiles have been produced through grit blasting procedures. The parameters for the different grit blasting processes have been selected based on the obtained

Al2024-T351 roughnesses presented in the previous subsection. Table 7.1 summarizes the chosen process properties for the surface treatment of Al2024-T351 adhesion samples.

Table 7.1:Grit Blasting Parameters for the Al2024 Adhesion Tests

Property	80 Grit	20 Grit	Steel
Pressure	0.55 MPa	0.55 MPa	1.38 MPa
Gas Nature	Nitrogen	Nitrogen	Nitrogen
Angle	45°	45°	45°

Four different surface roughnesses of 0.46µm, 1.74µm, 4.58µm and 7.34 µm were obtained, as shown in Figure 7.3.

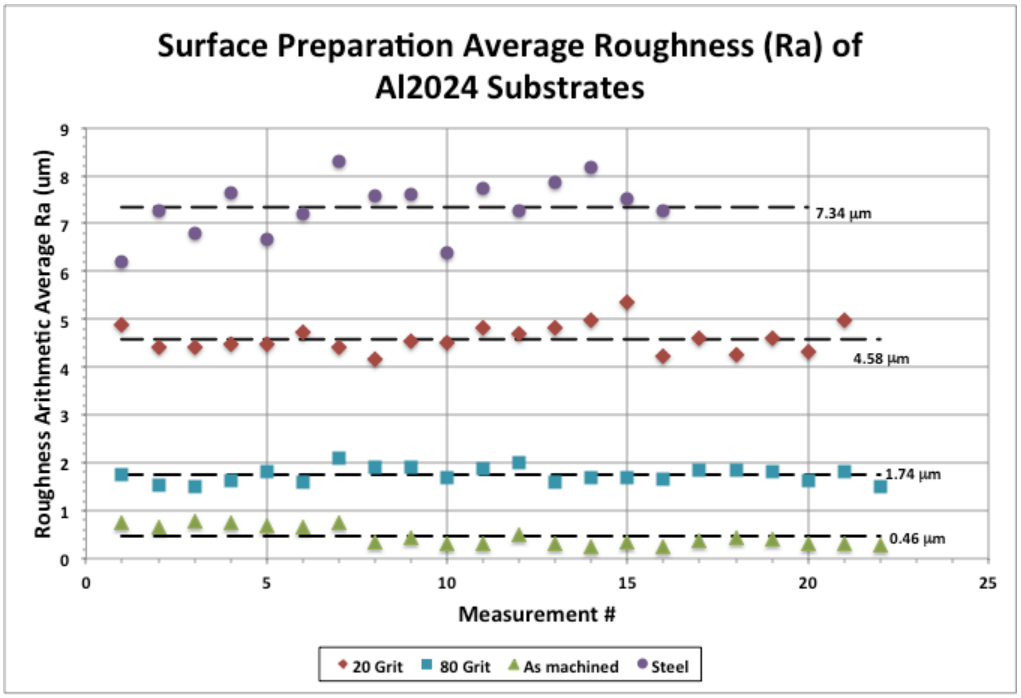

Figure 7.3: Substrate surface roughness measurement across 5 different samples with different surface profiles.

Table 7.2 shows the spraying parameters employed during the production of Al2024 coatings on Al2024-T351 bond plugs. Three passes have been used in order to produce a coating of thickness greater than 0.38 mm as required by the ASTM C633 standard. Regardless of the substrate roughness, all coating deposited had an average thickness of 0.762 ±0.12 mm. Once

sprayed, the coatings were machined down to approximately 0.56 mm using a lathe machine to obtain a surface thickness that is consistent across the entire coating surface.

Table 7.2: Spraying Parameters Used to Produce Coatings for the Bond Plugs Test Using Al2024 Powder

Parameters	Values
Gas Temperature	500 °C
Gas Pressure	3.44 MPa
Gas Nature	Nitrogen
Standoff Distance	25 mm
Traverse Velocity	15 mm/s
Nozzle Type	120 mm New Ultiflow Nozzle
Powder Feeder Wheel Type	320 Holes (Small Wheel)
Powder Feeding Rate	11.25 g/min
Powder Feeder Gas Flow Rate	30 SCFH
Powder Feeder Gas Nature	Nitrogen
Step Size	2 mm
Number of Passes	3

The coating bonding strength variation with the substrate roughness is depicted in Figure 7.4. It is to note that the adhesion value obtained for the surface roughness of 7.34 μm represents the adhesion strength of the glue used during testing. For those samples, the failure has occurred at the glue/coating interface such that the Al2024 adhesion strength is in fact higher than 82 MPa.

The lowest bond strength is obtained for a surface roughness of 1.74 μm. A decrease in roughness down to 0.46 μm or an increase up to 4.58 μm increases the resulting adhesion strength.

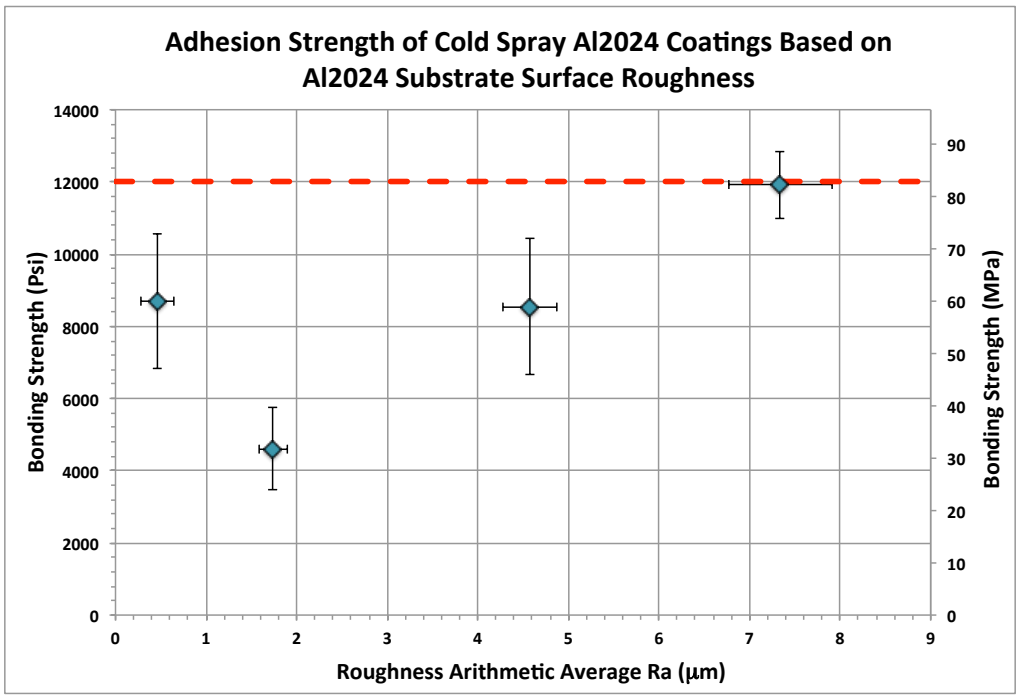

Figure 7.4: Al2024 coating bond strength on Al2024-T351 substrate where the red dotted line represents the average glue strength.

The adhesion strength values obtained for different surface substrate preparation are summarized in Table 7.3.

Table 7.3: Al2024 Adhesion Strength Summary

Surface Preparation medium	Ra (µm)	Bond strength (MPa)	Standard deviation (MPa)
As machined	0.46	59.93	±12.79
80 Grit	1.74	31.73	±7.89
20 Grit	4.58	58.90	±13.04
Steel	7.34	>82.24	±6.44

7.2 Adhesion Strength Test for the Pure Aluminum Powder on Al7075 Substrates

7.2.1. Al7075 Surface Preparation

Different abrasive media have been used to grit blast the Al7075-T6 substrate surface at different pressures ranging between 0.42 MPa and 1.38 MPa. Figure 7.5 shows the roughness arithmetic average (Ra) of the surface based on the grit blasting medium and pressure. For the alumina and ferrosilicate surface treatment, a grit blasting time of 20 seconds was used. However, longer times reaching 10 to 15 seconds have been utilized for the grit blasting procedure using steel abrasive in order to obtain a uniform surface roughness and reach profiles larger than 5 μm. Due to ferrosilicate embedment issues, longer grit blasting times or higher pressures were not tested.

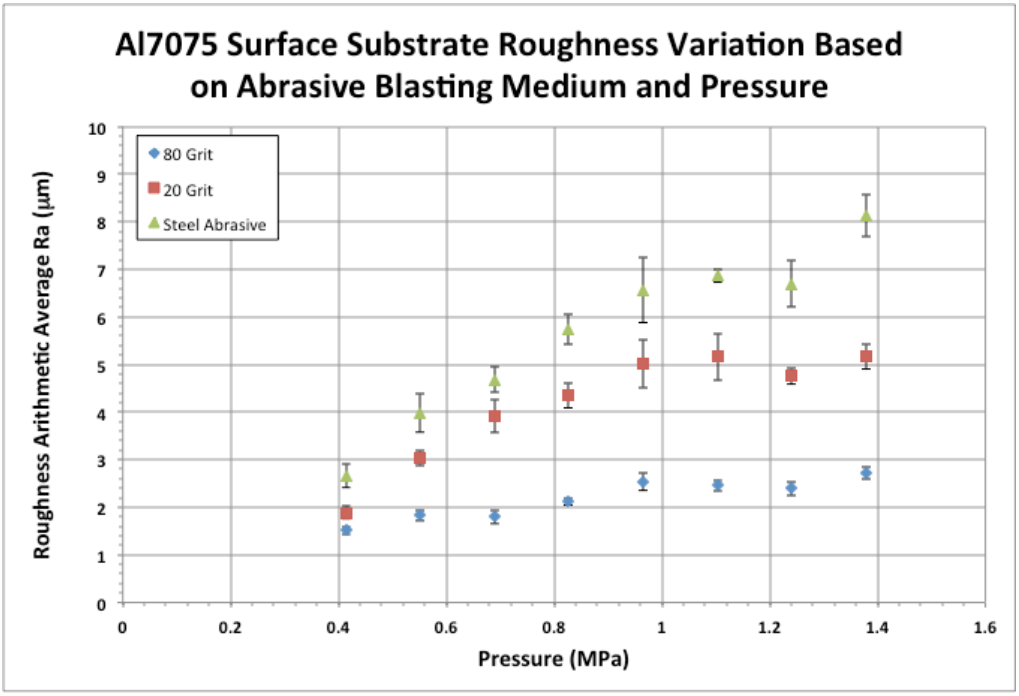

Figure 7.5: Al7075-T6 substrate surface roughness obtained through a grit blasting procedure using various abrasive medium and process pressures.

Based on the obtained results, surface roughnesses ranging between 0.41 μm and 8.1 μm were achieved through the use of different abrasive mediums and pressures. Due to the higher substrate surface hardness of the Al7075-T6 material, for the same surface treatment process, the

resulting roughnesses were lower than for the Al2024 material. Once again, the roughness profiles increase linearly with the substrate surface treatment process pressure. Larger and harder grits produce greater craters through plastic deformation on the substrate surface. Figure 7.6 depicts the substrate surface peaks and valleys size obtained when grit blasted at 0.55 MPa and 1.38 MPa using different abrasive mediums. Do to the increased grit blasting time, issues regarding the surface profile homogeneity encountered previously for the preparation of Al2024-T351 surfaces have been eliminated. As shown in the figure below, uniform coverage of the surface is achieved when treated using steel abrasives at all pressures.

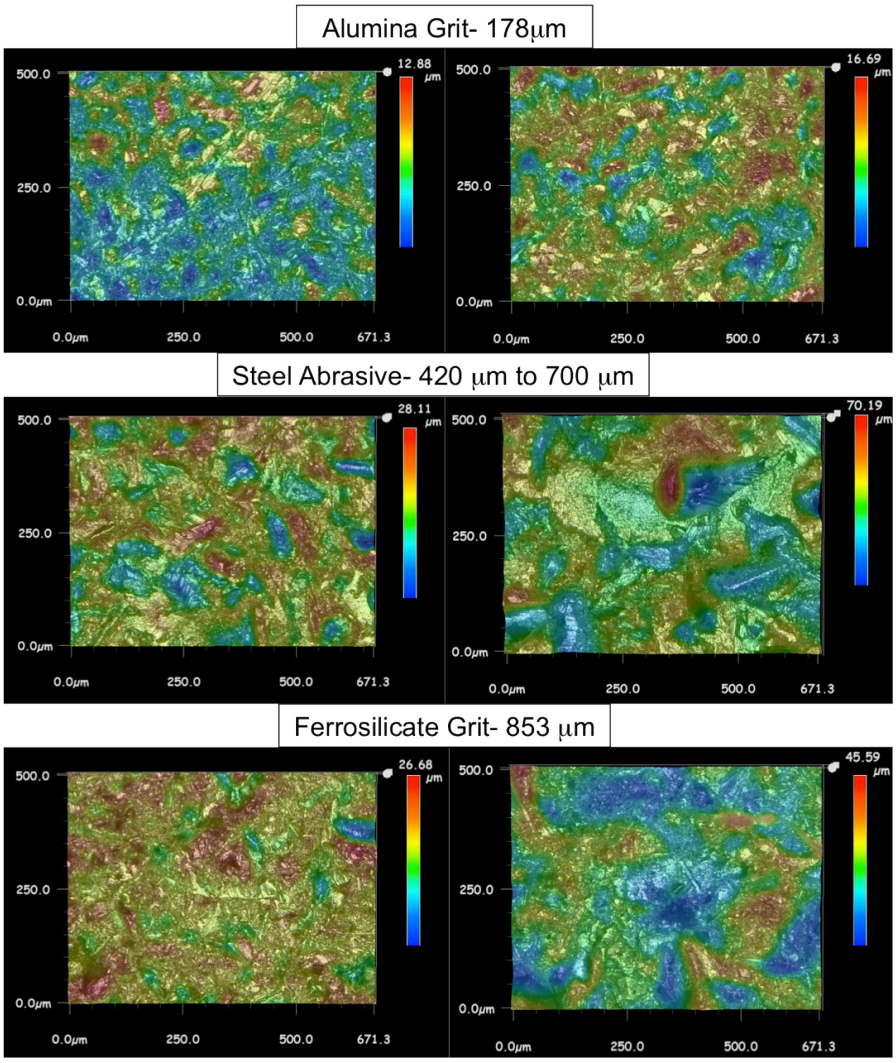

Figure 7.6: 3D scans of the Al7075-T6 surface profile grit blasted using different abrasive mediums at 0.55 MPa (left) and 1.38 MPa (right).

7.2.2. Adhesion Strength Test for Pure Aluminum Powder on Al7075 Substrates

The grit blasting parameters used to prepare the Al7075-T6 adhesion sample surfaces are presented in Table 7.4. The parameters have been chosen based on the results presented in the previous subsection and consequently on the surface roughness they generate.

Table 7.4:Grit Blasting Parameters for the Pure Aluminum Bond Plugs Tests

Property	80 Grit	20 Grit
Pressure	0.69 MPa	0.83 MPa
Gas Nature	Nitrogen	Nitrogen
Angle	45°	45°

Figure 7.7 depicts the average surface roughness measured across six samples. The adhesion of the pure aluminum coatings was tested for substrate surface roughnesses of 0.62 μm, 2.41 μm and 5.29 μm.

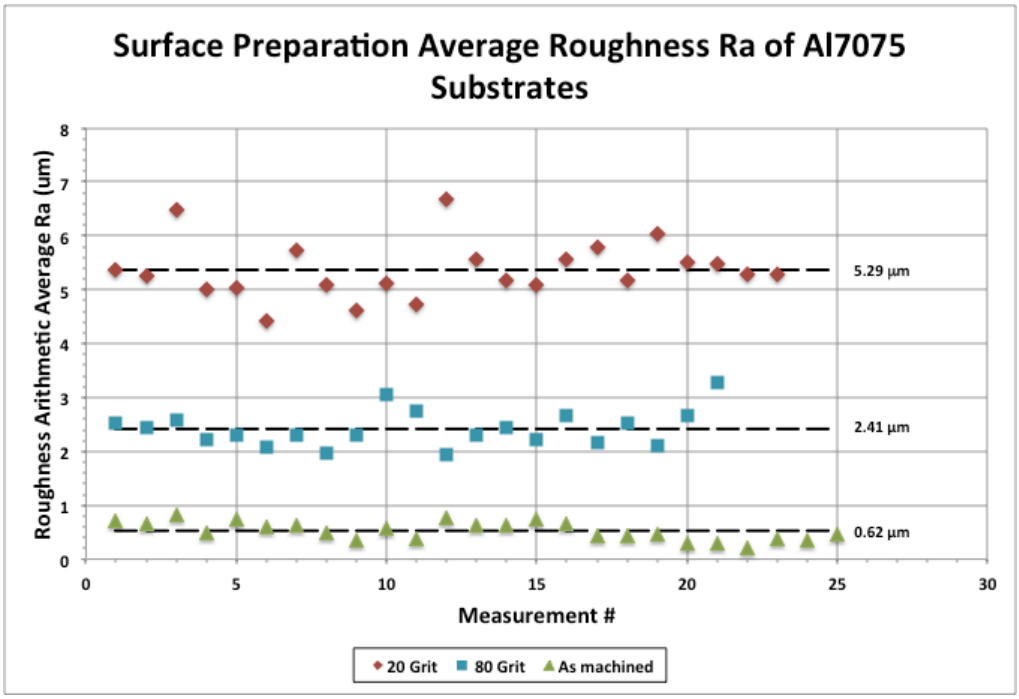

Figure 7.7: Substrate surface roughness measurement across 5 different samples with different surface profiles.

Table 7.5 presents the spraying parameters used to produce the pure aluminum coatings on the bond plugs surface. Three passes have been sprayed and a coating thickness of approximately 1.6 ±0.3 mm and 1.78 ±0.41 mm has been obtained for the as machined and grit blasted surfaces respectively. Subsequently, the coatings have been machined down to 0.56 mm in order to produce a flat coating surface as required by the standard.

Table 7.5: Spraying Parameters used to Produce Coatings for the Bond Plugs Test using Pure Aluminum Powder

Parameters	Values
Gas Temperature	500 °C
Gas Pressure	3.44 MPa
Gas Nature	Nitrogen
Standoff Distance	25 mm
Traverse Velocity	15 mm/s
Nozzle Type	120 mm New Ultiflow Nozzle
Powder Feeder Wheel Type	320 Holes (Small Wheel)
Powder Feeding Rate	4 g/min
Powder Feeder Gas Flow Rate	30 SCFH
Powder Feeder Gas Nature	Nitrogen
Step Size	2 mm
Number of Passes	3

Figure 7.8 presents the adhesion strengths achieved for the different substrate surface preparation procedures. All samples failed at the coating substrate interface in a manner characteristic to adhesion failure. The lowest strength of 29.1 MPa has been obtained for a substrate surface roughness of 2.41 μm. Larger strengths are obtained for coatings sprayed on substrates characterized by low roughness and a roughness of 5.29 μm. The presence of high standard deviations in the bonding strength values is probably caused by the presence of inconsistencies due to possible grit embedment. Moreover, the standard deviation in the case of the as machined surface could have been caused by any discrepancies created during machining.

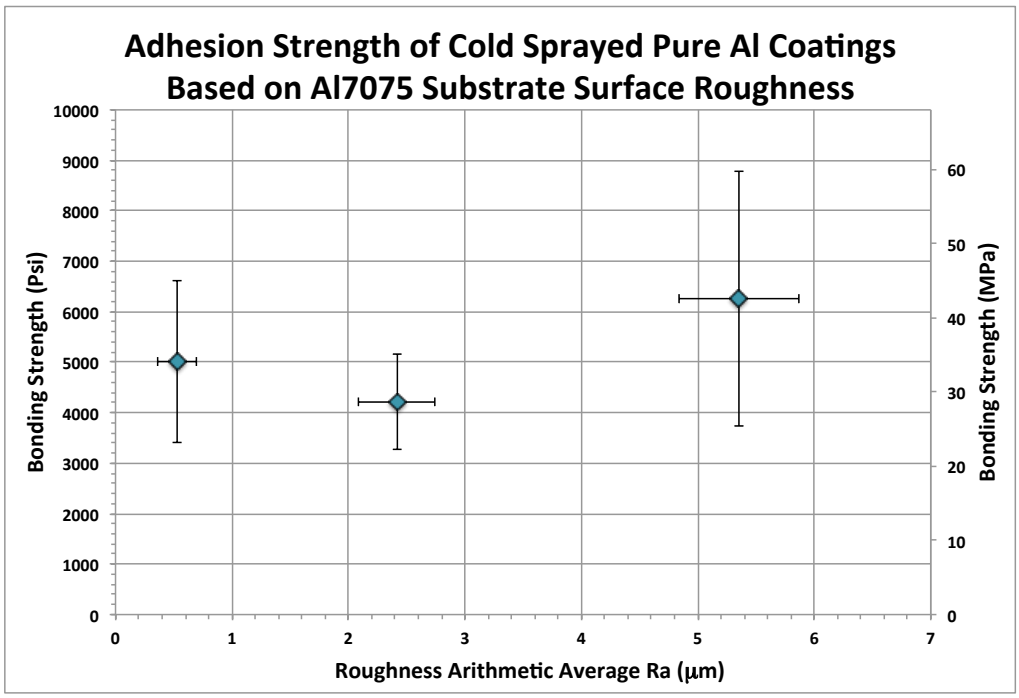

Figure 7.8: Pure aluminum coating bond strength on Al7075 substrate.

Table 7.6 summarizes the obtained adhesion strengths for different substrate surface roughness.

Table 7.6: Pure Aluminum Adhesion Strength Summary

Surface Preparation medium	Ra (μm)	Bond strength (MPa)	Standard deviation (MPa)
As machined	0.62	34.57	±11.1
80 Grit	2.41	29.1	±6.53
20 Grit	5.29	43.12	±17.46

Based on the obtained results, both the pure aluminum and Al2024 coatings have adhesion strength of approximately 30 MPa (with approximate surface roughness of 2 μm) when sprayed on surfaces grit blasted using 80 alumina grits. This means that both coatings should behave similarly and withstand a comparable stress when tested under identical conditions. However, for other surface preparation procedures, the Al2024 coatings should provide superior mechanical properties.

7.3 Adhesion/Cohesion Strength Mechanisms

This section analyses the effect of the surface profile features on the coating adhesion strength. It will discuss about the bonding mechanisms that control the coating adhesion for various surface preparation procedures of both the Al2024 and pure aluminum powders.

7.3.1. Particle Surface Contact Area

Based on the obtained results, the substrate surface profile affects the bonding process of the particles during the coating production. The substrate/coating interface state and coating initiation is influenced by the substrate surface asperities size. As the unevenness of the substrate surface is amplified so is the surface contact area. As a consequent result, the mechanical and metallurgical interactions between the particle and substrate material during impact is significantly affected and amplified. Figure 7.9 illustrates the concept that connects the surface contact area to the coating adhesion strength.

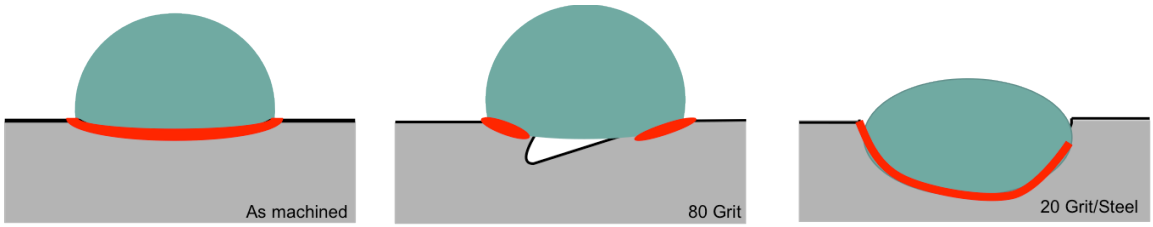

Figure 7.9: Illustration of the particle surface contact area based on substrate surface roughness.

Figure 7.9 schematically illustrates the type of contact that exists between the particle and substrate surface for different boundary waviness and void size, assuming an oxide free interaction. The degree of deformation and preferential deposition of the particles is affected by the particle size relative to the voids dimensions. For a smooth substrate surface, the particle metal jetting phenomenon and deformation process is not hindered or affected by any surface boundary defects, irregularities, voids or valleys. As such, once the oxide layers are disrupted, the contact area between the clean metal surfaces is only limited by the particle size after deformation under high pressure. As the number of anchoring sites is limited on a smooth substrate surface, the adhesion of the first coating layer occurs through metallurgical bonding or/and through mechanical interlocking as the substrate surface deforms during the particles impact. For a

substrate surface profile altered through a grit blasting procedure using an 80 grit mesh size medium to create a roughness close to 2 μm, the coating adhesion to the substrate surface is deteriorated. This type of surface, which is characterized by cavities, does not allow proper deformation and deposition of particles that are larger than the created surface irregularities. The voids found at the particle/substrate interface disable any contact that might create bonding and therefore lead to a reduction in the location of possible mechanical anchoring and metallurgical bonding as shown in Figure 7.9. In the case of a substrate roughness close to 5 μm, the results presented in Figure 7.4 and Figure 7.8 show an increase in adhesion for both the Al2024 and pure aluminum coatings respectively. A higher roughness exhibits larger asperities and surface irregularities, which presumably facilitate particle deposition and deformation. The particles tend to properly fit inside the cavities or enfold around the surface peaks and valleys, which increases the contact area and the number of possible pure metallic bonding. As a consequence, the particle size relative to the craters created through the grit blasting procedure is an important factor that greatly influences the type of interaction necessary for proper adhesion between the particle and substrate surface.

Figure 7.10 shows the cross section of the Al2024 coatings after being tested in adhesion. The micrographs shown give details on the type of failure that has occurred at the coating/substrate interface for different substrate roughnesses. It is noticed from Figure 7.10a that coatings sprayed on an as machined surface display good adhesion but low internal cohesion that result in intermittent disjunction of single particles and portion of the coating near the substrate interface. Based on Figure 7.10b, the low adhesion values reported for coatings sprayed on a substrate surface roughness of 1.74 μm result from poor particle mechanical anchoring within the substrate surface. Small voids and discontinuous particle contact with the substrate surface might limit the adhesion strength to values close to 39 MPa. Small amount of de-cohesion between individual particles is also observed. It is seen from Figure 7.10c that for larger substrate surface roughnesses, de-cohesion between particles is also observed similarly as in the other cases. However, the coating adhesion strength was able to reach values up to 77 MPa.

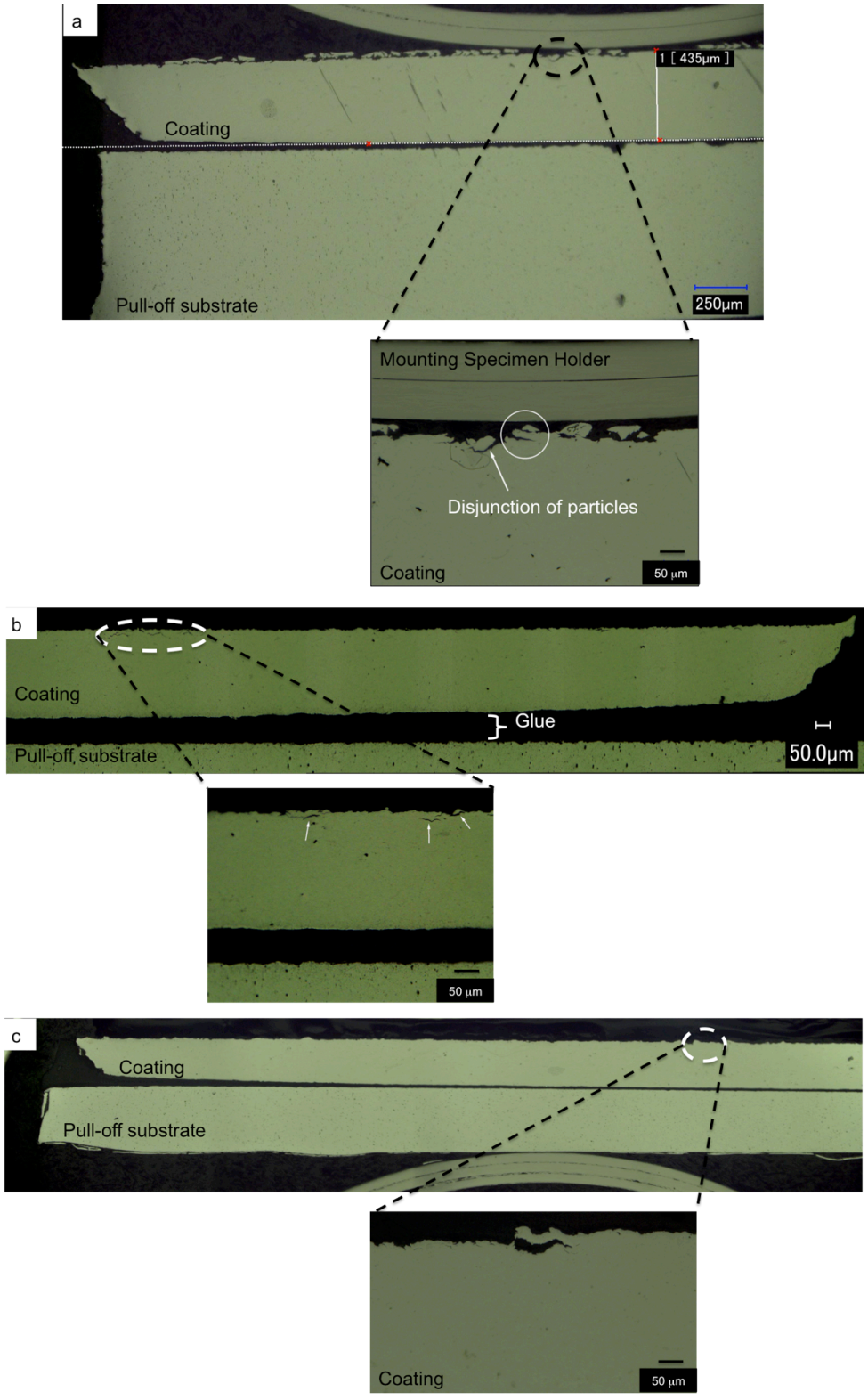

Figure 7.10: Al2024 coating and substrate interface after the adhesion test, a) for the as machined substrate surface b) for the 80 grit surface substrate preparation and c) for the 20 grit substrate preparation.

Figure 7.11 shows the pure aluminum deposits cross-sectional area following the adhesion test for all three surface preparation procedures with zoomed-in inserts of the coating profile at the failure side.

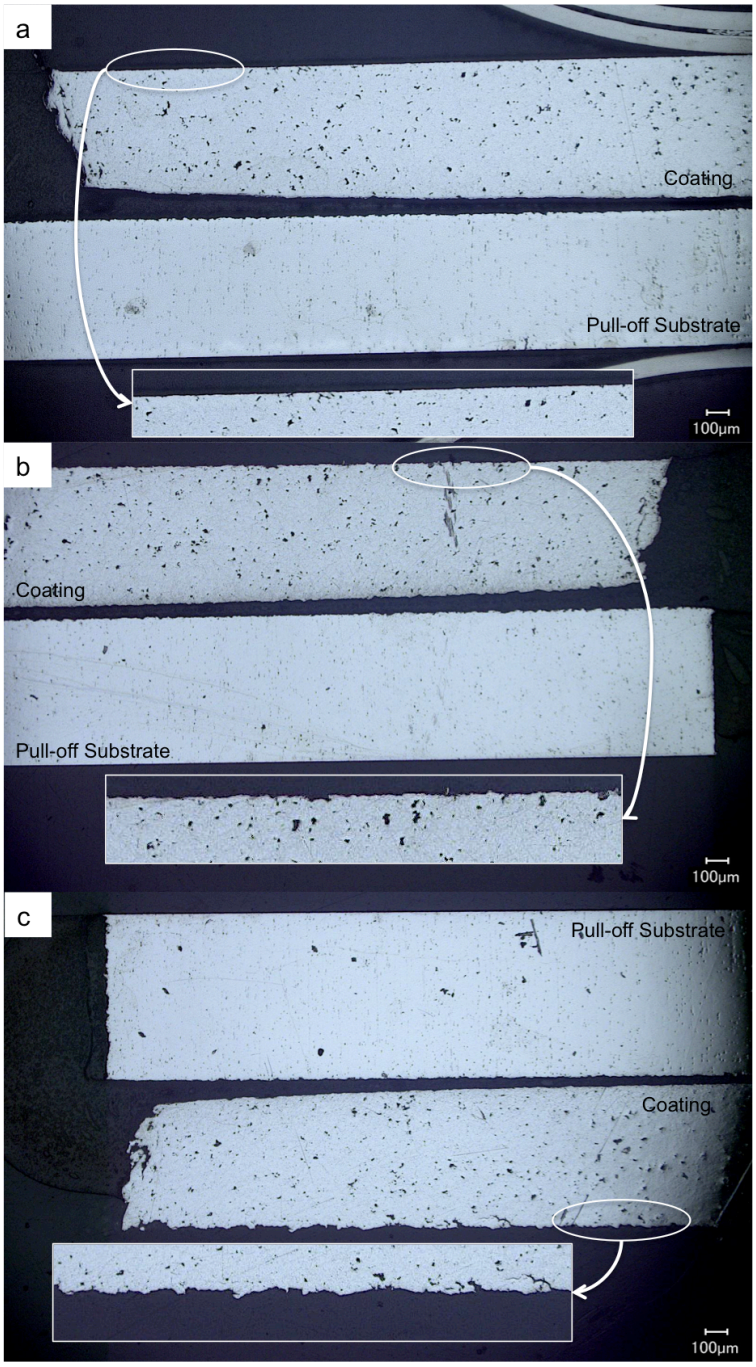

Figure 7.11: Pure aluminum coating and substrate interface after the bond plugs test, a) for the as machined substrate surface b) for the 80 grit surface substrate preparation and c) for the 20 grit substrate preparation.

Due to the smooth fracture interface, Figure 7.11a supports that metallurgical bonding or/and mechanical anchoring produced during the deformation of the substrate surface at the particle impact process are the main adhesion mechanisms that provide particle adhesion during its deposition. The cross-section of the coating sprayed on a substrate roughness of 5.29 μm after the adhesion test is shown in Figure 7.11c. Inter-particle de-cohesion and coating surface irregularity is evidence of proper particle mechanical interlocking and metallurgical bonding. The low adhesion strength and coating surface waviness upholds that low substrate surface roughness profile (~2.41 μm) influences the particle deformation process and impedes its adhesion.

7.3.2. Particle Hardness and Deformation Process

Based on the results, the Al2024 particles tend to adhere more strongly to the substrate surface than the pure aluminum for specific substrate surface profiles. The deformation process of the individual particles during impact is influenced by the hardness of the particles and substrate material [121]. When the sprayed particles are softer than the substrate, they experience extensive deformation through the dissipation of kinetic energy into plastic energy during impact. High particle deformation is known to lead to metal jetting, increased interfacial contact area, proper particle oxide layer removal process and improved bonding strength. Despite the low hardness and lack of strength of pure aluminum particles used in this study, their adhesion strength to the substrate was inferior to the adhesion between the Al2024 particles and Al2024-T351 substrate material. The harder Al2024 particles can induce larger substrate deformation at the interfacial zone during impact, which can lead to higher particle mechanical anchoring. Therefore, a larger particle penetration depth into the substrate surface can lead to an improved particle mechanical interlocking and consequently larger coating adhesion strengths. The increased deformation of both the particle and substrate surface permits a better insertion of the particles into the substrate voids increasing the surface bonding area.

The adhesion strength results obtained through the bond plug tests justify the need to evaluate the maximum load carrying capacity of the pure aluminum thread repairs presented in Chapter 6. Despite withstanding the preliminary required torque, the actual structural capacity of the system should be evaluated in order to determine the repair safety factor.

Obtaining a representative approximation of the shear stress applied to the coating/substrate interface during the torque test is difficult due to the indeterminate friction coefficient and unpredictable material surface roughness, which affects the torque-tension relationship. However, it is suitable to state that only the Al2024 repairs have failed during the machining procedure, which indicates that the stress level reached during the machining significantly influences the repair adhesion strength prior to testing. The low wear resistance, high ductility, good machinability and low strength of the pure aluminum coatings reduces the required tool cutting axial force and power needed to remove the necessary material. These material properties in addition to the large surface area of the repaired 88.9 mm diameter component reduce the shear stress applied at the coating/substrate interface and preserve the particle adhesion strength obtained after the CS process. Finally, large machining stresses involved during the Al2024 threads restoration are believed to be responsible of reducing the load carrying capacity of the repairs by disturbing the coating/substrate interface stress state. Lack of control and precision during the machining procedure generates large inconsistencies between the obtained Al2024 repair load carrying capacities.

It is to note that the particle size and morphology affect the in-flight particle velocity, deformation, deposition efficiency and particle stacking process. Due to their low inertia, smaller particles tend to accelerate to velocities closer to that of the gas flow, which increases their available kinetic energy for plastic deformation. The deceleration effect of the bow shock region on the particle deposition process is influenced by the particle density and size. Moreover, according to data found in the literature [159], [160], the effect of strain rate hardening is larger in smaller particles, which reduces their ability to plasticity deform. The heat conduction within smaller particles can be more substantial than in larger particles, which can affect the strain localisation, the adiabatic shear instability and as a result the deformation and particle jetting phenomenon. In the present study, the degree of influence of particle shape over particle size on the deposition process has not been fully investigated to provide insight on the matter. Similarly, the influence of the particle chemical composition on the deformation process has not been the focus of this study.

Variation in Al2024 deposition efficiency has been encountered after the previous adhesion tests and is described in details in Appendix III. Due to the sudden and large decrease in deposition efficiency, additional repairs of the Al2024-T351 threads have not been produced

using new substrate surface procedures to attempt increasing the deposition adhesion strength. Despite being able to deposit the powder at a minimal rate, to repair more threads would have required resources (i.e. powder material and gas) of industrial capacity. Moreover, repairs produced at low deposition efficiency are economically unsuited for any type of manufacturing industry.

CHAPTER 8

Nozzle Properties Influence on Powder Flow Distribution and Deposition

Inconsistencies in powder deposition distribution have been observed during the repair of large components presented in the previous chapters. After long periods of spray, it was noticed that the polymer nozzle experiences severe erosion on its internal walls. Therefore, the current chapter analyses the powder feeding rate influence on the nozzle wear rate and location. The effect of the nozzle erosion on the particle exit velocity and flow distribution is also investigated through the use of the cold spray meter.

The polymer nozzles had to be replaced once the wear significantly altered their internal geometry and dimensions. Thus, in order to reduce the occurrence of nozzle wear and replacement, ceramic nozzles have been machined and used to generate preliminary deposition of Al2024 on Al2024-T351 flat substrates. The achieved deposition efficiency and coating quality has been analyzed and presented in the current chapter.

8.1 Polymer Nozzle Wear

The erosion of the PBI nozzle occurs during the collision of Al2024 particles with the nozzle interior walls and is influenced by the powder flow characteristics. The wear rate has been examined for two PBI nozzles; a new nozzle with no wear and a worn nozzle that has previously experienced erosion. Table 8.1 presents the material removal rate of both nozzles after a series of sprays conducted at 500 °C and 3.45 MPa. The material removal rate with respect to the spray time and the powder mass feeding rate are specified. The powder feeder gas flow rate was set to 30 SCFH for all tests.

Table 8.1: Material Removal Rate of Polymer Nozzles During the Spray of Al2024 Powder

	Powder feeding rate (g/min)	Time sprayed (minutes)	Material Removed (g/min)
		New Nozzle	
Spray N1	1 g/min	~ 10 minutes	0.0077
Spray N2	11.25 g/min	~ 10 minutes	0.0021
		Worn Nozzle	
Spray O1	1 g/min	~ 10 minutes	0.0062
Spray O2	11.25 g/min	~ 3 minutes	0.0023

The obtained results indicate that the material removal process and rate remains consistent for both nozzles despite their difference in initial erosion level. The average material removal rate is 0.0070 g/min and 0.0022 g/min for powder feeding rates of 1 g/min and 11.25 g/min respectively. The trajectories of the injected particles is hypothesized to change based on the total mass of inserted particles, which would support the obtained results.

The interference level between individual particles inside the flow increases with increasing powder feeding rates, which can lead to a decrease in individual particle velocity and energy. As a consequence, the stress involved during the impact of particles with the nozzle walls is reduced and the erosion process weakened. Furthermore, large mass feeding rates (i.e. 11.25 g/min) can cause obstruction across the powder inlet hole and initiate inconsistent feeding and

unpredictable particle trajectory. Inhomogeneous powder entry at the nozzle inlet can also affect the nozzle wear rate, profile and location.

The nozzle erosion site is located near the powder inlet and remains consistent throughout the first nozzle step (i.e. 31.75 mm from the inlet) as illustrated in Figure 8.1. Due to possible flow swirling, the wear profile path is interrupted at the second step and appears at different locations on the nozzle internal periphery. Finally, the eroded area increases at the nozzle exit walls as demonstrated in Figure 8.1.

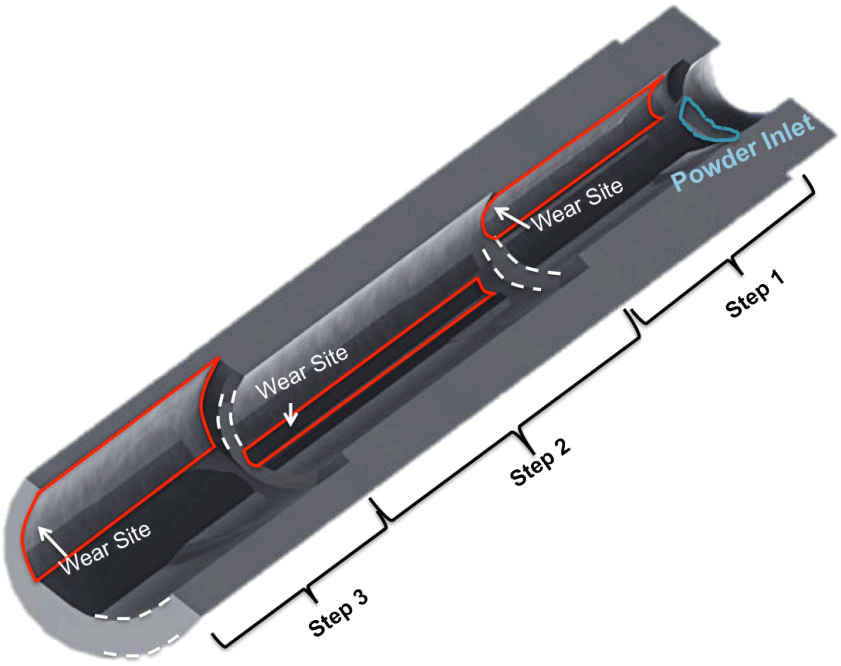

Figure 8.1: Illustration of the polymer nozzle erosion site and location.

It is worth mentioning that only limited marks of erosions were observable on the opposite wall of the powder inlet, which indicates that the particle rebounding process inside the nozzle is limited and/or the particles that do reach the opposite side lack energy. The trajectory of the particles obtained inside the nozzle during the tests might differ for a different powder feeding gas flow rate. A larger gas flow rate would facilitate the propulsion of the particles inside the nozzle towards the wall opposite to the powder inlet, which would cause variation in particle flow and nozzle erosion process. Figure 8.2 depicts the nozzle exit diameter before and after the erosion process and emphasizes on the nozzle loss of circularity due to the wear process.

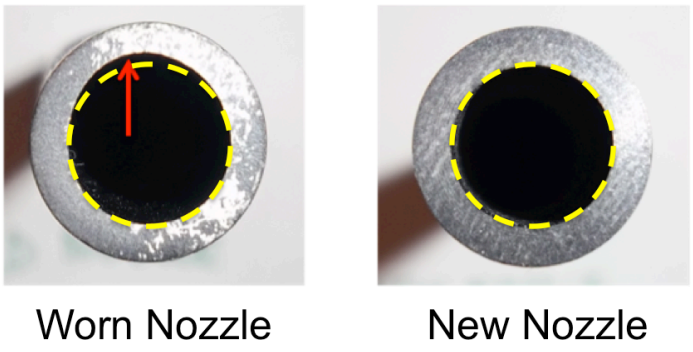

Figure 8.2: Erosion sustained at the exit of the nozzle.

8.2 Influence of Nozzle Internal Geometry on Powder Deposition

To analyze the influence of nozzle wear on the deposition process, single line coatings have been produced with the use of a new (i.e. presents no visible erosion) and worn polymer nozzle. As shown in Figure 8.3, the coatings have been produced across two different spraying directions perpendicular to one another. The powder injection point has been placed perpendicular and parallel to the spraying direction 1 and direction 2 respectively.

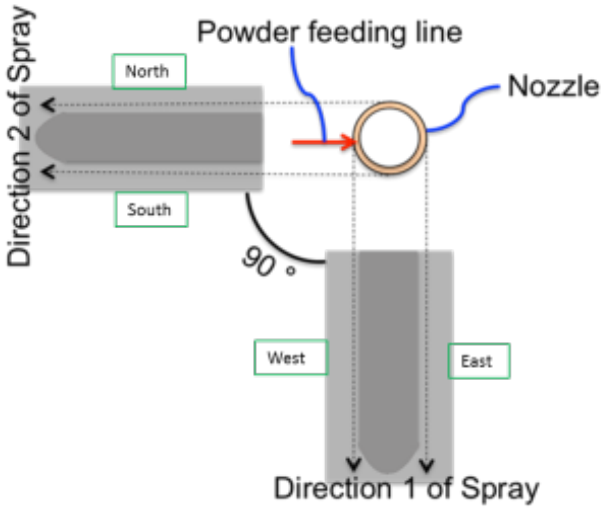

Figure 8.3: Single line coatings set-up illustration.

The coatings have been sprayed using the parameters presented in Table 8.2 on small 25.4 mm by 19.05 mm Al2024-T351 substrate material grit blasted using the early aluminum oxide 80 mesh procedure.

Table 8.2: Single Line Coating Spraying Parameters

Parameters	Values
Gas Temperature	500 °C
Gas Pressure	3.44 MPa
Gas Nature	Nitrogen
Standoff Distance	25 mm
Traverse Velocity	15 mm/s
Powder Feeder Wheel Type	320 Holes (Small Wheel)
Powder Feeding Rate	11.25 g/min
Powder Feeder Gas Flow Rate	30 SCFH
Powder Feeder Gas Nature	Nitrogen
Number of Passes	6

The single line coatings were scanned using the 3D microscope and the obtained profiles are shown in Figure 8.4 to Figure 8.7. Dotted lines have been added to Figure 8.4 to define and distinguish regions of high deposition, low deposition and erosion zones. These regions describe the transition process of particle deposition influenced by their resulting trajectory across the nozzle exit flow as described in subsection 6.1.1. The coatings sprayed with the new nozzle are depicted in Figure 8.4 and Figure 8.5 for depositions obtained along direction 1 and direction 2 respectively. Both coatings are symmetrical with respect to the high deposition zone and the thickness is similar in both spraying directions.

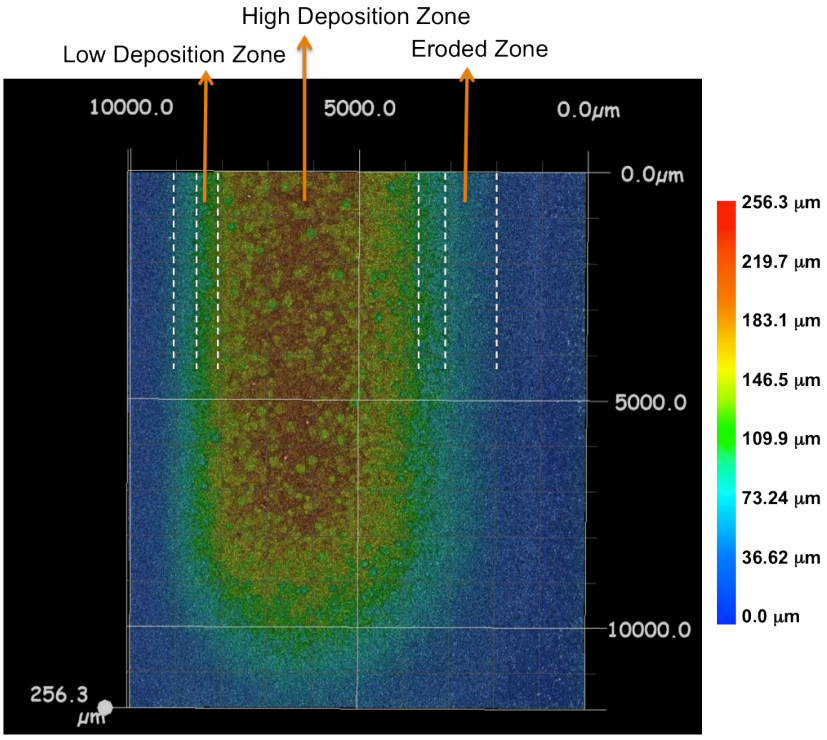

Figure 8.4: Single line deposition along direction 1 using a new polymer nozzle.

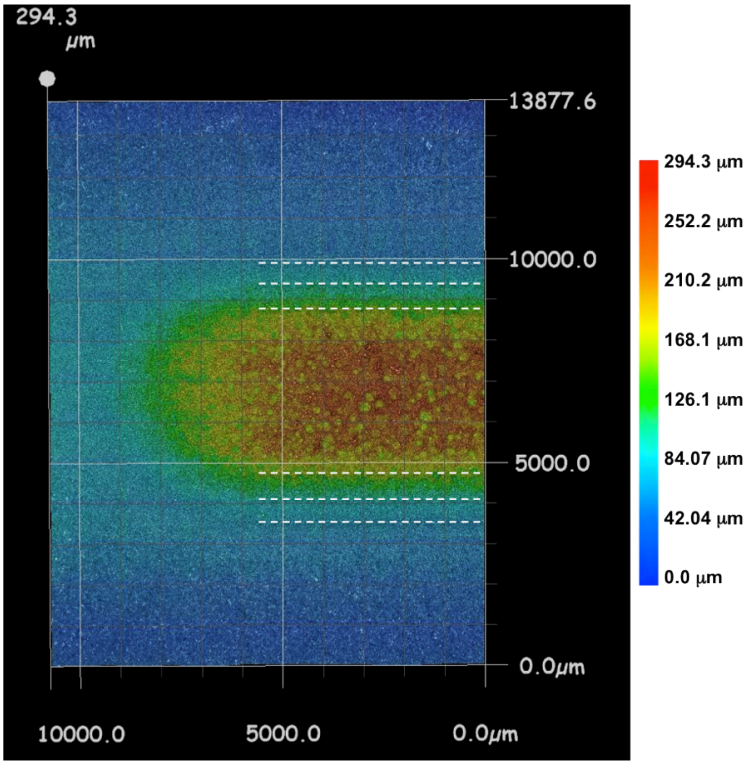

Figure 8.5: Single line deposition along direction 2 using a new polymer nozzle.

The lines obtained using the old nozzle are asymmetrical with respect to the center of the coating. In direction 1, the erosion zone is almost 3 times larger on the west side than on the east side. In direction 2, the erosion zone on the north side of the coating is nearly 6 times larger than the same zone on the south side of the coating. Moreover, the coating thickness increases from 269.5µm from direction 1 to 359.5µm in direction 2.

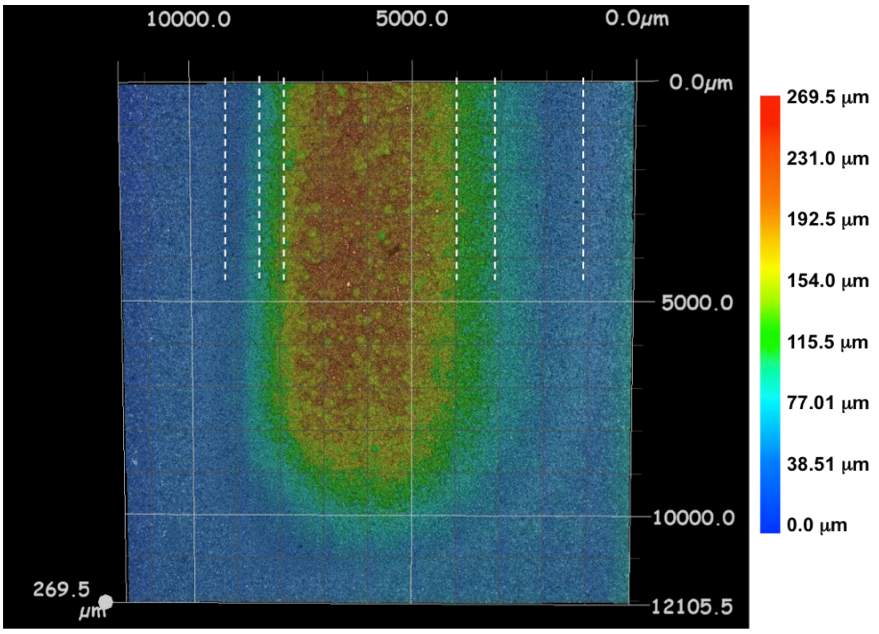

Figure 8.6: Single line deposition along direction 1 using a worn polymer nozzle.

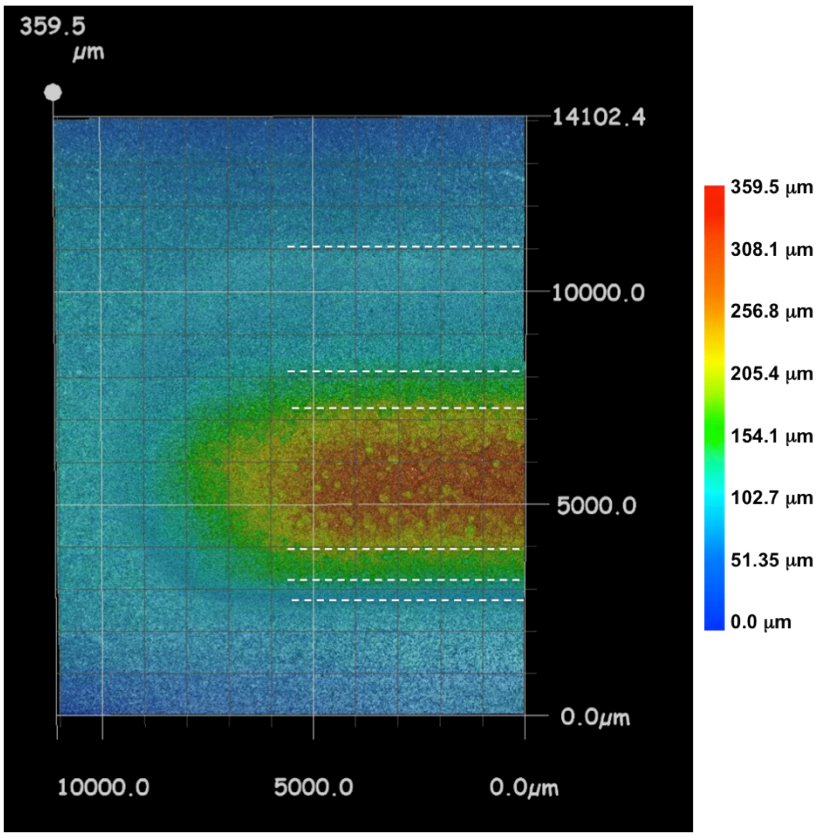

Figure 8.7: Single line deposition along direction 2 using a worn polymer nozzle.

Table 8.3 summarizes the dimensions of different deposition zones obtained during the use of both nozzles and along both directions. Based on the results, the particle deposition process is influenced by the nozzle erosion. The eroded part of the nozzle spreads the exiting powder stream but decreases the width of the effective deposition. It is observed that for coatings generated using the worn nozzle, the width of the high deposition zone is decreased but its thickness is increased, which indicates that the particle deposition efficiency isn't altered but rather shifted in location and limited in size. As a consequence, during the spray of large repairs, the coating requires additional layers to overcompensate for the loss of deposition in distinct regions (i.e. low deposition and eroded zones) under the nozzle.

Table 8.3: Al2024 Single Line Coating Characteristics Summary

	Width of High Deposition Zone (mm)	Width of Low Deposition Zone (mm)	Width of the Eroded Zone (mm)	Total Width of Line (mm)	Thickness of Coating (μm)
			NEW NOZZLE		
Direction 1	≈ 4.1 mm	0.3 mm (west) to 1.2 mm (east)	0.5 mm (west) to 0.8 mm (east)	6.9 mm	≈256.3 μm
Direction 2	≈4 mm	0.5 mm	0.5 mm	6.0 mm	≈294.3 μm
			WORN NOZZLE		
Direction 1	≈3.8 mm	0.75 mm	0.75 mm (west) to 1.5 mm (east)	7.25 mm	≈269.5 μm
Direction 2	≈3.5 mm	0.5 mm (south) to 1 mm (north)	0.5 mm (south) to 2.8 mm (north)	8.3 mm	≈359.5 μm

The following subsection will present the effect of nozzle wear on the coating accumulation process and multi-line deposition.

8.2.1. Nozzle Wear Influence on Coating Growth Process

New and worn polymer nozzles were used to deposit regular single and five layers Al2024 coatings on small Al2024-T351 substrates. Table 8.4 presents the spraying parameters used during the process.

Table 8.4:Spraying Parameters for Flat Substrates

Parameters Selection	Values
Gas Temperature	500 °C
Gas Pressure	3.44 MPa
Gas Nature	Nitrogen
Standoff Distance	0.25 mm
Traverse Velocity	15 mm/s
Powder Feeder Wheel Type	320 Holes (Small Wheel)
Powder Feeding Rate	11.25 g/min
Powder Feeder Gas Flow Rate	30 SCFH
Powder Feeder Gas Nature	Nitrogen
Step Size	2mm

Figure 8.8 shows the single layer coatings microstructure and thickness obtained using a new and worn nozzle. A difference of 73.69 μm exists between the two depositions; a thicker coating is produced with the unworn nozzle. Both coatings were dense, which indicates that the particle deformation process during impact is not altered. Despite showing in the previous section that the nozzle wear process mainly influences the position of the effective deposition, it seems, based on the current results, that further nozzle erosion also causes a decrease in particle deposition efficiency. Thus, the discontinuous nature of the powder deposition when sprayed with an eroded nozzle is also followed by a severe decrease in material growth. As such, a wear threshold value should exist to express the beginning of particle deposition efficiency decrease. Factors that might be responsible for such decrease are the resulting bow shock dimensions and geometry and selective flow saturation, which can affect the particle momentum prior to its impact with the substrate surface.

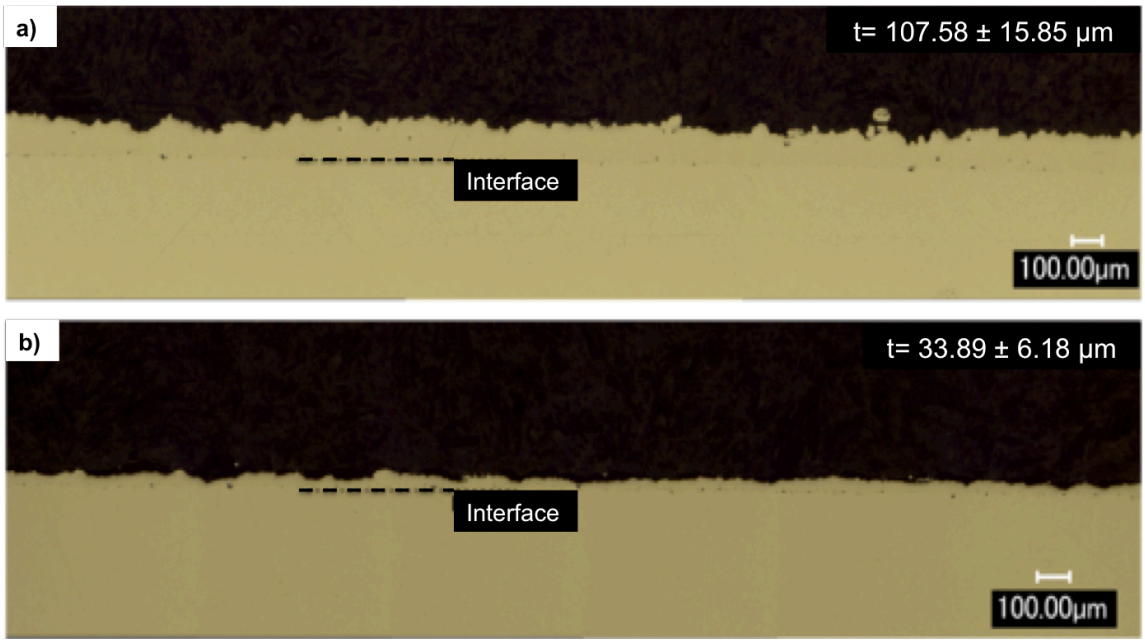

Figure 8.8: 1 layer coatings obtained using a) new polymer nozzle and b) old polymer nozzle.

Figure 8.9 depicts the multilayer dense coatings obtained using both nozzles. The growth rate is evidently higher when sprayed with a nozzle that has not been altered through an erosion process.

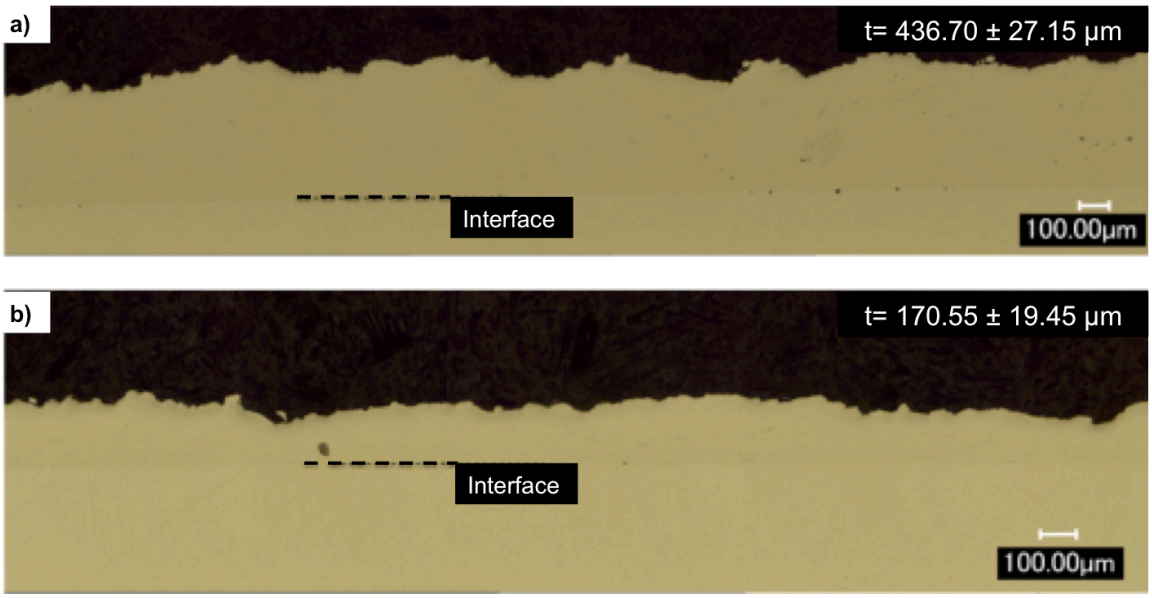

Figure 8.9: 5 layer coatings obtained using a) new polymer nozzle and b) old polymer nozzle.

Using the measured average coating thickness deposited using the worn nozzle reveals that the deposition progression from a single layer to a multilayer is proportional and that the deposition rate is maintained. A single layer of 33 μm grows to 170 μm when the spraying process is prolonged and the amount of deposited particles increased. However, the coating thickness sprayed with an unworn nozzle increases from 107 μm to only 436 μm from a single to a quintuple increase in layers respectively. The uniform and symmetrical particle deposition exposes the entire coated area to equal impingement from subsequent particle deposition, which could explain the disproportionate coating growth. Increased impingement processes further increase the particle deformation, contact level and micro voids reduction, which result in coating thickness reduction.

It is important to mention that the deposition efficiency of the Al2024 powder using the unworn nozzle has severely decreased for the tests conducted in the current chapter. The thickness obtained using the same process parameters and substrate preparation procedures than the ones initially used for the preliminary tests, presented in Chapter 5, have now generated coatings that are less than half the thickness obtained at the start of the research. Appendix III discusses in more details about the experienced variations and the different tests that have been conducted to understand the origin and cause of such change in particle deposition efficiency.

8.3 Powder Flow, Velocity and Particle Size Distribution

The current subsection studies the effects of nozzle wear on particle trajectory within the flow. The particle effective deposition deviation from the center of the flow has been studied further through the production of single spot sprays by placing the gun in a stationary position. Moreover, particle in-flight properties and location within the gas stream at the exit of the nozzle have been analysed for both the unworn and worn nozzle using a cold spray meter.

8.3.1. Particle Trajectory at the Exit of an Unworn Nozzle

Figure 8.10 shows the spot deposition profile sprayed at maximum parameters and SOD of 25 mm. Theoretically, deposition gradually and symmetrically decreases from the center of the expanding flow towards the jet periphery (i.e increasing axial position). Particles near the flow boundary rebound from the substrate surface due to a lack of velocity, which leaves the substrate

with an eroded like surface as it undergoes deformation during particle impact. The progressive nature of the particle deposition across the jet stream is clearly observed in Figure 8.10 from the cone like shaped circular structure. The volume of deposited particles reaches its peak 286.7 µm thickness near the center of the nozzle and decreases gradually toward the jet boundary to 81.90 µm. The slight shift of the effective deposition zone from the nozzle axis is the result of complex particles flow dynamics. The particle flow inside the jet stream appears to be independent of the powder inlet location as the deposition pattern is not repulsed or attracted towards it. The resulting coating surface crater like roughness is caused by the selective particle deposition position and impingement of successive particle impact

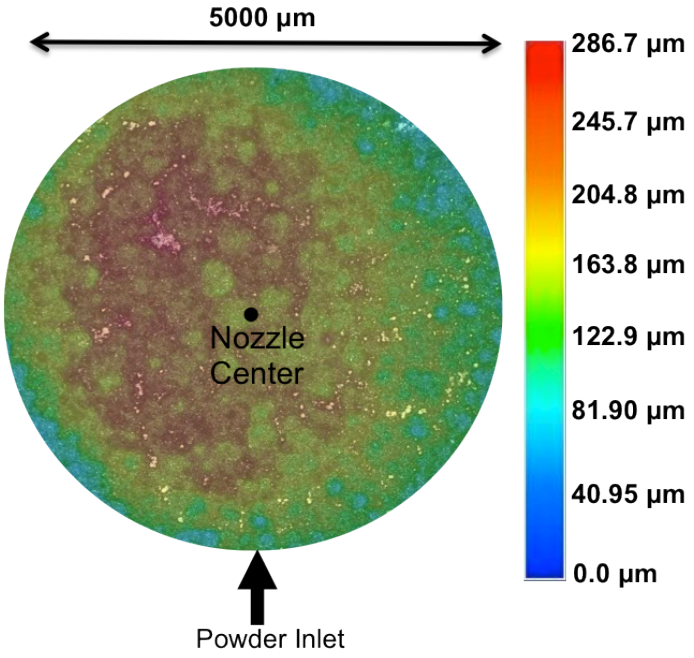

Figure 8.10: 3D scan of the single Al2024 spot spray surface profile using an unworn PBI nozzle.

8.3.2. Particle Trajectory at the Exit of a Worn Nozzle

Figure 8.11 presents the unconventional shape of the spray spot obtained when using the worn nozzle. The deposited pattern diverges from the regular circular shape and drastic loss in substrate surface coverage is experienced. No deposition was observed outside the 5 mm shown area. Powder is only deposited on a small portion of the surface that is within the limits of half of the stream jet diameter. The substrate under the nozzle central axis has mainly undergone plastic

deformation due to rebounding particles and only slight deposition. This validates the results presented previously concerning the low deposition growth process caused by particle flow deflection. Moreover, the particle effective deposition is favourably located to the right side of the powder inlet. Based on the PBI nozzle erosion patterns illustrated in subsection 0, the powder inside the flow is strictly concentrated at the first wear location near the powder entry. This supports the hypothesis that the powder distribution inside the flow is the same during its entry and exit of the diverging nozzle section and consequently the same erosion patterns are obtained at those locations. However, the exact flow evolution inside the nozzle still remains unknown.

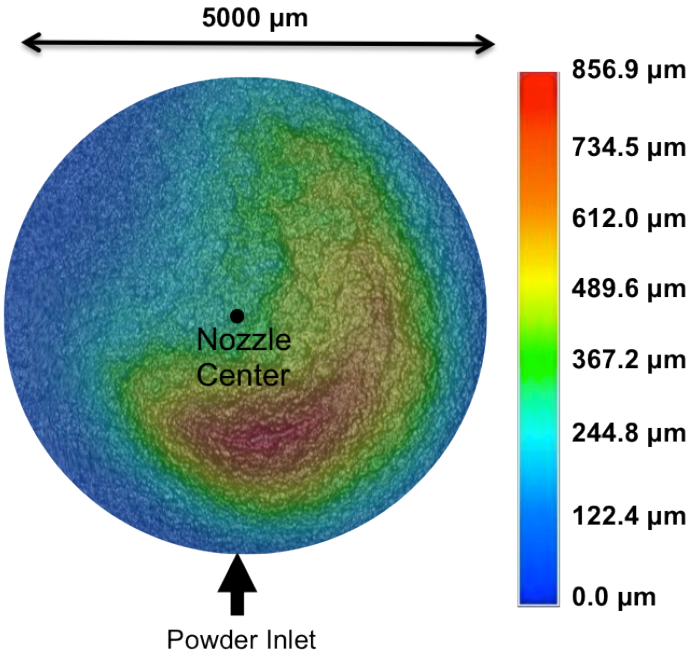

Figure 8.11: 3D scan of the single Al2024 spot spray surface profile using a worn PBI nozzle.

It is to note, that the spot spray time was longer for the current spray than for the deposition obtained using an unworn nozzle, which partially explains the drastic increase in deposition thickness in the current case, particle concentration inside the flow being the other governing factor.

8.3.1. Unworn Polymer Nozzle Particle In-Flight Properties

Figure 8.12 depicts the Al2024 flow rate distribution at a distance of 25 mm from the unworn nozzle exit during spray at maximum parameters. Readings have been made every 1 mm on a 9 mm by 9 mm grid but only the locations at which the flow rates are larger than zero are presented. Moreover, as recommended by the CSM manufacturer only values with a minimal 1% precision have been used for analysis. The set of points have been connected using a linear interpolating surface function in Matlab, which is estimated to be sufficiently accurate for the current type of analysis.

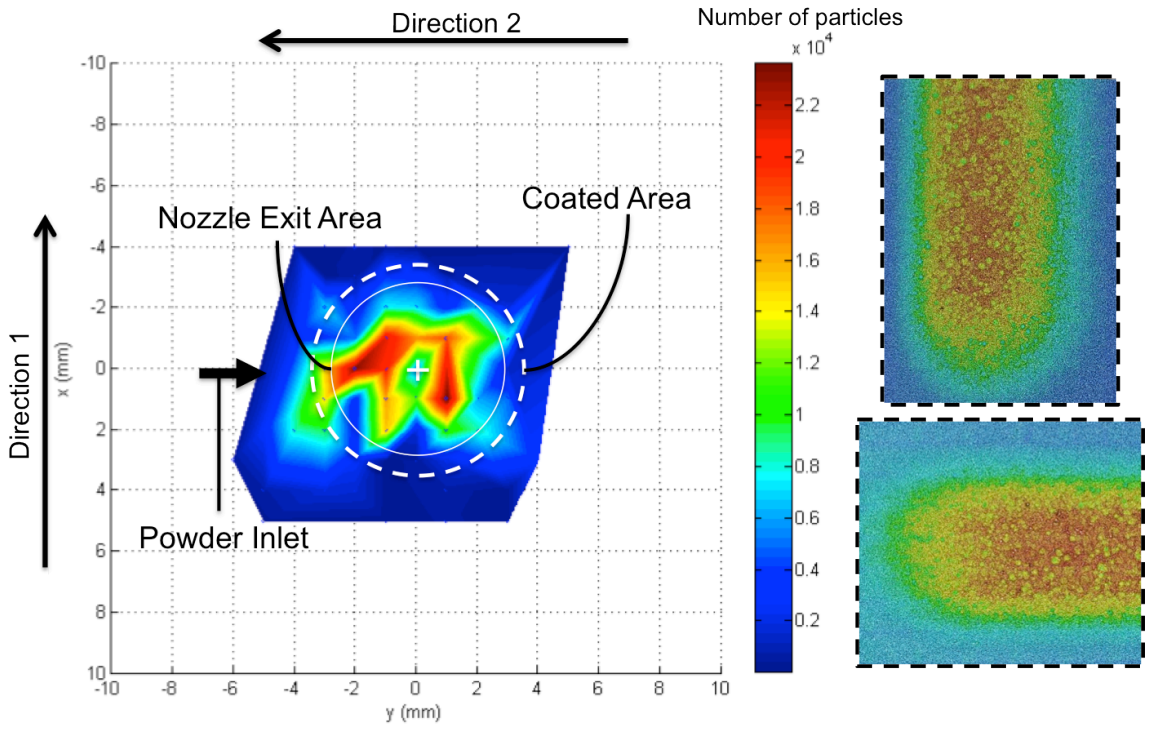

Figure 8.12: Particle flow rate distribution mapping of the flow exiting an unworn nozzle.

Based on the values presented in Table 8.3 in section 8.2, the 7 mm coated area (i.e. deposition and eroded zones) is outline in the figure below along with the nozzle exit approximate 6 mm diameter. The surface of the single line coatings have been inserted in the figure below to facilitate the comparison between the flow rate data and obtained coating profiles. The highest flow rate values are restricted within the limits of the coated zone where a maximum value of 23670 particles/ 5s is recorded. The flow rate decreases to 340 particles/ 5 s and to 1370

particles/ 5 s towards the upper/lower and left/right coated hemisphere respectively. The particle flow rate is slightly shifted towards the powder inlet. Slight wear is observable in the nozzle due to the numerous but limited sprays produced for the current study, which might explain the minor shift in deposition. The obtained flow rate distribution confirms the symmetrical deposition obtained during the spray of the single line coating in direction 2. It also supports the slightly shifted material growth location to the left side during the spray of the single line coating along direction 1 and the spot spray deposition profile. Therefore, the particle distribution inside the flow at the exit of the nozzle is the major factor affecting the coating deposition process and resulting thickness.

Figure 8.13 illustrates the recorded particle velocity at different locations inside the flow. Based on the deposition parameters outlined in the figure below, the majority of the particles that deposit onto the substrate surface travel at velocities ranging between 579 ± 85.33 m/s and 596 ± 86.7 m/s. These velocities correlate well with the values found in the literature for 20 μm aluminum particle critical velocities of 620-660 m/s [18]. Moreover, as described in section 2.3.4, the particle critical velocity for proper deposition decreases with increasing temperature and particle size.

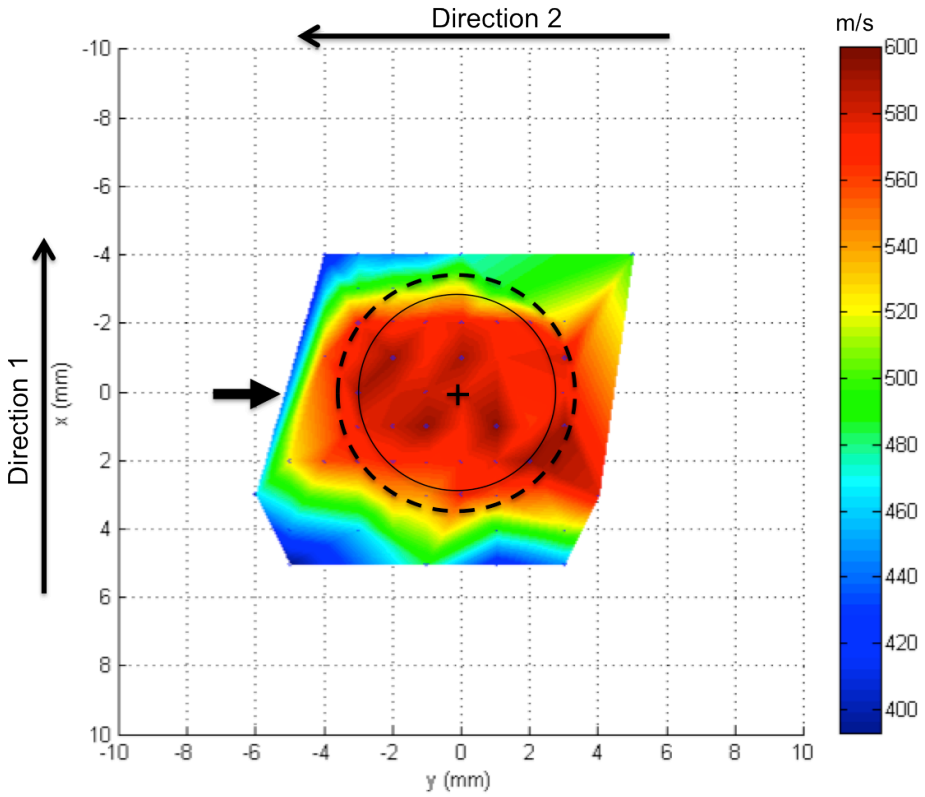

Figure 8.13: Particle velocity distribution mapping of the flow exiting an unworn nozzle.

A stagnation temperature of 500 °C allows particles to heat during their flight inside the nozzle, which softens the particles before their impact with the substrate surface. A softer particle undergoes a larger plastic deformation, which increases the effectiveness of the oxide removal process and the metal-to-metal contact.

Figure 8.14 shows the average diameter of the particles at different locations in the flow recorded during the particle in-flight properties measurements. The average dimension of the particles found within the coated area range between 37 ± 5.77 μm and 40 ± 8.22 μm

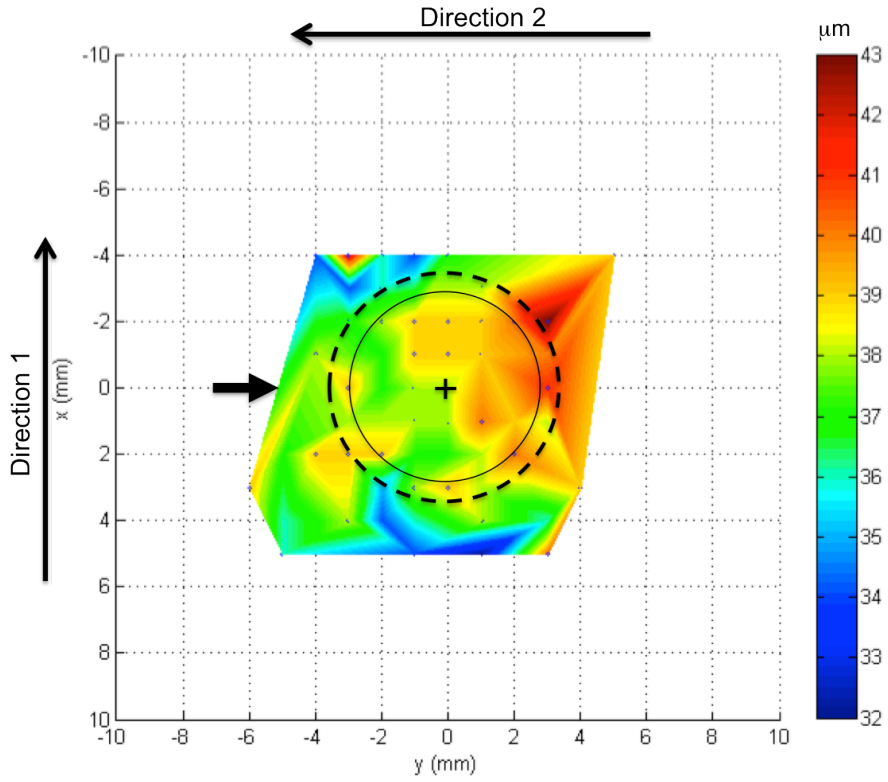

Figure 8.14: Particle diameter distribution mapping of the flow exiting an unworn nozzle.

Due to the low sphericty of some of the Al2024 particles and their rotation inside the flow, the recorded dimensions using the CSM could have been overestimated. Nevertheless, based on the obtained particle in-flight properties, the deposition process is mainly influenced by the particle flow rate distribution inside the gas stream and perhaps also by the particle kinetic energy before impact.

8.3.2. Worn Polymer Nozzle Particle In-Flight Properties

Figure 8.15 depicts the obtained particle flow rate distribution at a SOD of 25 mm and maximum spray parameters using the worn nozzle. The data at each position was acquired with the use of the CSM and then compiled using Matlab. In order to avoid flow perturbation from the shock wave created during the impact of the stream with the substrate surface, no substrate material was placed under the flow. Only values larger than zero and with sufficient precision have been used for the following analysis.

As expected, the flow continues to expand outside the nozzle such that the stream cross-sectional area reaches a diameter of approximately 8 mm, which correlates well with the data presented in Table 8.3. However, as shown in section 8.2, effective deposition is only constrained in a 2 mm region characterized by the highest particle flow rate, which corresponds to 63080 particles/ 10 s. This confirms that the lack of deposition in other regions under the stream is also caused by a separation of particles inside the flow rather than just a lack of particle bonding energy.

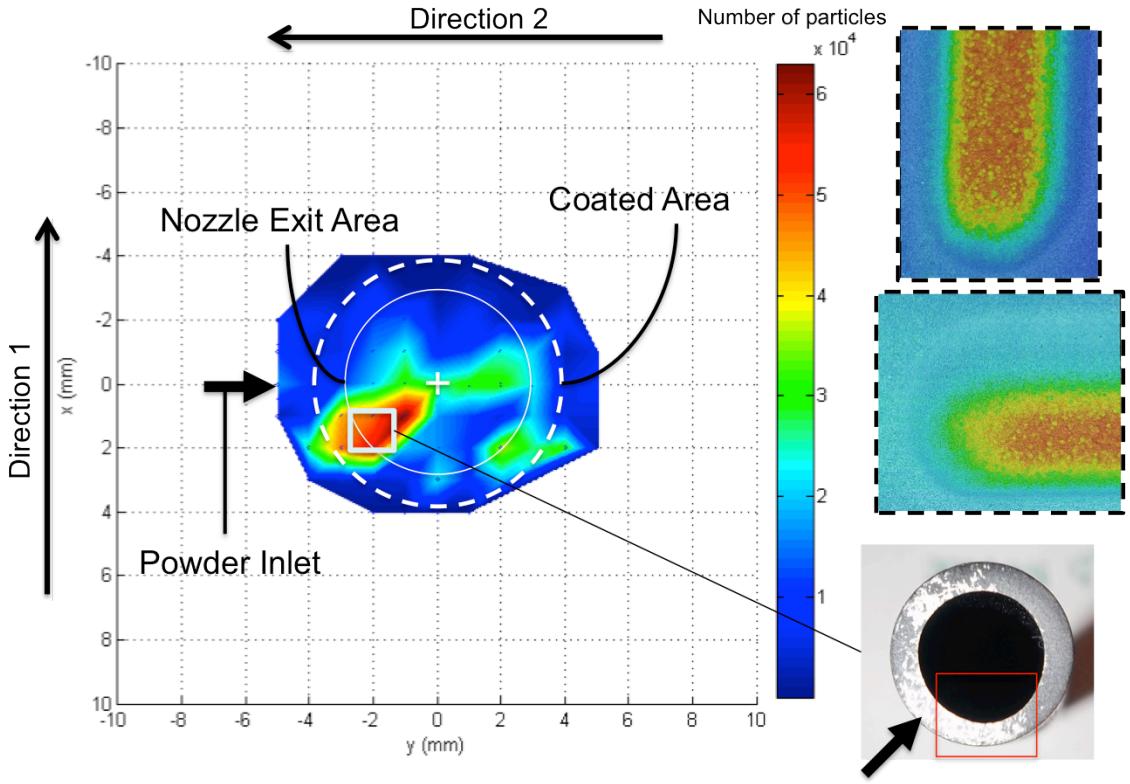

Figure 8.15: Particle flow rate distribution mapping of the flow exiting a worn nozzle.

The position of the highest particle flow rate matches the location of the nozzle erosion, which suggests that the nozzle wear process affects the resulting flow dynamics. Inserts of the single line coatings obtain in section 8.2 are added in the figure above to validate the obtained results; deposition is obtained based on the particle flow distribution.

Figure 8.16 illustrates the particle velocity inside the flow. Gradual decrease in velocity from 743 ± 181.25 m/s to 328 ± 27.02 m/s is observed across direction 1. As such, based on the

obtained single line coatings and flow rate distribution, particles with velocity lower than 500 m/s don't have sufficient kinetic energy to bond to the substrate surface. Consequently the deposition is shifted and concentrated to the lower hemisphere of the flow.

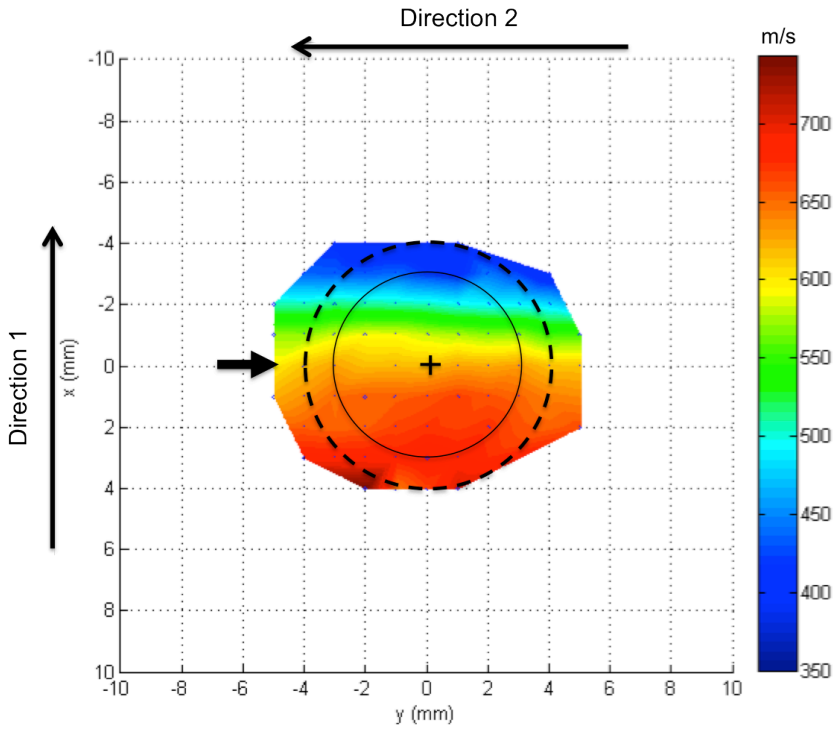

Figure 8.16: Particle velocity distribution mapping of the flow exiting a worn nozzle.

Figure 8.17 depicts the particle diameter distribution inside the gas stream. Large particles of 52 ± 20.39 μm diameter are seen at the periphery of the upper flow hemisphere where the recorded particle velocity is of 328 ± 27.02 m/s. Larger particles require more energy to be accelerated and as a result experience lower spray velocities. At the center of the nozzle particles with an average diameter of 40 ± 9.2 μm are found. Overall, the flow dynamics obtained in consequence to the nozzle erosion process do not seem to affect the particle distribution in terms of their specific diameter. However, since high standard deviation values are obtained for particle diameter it is difficult to give a firm conclusion.

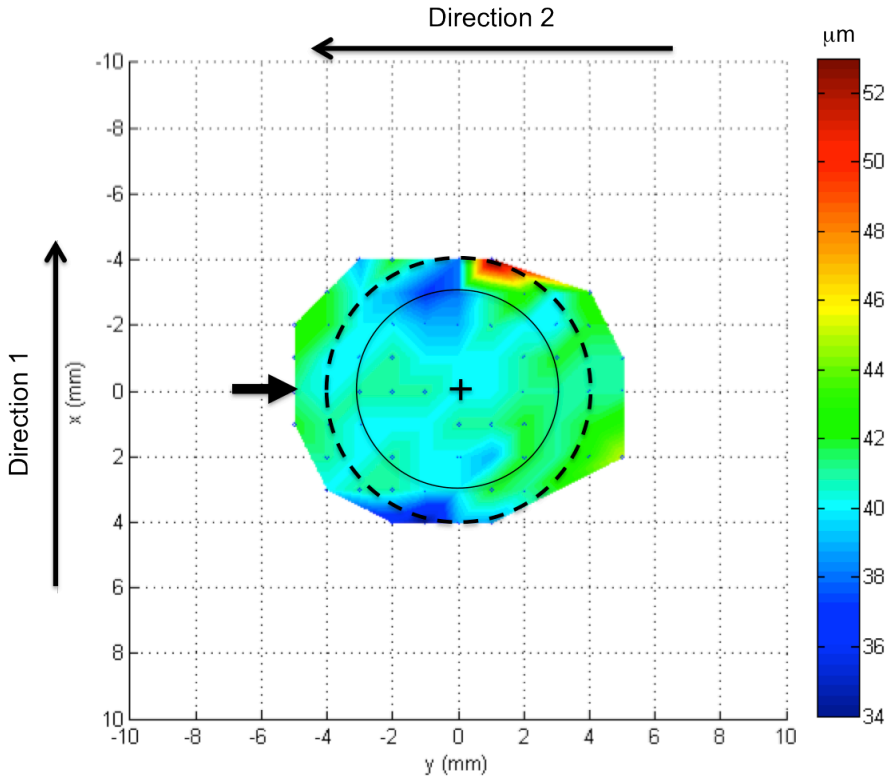

Figure 8.17: Particle diameter distribution mapping of the flow exiting a worn nozzle.

The recorded particle diameters are highly affected by their shape and their rotation within the flow. For non-spherical particles, the resulting projected area captured by the CSM can overestimate the resulting particle diameter.

The influence of the PBI erosion process on the particle flow rate distribution is evident from the particle in-flight properties obtained using the CSM system. The particles inside the flow preferentially travel at the wear zone, which limits the coated area. Moreover, the difference between the particle flow rate distribution obtained using an unworn and worn nozzle suggest that the particle flow dynamic inside the nozzle varies with the wear process.

8.4 Ceramic Nozzle

The following subsection presents the preliminary Al2024 depositions generated using Mica ceramic nozzles. The effect of internal nozzle roughness on the particle deposition process is also investigated.

The CGDS process pressure and temperature have been varied in order to identify their influence on the particle deposition and deformation upon impact. The CGDS parameters that were kept constant during these tests are presented in Table 8.5. The coatings have been produced on small 25.4 mm by 19.05 mm Al2024-T351 coupons. The substrate material has been grit blasted using aluminum oxide grits following the surface preparation procedure presented in section 0.

Table 8.5: CGDS Parameters Held Constant During the Initial Development of Al2024 Deposition Ability Matrix

Parameters	Values
Nozzle Type	Mica ceramic
Increment Size	2 mm
Number of Passes	5
Nozzle Traverse Velocity	15 mm/s
Powder Feeder Wheel	320 Small Wheel
Powder Feeder Gas Rate	30 SCFH
Powder Feeder Rate	11.25 g/min
Standoff Distance	25 mm

8.4.1. Ceramic Nozzle With Internal Roughness

The first Mica (also known as Mykroy/Mycalex) ceramic nozzle used in this study has been machined using only carbide drills. However, due to the brittle and abrasive nature of the glass-bonded mica ceramic, inconsistent chipping of the material during cutting has produced a rough internal nozzle surface. Despite the small observable internal wall waviness, the ceramic nozzle has been used to produce preliminary Al2024 depositions.

Figure 8.18 shows the combination of tested temperatures and pressures. It can be seen from the figure below that the parameters at which the Al2024 powder can be sprayed are limited to minimal pressure and temperature of 1.72 MPa and 200 °C respectively. At 350 °C, the particles start to deposit inside the ceramic nozzle walls. At a temperature of 400 °C the nozzle clogs quickly and the gas stream through the nozzle is blocked.

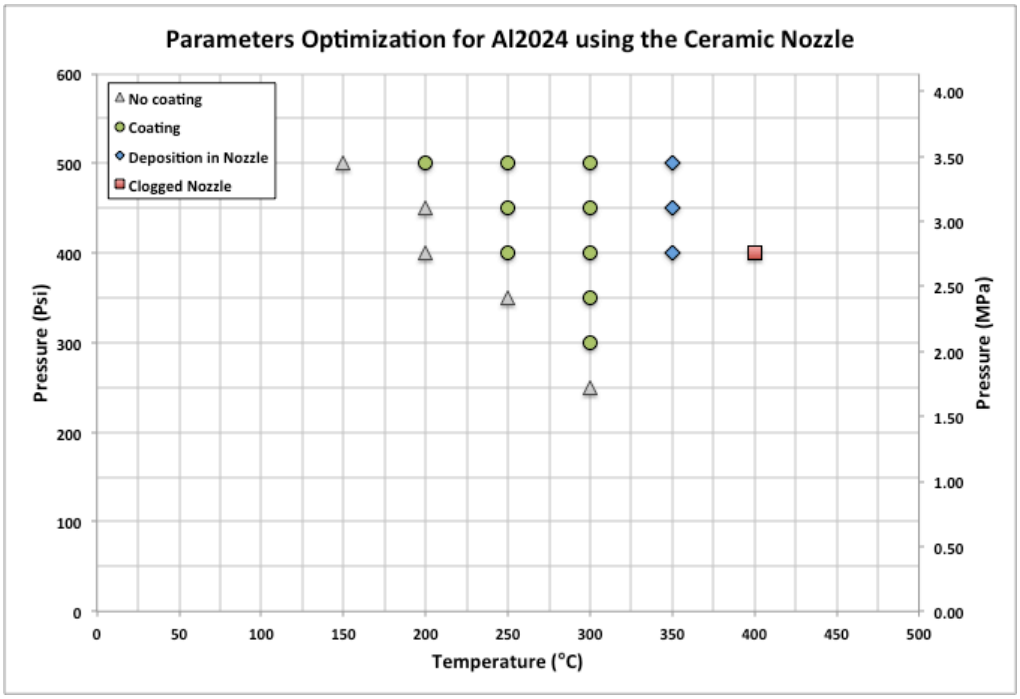

Figure 8.18: Parameters mapping of Al2024 sprayed with a ceramic nozzle.

Figure 8.19 shows the ceramic nozzle before and after sprays involving deposition inside the nozzle and clogging of the nozzle.

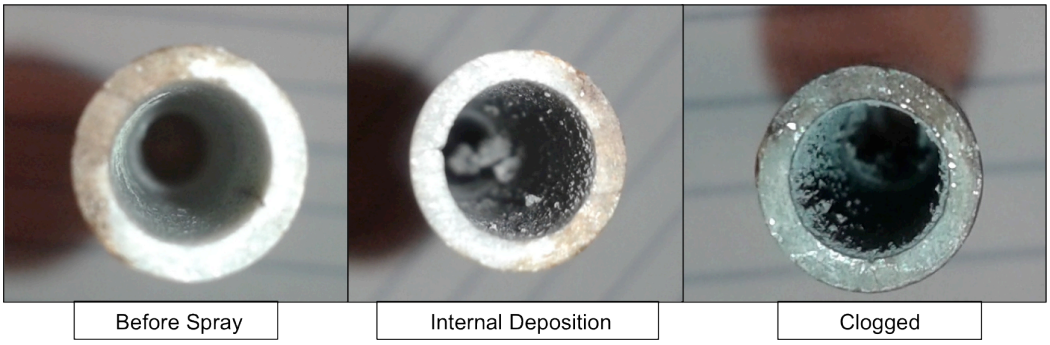

Figure 8.19: Ceramic nozzle before and after sprays.

Figure 8.20 displays the coating thickness obtained at different process pressures and temperatures. The coating thickness at temperatures lower than 300 °C is similar to that obtained using the PBI nozzle as it diverges only by few microns.

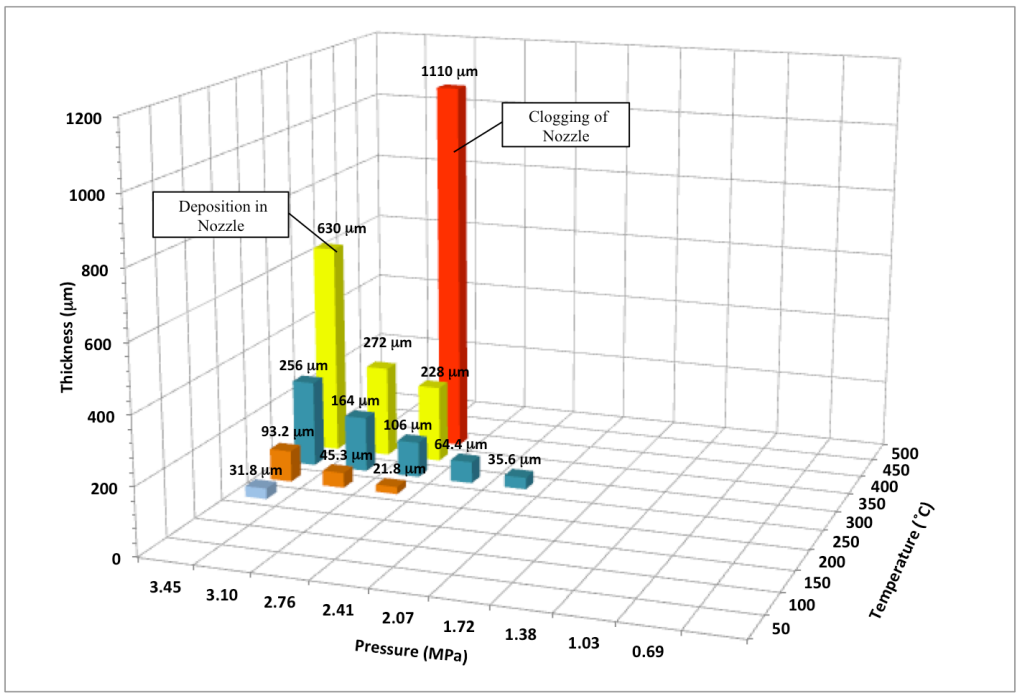

Figure 8.20: Al2024 coating thickness when sprayed with a ceramic nozzle at different pressures and temperatures. Obtained thickness values are shown above each corresponding combination of parameters.

Figure 8.21 to Figure 8.23 depict the coatings cross sections obtained at different process pressures and temperatures. At temperatures higher than 300 °C, the coating is characterized by a high degree of porosity. At lower temperatures, the coating density increases, as shown in Figure 8.23, but so does its surface roughness. At higher process temperatures, higher particle deposition efficiencies are obtained when using the ceramic nozzle. As observed previously, the particle impact process with the nozzle internal walls affects its properties and deposition. The thermal diffusivity and conductivity difference between the ceramic and PBI nozzle material are major factors that influence the deformation and deposition process of the Al2024 particles. The thermal diffusivity is of $1.31 \cdot 10^{-6}$ m^2/s and $3.39 \cdot 10^{-7}$ m^2/s for the ceramic and PBI material respectively. The heat rate flow through the ceramic nozzle is larger than for the PBI, which enables it to reach higher temperatures during the spray process. Thus, during smearing and bouncing of the powder inside the nozzle, particles get preheated to a larger extent and reach a larger thermal energy inside the ceramic nozzle than within the PBI nozzle. Higher particle temperature decrease the particle critical energy required for proper deposition and increase the particle softness. The plastic flow effectiveness within particles during their impact process increases with particle temperature.

At a stagnation temperature of 300 °C and pressure lower than 3.10 MPa, the particles are well deformed and the resulting coatings are dense as shown in Figure 8.23. As mentioned previously, the particle deformation level and flattening ratio increases with increasing temperature. However, subsequent increase in temperature triggers an important change in the particle deformation process. As shown in Figure 8.21 and Figure 8.22, the deposited particles retain their initial size and geometry. It is believed that at higher temperatures the particles lose enough momentum during their smearing process with the hot ceramic walls so that only a minimal amount of energy can be dissipated through plastic deformation. The impingement effect of subsequent particles can help increase the particle deformation and consequently the coating density. However, as shown in Figure 8.21 the coating cooling process during deposition greatly decreases the impingement effect and the particles found at the top layer of each passes preserve their sphericity.

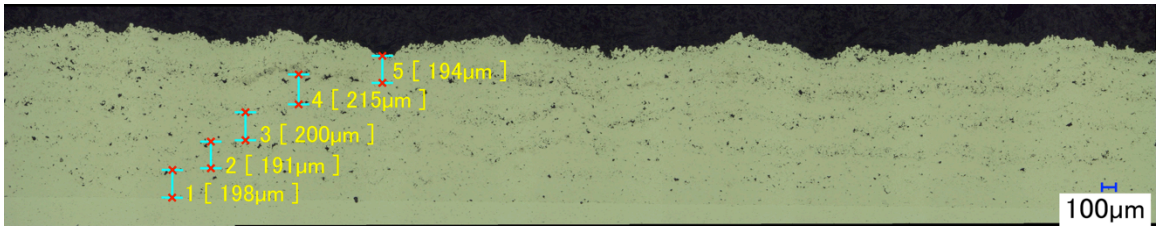

Figure 8.21: Al2024 coating deposited at 400 °C and 2.76 MPa using a Mica ceramic nozzle.

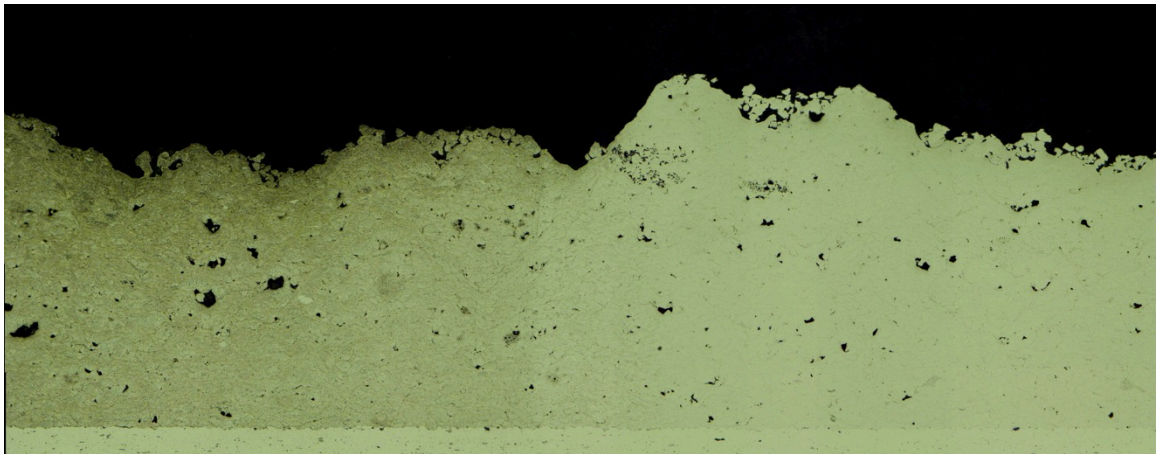

Figure 8.22: Al2024 coating deposited at 350 °C and 3.45 MPa using a Mica ceramic nozzle.

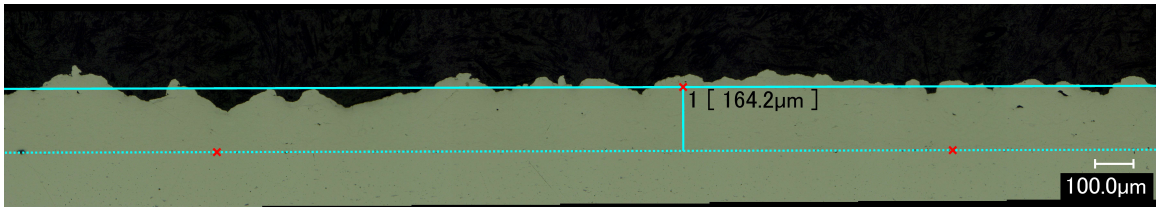

Figure 8.23: Al2024 coating deposited at 300 °C and 3.10 MPa using a Mica ceramic nozzle.

Figure 8.24 shows the porosity levels of the porous coatings obtained at different spray parameters. At 400 °C and 2.76 MPa, the coating porosity reaches 2.21 ± 1.0% due to the lack of particle deformation between each deposited material layer. At 3.45 MPa, the porosity increases from 0.42 ± 0.25% to 0.84 ± 0.24% with an increase in temperature from 300 °C to 350 °C. As the nozzle wall temperature increases with gas temperature, the particle smearing and rubbing degree is accentuated. During the bouncing process of the particles on the hot ceramic wall, the particle kinetic energy is converted into thermal energy. This decrease in particle momentum reduces the particle plastic flow during impact and consequently decreases its ability to fill voids. In addition, any previous particle deposition inside the nozzle would affect the kinetic energy of subsequently sprayed powder. Moreover, at 350 °C the coating porosity increases from 0.48 ± 0.23% to 0.84 ± 0.24% with an increase of pressure from 3.10 MPa to 3.45 MPa.

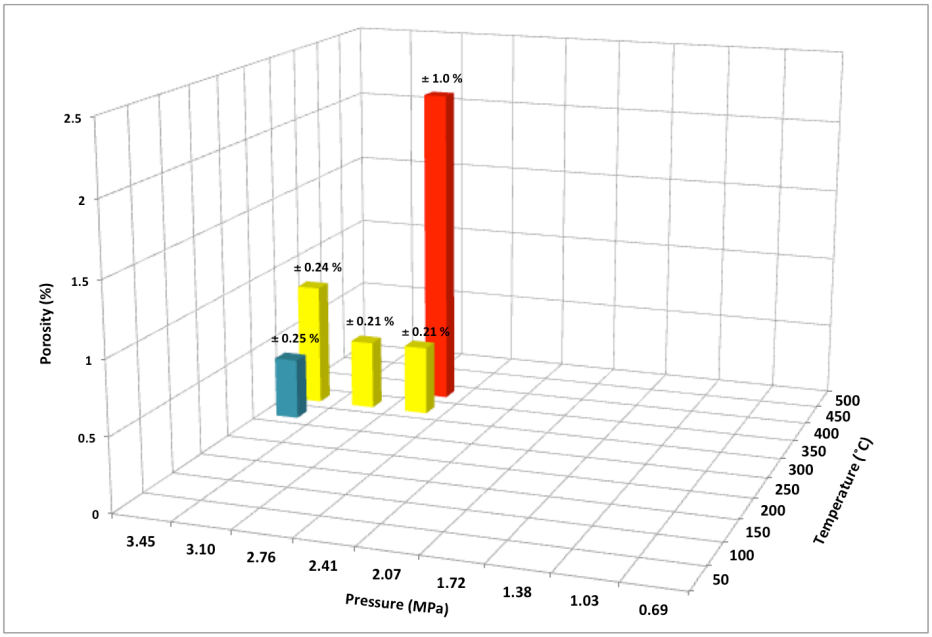

Figure 8.24: Al2024 coating porosity when sprayed with a ceramic nozzle at different pressures and temperatures. Standard deviation values are given above each result.

An increase in process pressure can increase the particle velocity sufficiently to induce its deposition but insufficiently to induce proper plastic deformation during its impact. Figure 8.25 shows the roughness of the coatings surface obtained at different process parameters. The roughness increases with coating thickness and consequently with the process pressure and temperature. At 400 °C and 3.45 MPa, the roughness reaches 28.58 ± 3.87 μm. High particle deposition efficiency along with low particle deformation results in high coating roughness.

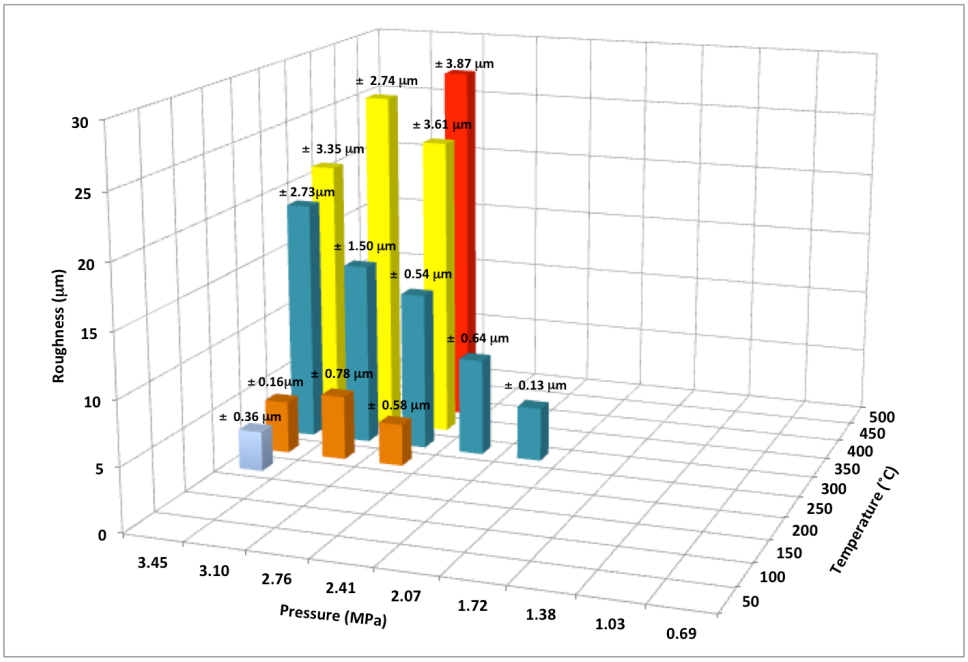

Figure 8.25: Al2024 coating roughness when sprayed with a ceramic nozzle at different pressures and temperatures. Standard deviation values are given above each result.

The use of carbide drills has led to the creation of an important internal nozzle surface roughness measured to be 3.7 μm near the exit, which have facilitated the particle deposition inside the nozzle by acting as a trap. Once the powder is lodged within the nozzle internal walls, subsequent powder accumulation is observed onto the previously lodged Al2024 powder. Higher spraying temperatures ease powder deformation and thus increase the possibility of powder lodging at locations of irregularities formed by the internal nozzle wall roughness. It is to note that a sodium hydroxide solution has been used to dissolve the aluminum alloy deposited inside the nozzle.

To verify the effect of particle smearing and impact process on the nozzle internal wall state, the ceramic nozzle has been split and 3D scans of the internal walls have been made. Figure 8.26 and Figure 8.27 show the resulting roughness after multiple sprays of the wall opposite and close to the powder inlet respectively. It is seen from Figure 8.26 a, d and h that the internal surface of the ceramic nozzle opposite to the powder inlet and near the internal steps is smooth. Moreover, the roughness seems to increase uniformly throughout the nozzle.

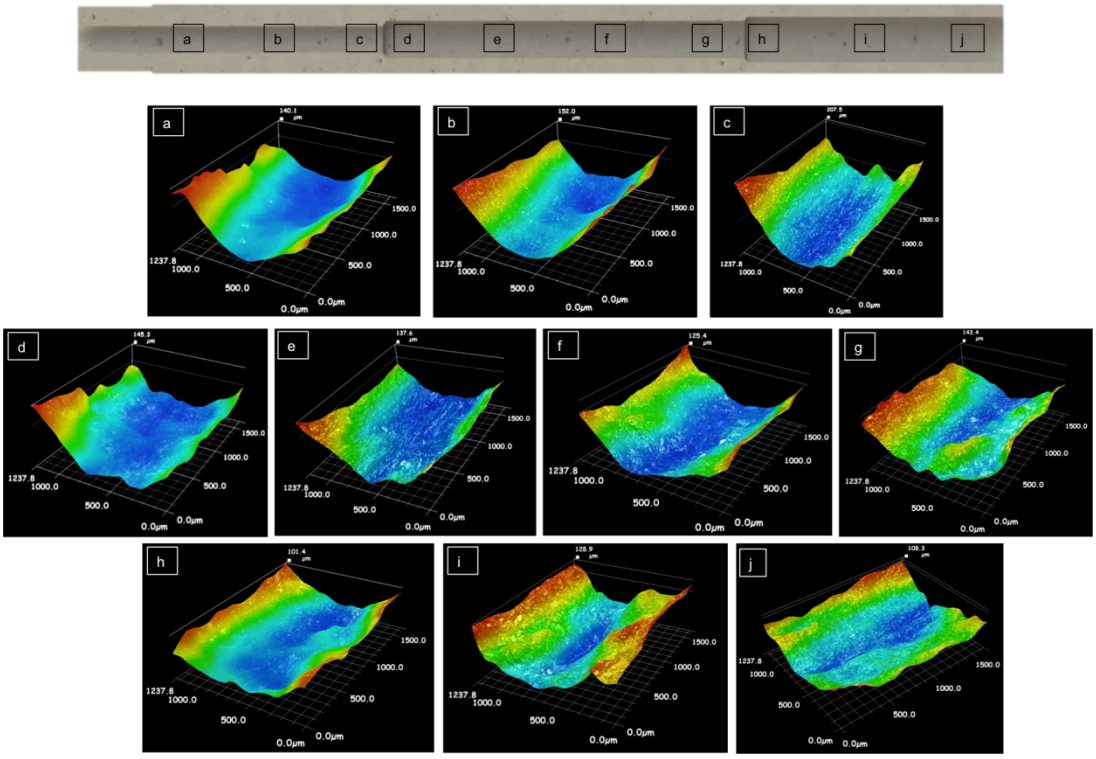

Figure 8.26: 3D scans of the ceramic internal walls of the nozzle opposite to the powder inlet. Where a) to c) are scans of the first step, d) up to g) represent scans at the second step and h) up to j) are the 3D scans of the last step before the exit of the nozzle.

Similarly, Figure 8.27 also shows that the roughness of the surface walls increases homogeneously across the nozzle length.

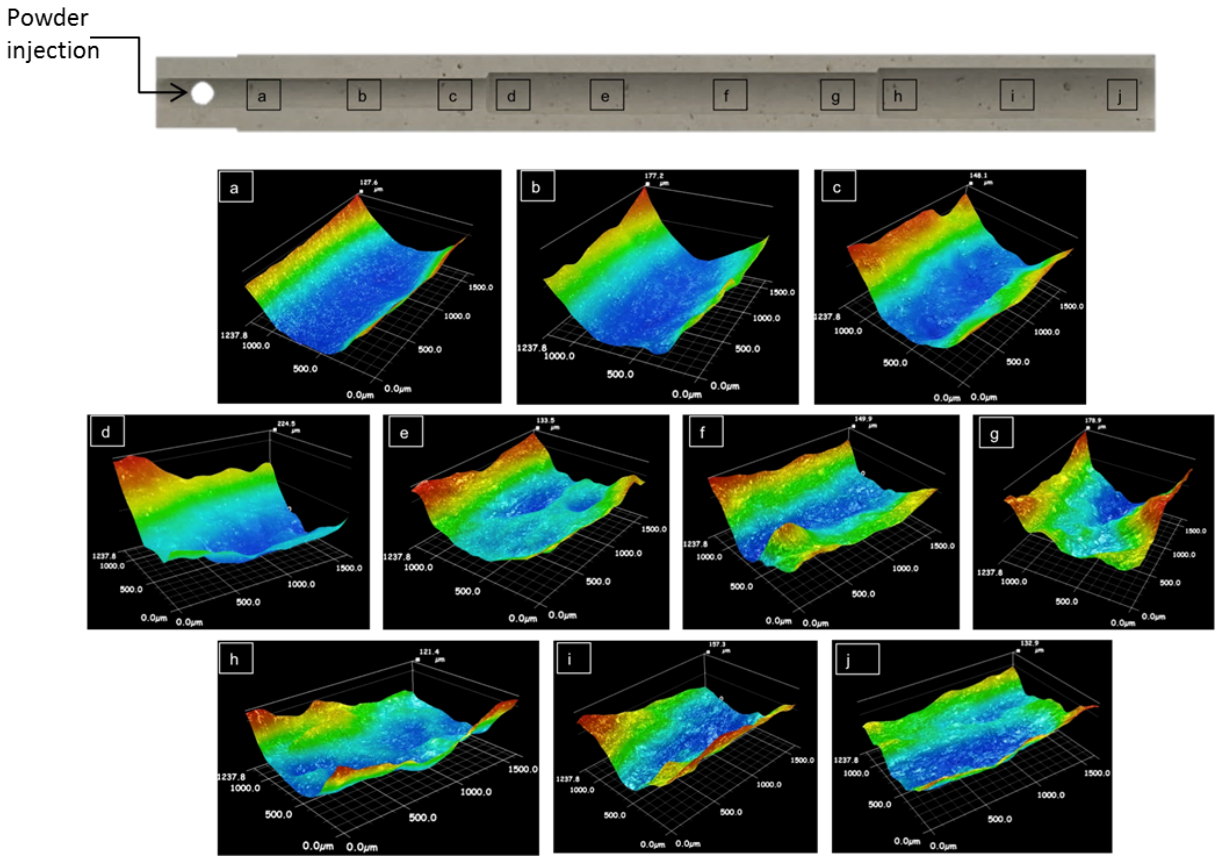

Figure 8.27: 3D scans of the ceramic nozzle internal walls at the powder inlet side. Where a) to c) are scans of the first step, d) up to g) represent scans at the second step and h) up to j) are the 3D scans of the last step before the exit of the nozzle.

Figure 8.28 shows the difference in roughness at different location in the nozzle. The region near each step seems to be intact since the powder is unable to hug the vicinity of the 90° edge during its flight down to the exit. However, it is to note that the degree of material removal rate of the ceramic nozzle is way lower than the wear observed during the spray with the PBI nozzle. Also, the ceramic surface wears evenly across the diameter and length of the nozzle, which differs from the preferred material removal location experienced for the polymer nozzle.

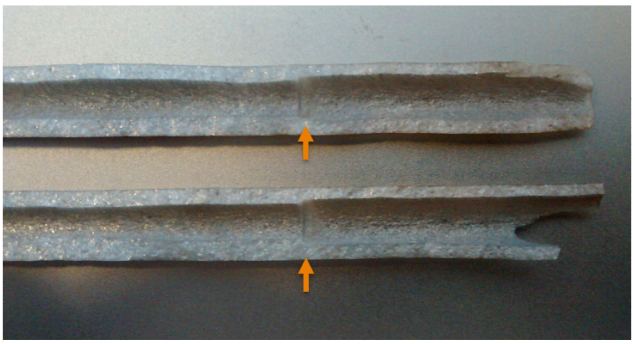

Figure 8.28: Ceramic nozzle internal roughness. The arrows point to the location of low roughness, which is situated at each start of a step.

The next subsection studies the influence of nozzle initial roughness on the particle internal deposition and nozzle clogging.

8.4.2. Restrained Internal Roughness

The second Mica ceramic nozzle studied in this work has been machined using carbide drills and the last 0.38 mm of material has been removed using carbide reamers. The nozzle internal walls were smoother than those obtained using only carbide drills. Table 8.6 presents the parameters that have been tested and indicates whether or not deposition or clogging issues have been encountered. The parameters that have been held constant during these tests are the same as those presented in Table 8.5.

Table 8.6: Ceramic Nozzle Clogging and Deposition

Pressure (MPa)	Temperature (°C)	Clogging/Deposition
2.07	350	No
2.76	350	No
3.10	350	No
3.10	400	No
3.45	450	No
3.45	500	Slight Deposition

Results show that particles start to deposit on the nozzle walls only at the highest spraying parameters (i.e. 500 °C and 3.45 MPa). Figure 8.29 depicts the particle deposition location inside the ceramic nozzle. Clogging of the nozzle might have occurred if the spray time was set to longer periods of time, as the deposition process is facilitated by the previously deposited particles.

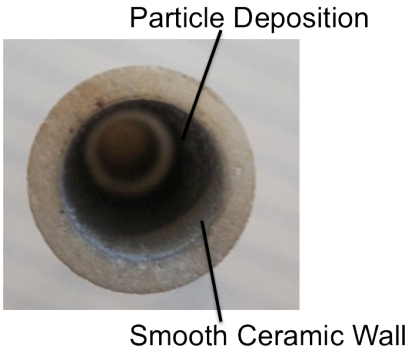

Figure 8.29: Al2024 deposition inside a ceramic nozzle during a spray at 500 °C and 3.45 MPa.

The nozzle initial roughness is one of the main factors enabling particle deposition inside the nozzle. As noted previously, the wall roughness increases with spray time due to the repetitive impact of particle with the nozzle internal surface, which brings the internal deposition process to vary with time. Moreover, the material removal of the ceramic walls is uniform, which should decrease the wear influence on the powder flow distribution and give better results in terms of coating repeatability. The deformation of the nozzle upon powder impact might be avoided by using a wear resistance nozzle characterized by a high hardness. Finally, since the particles have the ability to gain thermal energy through heat transfer from the nozzle, a lower gas temperature can be used to spray Al2024 coatings, which could be beneficial to prevent affecting the substrate material heat treatment.

CHAPTER 9

Conclusion, Recommendations and Future Work

Conclusions drawn from the current work regarding the use of the cold gas dynamic spray process for the repair of aluminum alloy components will be summarized in the following chapter. The main results concerning the influence of the spray parameters on particle deformation and deposition process of both the pure aluminum and Al2024 particles onto Al6061-T6, Al7075-T6 and/or Al2024-T351 components will be briefly reviewed. Coatings properties and performance during mechanical testing will also be summarized. Recommendations towards improving the coatings adhesion strength and reducing the polymer nozzle erosion will be presented based on the preliminary tests conducted in this study.

Future work to be completed in order to ensure the coating deposition process is optimized for the repair of components. Additional tests that are considered essential to determine the coatings limitations in performance will be discussed.

9.1 Conclusions

In the present study, the use of the CGDS process for the repair and restoration of aluminum alloy nose landing gear steering actuator threads found on the Boeing 757 aircraft was investigated. Moreover, the ability to deposit Al2024 coatings onto Al2024-T351 substrates using a commercially available high pressure system was also studied.

The obtained results demonstrate that large 7 mm thick ***pure aluminum coatings*** can be deposited, without delamination, on 88.9 mm diameter circular Al6061-T6 and Al7075-T6 components. Coatings were preliminary deposited on small flat substrates to investigate the effect of spraying processes on coating quality and properties. It was found that the largest deposition efficiency was achieved at the highest spraying pressure and temperature of 3.45 MPa and 500 °C respectively. Lowering the mass feeding rate to 4 g/min has led to a major decrease in coating porosity through the enhancement of particle deformation processes. A decrease in coating hardness was observed for depositions obtained at high spraying temperatures, which have led to believe that stress relief annealing conditions were reached in the pure aluminum coatings. Thus, the induced heat treatment may have provided sufficient thermal energy to initiate material softening, increase the ductility and release the internal residual stresses inside the coating. In addition to the particle deposition process effect on coating quality, it was demonstrated that a discontinuous nozzle movement across the large circular component surface generates porosities ranging from 1.81 ± 0.16% to 13.50 ± 0.65% within the coating thickness. The inherent distribution of particle properties within the flow have led to pyramidal-like deposition growth and consequently to poor coating overall quality. It was then shown that using a continuous nozzle displacement drastically changes the deposition process and improves the obtained coating properties and machinability. As a result, 3.75-12UNJ-3A threads were successfully machined within the pure aluminum coatings. The CGDS repaired threads were able to withstand a torque of at least 303 N·m, which exceeded the 203 N·m torque requirement set by the Boeing Company. Moreover, to avoid affecting the component base material properties, the substrate surface temperature was successfully held below 93 °C, during the entire repair process, mainly through the use of an air cooling system placed opposite to the hot gas flow.

Al2024 powder material was successfully deposited onto Al2024-T351 substrates of different size and geometry. Preliminary tests produced on small flat substrates have

demonstrated that at 500 °C a minimal pressure of 1.72 MPa is required to generate deposition. Similarly, at 3.45 MPa a minimal temperature of 200 °C is necessary to produce a coating. The highest deposition efficiency was reached at the highest spraying parameters (i.e. 500 °C and 3.45 MPa). All coatings generated within this study were dense as a result of particle softening and impingement effects. The optimal standoff distance to efficiently deposit Al2024 was evaluated to range from 15 mm to 25 mm. At those distances, the ambient atmosphere and the bow shock have limited influence on the particle kinetic energy, which allows them to reach the critical velocity necessary for proper deposition. In addition, the influence of mass feeding rate on the coating hardness has been studied. Obtained results have shown that an increase in mass feeding rate to rates larger than 11.25 g/min decreases the coating hardness to 127 $HV_{0.3}$ due to flow saturation. Obstructing the flow reduces the ability of individual particles to reach sufficient velocities to produce proper strain hardening. The Al2024 deposition hardness was evaluated at various test loads and a reverse indentation size effect (RISE) has been observed. The load dependant hardness results were attributed to a number of phenomena, including porosity, low particle cohesion strength, material yielding, elastic/plastic deformation, friction and equipment vibration. The coating hardness has also been discovered to increase from the substrate/coating interface to the coating surface. Similarly, at the interface, the coating resistance to deformation increases with increasing thickness. Both variations in hardness are believed to result from annealing processes induced inside the coating during the deposition process at high gas flow temperatures. The properties acquired are dependent on the spray temperature and time. Annealing the cold worked coating leads to the relaxation of internal residual stresses and to a decrease in dislocation density.

Al2024 repairs of 1.5-12UNJ-3A threads produced in this study have exhibited very low adhesion strengths. Coatings have either failed during machining or at stresses lower than 6.2 MPa during shear tests. To resolve this issue and increase the coating performance, adhesion tests were performed according to the ASTM C633 standard for different substrate surface roughnesses. Obtained results have demonstrated that an increase in substrate surface profile drastically increases the coating adhesion strength. For Al2024 coatings, an increase in roughness from 1.74 μm to 4.58 μm increased the coating adhesion strength from 31.73 ± 7.89 MPa to 58.90 ± 13.04 MPa. A further increase in surface profile to 7.34 μm generated coatings with adhesion strengths too high to be recorded (i.e. >82.24 MPa). Similar conclusion have been established for the deposition of pure aluminum coatings; an increase in substrate surface

roughness from 2.41 μm to 5.29 μm leads to an increase in coating adhesion from 29.1 ± 6.53 MPa to 43.12 ± 17.46 MPa. Moreover, smoother surfaces have shown to generate higher coating adhesion strengths compared to surfaces with roughness ranging between 1 μm to 3 μm. The resulting substrate surface area, the particle impact process, the substrate plastic deformation process, the particle size relative to the substrate surface irregularities dimensions and the particle fit level inside the substrate cavities influence the resulting adhesion strength. All these factors affect the resulting mechanical and metallurgical particle bonding potential. Additionally, results in this study have validated the benefits of substrate preheating procedures on the coating adhesion strength. Thus, to improve the coating performance and load carrying capacity, it is recommended to increase the substrate surface roughness and preheat the component surface.

Finally, results have shown that the polymer nozzle wear process highly influences the particle distribution inside the flow. The particle separation process within the flow reduces the deposition uniformity and coating thickness growth rate.

9.2 Recommendations

To enhance the Al2024 particle bonding area and deformation process during the repair of intricate components, the coating/substrate interface should be machined at an angle of 60° or in a curved shape instead of 45°or 90°. Results in this research have shown that particle sprayed on steep surfaces lack in deformation, which can produce low particle-to-particle and particle-to-substrate contact.

Based on obtained results, the coating machining process must be highly controlled in order to avoid premature coating adhesion failure. Poor control of the cutting velocity and rate can induce additional stresses at the coating/substrate interface, which would lead to a decrease in repair performance.

To minimize the effect of PBI nozzle wear on the coating quality and deposition process, the nozzle should be replaced at the first sign of wear. To avoid frequent nozzle replacement, a mica ceramic nozzle could be used instead. However, despite the promising results obtained using the ceramic nozzle in this study, further research regarding the influence of material nozzle on particle energy and deposition process is required in order to optimize the coating quality.

9.3 Future Work

The research conducted within this study is part of a broader project that intends to evaluate the use of the CGDS process for the dimensional restoration and repair of aerospace structural components. The tests and repairs produced within the current study only cover a minor portion of the preliminary experiments necessary to bring the CGDS at the industrialization phase as a repair technology for structural parts. Further investigation is required to understand the mechanisms involved during the particle impact, deformation and deposition process with different surface profiles in order to optimize the coating adhesion strength. Further analysis on the influence of different process parameters combinations (i.e. standoff distance, nozzle material and geometry, particle size distribution and geometry, carrier gas nature…) on the coating properties is necessary to confirm that the deposition process is optimized for the repair of structural nature. Future work should also focus on the evaluation of the repair performance under various testing conditions such as impact, fatigue, wear and corrosion.

References

[1] V. K. Champagne, "The Repair of Magnesium Rotocraft Components by Cold Spray," *Journal of failure analysis and prevention*, vol. 8, pp. 164–175, 2008.

[2] R. C. Dorward and T. R. Pritchett, "Advances aluminum alloys for aircraft and aerospace applications," *Materials and Design*, vol. 9, no. 2, pp. 63–69, 1988.

[3] T. Dursun and C. Soutis, "Recent developments in advanced aircraft alumiunum alloys," *Materials and Design*, vol. 56, pp. 862–871, 2014.

[4] C. Brady, "The 737 Technical Site," 1999. [Online]. Available: http://www.b737.org.uk/production.htm. [Accessed: 15-Feb-2015].

[5] S. Nowotny, S. Scharek, E. Beyer, and Ka.-H. Ritcher, "Laser Beam Build-Up Welding: Precision in Repair, Surface Cladding, and Direct 3D Metal Deposition," *Journal of Thermal Spray Technology*, vol. 16, no. 3, pp. 344–348, Sep. 2007.

[6] D. Harvey and T. Marrocco, "The Potential of the Cold Spray Process for the Repair and Manufacture of Aluminium Alloy Parts," in *ICAA13: 13th International Conference on Aluminum Alloys*, H. Weiland, A. D. Rollett, and W. A. Cassada, Eds. John Wiley & Sons, Inc., 2012, pp. 257–263.

[7] M. Bray, A. Cockburn, and W. O'Neill, "The Laser-assisted Cold Spray process and deposit characterisation," *Surface and Coatings Technology*, vol. 203, pp. 2851–2857, 2009.

[8] "Universal Method of Bonding Steel Repairs to Aluminum Structures," *Small Buisness Innovation Research-US Government*, 2007. [Online]. Available: https://www.sbir.gov/sbirsearch/detail/331786. [Accessed: 15-Feb-2015].

[9] R. Ghelichi, S. Bagherifard, D. MacDonald, I. Fernandez-Pariente, B. Jodoin, and M. Guagliano, "Experimental and numerical study of residual stress evolution in cold spray coating," *Applied Surface Science*, vol. 288, pp. 26–33, 2014.

[10] F. Gärtner, T. Schmidt, T. Stoltenhoff, and H. Kreye, "Recent Developments and Potential Applications of Cold Spraying," *Adv. Eng. Mater.*, vol. 8, no. 7, pp. 611–618, 2006.

[11] A. Astarita, M. Durante, A. Langella, M. Montuori, and A. Squillace, "Mechanical characterization of low-pressure cold-sprayed metal coatings on aluminium," *Surf. Interface Anal.*, vol. 45, no. 10, pp. 1530–1535, 2013.

[12] R. Lupoi and W. O'Neill, "Deposition of metallic coatings on polymer surfaces using cold spray," *Surface and Coatings Technology*, vol. 205, pp. 2167–2173, 2010.

[13] P. C.King, A. Poole J., S. Horne, R. De Nys, S. Gulizia, and M. Z. Jahedi, "Embedment of copper particles into polymers by cold spray," *Surf. Coat. Technol.*, vol. 216, pp. 60–67, Nov. 2012.

[14] M. Gardon, A. Latorre, M. Torrell, S. Dosta, J. Fernández, and J. M. Guilemany, "Cold gas spray titanium coatings onto a biocompatible polymer," *Mater. Lett.*, vol. 106, pp. 97–99, Sep. 2013.

[15] X. Guo, G. Zhang, W.-Y. Li, L. Dembinski, Y. Gao, H. Liao, and C. Coddet, "Microstructure, microhardness and dry friction behavior of cold-sprayed tin bronze coatings," *Appl. Surf. Sci.*, vol. 254, no. 5, pp. 1482–1488, Dec. 2007.

[16] W.-Y. Li, G. Zhang, H. L. Liao, and C. Coddet, "Characterizations of cold sprayed TiN particle reinforced Al2319 composite coating," *J. Mater. Process. Technol.*, vol. 202, no. 1–3, pp. 508–513, Jun. 2008.

[17] A. Bacciochini, M. I. Radulescu, M. Yandouzi, G. Maines, J. J. Lee, and B. Jodoin, "Reactive structural materials consolidated by cold spray: Al–CuO thermite," *Surf. Coat. Technol.*, vol. 226, pp. 60–67, 2013.

[18] J. L. Heli Koivuluoto, “Microstructural Studies of Cold Sprayed Copper, Nickel, and Nickel-30% Copper Coatings,” *J. Therm. Spray Technol.*, vol. 16, no. 4, pp. 488–497, 2007.
[19] H.-K. Kang and S. B. Kang, “Tungsten/copper composite deposits produced by a cold spray,” *Scr. Mater.*, vol. 49, no. 12, pp. 1169–1174, Dec. 2003.
[20] A. Sova, V. F. Kosarev, A. Papyrin, and I. Smurov, “Effect of Ceramic Particle Velocity on Cold Spray Deposition of Metal-Ceramic Coatings,” *J. Therm. Spray Technol.*, vol. 20, no. 1–2, pp. 285–291, Oct. 2010.
[21] D. Goldbaum, M. Shockley, R. R. Chromik, A. Rezaeian, S. Yue, J.-G. Legoux, and E. Irissou, “The Effect of Deposition Conditions on Adhesion Strength of Ti and Ti6Al4V Cold Spray Splats,” *J. Therm. Spray Technol.*, vol. 21, no. 2, pp. 288–303, Mar. 2012.
[22] J.-G. L. Eric Irissou, “Investigation of Al-Al2O3 Cold Spray Coating Formation and Properties,” vol. 16, no. 5, pp. 661–668, 2007.
[23] P. D. Eason, J. A. Fewkes, S. C. Kennett, T. J. Eden, K. Tello, M. J. Kaufman, and M. Tiryakioglu, “On the characterization of bulk copper produced by cold gas dynamic spray processing in as fabricated and annealed conditions,” *Material Science and Engineering A*, vol. 528, pp. 8174–8178, 2011.
[24] H. J. K. J. C. Lee, “Repair of Damaged Mold Surface by Cold-Spray Method,” *CIRP Ann. - Manuf. Technol.*, no. 1, pp. 577–580, 2007.
[25] M. Yandouzi, S. Gaydos, D. Guo, R. Ghelichi, and B. Jodoin, “Aircraft Skin Restoration and Evaluation,” *J. Therm. Spray Technol.*, vol. 23, no. 8, pp. 1281–1290, Aug. 2014.
[26] M. Faccoli, G. Cornacchia, D. Maestrini, G. P. Marconi, and R. Roberti, “Cold Spray Repair of Martensitic Stainless Steel Components,” *J. Therm. Spray Technol.*, vol. 23, no. 8, pp. 1270–1280, Aug. 2014.
[27] D. H. V. Champagne, “Critical Assessment 11: Structural repairs by cold spray,” *Mater. Sci. Technol.*, vol. 31, no. 6, pp. 627–634, 2015.
[28] J. E. Timothy, “cold Spray Repair of the F-18 AMAD,” presented at the CTMA Symposium 2012, North Island, CA, 25-Mar-2012.
[29] N. Matthews, R. Jones, and G. C. Sih, “Application of supersonic particle deposition to enhance the structural integrity of aircraft structures,” *Sci. China Phys. Mech. Astron.*, vol. 57, no. 1, pp. 12–18, Dec. 2013.
[30] “ARL center for cold spray-applications,” *ARL- United States Army Research Laboratory*. [Online]. Available: http://www.arl.army.mil/www/default.cfm?page=375. [Accessed: 29-Apr-2015].
[31] “Using 3D Painting to Build and Repair Parts,” *GE Global Research*. [Online]. Available: http://www.geglobalresearch.com/news/press-releases/ge-researchers-experiment-with-3d-painting-to-build-up-and-repair-parts. [Accessed: 29-Apr-2015].
[32] J. Singh and D. E. Wolfe, “Review Nano and macro-structured component fabrication by electron beam-physical vapor deposition (EB-PVD),” *J. Mater. Sci.*, vol. 40, no. 1, pp. 1–26, Jan. 2005.
[33] F. C. C. Jr, *Manufacturing Technology for Aerospace Structural Materials*. Elsevier, 2011.
[34] W. D. Callister, *Materials Science And Engineering: An Introduction*. John Wiley & Sons, 2007.
[35] D. E. Laughlin and K. Hono, *Physical Metallurgy: 3-Volume Set*. Newnes, 2014.
[36] W. T. Yost and J. H. Cantrell, “The Effects of Artificial Aging of Aluminum 2024 on its Nonlinearity Parameter,” in *Review of Progress in Quantitative Nondestructive Evaluation*, D. O. Thompson and D. E. Chimenti, Eds. Springer US, 1993, pp. 2067–2073.
[37] A. I. H. Committee, *ASM handbook: Heat treating*. ASM International, 1991.
[38] D. M. Mattox, *Handbook of Physical Vapor Deposition (PVD) Processing*. William Andrew, 2010.

[39] S. J. Bull, “Correlation of Microstructure and Properties of Hard Coatings,” *Vacuum*, vol. 43, pp. 387–391, 1992.
[40] V. K. Champagne, *The Cold Spray Materials Deposition Process: Fundamentals and Applications*. Elsevier, 2007.
[41] S. B. L. Molent, “Life assessment and repair of fatigue damaged high strength aluminium alloy structure using a peening rework method,” *Eng. Fail. Anal. - ENG FAIL ANAL*, vol. 15, no. 1, pp. 62–82, 2008.
[42] E. Toyserkani, A. Khajepour, and S. F. Corbin, *Laser Cladding*. CRC Press, 2004.
[43] L. Sexton, S. Lavin, G. Byrne, and A. Kennedy, “Laser cladding of aerospace materials,” *J. Mater. Process. Technol.*, vol. 122, no. 1, pp. 63–68, Mar. 2002.
[44] E. Schubert, T. Seefeld, A. Rinn, and G. Sepold, “Laser beam cladding: A flexible tool for local surface treatment and repair,” *J. Therm. Spray Technol.*, vol. 8, no. 4, pp. 590–596, Dec. 1999.
[45] T. Torims, *The application of laser cladding to mechanical component repair, renovation and regeneration*. DAAAM International, 2003.
[46] C. L. Sexton, “Hardfacing: Traditional versus laser.” [Online]. Available: www.laserage.ie. [Accessed: 19-Mar-2015].
[47] L. Thivillon, P. Bertrand, B. Laget, and I. Smurov, “Potential of direct metal deposition technology for manufacturing thick functionally graded coatings and parts for reactors components,” *J. Nucl. Mater.*, vol. 385, no. 2, pp. 236–241, Mar. 2009.
[48] J. R. Davis, *Handbook of Thermal Spray Technology*. ASM International, 2004.
[49] D. L. Hale, W. D. Swank, and D. C. Haggard, “In-Flight particle measurements of twin wire electric arc sprayed aluminum,” *J. Therm. Spray Technol.*, vol. 7, no. 1, pp. 58–63, Mar. 1998.
[50] A. P. Newbery, P. S. Grant, and R. A. Neiser, “The velocity and temperature of steel droplets during electric arc spraying,” *Surf. Coat. Technol.*, vol. 195, no. 1, pp. 91–101, May 2005.
[51] A. P. Newbery and P. S. Grant, “Large arc voltage fluctuations and droplet formation in electric arc wire spraying,” *Powder Metall.*, vol. 46, no. 3, pp. 229–235, Oct. 2003.
[52] Y. X. Chen, X. B. Liang, Y. Liu, S. C. Wei, and B. S. Xu, “Effect of heat treatment on microstructure and residual stress of wire arc sprayed high carbon steel coating,” *Surf. Eng.*, vol. 26, no. 6, pp. 407–412, Aug. 2010.
[53] A. Vardelle, M. Vardelle, and P. Fauchais, “Influence of velocity and surface temperature of alumina particles on the properties of plasma sprayed coatings,” *Plasma Chem. Plasma Process.*, vol. 2, no. 3, pp. 255–291, Sep. 1982.
[54] M. P. D. Apelian, “Melting and solidification in plasma spray deposition — phenomenological review,” *Int. Met. Rev.*, vol. 28, pp. 271–294, 1982.
[55] “High Velocity Oxygen Fuels Coatings,” *Thermal Spray Coatings - A&A Company, Inc.* [Online]. Available: http://www.thermalspray.com/hvof-coating/. [Accessed: 17-Mar-2015].
[56] C. M. Hackett, G. S. Settles, and J. D. Miller, “On the gas dynamics of HVOF thermal sprays,” *J. Therm. Spray Technol.*, vol. 3, no. 3, pp. 299–304, Sep. 1994.
[57] M. Li and P. D. Christofides, “Modeling and Control of High-Velocity Oxygen-Fuel (HVOF) Thermal Spray: A Tutorial Review,” *J. Therm. Spray Technol.*, vol. 18, no. 5–6, pp. 753–768, Mar. 2009.
[58] E. Irissou, J.-G. Legoux, A. N. Ryabinin, J. Bertrand, and C. Moreau, “Review on Cold Spray Process and Technology: Part I-Intellectual Property,” *Journal of Thermal Spray Technology*, vol. 17, no. 4, pp. 495–516, Dec. 2008.
[59] R. C. Dykhuizenq and M. F. Smith, “Gas Synamic Principles of Cold Spray,” *Journal of Thermal Spray Technology*, vol. 7, no. 2, pp. 205–212, Jun. 1998.

[60] A. Moridi, S. M. Hassani-Gangaraj, M. Guagliano, and M. Dao, "Cold spray coating: review of material systems and future perspectives," *Surface Engineering*, vol. 36, no. 6, pp. 369–395, 2014.
[61] T. Schmidt, H. Assadi, F. Gartner, H. Richter, T. Stoltenhoff, H. Kreye, and T. Klassen, "From Particle Acceleration to Impact and Bonding in Cold Spraying," *Journal of Thermal Spray Technology*, vol. 18, no. 5–6, pp. 794–808, Dec. 2009.
[62] A. Sova, S. Grigoriev, A. Okunkova, and I. Smurov, "Potential of cold gas dynamic spray as additive manufacturing technology," *Internation journal of advanced manufacturing technology*, vol. 69, pp. 2269–2278, 2013.
[63] R. Lupoi and W. O'Neill, "Powder stream characteritics in cold spray nozzles," *Surf. Coat. Technol.*, vol. 206, pp. 1069–1076, 2011.
[64] A. H. Shapiro, *The dynamics and thermodynamics of compressible fluid flow*, vol. 1, 2 vols. John Wiley & Sons, 1953.
[65] P. Richer, "Development of conventional and Nanocrystalline Bond Coats by Cold Gas Dynamic Spraying for Aerospace Thermal Barrier Coatings," University of Ottawa, 2010.
[66] T. Stoltenhoff, H. Kreye, and H. J. Richter, "An analysis of the cold spray process and its coatings," *Journal of Thermal Spray Technology*, vol. 11, no. 4, pp. 542–550, Dec. 2002.
[67] P. J.Pritchard, *Fox and McDonald's Introduction to Fluid Mechanics*, 8th ed. John Wiley & Sons, Inc., 2011.
[68] B. Jodoin, L. Ajdelsztajn, E. Sansoucy, A. Zúñiga, P. Richer, and E. J. Lavernia, "Effect of particle size, morphology, and hardness on cold gas dynamic sprayed aluminum alloy coatings," *Surf. Coat. Technol.*, vol. 201, no. 6, pp. 3422–3429, Dec. 2006.
[69] J. Pattison, S. Celotto, A. Khan, and W. O'Neill, "Standoff distance and bow shock phenomena in the Cold Spray process," *Surf. Coat. Technol.*, vol. 202, no. 8, pp. 1443–1454, Jan. 2008.
[70] V. F. Kosarev, S. V. Klinkov, A. P. Alkhimov, and A. N. Papyrin, "On some aspects of gas dynamics of the cold spray process," *J. Therm. Spray Technol.*, vol. 12, no. 2, pp. 265–281, Jun. 2003.
[71] S. Vladimirovich Klinkov, V. Fedorovich Kosarev, and M. Rein, "Cold spray deposition: Significance of particle impact phenomena," *Aerosp. Sci. Technol.*, vol. 9, pp. 582–591, 2005.
[72] T. Schmidt, F. Gartner, H. Assadi, and H. Kreye, "Development of a generalized parameter for cold spray deposition," *Acta Materialia*, vol. 54, pp. 729–742, 2006.
[73] W.-Y. Li, C.-J. Li, and H. Liao, "Significant influence of particle surface oxidation on deposition efficiency, interface microstructure and adhesive strength of cold-spray copper coatings," *Applied Surface Science*, vol. 256, pp. 4953–4958, 2010.
[74] M. Grujicic, J. R. Saylor, D. E. Beasley, W. S. DeRosset, and D. Helfritch, "Computational analysis of the interfacial bonding between feed-powder particles and the substrates in the cold-gas dynamic-spray process," *Appl. Surf. Sci.*, vol. 219, pp. 211–227, 2003.
[75] M. Grujicic, C. L. Zhao, W. S. DeRosset, and D. Helfritch, "Adiabatic shear instability based mechanism for particles/substrate bonding in the cold-gas dynamic -spray process," *Materials and Design*, vol. 25, pp. 681–688, 2004.
[76] X. M. Meng, J. . Zhang, W. Han, and J. Zhao, "Numerical and experimental investigation on effect of impact velocity on particle deposition characteristics in cold spraying," *Materials Research Innovation*, vol. 15, no. 4, pp. 283–289, 2011.
[77] T. Hussain, D. G. McCartney, and P. H. Shipway, "Impact phenomena in cold-spraying of titanium onto various ferrous alloys," *Surface and Coatings Technology*, vol. 205, pp. 5021–5027, 2011.
[78] P. C.King and M. Jahedi, "Relationsjip between particle size and deformation in the cold spray process," *Applied Surface Science*, vol. 256, pp. 1735–1738, 2010.

[79] K. Kim, M. Watanabe, K. Mitsuichi, K. Iakoubovskii, and S. Kuroda, "Impact bonding and rebounding between kinetically sprayed titanium particle and steel substrate revealed by high-resolution electron microscopy," *Journal of Physics D: Applied Physics*, vol. 42, pp. 1–5, 2009.

[80] Y. Xiong, X. Xiong, S. Yoon, G. Bae, and C. Lee, "Dependence of Bonding Mechanisms of Cold Sprayed Coatings on Strain-Rate-Induced Non-Equilibrium Phase Transformation," *Journal of Thermal Spray Technology*, vol. 20, no. 4, pp. 860–865, Jun. 2011.

[81] X.-T. Luo, C.-X. Li, F.-L. Shang, G.-J. Yang, Y.-Y. Wang, and C.-J. Li, "High velocity impact induced microstructure evolution during deposition of cold spray coatings: A review," *Surf. Coat. Technol.*, vol. 254, pp. 11–20, Jun. 2014.

[82] Y. Xiong, K. Kang, G. Bae, S. Yoon, and C. Lee, "Dynamic amorphization and recrystallization of metals in kinetic spray process," *Applied Phisics Letters*, vol. 92, pp. 1–3, Dec. 2008.

[83] Y. Zou, W. Qin, E. Irissou, J.-G. Legoux, S. Yue, and J. A. Szpunar, "Dynamic recrystallization in the particle/particle interfacial region of cold-sprayed nickel coating: Electron backscatter diffraction characterization," *Scripta Materialia*, vol. 61, pp. 899–902, 2009.

[84] V. V. Sobolev, J. M. Guilemany, J. Nutting, and J. R. Miquel, "Development of substrate-coating adhesion in thermal spraying," *International Materials Reviews*, vol. 42, no. 3, pp. 117–136, 1997.

[85] V. K. Champagne, D. Helfritch, P. Leyman, S. Grendahl, and B. Klotz, "Interfacial material mixing formed by the deposition of copper on aluminum by means of the cold spray process," *Journal of Thermal Spray Technology*, vol. 14, no. 3, pp. 330–334, Sep. 2005.

[86] L. Ajdelsztajn, B. Jodoin, G. E. Kim, and J. M. Schoenung, "Cold spray deposition of nanocrystalline aluminum alloys," *Metallurgical and Materials Transactions A*, vol. 36A, pp. 657–666, Mar. 2005.

[87] T. Hussain, D. G. McCartney, P. H. Shipway, and D. Zhang, "Bonding mechanisms in cold spraying: the contributions of metallurgical and mechanical components," *Journal of Thermal Spray Technology*, vol. 18, no. 3, pp. 364–379, Sep. 2009.

[88] D. Giraud, "Etude des composantes mécanique et métallurgique dans la liaison revêtement-substrat obtenue par projection dynamique par gaz froid pour les systèmes «Aluminium/Polyamide 6,6 » et « Titane/TA6V »," L'école national supérieur des mines de Paris, 2014.

[89] R. Ghelichi and M. Guagliano, "Coating by the cold spray process: a state of the art.," *Frattura Ed Integrità Strutturale*, vol. 8, pp. 30–44, 2009.

[90] A. O. Tokarev, "Structure of aluminum powder coatings prepared by cold gas dynamic spraying," *Metal Science and Heat Treatment*, vol. 38, no. 3, pp. 136–139, 1996.

[91] T. Marrocco, D. G. McCartney, P. H. Shipway, and A. J. Sturgeon, "Production of titanium deposits by cold-gas dynamic spray: Numerical modeling and experimental characterization," *Journal of Thermal Spray Technology*, vol. 15, no. 2, pp. 263–272, Jun. 2006.

[92] C. W. Ziemian, M. M. Sharma, B. D. Bouffard, T. Nissley, and T. J. Eden, "Effects of substrate surface roughening and cold spray coating on the fatigue life of AA2024 specimens," *Materials and Design*, vol. 54, pp. 212–221, 2014.

[93] W. A. González-Hermosilla, D. Chicot, J. Lesage, J. G. La Barbera-Sosa, I. C. Gruescu, M. H. Staia, and E. S. Puchi-Cabrera, "Effect of substrate roughness on the fatigue behavior of a SAE 1045 steel coated with a WC–10Co–4Cr cermet, deposited by HVOF thermal spray," *Material Science and Engineering A*, vol. 527, pp. 6551–6561, 2010.

[94] M. F. Bahnou, P. Nylén, and J. Wigren, “Effect of grit blasting and spraying angle on the adhesion strength of a plasma-sprayed coating,” *Journal of Thermal Spray Technology*, vol. 13, no. 4, pp. 508–514, Dec. 2004.
[95] D. Sen, N. M. Chaven, D. S. Rao, and G. Sundararajan, “Influence of grit blasting on the roughness and the bond strength of detonation sprayed coating,” *Journal of Thermal Spray Technology*, vol. 19, no. 4, pp. 805–815, Jun. 2010.
[96] Z. Arabgol, H. Assadi, T. Schmidt, F. Gartner, and T. Klassen, “Analysis of Thermal History and Residual Stress in Cold-Sprayed Coatings,” *J. Therm. Spray Technol.*, vol. 23, no. 1–2, pp. 84–90, Jan. 2014.
[97] V. Luzin, K. Spencer, and M.-X. Zhang, “Residual stress and thermo-mechanical properties of cold spray metal coatings,” *Acta Materialia*, vol. 59, pp. 1259–1270, 2011.
[98] M. Saleh, V. Luzin, and K. Spencer, “Analysis of the residual stress and bonding mechanism in the cold spray technique using experimental and numerical methods,” *Surf. Coat. Technol.*, vol. 252, pp. 15–28, Apr. 2014.
[99] T. S. Price, P. H. Shipway, and D. G. McCartney, “Effect of cold spray deposition of a titanium coating on fatigue behavior of a titanium alloy,” *Journal of Thermal Spray Technology*, vol. 15, no. 4, pp. 507–512, Dec. 2006.
[100] T. Suhonen, T. Varis, S. Dosta, M. Torrell, and J. M. Guilemany, “Residual stress development in cold sprayed Al, Cu and Ti coatings,” *Acta Materialia*, vol. 61, pp. 6329–6337, 2013.
[101] W. B. Choi, L. Li, V. Luzin, R. Neiser, T. Gnäupel-Herold, H. J. Prask, S. Sampath, and A. Gouldstone, “Integrated characterization of cold sprayed aluminum coatings,” *Acta Mater.*, vol. 55, no. 3, pp. 857–866, Feb. 2007.
[102] A. Moridi, S. M. Hassani-Gangaraj, S. Vezzu, and M. Guagliano, “Number of passes and thickness effect on mechanical characteristics of cold spray coating,” *Procedia Engineering*, vol. 74, pp. 449–459, 2014.
[103] S. Rech, A. Trentin, S. Vezzu, E. Vedelago, J.-G. Legoux, and E. Irissou, “Different Cold Spray Deposition Strategies: Single- and Multi-layers to Repair Aluminium Alloy Components,” *J. Therm. Spray Technol.*, vol. 11, pp. 1–14, Aug. 2014.
[104] G. E. Totten, *Handbook of Residual Stress and Deformation of Steel*. ASM International, 2002.
[105] X. Sun, *Failure Mechanisms of Advanced Welding Processes*. Elsevier, 2010.
[106] S. H. Teoh and K. H. Lee, *Fracture of Engineering Materials and Structures*. Springer Science & Business Media, 2012.
[107] B. Jodoin, F. Raletz, and M. Vardelle, “Cold spray modeling and validation using an optical diagnostic method,” *Surf. Coat. Technol.*, vol. 200, no. 14–15, pp. 4424–4432, Apr. 2006.
[108] M.-W. Lee, J.-J. Park, D.-Y. Kim, S. S. Yoon, H.-Y. Kim, S. C. James, S. Chandra, and T. Coyle, “Numerical Studies on the Effects of Stagnation Pressure and Temperature on Supersonic Flow Characteristics in Cold Spray Applications,” *J. Therm. Spray Technol.*, vol. 20, no. 5, pp. 1085–1097, Mar. 2011.
[109] S. Yin, X. Suo, H. Liao, Z. Guo, and X. Wang, “Significant influence of carrier gas temperature during the cold spray process,” *Surf. Eng.*, vol. 30, no. 6, pp. 443–450, Apr. 2014.
[110] J. Wu, H. Fang, S. Yoon, H. Kim, and C. Lee, “Measurement of particle velocity and characterization of deposition in aluminum alloy kinetic spraying process,” *Appl. Surf. Sci.*, vol. 252, no. 5, pp. 1368–1377, Dec. 2005.
[111] S. H. Zahiri, D. Fraser, S. Gulizia, and M. Jahedi, “Effect of processing conditions on porosity formation in cold gas dynamic spraying of copper,” *J. Therm. Spray Technol.*, vol. 15, no. 3, pp. 422–430, Sep. 2006.

[112] K. Taylor, B. Jodoin, and J. Karov, “Particle loading effect in cold spray,” *J. Therm. Spray Technol.*, vol. 15, no. 2, pp. 273–279, Jun. 2006.
[113] É. I. J. G. Legoux, “Effect of Substrate Temperature on the Formation Mechanism of Cold-Sprayed Aluminum, Zinc and Tin Coatings,” *J. Therm. Spray Technol.*, vol. 16, no. 5, pp. 619–626, 2007.
[114] H. W. M. Fukumoto, “Effect of Substrate Temperature on Deposition Behavior of Copper Particles on Substrate Surfaces in the Cold Spray Process,” vol. 16, no. 5, pp. 643–650, 2007.
[115] G. B. Peter C. King, “An Experimental and Finite Element Study of Cold Spray Copper Impact onto Two Aluminum Substrates,” *J. Therm. Spray Technol.*, vol. 19, no. 3, pp. 620–634, 2009.
[116] X. W. Shuo Yin, “Examination on Substrate Preheating Process in Cold Gas Dynamic Spraying,” *J. Therm. Spray Technol.*, vol. 20, no. 4, pp. 852–859, 2011.
[117] S. Rech, A. Trentin, S. Vezzu, J.-G. Legoux, E. Irissou, and M. Guagliano, “Influence of Pre-Heated Al 6061 Substrate Temperature on the Residual Stresses of Multipass Al Coatings Deposited by Cold Spray,” *J. Therm. Spray Technol.*, vol. 20, no. 1–2, pp. 243–251, Jan. 2011.
[118] M. Yu, W.-Y. Li, F. F. Wang, and H. L. Liao, “Effect of preheating on deformation in cold spraying dissimilar combinations,” *Surf. Eng.*, vol. 30, no. 5, pp. 329–334, Dec. 2013.
[119] M. Y. X. K. Suo, “Effect of Substrate Preheating on Bonding Strength of Cold-Sprayed Mg Coatings,” *J. Therm. Spray Technol.*, vol. 21, no. 5, 2012.
[120] B. R. Marple and C. Moreau, *Thermal Spray 2003: Advancing the Science And Applying the Technology*, Illustrated edition edition. Materials Park, OH: ASM International, 2003.
[121] S. Yin, X. Suo, J. Su, Z. Guo, H. Liao, and X. Wang, “Effects of Substrate Hardness and Spray Angle on the Deposition Behavior of Cold-Sprayed Ti Particles,” *J. Therm. Spray Technol.*, vol. 23, no. 1–2, pp. 76–83, Apr. 2013.
[122] F. F. Xuemei Wang, “Characterization and Modeling of the Bonding Process in Cold Spray Additive Manufacturing,” *Addit. Manuf.*, 2015.
[123] S. Yin, Y. Sun, X. Wang, Z. Guo, and H. Liao, “Effect of Spray Angle on Temperature Distribution within the Metallic Substrate in Cold Spraying,” *J. Therm. Spray Technol.*, vol. 22, no. 6, pp. 983–991, May 2013.
[124] S. H. Zahiri, W. Yang, and M. Jahedi, “Characterization of Cold Spray Titanium Supersonic Jet,” *J. Therm. Spray Technol.*, vol. 18, no. 1, pp. 110–117, Nov. 2008.
[125] C. Widener, M. Carter, and G. Crawford, “CS repair ad refubishment development at SDSM& T,” presented at the CSAT 2015, Worcester,MA, 23-Jun-2015.
[126] A. Papyrin, V. Kosarev, S. Klinkov, A. Alkhimov, and V. M. Fomin, *Cold Spray Technology*. Elsevier, 2006.
[127] H. Herman, S. Sampath, and R. McCune, “Thermal Spray: Current Status and Future Trends,” *MRS Bull.*, vol. 25, no. 07, pp. 17–25, Jul. 2000.
[128] S. Sampath, X. Y. Jiang, J. Matejicek, L. Prchlik, A. Kulkarni, and A. Vaidya, “Role of thermal spray processing method on the microstructure, residual stress and properties of coatings: an integrated study for Ni–5 wt.%Al bond coats,” *Mater. Sci. Eng. A*, vol. 364, no. 1–2, pp. 216–231, Jan. 2004.
[129] D. A. MacDonald, “Restoration of Aluminum Aerospace Parts and Coatings using Cold Gas Dynamic Spraying,” Univeristy of Ottawa, Ottawa, Canada, 2014.
[130] D. J. C. A. C. Hall, “The effect of a simple annealing heat treatment on the mechanical properties of cold-sprayed aluminum,” *J. Therm. Spray Technol.*, vol. 15, no. 2, pp. 233–238, 2006.

[131] T. H. Van Steenkiste, J. R. Smith, and R. E. Teets, "Aluminum coatings via kinetic spray with relatively large powder particles," *Surf. Coat. Technol.*, vol. 154, no. 2–3, pp. 237–252, May 2002.
[132] V. K. Champagne, D. J. Helfritch, M. D. Trexler, and B. M. Gabriel, "The effect of cold spray impact velocity on deposit hardness," *Model. Simul. Mater. Sci. Eng.*, vol. 18, no. 6, p. 065011, Sep. 2010.
[133] K. Balani, T. Laha, A. Agarwal, J. Karthikeyan, and N. Munroe, "Effect of carrier gases on microstructural and electrochemical behavior of cold-sprayed 1100 aluminum coating," *Surf. Coat. Technol.*, vol. 195, no. 2–3, pp. 272–279, May 2005.
[134] D. L. Gilmore, R. C. Dykhuizen, R. A. Neiser, M. F. Smith, and T. J. Roemer, "Particle velocity and deposition efficiency in the cold spray process," *J. Therm. Spray Technol.*, vol. 8, no. 4, pp. 576–582, Dec. 1999.
[135] X. K. Suo, T. K. Liu, W. Y. Li, Q. L. Suo, M. P. Planche, and H. L. Liao, "Numerical study on the effect of nozzle dimension on particle distribution in cold spraying," *Surf. Coat. Technol.*, vol. 220, pp. 107–111, Apr. 2013.
[136] F. Raletz, M. Vardelle, and G. Ezo'o, "Critical particle velocity under cold spray conditions," *Surf. Coat. Technol.*, vol. 201, no. 5, pp. 1942–1947, Oct. 2006.
[137] H. Fukanuma, N. Ohno, B. Sun, and R. Huang, "In-flight particle velocity measurements with DPV-2000 in cold spray," *Surf. Coat. Technol.*, vol. 201, no. 5, pp. 1935–1941, Oct. 2006.
[138] X.-J. Ning, J.-H. Jang, and H.-J. Kim, "The effects of powder properties on in-flight particle velocity and deposition process during low pressure cold spray process," *Aplied surface science*, vol. 253, pp. 7449–7455, 2007.
[139] M. T. DeMeuse, *High Temperature Polymer Blends*. Elsevier, 2014.
[140] "MatWeb Material Property Data," *MAtWeb*, 2015-1996. [Online]. Available: http://www.matweb.com/services/services.aspx. [Accessed: 19-May-2015].
[141] A. List, F. Gärtner, T. Schmidt, and T. Klassen, "Impact Conditions for Cold Spraying of Hard Metallic Glasses," *J. Therm. Spray Technol.*, vol. 21, no. 3–4, pp. 531–540, Feb. 2012.
[142] T. Stoltenhoff, C. Borchers, F. Gartner, and H. Kreye, "Microstructures and Key Properties of Cold-Sprayed and Thermally Sprayed Copper Coatings," *Surf. Coat. Technol.*, vol. 200, pp. 4947–4960, 2006.
[143] R. S. Lima, A. Kucuk, C. C. Berndt, J. Karthikeyan, C. M. Kay, and J. Lindemann, "Deposition efficiency, mechanical properties and coating roughness in cold-sprayed titanium," *J. Mater. Sci. Lett.*, vol. 21, no. 21, pp. 1687–1689, Nov. 2002.
[144] Y. Zhang, N. Brodusch, S. Descartes, R. R. Chromik, and R. Gauvin, "Microstructure refinement of cold-sprayed copper investigated by electron channeling contrast imaging," *Microsc. Microanal. Off. J. Microsc. Soc. Am. Microbeam Anal. Soc. Microsc. Soc. Can.*, vol. 20, no. 5, pp. 1499–1506, Oct. 2014.
[145] K. Balani, A. Agarwal, S. Seal, and J. Karthikeyan, "Transmission electron microscopy of cold sprayed 1100 aluminum coating," *Scr. Mater.*, vol. 53, no. 7, pp. 845–850, Oct. 2005.
[146] G. R. Anstis, P. Chantikul, B. R. Lawn, and D. B. Marshall, "A critical evaluation of indentation techniques for measuring fracture toughness: I, Direct crack measurements," *J. Am. Ceram. Soc.*, vol. 64, no. 9, pp. 533–538, 1981.
[147] M. Atkinson, "Further analysis of the size effect in indentation hardness tests of some metals," *J. Mater. Res.*, vol. 10, no. 11, pp. 2908–2915, 1995.
[148] A. A. Elmustafa and D. S. Stone, "Indentation size effect in polycrystalline F.C.C. metals," *Acta Mater.*, vol. 50, no. 14, pp. 3641–3650, Aug. 2002.
[149] K. Sangwal, "On the reverse indentation size effect and microhardness measurement of solids," *Mater. Chem. Phys.*, vol. 63, no. 2, pp. 145–152, Feb. 2000.

[150] X.-L. Gao, “An expanding cavity model incorporating strain-hardening and indentation size effects,” *Int. J. Solids Struct.*, vol. 43, no. 21, pp. 6615–6629, Oct. 2006.
[151] G. M. Pharr, E. G. Herbert, and Y. Gao, “The Indentation Size Effect: A Critical Examination of Experimental Observations and Mechanistic Interpretations,” *Annu. Rev. Mater. Res.*, vol. 40, no. 1, pp. 271–292, 2010.
[152] Q. Wang, N. Birbilis, and M.-X. Zhang, “Process optimisation of cold spray Al coating on AZ91 alloy,” *Surf. Eng.*, vol. 30, no. 5, pp. 323–328, Jan. 2014.
[153] S. Grigoriev, A. Okunkova, A. Sova, P. Bertrand, and I. Smurov, “Cold spraying: From process fundamentals towards advanced applications,” *Surf. Coat. Technol.*, vol. 268, pp. 77–84, Apr. 2015.
[154] R. C. Dykhuizen and M. F. Smith, “Gas dynamic principles of cold spray,” *J. Therm. Spray Technol.*, vol. 7, no. 2, pp. 205–212, Jun. 1998.
[155] V. F. Kosarev, S. V. Klinkov, A. P. Alkhimov, and A. N. Papyrin, “On some aspects of gas dynamics of the cold spray process,” *J. Therm. Spray Technol.*, vol. 12, no. 2, pp. 265–281, Jun. 2003.
[156] C.-J. Li, W.-Y. Li, Y.-Y. Wang, G.-J. Yang, and H. Fukanuma, “A theoretical model for prediction of deposition efficiency in cold spraying,” *Thin Solid Films*, vol. 489, no. 1–2, pp. 79–85, Oct. 2005.
[157] P. Richer, B. Jodoin, and L. Ajdelsztajn, “Substrate roughness and thickness effects on cold spray nanocrystalline Al−Mg coatings,” *J. Therm. Spray Technol.*, vol. 15, no. 2, pp. 246–254, Jun. 2006.
[158] “Opta Minerals Inc.,” 2014. [Online]. Available: http://optaminerals.com/Abrasives. [Accessed: 30-Mar-2015].
[159] I. M. Hutchings, “Strain rate effects in microparticle impact,” *J. Phys. Appl. Phys.*, vol. 10, no. 14, p. L179, Oct. 1977.
[160] P. C. King and M. Jahedi, “Relationship between particle size and deformation in the cold spray process,” *Appl. Surf. Sci.*, vol. 256, no. 6, pp. 1735–1738, Jan. 2010.

Appendix I

Temperature and Time Exposure Limits for Aluminum Alloys

ALLOY	CONDITION	MAXIMUM CUMULATIVE TIME – HOURS 1/						
		250°F (121°C)	275°F (135°C)	300°F (149°C)	325°F (165°C)	350°F (177°C)	375°F (191°C)	600°F (316°C)
2014	–T6XX –W	32 4/ 32 4/	32 4/ 32 4/	10 32 4/	10 10	2 1	1/2 3/	3/
2024 2124 2219	–T6X, –T72 –T8XX	32 4/ 32 4/	32 4/ 32 4/	10 10	10 10	1 7	1/2 2	3/ 3/
2090	–T6X –T8X	1 1	1 1	1 1	3/4 3/4	3/4 3/4	3/4 3/4	3/ 3/
6061	–T6XX	32 4/	32 4/	10	10	3	3/4	3/
7075 7178	–T6XX –W –T76XX	32 4/ 10 32 4/	8 1 10	2 3/ 4	3/4 3/ 1	3/ 3/ 1/2	3/ 3/ 3/	3/ 3/ 3/
7049 7075	–T73XX	32 4/	32 4/	10	3	3/4	3/	3/
7050 7075 7175	–T74XX	32 4/	8	2	3/4	3/	3/	3/
7079	–T6XX	10	1	3/	3/	3/	3/	3/
8090	–T8X	2/	2/	10	3/	3/	3/	3/

NOTES: 1/ The sum of fractional times at different temperatures must not exceed one, e.g., for a 6061 part exposed at 300°F (149°C) for 5 hours, another 5 hours at 325°F (163°C) or another 1–1/2 hours at 350°F (177°C) is acceptable.

2/ Do not form or straighten at this temperature to avoid orange peel or excessive residual stresses.

3/ Do not form or straighten at this temperature to avoid overheating and loss in strength.

4/ Times in excess of 32 hours require review by Material and Process (Dept. 679) prior to exceeding 32 hours exposure.

Figure A 1: Exposure time and temperatures for aluminum alloys materials to avoid softening.

Appendix II
Adhesion Test Preparation Procedure

Mounting procedure of FM1000 on samples

1. Machine minimal thickness off of coatings to ensure surface is flat.

2. Remove the FM1000 glue from refrigerator and put in a stove at 70-80^{o}C for 45 min to 1 h. This will ensure there is no humidity in the glue.

3. Grit blast the uncoated bond plug with Al_2O_3 80 mesh at an angle of 45 degree, at a pressure of 0.34 MPa and a distance of 50.8 mm-127 mm.

4. Preheat the stove to 190^{o}C (this will guarantee a minimum temperature of 177 °C everywhere in the oven).

5. Sand the faces of machined sample on a 240 grit paper without applying pressure in a slow figure eight shape. Clean the face with compress air to remove all dust and residue. The goal of this step is to have raw metal. Do not touch the surface with fingers.

6. Place the coated sample on the bottom part of the fixture.

7. Carefully place disk of glue on each sample.

8. Put the opposite sample gently on the FM1000 glue.

9. Ensure that the two bond plugs are aligned perfectly.

10. Use a torque wrench at a torque of 3.0 Nm to tighten the samples.

11. Place the fixture in the oven for at least 2 hours at 190 ^{o}C.

12. After 2 hours of curing, turn oven off and let it cold down while keeping the stove door closed.

13. When the fixtures are cool, remove the samples from the oven. The glue should have changed to yellow. Disassemble all the sample of the fixture without imposing forces on the samples (take them gently by the two sides and without tension, compression or shear force).

14. Test the samples.

Appendix III
Al2024 Powder Deposition Inconsistency

Inconsistencies in the deposition of Al2024 powder have been encountered in the course of the current research. Initial tests have been produced using a single 5 kg powder container immediately after it has been acquired and received. Later in the project, another 5 kg container from a different batch has been opened and used to continue the tests. However, major variations in the deposition efficiency have been detected during the spray of the powder from the second container. These discrepancies have limited the number of produced and tested cold sprayed repairs using the Al2024 powder.

The first row in Table A 1 shows the obtained initial cold sprayed full repair of 38 mm diameter Al2024-T351 substrates. Figure 1a depicts a successful 3.8 mm cold spray repair. However, a coating of only 1 mm was produced using the same process parameters but a second powder batch, as shown in Figure 1b. Furthermore, Figure 2a and Figure 2b show the difference in coating surface profile when sprayed using the initial batch and new batch respectively, from which a major difference in deposition (i.e thickness) can be observed. The last row in the table below shows the general microstructure of the Al2024 coatings, obtained at the start of the research, on Al2024-T351 flat substrates. The average thickness of the presented coating sprayed at 500 ˚C and 3.45 MPa reaches approximately 1000 µm. The deposition obtained with the powder from the second batch only reaches 288 µm, which is less than half of the initial deposition efficiency. Moreover, despite the differences in deposition, all coatings produced using different containers were still dense.

Table A 1:Al2024 Powder Deposition Variation

	Powder Batch 1	Powder Batch 2
Al2024 coating on 1.5inch diameter substrate	1a 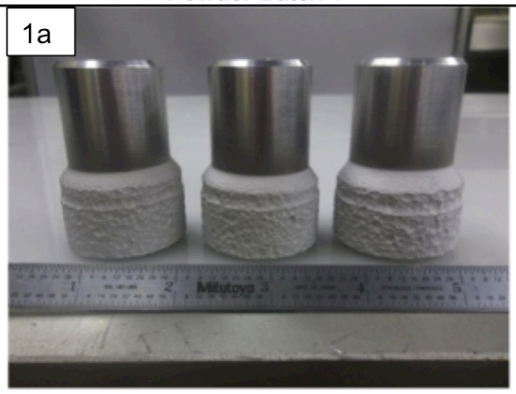 Coating thickness: ~3.80 mm	1b 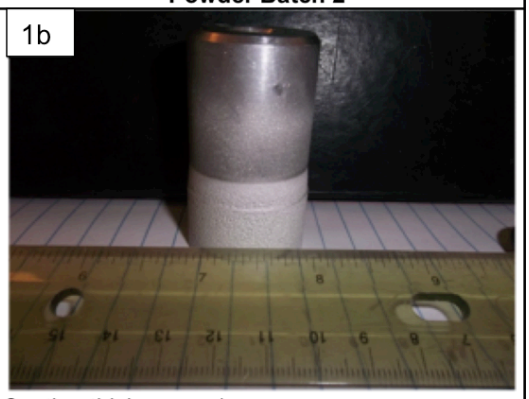 Coating thickness: ~1 mm
Al2024c coating on flat substrate	2a 	2b 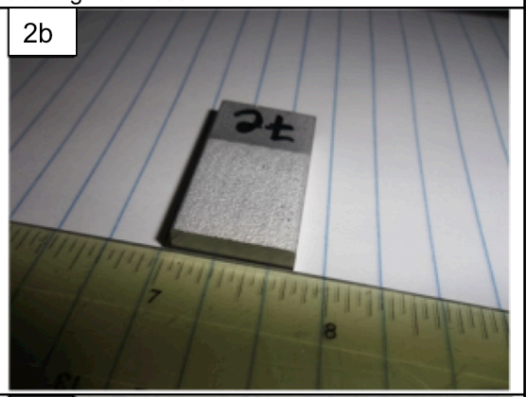
Coating (3a and 3b) thickness	3a 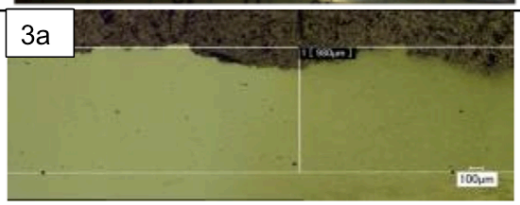 Coating thickness: ~1000 μm	3b 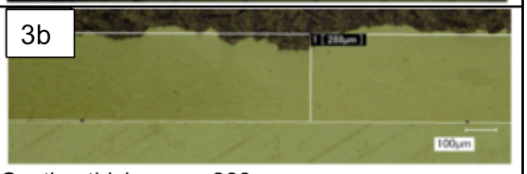 Coating thickness: ~288 μm

The first step that was undertaken to understand the cause of such decrease in powder deposition efficiency was the analysis of the powder size using the scanning electron microscope. Figure A 2 depicts the obtained results and shows that a large gap in powder size distribution was discovered between the two used containers. The first Al2024 powder batch seems to be mostly composed of spherical particles less than 20 μm while the second container seems to be a mixture of irregularly shaped particles larger than 20 μm. After this brief examination, the powder from the second batch was sieved to a specific 0- 20 μm size range using a W. S. Tyler (model RX-29) sieving machine.

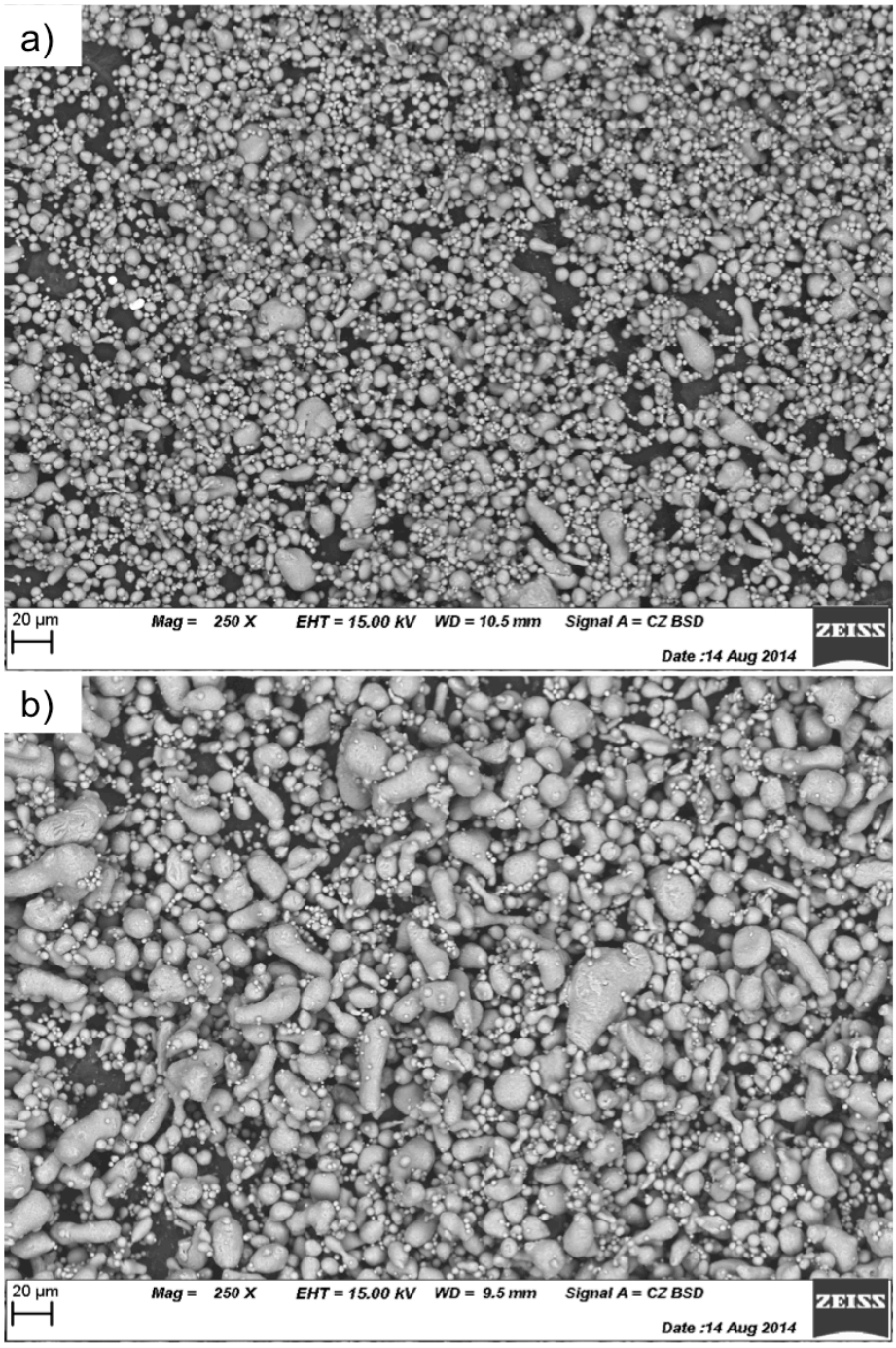

Figure A 2: Powder size distribution variation between different Al2024 containers a) first container and b) second container.

The sieved powder was sprayed and the obtained coating is shown in Figure A 3. The generated dense deposition reaches only a thickness of 214.35 ± 14.97 µm.

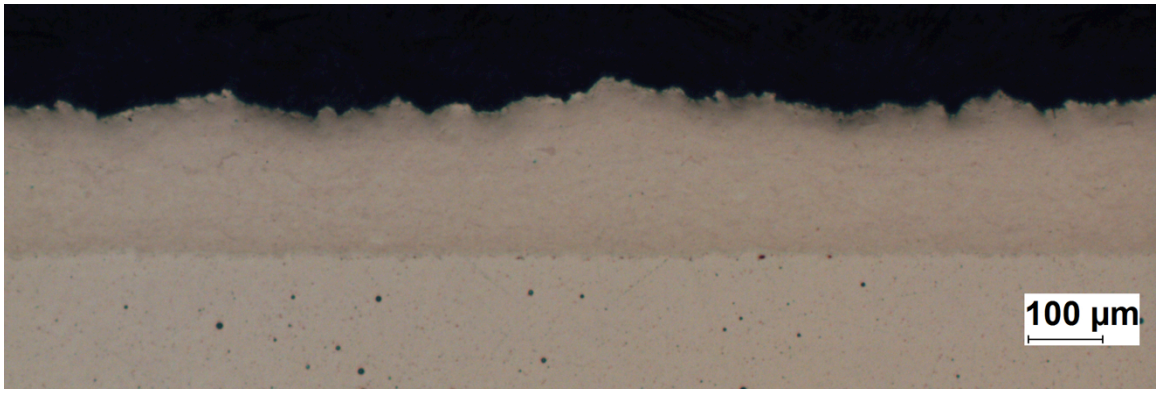

Figure A 3: Al2024 coating sprayed using a second powder container at 11.25 g/min with particle size less than 20 µm.

Based on this result, it was concluded that the initial coatings have not been primarily composed of small spherical particles. Subsequently, it was discovered that the SEM micrographs shown in Figure A 2 where not representative of the powder size distribution as the powder samples have been taken in opposite locations inside the container. When the analysis was undertaken, only a small quantity of the initial powder was left in the bottom of the first container while for the second container, the examined powder was acquired from the very top of the powder mass inside the container. Since the second container was unused for couple of months after its purchase, intrinsic sieving inside the container occurred. Small particles where displaced to the bottom of the container, which created a gradual particle size variation inside the container, which explains the large particle distribution obtained during the SEM examination.

Subsequently to the discovery of the presence of inherent sieving inside the second container, coatings were sprayed after the container was well shaken to avoid preferential particle distribution. The obtained dense coating is shown in Figure A 4 and its thickness reaches 355.61 ± 9.61 µm. To examine in more details the degree of decrease in powder deposition efficiency using the second container, coatings were sprayed at various mass feeding rates and compared with the results obtained at the start of the project.

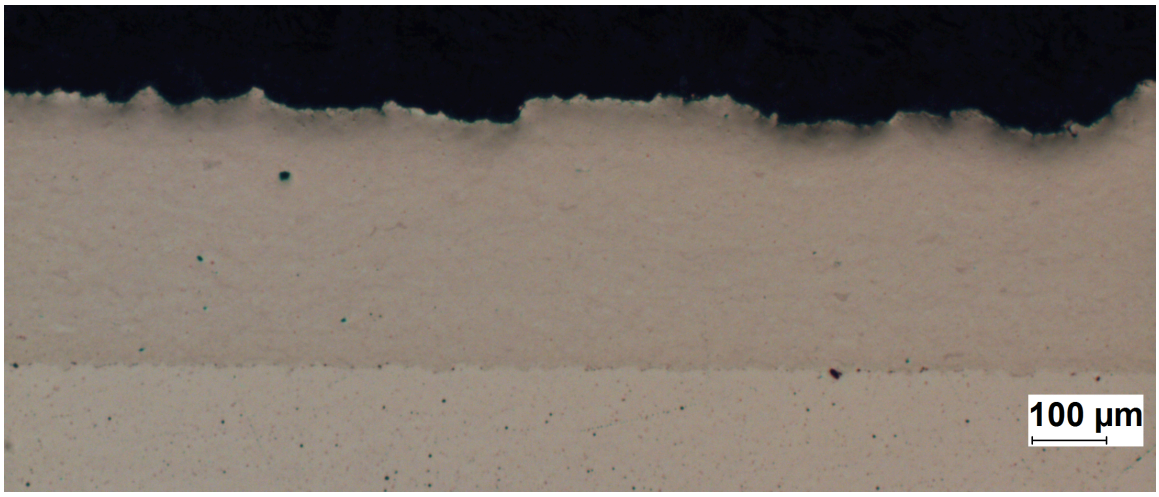

Figure A 4: Coating sprayed at 11.25 g/min mass feeding rate using the second Al2024 container after it was well shaken to avoid preferential size distribution.

Figure A 5 shows the Al2024 coating thickness obtained for different powder feeding rates sprayed using the second 5 kg container at maximum process parameters. It also compares the thicknesses with the ones generated at the start of the project using the first Al2024 container. The average difference in thickness for mass feeding rates ranging between 11.25 g/min and 21 g/min is approximately 520 µm. At a feeding rate of 18 g/min, the coating thickness reached 836.78± 35.46 µm while this thickness was achieved only at 11.25 g/min at the start of the project using the first powder container. The coating deposition still grows linearly with increasing mass feeding rates, using the second powder batch, but at a lower rate.

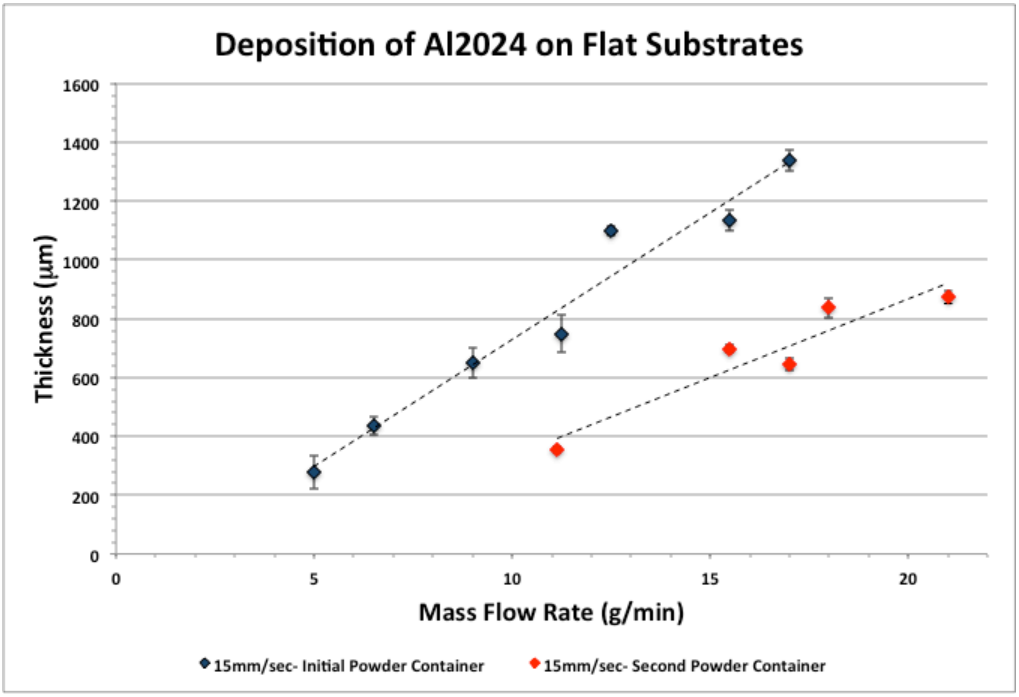

Figure A 5:Al2024 coating thickness before and now.

Figure A 6 shows cross-sections of the deposition obtained at 500 °C and 3.45 MPa using the second 5 kg container of Al2024 powder at various mass feeding rates. Besides having what appears to be large size porosity at few locations, all coatings are dense.

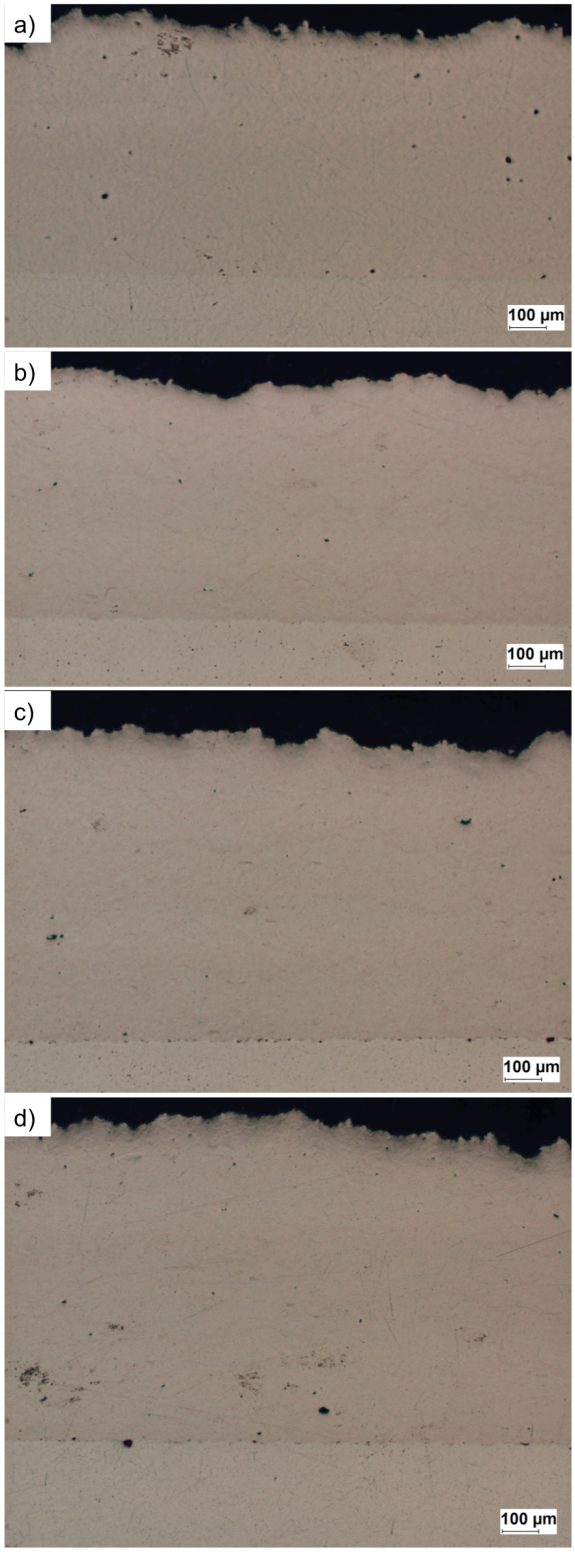

Figure A 6: New batch of Al2024 coatings obtained for different powder feeding rates; a) 15.5 g/min b) 17 g/min, c) 18 g/min and d) 21 g/min.

The problem surrounding the poor powder deposition efficiency was then focused on the possibility of being a result of humidity in the powder, which could cause particle agglomeration and affect the powder mass feeding rate. Even if the powder container was stored in a low humidity (<25 %) room (i.e. not in a humidity controlled cabinet due to the lack of space for a 5 kg container), lack of control on the room aeration from the adjacent laboratory space through the door, increased the possibility of powder humidity issues. Thus, to eliminate any possibilities of powder agglomeration due to humidity, a specific quantity of powder has been dried at 80 °C for 3 hours before spaying at a mass feeding rate of 11.25 g/min. Figure A 7 shows the obtained coating, which has a thickness of 398.26 ± 27.09 μm, which represents an increase of approximately 43 μm in deposition. This thickness is however still 602 μm thinner than the initial Al2024 coatings. Therefore, humidity seems to not be the factor influencing the powder deposition process.

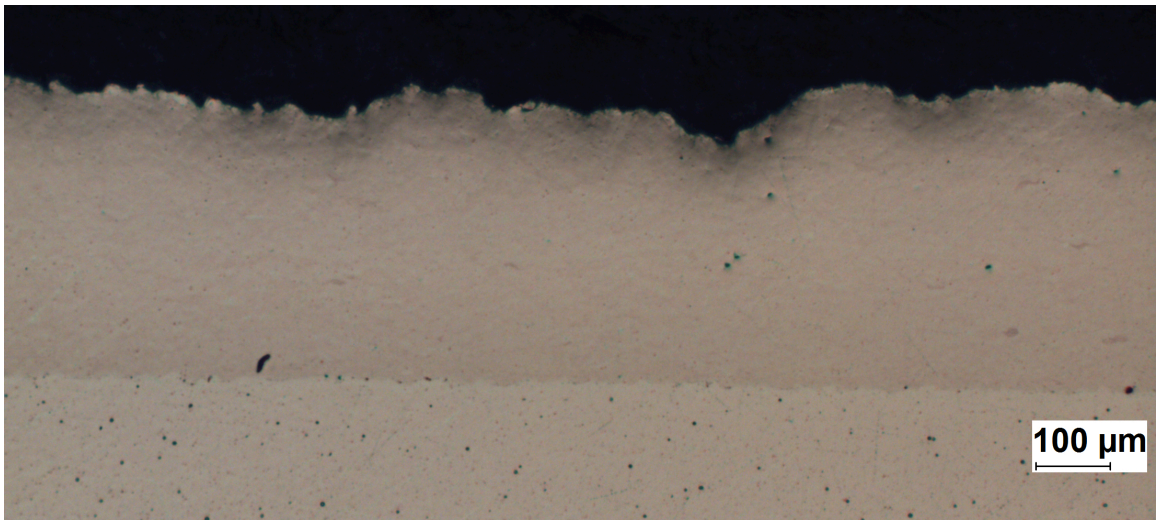

Figure A 7: Al2024 coating sprayed at 11.25 g/min at maximum parameters using dried powder from the second container.

The powder chemical composition was also verified through the EDS analysis and dissimilarities with the initial powder have not been detected.

Additional brief tests were conducted to verify the spray process parameters required to reach the original coating thickness. The first generated coating was obtained using 11.25 g/min but double the number of passes (i.e. 10 passes). The resulting coating cross-section is shown in

Figure A 8 and its thickness reaches 830.4 ± 32.33 µm. Based on the results presented in Figure A 5, the coating growth process is gradual and proportional to the number of passes. Thus, more than double the amount of passes need to be used to acquire the original coating thickness and based on the results from Figure A 5, more than double the amount of powder needs to be sprayed as well.

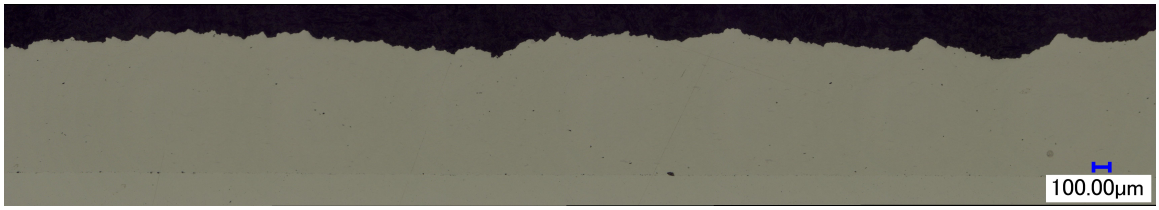

Figure A 8: Coating generated using Al2024 powder from the second container and sprayed at maximal parameters using 11.25 g/min and 10 passes.

The last test that was conducted, using the powder from the second container, is the production of a coating using a nozzle traverse speed of 5 mm/s, which represents the third from what was initially used (i.e. 15 mm/s). Figure A 9 shows the micrograph of the 1134 ± 66.10 µm dense obtained coating.

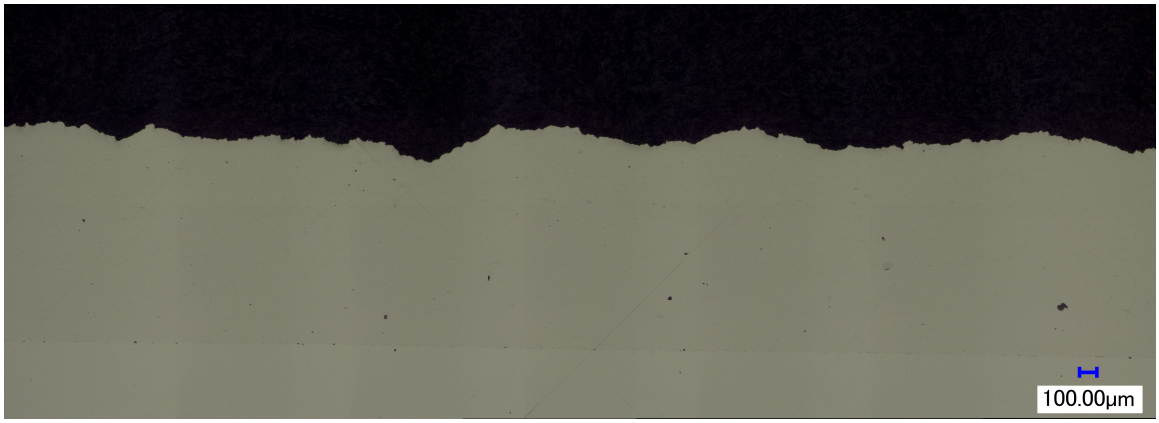

Figure A 9: Coating generated using Al2024 powder from the second container and sprayed at maximal parameters using 11.25 g/min and a gun traverse speed of 5mm /sec.

As such, using the same powder feeding rate of 11.25 g/min, a 5 mm/s gun traverse speed is required to achieve the initial coating thickness.

Two other Al2024 powder containers that have been ordered and received at the same time as the two analyzed ones have also been examined. The results also showed a large decrease in powder deposition efficiency. A difference in oxide film thickness between the powders might be the cause of such deposition discrepancies. A larger particle oxide layer absorbs a larger amount of energy during the particle impact. Thus, the particle kinetic energy would predominantly be dissipated to break the oxide layer, which would decrease the particle deformation process and consequently its deposition and adhesion. This, however, has not been further analyzed in the current study.

At this stage of the research, due to the severe decrease in Al2024 powder deposition efficiency, no further repairs of components have been produced. The powder and gas consumption required to achieve full restoration of the component dimensions would have exceeded our resources. Also, the deposition rate obtained at the maximum spray parameters would not of been a practical and/or reasonable solution for a repair process in any industry.